

Tracing Baryons in the Warm Hot Intergalactic Medium using Broad Lyman- α Absorbers

A thesis submitted
in partial fulfillment for the award of the degree of

Master of Science

in

Astronomy and Astrophysics

by

Sameer Patidar

under the guidance of

Dr. Vikram Khaire and Dr. Anand Narayanan



**Department of Earth and Space Sciences
Indian Institute of Space Science and Technology
Thiruvananthapuram, India**

May 2024

Certificate

This is to certify that the thesis titled *Tracing Baryons in the Warm Hot Intergalactic Medium using Broad Lyman- α Absorbers* submitted by **Sameer Patidar**, to the Indian Institute of Space Science and Technology, Thiruvananthapuram, in partial fulfillment for the award of the degree of **Master of Science in Astronomy and Astrophysics** is a bona fide record of the original work carried out by him under our supervision. The contents of this thesis, in full or in parts, have not been submitted to any other Institute or University for the award of any degree or diploma.

Dr. Vikram Khaire
Inspire Professor
Department of Earth and
Space Sciences, IIST

Dr. Anand Narayanan
Professor
Department of Earth and
Space Sciences, IIST

Dr. Rama Rao Nidamanuri
Professor and Head of Department
Department of Earth and Space Sciences, IIST

Place : Thiruvananthapuram
Date : 10 May 2024

Declaration

I declare that this thesis titled ***Tracing Baryons in the Warm Hot Inter-galactic Medium using Broad Lyman- α Absorbers*** submitted in partial fulfillment for the award of the degree of **Master of Science in Astronomy and Astrophysics** is a record of the original work carried out by me under the supervision of **Dr. Vikram Khare** and **Dr. Anand Narayanan**, and has not formed the basis for the award of any degree, diploma, associateship, fellowship, or other titles in this or any other Institution or University of higher learning. In keeping with the ethical practice in reporting scientific information, due acknowledgments have been made wherever the findings of others have been cited.

Place : Thiruvananthapuram

Sameer Patidar

Date : 10 May 2024

(SC19B161)

Dedicated to Daddu & Dadi...

Acknowledgement

I take this opportunity to express my heartfelt gratitude to my supervisors Dr. Vikram Khaire and Dr. Anand Narayanan for their valuable guidance and support throughout the project. I thank Dr. Vikram Khaire for arranging meetings at very unearthly hours also and Dr. Anand Narayanan whose office doors were always open for discussions. I would also like to thank all other faculty members including Dr. Anandmayee Tej, Dr. Samir Mandal, Dr. Jagadheep D, Dr. Resmi L and Dr. Sarita Vig for their invaluable time and making the course-work an enjoyable ride. I also thank Dr. Thomas Shanks for providing us with the valuable data from VIMOS survey.

I am grateful to all my family members including two loving *Canis lupus familiaris* Jonty and Dom, whose love and consistent support allowed me to withstand all the difficulties and helped me grow and prosper. I am thankful to all my friends, especially Jay, Harshit, Sankalp, Prajwal, Shriya and all my cricket buddies, to create such a fun-filled environment which felt like home away from home and for all the memories which I'll cherish for lifetime. I would also like to thank my seniors Mrs. Surya for extended discussions on learning VPFIT and Mr. Dheeraj to acquaint me with using CLOUDY.

Last but not the least I would like to thank my psychiatrists Dr. Kumar and Dr. Rashmi, perhaps, without whom I would not have been in a state to continue the course. And I apologise to everyone else whose name is not mentioned or inaptly missed.

Sameer Patidar

Abstract

Baryons have an intricate structure in our present universe ($z \sim 0$). Around 80% of them are residing outside the collapsed structures of galaxies, groups and galaxy clusters in the intergalactic medium (IGM). Even in IGM they exist in multi-phase structure, viz in cool ($T \sim 10^4$ K) photoionised phase in the form of Lyman- α forests, constituting about 30% of the total baryon budget and other 50% in the warm-hot phase called Warm Hot Intergalactic Medium (WHIM) with temperature in the ranges of $10^5 - 10^7$ K. The WHIM has been challenging to observe leading to uncertainties in the baryon census in this phase. This has led to ‘the missing baryon problem’ in the current universe which states that around 30% of the baryons in present universe are missing from our observations.

In the present work we aim to address these uncertainties. We use high S/N HST/COS data to probe WHIM using Broad Lyman- α Absorbers (BLAs). BLAs are absorbers which have been thermally broadened to Doppler parameters in excess $40-45$ km s $^{-1}$ due to high temperature which these BLAs trace. BLAs are expected to large reservoirs of baryons in the current universe, so we do a comprehensive survey of these BLAs to find the baryon content in them.

In the first part of the work we study an interesting absorber system towards the line of sight of quasar PG 0003+158, which has a BLA candidate. We first fit the Voigt profiles to the absorption lines in the absorber system and then model the ionisation conditions in the absorber cloud to infer its ionisation state. Along with studying the galaxy neighbourhood of the absorber system we infer that the absorber is residing in a galaxy under-dense region and could be tracing a reservoir of baryons in a large scale filamentary structure in the cosmic web or CGM of a

sub-L^{*} galaxy.

The second part of the work includes our ambitious goal of survey the BLAs. For this BLA survey we found 29 suitable BLA candidates along 22 sight lines. The survey has a total H I (Lyman- α) unblocked redshift pathlength of $\Delta z = 5.561$. We perform Voigt profile measurements on these absorbers and also model the ionisation conditions prevailing in these systems. We identified absorption from 15 distinct metal ions apart from H I absorption in our survey totalling to 711 absorption lines. We have modelled the ionisation conditions in 39 of the components in these 29 systems. Further, we use the results from the survey to estimate the baryon content of BLAs. We find that BLAs can contribute around 15-20 % to the total cosmic baryon energy density and could be potential reservoirs of the ‘missing baryons’.

Contents

Abstract	v
List of Figures	ix
List of Tables	xv
1 Introduction	1
1.1 Where are the baryons?	1
1.2 Detecting WHIM	3
1.3 Detecting WHIM using BLAs	4
1.4 Road-map for the Current Project	6
2 Data and Pre-processing	7
2.1 HST/COS data	7
2.2 Pre-processing	8
3 Voigt Profile Fitting	9
3.1 Voigt Profile	9
3.2 VPFIT	12
4 Modelling the Ionisation Conditions	16
4.1 Ionisation Modelling	16
4.2 CLOUDY	16
4.3 Ionization Model Based Parameter Estimation	18

5 Absorber towards PG 0003+158	21
5.1 Component structure of the absorber system	21
5.2 Voigt profile fitting	23
5.3 Ionization Modelling of the Absorber	27
5.4 Origin of O VI in the Absorber	34
5.5 Galaxy environment of the absorber	35
6 Hunt for BLAs : The Survey	39
6.1 Shortlisting the BLA candidates	39
6.2 Survey methodology	42
6.3 Survey statistics	42
7 Estimating Ω_b(BLA)	61
7.1 Methodology to determine Ω_b (BLA)	61
7.2 Selecting the absorber samples	65
7.3 Comparison with literature	70
7.4 Contribution to Ω_b	71
8 Conclusions and Future Work	74
8.1 Conclusions	74
8.2 Future work	76
References	77
Appendices	81
A Sight lines shortlisted for survey	81
B HST/COS observations	83
C Survey results	85

List of Figures

1.1	Baryon budget at low redshift universe ($z \sim 0$). Credits : Shull et al. (2012)	3
1.2	Slice of spectrum of quasar HE0153-4520 ($z_{em} = 0.4510$). Credits : Danforth et al. (2016)	4
1.3	A BLA blended with other Ly α absorption lines towards the LOS of quasar PG1116+215 ($z_{em} = 0.176$). Credits : Richter (2020)	5
3.1	Simulated Voigt profiles for different Doppler parameters. X-axis is the velocity from the central wavelength, taken as a proxy of wavelength	11
3.2	Simulated Voigt profiles for different column densities. X-axis is the velocity from the central wavelength, taken as a proxy of wavelength	12
3.3	Input to VPFIT and output from VPFIT	14
3.4	An example 2 component fit as displayed in VPFIT	15
4.1	Schematic of a CLOUDY simulation showing how CLOUDY adds slabs until given stopping column density is reached by taking in account the background radiation	18
4.2	Posterior distribution of n_H and Z for the randomly selected model added with Gauassain noise	20
5.1	System plot of the absorption system. Reference velocity taken at $z = 0.347586$	26

5.2	CIE solution for component II. The figure shows the metallicity found for various densities. At high densities no variation in metallicity is seen.	29
5.3	Modelled and observed column densities for the component III based on photoionization modelling. Red error bars shows the observed column densities and corresponding $1-\sigma$ errors in column densities. The green and orange filled circles are the modelled column densities for the including O VI and excluding O VI case of PIE modelling. And the light green and light orange lines are modelled column densities with densities and metallicity sampled from normal distributions of $\log n_H$ and $\log Z$ of including O VI and excluding O VI case respectively.	32
5.4	Galaxies around the absorber color-coded with their velocity separation from the absorber.	37
6.1	No. of different metal ions in all the 29 absorber systems.	40
6.2	No. of components identified for H I and different metal ions.	43
6.3	Distribution of column densities (left panel) and redshift (right panel) of 97 H I components.	44
6.4	Distribution of b parameters of 97 H I components.	45
6.5	$b(\text{O VI})$ vs $b(\text{H I})$ plot. The orange dashed line is the $b(\text{H I}) = 4b(\text{O VI})$ line and blue dashed line shows the $b(\text{H I}) = b(\text{O VI})$ line.	46
6.6	$N(\text{H I})$ vs $b(\text{H I})$ plot for the 97 H I components. The vertical black dashed line denotes our threshold for line to be considered as BLA.	48
6.7	Distribution of column densities (left panel) and redshift (right panel) of 35 O VI components.	49
6.8	Distribution of column densities (left panel) and redshift (right panel) of 19 Si II components.	50
6.9	Distribution of column densities (left panel) and redshift (right panel) of 36 Si III components.	50
6.10	Distribution of column densities (left panel) and redshift (right panel) of 20 Si IV components.	51

6.11	Distribution of column densities (left panel) and redshift (right panel) of 23 C II components	52
6.12	Distribution of column densities (left panel) and redshift (right panel) of 26 C III components	52
6.13	Distribution of column densities (left panel) and redshift (right panel) of 22 C IV components	53
6.14	Distribution of column densities (left panel) and redshift (right panel) of 14 N V components	54
6.15	Metallicity vs density for all 39 components estimated from ionisation modelling. Red error bars are the O VI components and green error bars are non-O VI components	55
6.16	Variation of density with N(H I) for all 39 components. Red error bars are from O VI absorbers and green error are from non-O VI absorbers	56
6.17	Variation of metallicity with N(H I) for all 39 components. Red error bars are the O VI components and green error bars are non-O VI components	57
6.18	Origin of O VI in 25 components from 17 O VI absorbers.	58
6.19	An example of CI case for an absorber towards the line of sight of SDSS J135712.61+170444 at $z_{abs} = 0.097869$ with $\log N(\text{H I}) [\text{cm}^{-2}] = 16.49$	58
6.20	Only example of PI case for an absorber towards the line of sight of 1ES 1553+113 at $z_{abs} = 0.187764$ with $\log N(\text{H I}) [\text{cm}^{-2}] = 12.76$	59
6.21	An example of uncertain case for an absorber towards the line of sight of PKS 0405-123 at $z_{abs} = 0.167125$ with $\log N(\text{H I}) [\text{cm}^{-2}] = 13.46$	59
7.1	Hydrogen ionisation fraction as a function of temperature.	64
C.1	System plot for the absorber along the LOS of 3C 263 at $z_{abs} = 0.140756$	86
C.2	$\log N(\text{H I}) [\text{cm}^{-2}] = 13.49$	87

C.3 System plot for the absorber along the LOS of PKS 0637-752 at $z_{abs} = 0.161064$	88
C.4 $\log N(\text{H I}) [\text{cm}^{-2}] = 13.60$	89
C.5 System plot for the absorber along the LOS of PKS 0637-752 at $z_{abs} = 0.417539$	90
C.6 $\log N(\text{H I}) [\text{cm}^{-2}] = 15.41$	91
C.7 System plot for the absorber along the LOS of PG 1424+240 at $z_{abs} = 0.147104$	92
C.8 $\log N(\text{H I}) [\text{cm}^{-2}] = 15.44$	94
C.9 $\log N(\text{H I}) [\text{cm}^{-2}] = 14.88$	94
C.10 System plot for the absorber along the LOS of PG 0003+158 at $z_{abs} = 0.386089$	95
C.11 $\log N(\text{H I}) [\text{cm}^{-2}] = 14.81$	96
C.12 System plot for the absorber along the LOS of PG 0003+158 at $z_{abs} = 0.421923$	97
C.13 $\log N(\text{H I}) [\text{cm}^{-2}] = 14.17$	98
C.14 System plot for the absorber along the LOS of PG 1216+069 at $z_{abs} = 0.282286$	99
C.15 $\log N(\text{H I}) [\text{cm}^{-2}] = 15.10$	101
C.16 $\log N(\text{H I}) [\text{cm}^{-2}] = 16.40$	101
C.17 System plot for the absorber along the LOS of SDSS J135712.61+170444 at $z_{abs} = 0.097869$	102
C.18 $\log N(\text{H I}) [\text{cm}^{-2}] = 16.49$	103
C.19 System plot for the absorber along the LOS of 1ES 1553+113 at $z_{abs} = 0.187764$	104
C.20 $\log N(\text{H I}) [\text{cm}^{-2}] = 12.76$	106
C.21 $\log N(\text{H I}) [\text{cm}^{-2}] = 13.88$	106
C.22 System plot for the absorber along the LOS of SBS 1108+560 at $z_{abs} = 0.463207$	107
C.23 $\log N(\text{H I}) [\text{cm}^{-2}] = 18.10$	109
C.24 $\log N(\text{H I}) [\text{cm}^{-2}] = 15.79$	109

C.25 System plot for the absorber along the LOS of PG 1222+216 at $z_{abs} = 0.378389$	110
C.26 $\log N(\text{H I}) [\text{cm}^{-2}] = 15.43$	112
C.27 System plot for the absorber along the LOS of PG 1116+215 at $z_{abs} = 0.138527$	113
C.28 $\log N(\text{H I}) [\text{cm}^{-2}] = 13.60$	114
C.29 System plot for the absorber along the LOS of H 1821+643 at $z_{abs} = 0.170006$	115
C.30 $\log N(\text{H I}) [\text{cm}^{-2}] = 13.68$	117
C.31 $\log N(\text{H I}) [\text{cm}^{-2}] = 13.35$	117
C.32 System plot for the absorber along the LOS of H 1821+643 at $z_{abs} = 0.224981$	118
C.33 $\log N(\text{H I}) [\text{cm}^{-2}] = 15.16$	120
C.34 $\log N(\text{H I}) [\text{cm}^{-2}] = 15.13$	120
C.35 System plot for the absorber along the LOS of PG 1121+422 at $z_{abs} = 0.192393$	121
C.36 $\log N(\text{H I}) [\text{cm}^{-2}] = 14.34$	123
C.37 $\log N(\text{H I}) [\text{cm}^{-2}] = 17.70$	123
C.38 System plot for the absorber along the LOS of PKS 0405-123 at $z_{abs} = 0.167125$	124
C.39 $\log N(\text{H I}) [\text{cm}^{-2}] = 13.46$	126
C.40 $\log N(\text{H I}) [\text{cm}^{-2}] = 15.98$	127
C.41 System plot for the absorber along the LOS of HE 0056-3622 at $z_{abs} = 0.043265$	128
C.42 $\log N(\text{H I}) [\text{cm}^{-2}] = 15.30$	129
C.43 System plot for the absorber along the LOS of PG 1216+069 at $z_{abs} = 0.006328$	130
C.44 $\log N(\text{H I}) [\text{cm}^{-2}] = 14.79$	131
C.45 System plot for the absorber along the LOS of 3C 263 at $z_{abs} = 0.063397$	132
C.46 $\log N(\text{H I}) [\text{cm}^{-2}] = 16.46$	133

C.47 System plot for the absorber along the LOS of PG 1222+216 at $z_{abs} = 0.054479$	134
C.48 $\log N(\text{H I}) [\text{cm}^{-2}] = 14.08$	136
C.49 $\log N(\text{H I}) [\text{cm}^{-2}] = 17.91$	136
C.50 System plot for the absorber along the LOS of RX J0439.6-5311 at $z_{abs} = 0.005568$	137
C.51 $\log N(\text{H I}) [\text{cm}^{-2}] = 16.11$	138
C.52 System plot for the absorber along the LOS of UKS 0242-724 at $z_{abs} = 0.063850$	139
C.53 $\log N(\text{H I}) [\text{cm}^{-2}] = 14.61$	140
C.54 System plot for the absorber along the LOS of PG 1259+593 at $z_{abs} = 0.046284$	141
C.55 $\log N(\text{H I}) [\text{cm}^{-2}] = 17.79$	142
C.56 System plot for the absorber along the LOS of PKS 1302-102 at $z_{abs} = 0.094839$	143
C.57 $\log N(\text{H I}) [\text{cm}^{-2}] = 14.96$	144
C.58 System plot for the absorber along the LOS of 3C 57 at $z_{abs} = 0.077430$	145
C.59 $\log N(\text{H I}) [\text{cm}^{-2}] = 13.30$	146
C.60 System plot for the absorber along the LOS of PMN J1103-2329 at $z_{abs} = 0.003934$	147
C.61 $\log N(\text{H I}) [\text{cm}^{-2}] = 16.29$	148
C.62 System plot for the absorber along the LOS of PHL 1811 at $z_{abs} = 0.080928$	149
C.63 $\log N(\text{H I}) [\text{cm}^{-2}] = 18.02$, all ions	151
C.64 $\log N(\text{H I}) [\text{cm}^{-2}] = 18.02$, C II, C IV, Si II and Si IV	151
C.65 System plot for the absorber along the LOS of PG 0832+251 at $z_{abs} = 0.017505$	152
C.66 $\log N(\text{H I}) [\text{cm}^{-2}] = 15.82$	154
C.67 $\log N(\text{H I}) [\text{cm}^{-2}] = 14.79$, excluding O I, Fe II and Al II	155
C.68 $\log N(\text{H I}) [\text{cm}^{-2}] = 18.22$	155

List of Tables

5.1	Component structure of the absorber system. Reference velocity at $z = 0.347586$	22
5.2	Parameters from Voigt profile fitting of the absorption lines. Velocity is taken to be zero at the redshift of O VI line of component II, i.e. $z = 0.347586$	24
5.3	Error calculated using χ^2 and the systematic uncertainty in column densities due to continuum fitting given in units of $\log[N (\text{cm}^{-2})]$. .	25
5.4	Column densities and corresponding $1-\sigma$ errors of the ions used in PIE modelling of the component III	31
5.5	Cloudy modelling solutions for absorber at $z \sim 0.34790$. In case of all ions χ^2 is calculated using the column densities of all the ions but for excluding O VI ion case, χ^2 is calculated by excluding O VI column density so as to show that this fits other ions very well.	31
5.6	Physical properties of the absorbers based on Voigt profile measu- rement and CLOUDY ionisation modelling. The PIE solution for absorber at $z \sim 0.34758$ is based on the excluding O VI case PIE solution of the absorber at $z \sim 0.34790$	33
5.7	Galaxies in the neighbourhood of the absorber system identified in VIMOS survey. Velocity is taken to be zero at $z = 0.347586$	36
6.1	Details of the 29 BLA candidate absorber system shortlisted for the survey.	41
6.2	Details of temperature estimation from Doppler parameters.	47

6.3	25 O VI components and origin of O VI in them	60
7.1	CIE properties of 37 BLA components. ^a Temperature estimated from Doppler parameters. ^b The excluded BLA component discussed in section 7.2.2	70
7.2	Ω_b (BLA) estimation using sample A	70
7.3	Ω_b (BLA) estimation using sample B	71
7.4	Ω_b (BLA) estimation using sample C	72
7.5	Baryon fraction in BLAs.	73
A.1	22 sight lines selected for the survey. Table 1 of Danforth et al. (2016).	82
B.1	HST/COS FUV observation details of the 22 sight lines selected for the survey. Table 2 of Danforth et al. (2016).	84

Chapter 1

Introduction

The standard Big Bang model of our universe shows that less than 5% ([Planck Collaboration et al. 2020](#)) of the total energy density of the universe is in the form of baryons. All the ‘ordinary’ matter which we see around us is made up of these baryons. Astronomers are interested in studying the distribution of these baryons to understand the evolution of the universe, formation of large scale structures. So, understanding this component of the universe is crucial for our comprehension of the cosmos.

1.1 Where are the baryons ?

While attempting the census of the baryons in the present universe, i.e at $z \sim 0$, cosmologists found that there is a shortfall from the total number obtained from the observations of Cosmic Microwave Background (CMB) and light element abundances predicted from big bang nucleosynthesis. In their study, [Fukugita et al. \(1998\)](#) were able to account for about half of the expected number of baryons. Using cosmological simulations, [Cen & Ostriker \(1999\)](#) also argued that about 50% of the baryons are yet to be detected. With time the surveys got better, however, recent surveys still show a deficit of $\sim 30\%$ ([Shull et al. 2012](#)). This came to be known as the “Missing Baryon Problem” at low redshift. At high redshift ($z > 3$), nearly all the baryons have been accounted for, with around 3% being collapsed in

stars and galaxies and remaining $\sim 97\%$ are found in cool ($\sim 10^4$ K) photo-ionised gas phase in the form of Ly α forests in intergalactic medium (IGM).

Figure 1.1 shows the distribution of baryons at low redshift. Only less than 20% of the baryons are in the form of collapsed structures in galaxies, circumgalactic medium (CGM), intercluster medium (ICM) and in cold gas (H I and He I). Rest of the 80% baryons are in diffused IGM, mainly in two phases, around 30% in cool photoionised phase observed through Ly α forests (Danforth & Shull 2008; Tilton et al. 2012) and remaining 50% are expected to be in Warm Hot Intergalactic Medium (WHIM). Out of these 50%, nearly 20% have been accounted mainly from the observations of Broad Lyman- α Absorbers (BLAs) (see section 1.3) and studies of O VI absorbers (Danforth & Shull 2008; Tilton et al. 2012; Tripp et al. 2008a; Savage et al. 2014). WHIM can also be traced by X-ray absorbers at temperatures above 10^6 K, by highly ionised species like O VII-VIII, Ne VIII-X, etc. However very few studies of such systems have been carried out because of unavailability of good X-ray data as these are very weak absorbers and are below the detection limits of current X-ray spectrographs (Yao et al. 2012) (see section 1.2 for more details on detection of WHIM) . And remaining $\sim 30\%$ are missing from the observations. We will describe BLAs in detail in section 1.3 as they we will be our ‘lamps’ in finding the baryons in WHIM.

Cosmological simulations (Cen & Ostriker 1999, 2006) shows that these ‘missing’ baryons are residing in WHIM which has very low densities ($10^{-6} - 10^{-4}$ cm $^{-3}$) and high temperatures ($10^5 - 10^7$ K). Simulations also show that WHIM is mainly formed via shock-heating of the in-falling gas from the IGM on the large scale structures. Because of its low density and temperature not high enough to emit in X-rays, it doesn’t emit detectable amount of radiation to be observed in emission. And because of high temperatures, the gas is too collisionally ionised to imprint significant absorption signatures in the spectra of the background objects. Because of these difficulties much of the WHIM is yet to be detected.

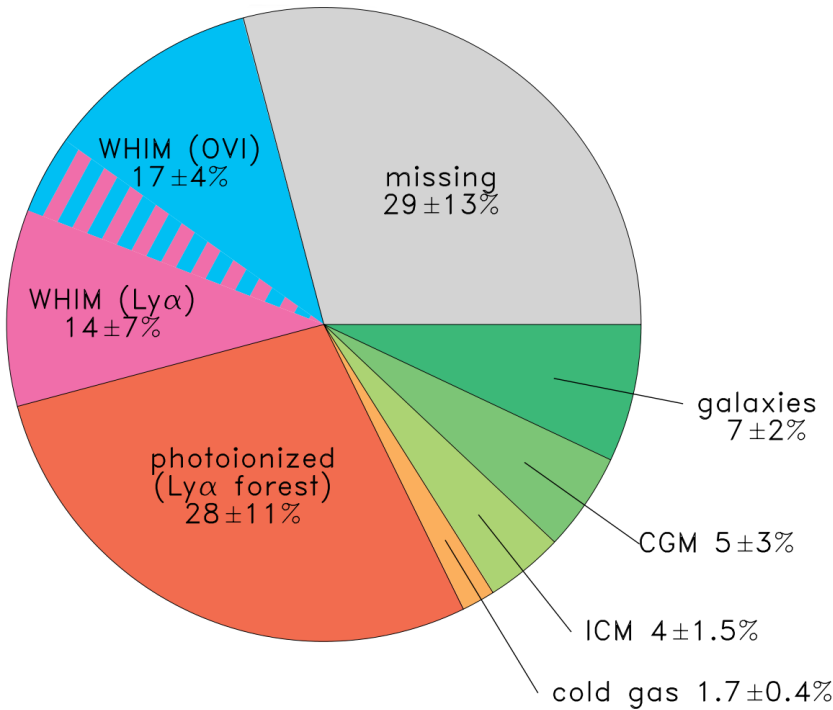


FIGURE 1.1: Baryon budget at low redshift universe ($z \sim 0$). Credits : [Shull et al. \(2012\)](#)

1.2 Detecting WHIM

As discussed in previous section that around 50% of the baryons are expected to be in WHIM, so in this section we describe how we can detect WHIM.

The WHIM is mainly detected with the help of quasars. The quasars are very bright sources of light, providing us an excellent source of background light. The matter in the intervening space between us and these quasars can leave absorption features in the spectra of these quasars, enabling us to ‘look’ at this matter as shown in figure 1.2. It shows the absorption from the gas in IGM, marked as red lines, from different intermediate redshifts, whereas green marked lines are galactic absorption lines. The WHIM can be traced by highly ionised species like O VI-VIII, Ne VIII-X, etc. as these arise in high temperature gas phase ([Tepper-García et al. 2013](#)). Apart from high temperature gas these lines can also arise from photoionised

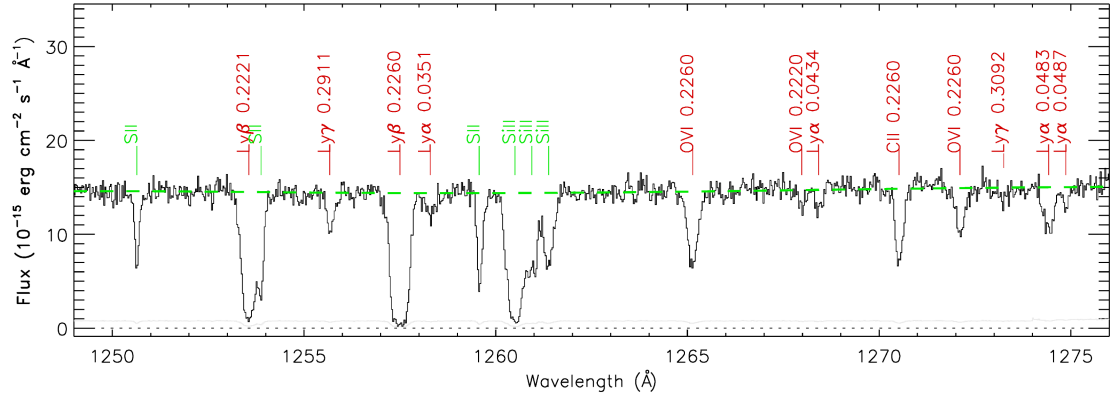


FIGURE 1.2: Slice of spectrum of quasar HE0153-4520 ($z_{em} = 0.4510$). Credits : Danforth et al. (2016)

gas phases. There are instances in the literature where the origin of these lines is uncertain, i.e whether they are coming from collisionally ionised or photoionised phase. For example, in their study of ionisation mechanisms of Ne VIII, Hussain et al. (2017) found that the observed column densities of Ne VIII and O VI can be explained by using the photoionisation models which also solves the problem of cooling in collisional ionisation at the predicted metallicities.

So detecting these lines doesn't assure that we they are probing WHIM. Nevertheless, unavailability of high S/N X-ray data also makes it difficult to study WHIM using these lines.

Because of high temperatures of WHIM, the absorption lines can get thermally broadened. So detecting such broad features can show possibility of tracing high temperature gas phase. This gives us an another way of probing WHIM by using Broad Ly α Absorbers (BLAs) which we describe in the next section.

1.3 Detecting WHIM using BLAs

Any Ly α absorption line with Doppler parameter (b) $\gtrsim 40\text{--}45 \text{ km s}^{-1}$ can be loosely called a BLA. These b values corresponds to temperatures of $9.7 \times 10^4 - 1.2 \times 10^5 \text{ K}$ assuming a complete thermal broadening. BLAs are expected to host

significant fraction of the baryons in the low-redshift universe (Richter et al. 2004, 2006; Lehner et al. 2006, 2007). In spite of low neutral fraction of H_I, these lines can be detected up-to the temperatures of $\sim 10^6$ K because of large abundance of Hydrogen. As these features are broad they are very shallow as compared to their narrower counterpart with same line strength. Thus high S/N data is required to detect BLAs. Detecting a BLA ensures that we are tracing WHIM. If a BLA is detected, then we can expect to see other highly ionised species as well.

However, several narrow components can also blend together resulting in broad features. Figure 1.3 shows such an example. The left panel shows the broad line and second panel shows the fitted profile with multiple components to the line. The red shaded region is the contribution from BLA and rest is the contribution of narrower components. So, a careful modelling has to be done for such absorbers. If we find a candidate BLA in such features then we need to show that the other kinematically concurrent species are arising from a collisionally ionised gas phase as is the case of WHIM. To do so, we need to model the ionisation conditions prevalent in the absorber cloud which we describe in chapter 4 in detail.

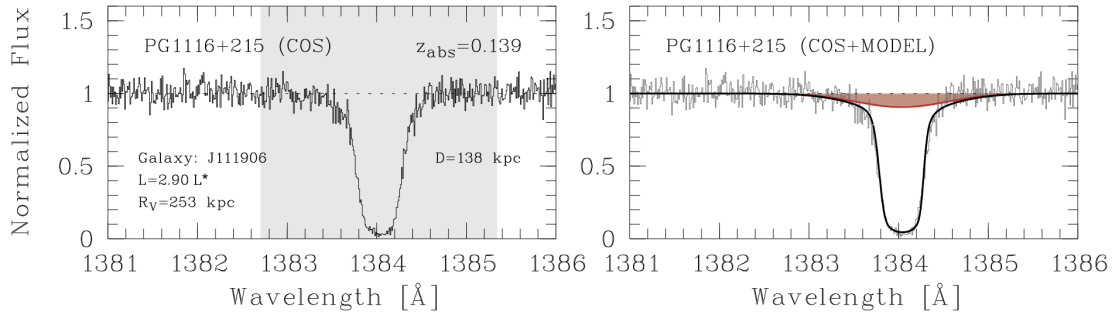


FIGURE 1.3: A BLA blended with other Ly α absorption lines towards the LOS of quasar PG1116+215 ($z_{em} = 0.176$). Credits : Richter (2020)

There have been studies of BLAs on small scales but as these are difficult to observe they show varying results. For instance, Lehner et al. (2007) have studied 7 AGN lines of sight to search for BLA candidates and estimated that BLAs contribute around 20% to the total baryonic energy density (Ω_b). However, a study by Danforth et al. (2010), which also studied 7 AGN lines of sight, report different

results. They estimate the contribution of BLAs to be around 14% in (Ω_b).

So, there is a need to do a large survey of these BLAs to realise the abundance of baryons in these cosmic reservoirs.

1.4 Road-map for the Current Project

In the current project we will be addressing the missing baryon problem with the help of BLAs. Currently, literature lacks comprehensive surveys of the BLAs on large datasets. So we will be doing a large survey of BLAs with high S/N HST/COS data. We will be doing Voigt profile measurements and will also model the ionisation conditions in the BLAs to infer their ionisation states. We will use results from this survey to estimate the baryon content in BLAs and their contribution to the total cosmic baryonic inventory (Ω_b).

The outline of this thesis is as follows : In chapter 2, we describe the data which we will be using for our survey of BLAs. In chapter 3 we mention our Voigt profile fitting routine. Chapter 4 describes the ionisation modelling of the absorbers and the method used for modelling. In chapter 5, we study a BLA candidate absorber system towards the LOS of quasar PG 0003+158 to test our methods. Chapter 6 describes our methodology for the survey, survey statistics and overall results from the survey. We discuss the estimation of Ω_b (BLA) in chapter 7 and we conclude by summarising the current work and directions for future work in chapter 8.

Chapter 2

Data and Pre-processing

2.1 HST/COS data

To detect BLAs we require very high S/N spectroscopic data of the background quasars. As we aim to probe the WHIM at low redshift and at low redshifts the Lyman- α and other Lyman transitions fall in the Far Ultra-Violet (FUV) region of the electromagnetic spectrum. So we need FUV data for our study.

We use FUV data from Cosmic Origins Spectrograph (COS) aboard Hubble Space Telescope (HST) as it provides us with highest S/N data compared to other FUV spectrographs like Space Telescope Imaging Spectrograph (STIS) which is also aboard HST. We use observations done in the FUV channel of COS with G130M and G160M gratings. The G130M grating gives a coverage of 900-1450 Å with resolving power (R) of around 12,000-16,000, whereas G160M grating samples the wavelength between around 1360 and 1775 Å and provide a resolving power of around 13,000-20,000. Together these gratings give coverage from around 1130 to 1790 Å with a median resolution of $R \sim 17,000$ (17.6 km s^{-1}).

The FUV detector of the COS comprises of two segments viz. A and B. This results in gap in the spectra of objects under observation. G130M and G160M gratings give a gap of 14.3 and 18.1 Å respectively. To overcome these gaps, different central wavelength settings are used for observations so that there are overlaps in the spectrum thus covering the gaps. The COS FUV data can be accessed through

the Hubble Spectral Heritage Archive (HSLA)¹ which provides all the raw and integrated COS FUV data publicly available in the Mikulsky Space Telescope Archive (MAST)². The HSLA hosts the observations of 799 quasars, AGNs and Seyferts.

Danforth et al. (2016) has surveyed the low redshift IGM with the highest quality HST/COS data available in the HSLA. They have chosen 82 UV-bright AGNs with redshifts $z_{AGN} < 0.85$ and spectra with typical S/N ratio $\gtrsim 15$ per COS resolution element. We use these 82 lines of sight for our study.

2.2 Pre-processing

The HST/COS data is over-sampled at 6 pixels per resolution element, so we re-sample the spectrum at an optimum binning of 2 pixels per resolution element. We use python package LINETOOLS³, which uses simple linear interpolation and flux conservation, to rebin the spectrum.

A continuum is fitted to the spectrum after rebinnning. To fit the continuum we again use the LINETOOLS package, which places the knots, points that mark the continuum, at regions with no absorption and emission features at uniform spacing in wavelength along with interactive human input. The continuum is created by interpolating these knots with lower order polynomials. Then the spectrum is normalised by this continuum for fitting the Voigt profiles to the absorption lines.

1. <https://archive.stsci.edu/missions-and-data/hsla>
2. <https://archive.stsci.edu/>
3. <https://github.com/linetools/linetools>

Chapter 3

Voigt Profile Fitting

3.1 Voigt Profile

The spectral lines are not infinitesimally peaked functions but rather have finite widths. This finite width or broadening can be attributed to the thermal motions of atoms (thermal broadening), quantum mechanical uncertainties in the energies of the transitions (natural broadening), collisions between excited atoms (collision broadening), etc. In astrophysical spectra the broadening is mainly thermal and natural broadening, the former results in Gaussian profile of the line whereas later gives a Lorentzian feature to the line profile. The convolution of these Gaussian and Lorentzian profiles results in what is known as the Voigt profile. The central region of an absorption line has a Gaussian shape whereas the extended wings show Lorentzian shape. So the absorption line in an astrophysical spectra can be modelled as Voigt profile.

The absorption profile at frequency ν can be written as :

$$f(\nu) = f_c e^{-\tau(\nu)}$$

where f , f_c , τ are spectral flux density, interpolated absorption-free continuum over the absorption profile and optical depth respectively.

If we assume that the absorbing atoms have a Gaussian velocity distribution

with mean velocity v_0 with respect to a reference frame, say S, then the optical depth is given by :

$$\tau(\nu) = N \frac{1}{\sqrt{\pi} b} \int_{-\infty}^{\infty} \sigma(\nu') e^{-\frac{(v-v_0)^2}{b^2}} dv \quad (3.1)$$

where N is the column density, b is the Doppler parameter, which is defined as $b = FWHM/2\sqrt{\ln 2}$; $FWHM$ is the full width at half maximum and $\sigma(\nu')$ is the cross-section offered by an atom moving with the velocity v to the photon of frequency ν in S and $\nu' = \nu/(1 - v/c)$, taking v to be positive for atoms receding away from the observer.

The Doppler parameter b , has contributions from both thermal and non-thermal components (e.g. turbulence, etc.), which can be written as :

$$b = \sqrt{b_{thermal}^2 + b_{non-thermal}^2} \quad (3.2)$$

And $b_{thermal}$ is related to temperature (T) of the gas by $b_{thermal} = \sqrt{\frac{2kT}{m}}$, where m is the mass of an atom and k is the Boltzmann constant.

We can get expression for cross-section in an atomic transition from the classical expression by taking in the factors of oscillator strength (f) and frequency dependence which results from the finite life-time of the upper level of the transition. This expression is given by :

$$\sigma = f \times \frac{1}{4\pi\epsilon_0} \frac{\pi e^2}{m_e c} \times \frac{1}{\pi} \frac{\frac{\gamma}{4\pi}}{(\nu - \nu_0)^2 + \frac{\gamma^2}{4\pi}} \quad (3.3)$$

where γ is the total damping constant (de-excitation rate of the upper level) and other symbols have their usual meanings for the fundamental constants ([Morton & Smith 1973](#)).

Using equations [3.3](#) & [3.1](#) and changing frequency (ν) to wavelength (λ) and putting values of the fundamental constants we get :

$$\tau(\lambda) = 1.498 \times 10^{-2} \frac{Nf\lambda}{b} H(a, u) \quad (3.4)$$

where $H(a, u)$ is called the Voigt function and given as :

$$H(a, u) = \frac{a}{\pi} \int_{-\infty}^{\infty} \frac{e^{-y^2}}{(u - y)^2 + a^2} dy; \quad a = \frac{\lambda\gamma}{4\pi b}; \quad u = -\frac{c}{b} \left(\left(1 + \frac{v}{c}\right) - \frac{\lambda}{\lambda_0} \right) \quad (3.5)$$

And λ_0 is the wavelength at the centre of the absorption profile. Clearly, the Voigt function is a convolution of gaussian and lorentizian functions. The absorption feature which is just $e^{-\tau(\lambda)}$, is called a Voigt profile.

Figure 3.1 shows simulated Voigt profile absorption lines with varying Doppler parameters at a fixed column density of 10^{13} cm^{-2} . It is evident from the figure 3.1 that as the b value increases the profile gets broader and shallower. So we require a very high S/N data to detect such shallow absorption features. Also, the optical depth at the center of the line decreases as b increases.

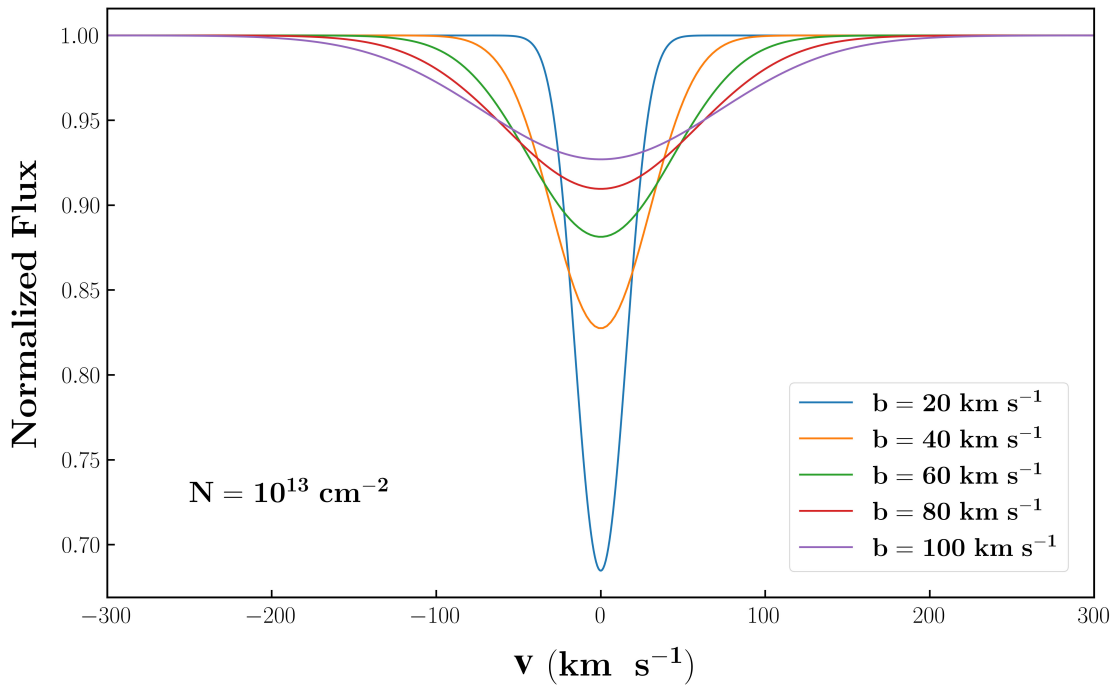


FIGURE 3.1: Simulated Voigt profiles for different Doppler parameters. X-axis is the velocity from the central wavelength, taken as a proxy of wavelength

Whereas figure 3.2 shows the variation of Voigt absorption profile with column densities at a fixed Doppler parameter of 50 km s^{-1} . Now, as the column density increases, the optical depth at the center of the line increases resulting in the drop in flux, finally leading to the saturation of the profile, i.e. flux dropping to 0. Further increase in column density leads to the spread of profile and absorption

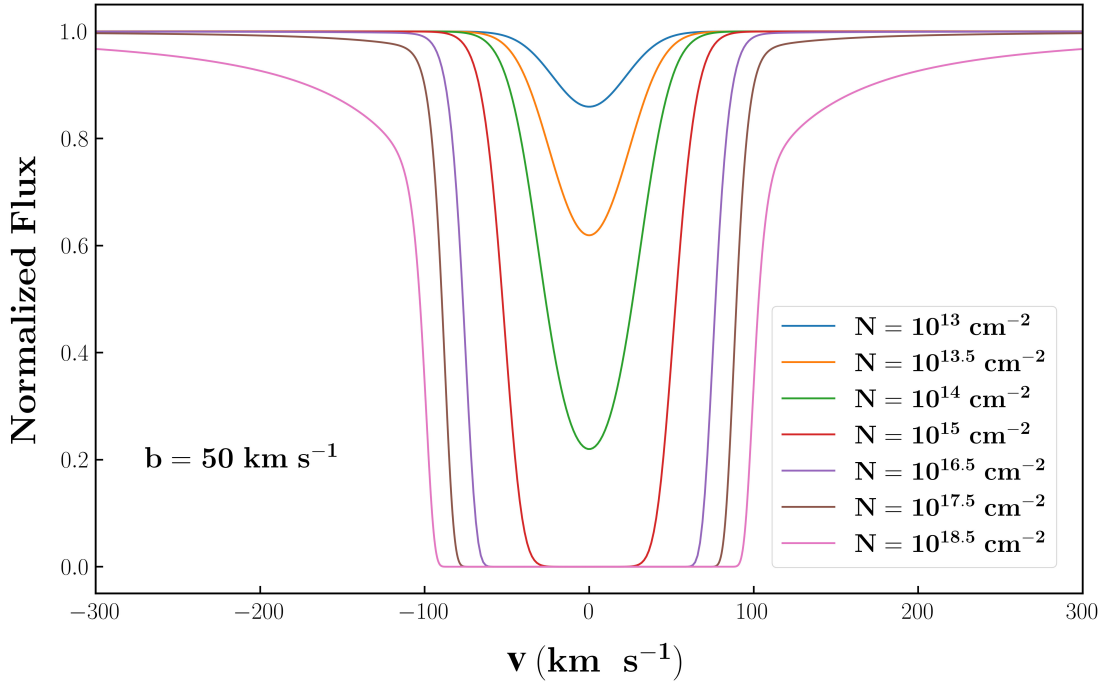


FIGURE 3.2: Simulated Voigt profiles for different column densities. X-axis is the velocity from the central wavelength, taken as a proxy of wavelength

from the wings also starts becoming prominent.

3.2 VPFIT

Fitting Voigt profiles to the absorption lines in the spectrum of quasars is a very tedious task. The absorption lines can have the blend of multiple components of the same line or can be contaminated from some other line falling in the absorption profile of the line of interest. Furthermore, the atomic data characterising the transitions have to be carefully used. All such challenges can't be solved using simple curve fitting tools available.

To fit the Voigt profiles to the absorption lines, we use Voigt profile fitting program (VPFIT) ([Carswell & Webb 2014](#)), which is developed specifically to deal with the absorption lines in astrophysical spectra . VPFIT minimises the χ^2 by varying the

parameters in the parameter space. It gives 3 parameters and associated $1-\sigma$ errors for each profile viz. redshift of the line (wavelength at centre of the absorption profile) , Doppler parameter (b) and column density of the ion causing the absorption. We give **VPFIT** an input file mentioning the continuum normalised spectrum, the wavelength region(s) to fit, initial guesses for the parameters and the ion for which we are fitting the absorption line. It also has a provision to include the instrument profiles in the form of line spread function (LSF) files. If LSF files are given, it then convolves the instrument profile and Voigt profiles. We use *HST/COS* LSF files available on the STScI website⁴. In **VPFIT**, we give the instrument profile as the LSF file of wavelength which lies between the fitting region of the line, if LSF file for such wavelengths is not available we then give the nearest wavelength LSF file available to the fitting region wavelengths. **VPFIT** can also fit multiple Voigt profiles to the absorption lines in case multiple components are seen in the absorption lines. An example of Voigt profile fitting using **VPFIT** is describe in section 3.2.2.

3.2.1 Line-identification

[Danforth et al. \(2016\)](#) have identified all the IGM absorber systems along each of the 82 lines of sight selected by them. They have also done the line identification of all the lines in each of the 82 spectra along with preliminary line fitting. However, their line fitting is not rigorous enough to be considered for our project as our results significantly depend on the line parameters. They have fitted the lines arising from same ions separately, leading to different parameters for the same ion. In principle, all the lines coming from a particular ion should be fitted simultaneously with same profiles, e.g. all the Lyman transitions should be fitted together rather than fitting Ly α , Ly β , etc. alone. This helps us to better constrain the line parameters. For our fitting routine we use the line identification done by [Danforth et al. \(2016\)](#) and use their results as initial guess for our fitting procedure.

4. <https://www.stsci.edu/hst/instrumentation/cos/performance/spectral-resolution>

3.2.2 Example

Figure 3.4 shows an example of fitting a Voigt profile to an absorption line using VPFIT. Figure 3.3a gives the snapshot of an VPFIT input file. In the first line we specify the continuum normalised spectrum (*pks0405_cont_norm.asc*) and give a wavelength region where the profile is to be fitted in units used in the spectrum (1138.8 - 1141.4) and we also give the LSF file as argument to *pfinst*. In the considered example, we fit the line with two C III components by giving initial guesses of redshift (0.166588 & 0.167018), Doppler parameter (39.7 & 35.3) and column density (13.51 & 14.42)

The figure 3.3b shows the output file from VPFIT. It gives us various statistics of the fit like number of iterations used (10), reduced χ^2 (1.380970), etc. and the fitted line parameters and their 1σ error.

It also displays the fit of the line as given in figure 3.4. The white step curve is the input spectrum and the green curve is the fitted Voigt profile. It shows that two components of C III 977 line are fitted. It also allows us to save the fit in a separate file allowing further analysis on the data.

```
%% pks0405_cont_norm.asc      1      1138.8 1141.4  pfinst=cos_G130M_lsf_1139_ltpos_3.dat !
C III    0.166588   0    39.7      0  13.51   0  0 !
C III    0.167018   0    35.3      0  14.42   0  0 !
```

(a) An example input file to VPFIT

```
%% pks0405_cont_norm.asc      1      1138.8000  1141.4500 pfinst=LSF/cos_G130M_lsf_1139_lt  !  0.000001   89  2023/10/18
! Stats: 10    1.380970   89   89  0.000  0  AICc:    168.04
C III    0.1665840347  0.0000068413      32.43483  2.80054          13.448245  0.023137  0 !
C III    0.1670200487  0.0000030011      37.42191  1.67116          14.328731  0.042370  0 !
```

(b) An example output file from VPFIT

FIGURE 3.3: Input to VPFIT and output from VPFIT

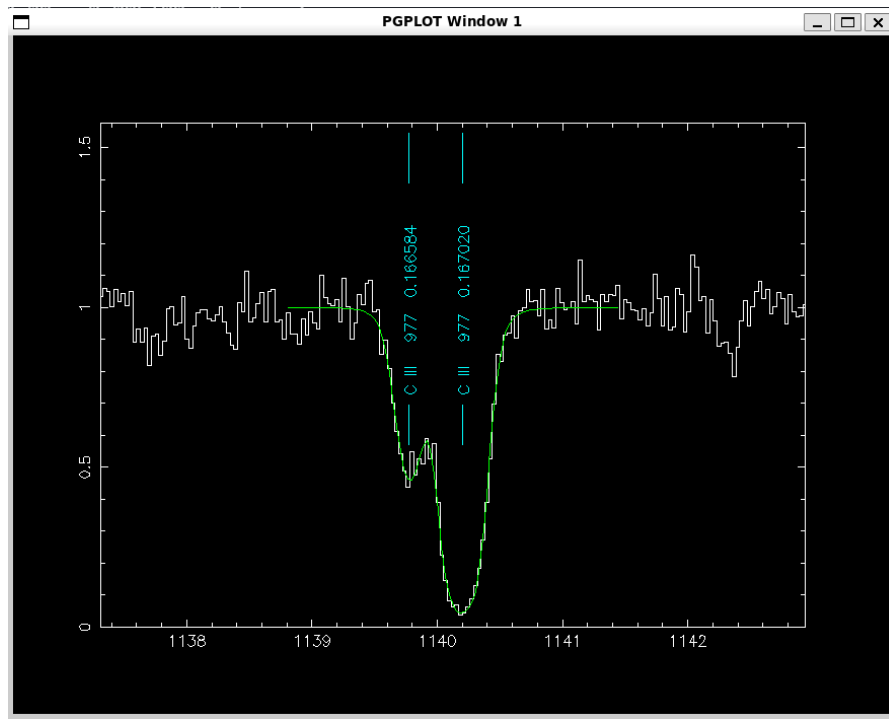


FIGURE 3.4: An example 2 component fit as displayed in VPFIT

We use VPFIT to fit the Voigt profiles to the absorption lines as described in this chapter. We use the column densities and Doppler parameters from Voigt profile fitting to model the ionisation conditions in the absorbers as described in next chapter.

Chapter 4

Modelling the Ionisation Conditions

4.1 Ionisation Modelling

Relying solely on Voigt profile measurements yields limited information about the absorbers. It gives us the Doppler parameter, which can be used at best to put an upper level on the temperature of the absorbing gas. We need to know the physical conditions underlying in the absorber cloud such as density, temperature, metallicity, etc. As discussed in chapter 1 that we need to show that the BLA is arising from a collisionally ionised phase, so that we can assure that we are indeed probing the WHIM and not just cool photoionised gas. And by modelling the ionization conditions prevalent in the absorber cloud we can address the aforementioned concerns.

4.2 CLOUDY

To model the ionization conditions prevailing in the absorbers, we use ionization modelling code **CLOUDY** ([Ferland et al. \(1998\); 2017](#)). **CLOUDY** is a 1-d radiative transfer code which considers processes like ionization, recombination, dissociation, and various chemical reactions among atoms, ions, and molecules. These processes determine the composition and abundance of different species in the absorber cloud. **CLOUDY** accounts for the radiation transfer within the gas cloud.

This includes the absorption, emission, and scattering of photons. The simulation considers how radiation interacts with the particles in the cloud, influencing its temperature, density, and ionization state.

It calculates the ionization equilibrium within the cloud, balancing ionization and recombination processes. It can perform equilibrium calculations for both photoionization and collisional ionization separately and simultaneously as well. To perform photoionization equilibrium calculations we give a model of extragalactic ionization radiation background, which mainly arises from AGNs and star formation activities, whereas for collisional ionization calculations we specify a temperature and then calculations are performed at this constant temperature. A combination of both will give results considering both types of ionizations simultaneously, such models are called hybrid models.

CLOUDY takes various input parameters like density, temperature, redshift, metallicity of the cloud, abundance pattern of the elements, background radiation model, etc. to perform the equilibrium calculations. It models the clouds as plane parallel slabs with uniform densities and metallicities, and continues to add such slabs until a given stopping criteria is met. As we have the neutral Hydrogen column density from Voigt profile fitting, we use it as stopping criteria for **CLOUDY** simulations. So **CLOUDY** continues to add the slabs until the column density of neutral Hydrogen in simulated clouds reaches our given value. Figure 4.1 shows the schematic of a **CLOUDY** simulation where neutral Hydrogen column density is used as a stopping criteria. **CLOUDY** gives us a lot of useful quantities, including column densities and ionization fractions of various ions, equilibrium temperature (for photoionization calculations), etc. We can use these quantities to get the insights on the physical conditions and ionisation state of the absorbers.

For all the **CLOUDY** models we set the abundance pattern of elements heavier than Helium to be that of solar abundance as given in [Grevesse et al. \(2010\)](#) and Helium abundance is set to 8.163×10^{-2} (by number relative to Hydrogen) based on the latest CMB measurements ([Planck Collaboration et al. 2020](#)). And for extragalactic radiation background model we use KS19 (Q18) model given in [Khaire & Srianand \(2019\)](#).

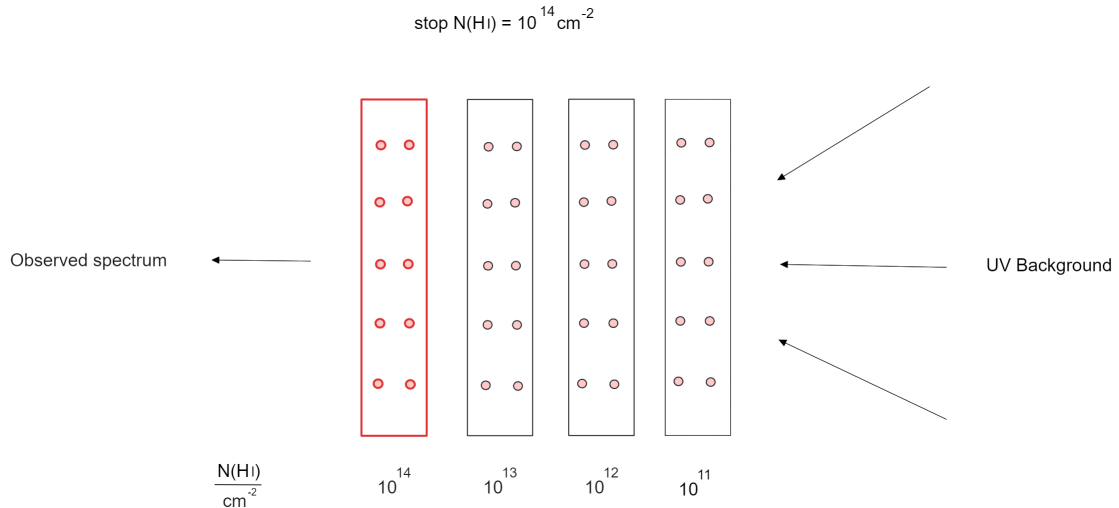


FIGURE 4.1: Schematic of a CLOUDY simulation showing how CLOUDY adds slabs until given stopping column density is reached by taking in account the background radiation

4.3 Ionization Model Based Parameter Estimation

As discussed in section 4.2, we use CLOUDY to get the physical conditions existing in the absorber clouds. The physical conditions are characterised by properties like density, temperature, metallicity, pressures, etc. We estimate these quantities based on CLOUDY simulations with methods described in Acharya & Khaire (2021).

We use the Bayesian MCMC inference approach as discussed in Acharya & Khaire (2021) to estimate the density (n_H) and metallicity (Z) of the absorber. We consider a dense grid of photoionization CLOUDY models with varying the density (n_H) and metallicity (Z) over certain range in the parameter space. We give the N(HI) column density from Voigt profile measurements as the stopping criteria for the CLOUDY calculations. We interpolate the column densities in log n_H and log Z space and then use MCMC to sample the posterior of these quantities to estimate the log n_H and log Z values that best fits the data, i.e. the column densities of the observed ions. CLOUDY also gives us the equilibrium temperature also for all the density and metallicity. So we can find the temperature of the absorber cloud by putting the density and metallicity solution which we get from the above procedure.

In case of collisional ionisation, we can follow the similar approach. If we can get an estimate of the temperature from some other means like using the Doppler parameters of the absorption lines, then we can use the same way of creating a 2D grid of CLOUDY models by fixing the temperature at the known temperature. When we give a constant temperature like this, CLOUDY performs collisional ionisation calculations. And if we don't know the temperature, then we can extend our 2D grid to a 3D one by varying the temperature also. And then use the same approach as in case of 2D grid to find the temperature as well.

In the below section we perform an inference test to check the above method of parameter estimation.

4.3.1 Parameter inference test

For this inference test, we consider a grid of photoionization CLOUDY models with $-5 \leq \log n_H \text{ (cm}^{-3}\text{)} \leq -1$ in steps of 0.02 and $-3 \leq \log Z/Z_{\odot} \leq 1$ in steps of 0.05. We take a random model from this grid and add Gaussian noise to the column densities of ions to mimic real world observations. We take 5 ions to estimate the n_H and Z value for this random model.

The randomly selected model has $\log n_H \text{ (cm}^{-3}\text{)} = -3.32$ and $\log Z/Z_{\odot} = -2.64$. We take C I, N V, O VI, Si II and Si III for the test. Figure 4.2 shows the posterior distribution of n_H and Z , which gives us the estimated value of $\log n_H \text{ (cm}^{-3}\text{)} = -3.33 \pm 0.03$ and $\log Z/Z_{\odot} = -2.63 \pm 0.06$ which matches with the n_H and Z values of the model within the errors. So, we see that the above mentioned method could be used to estimate parameters from CLOUDY models.

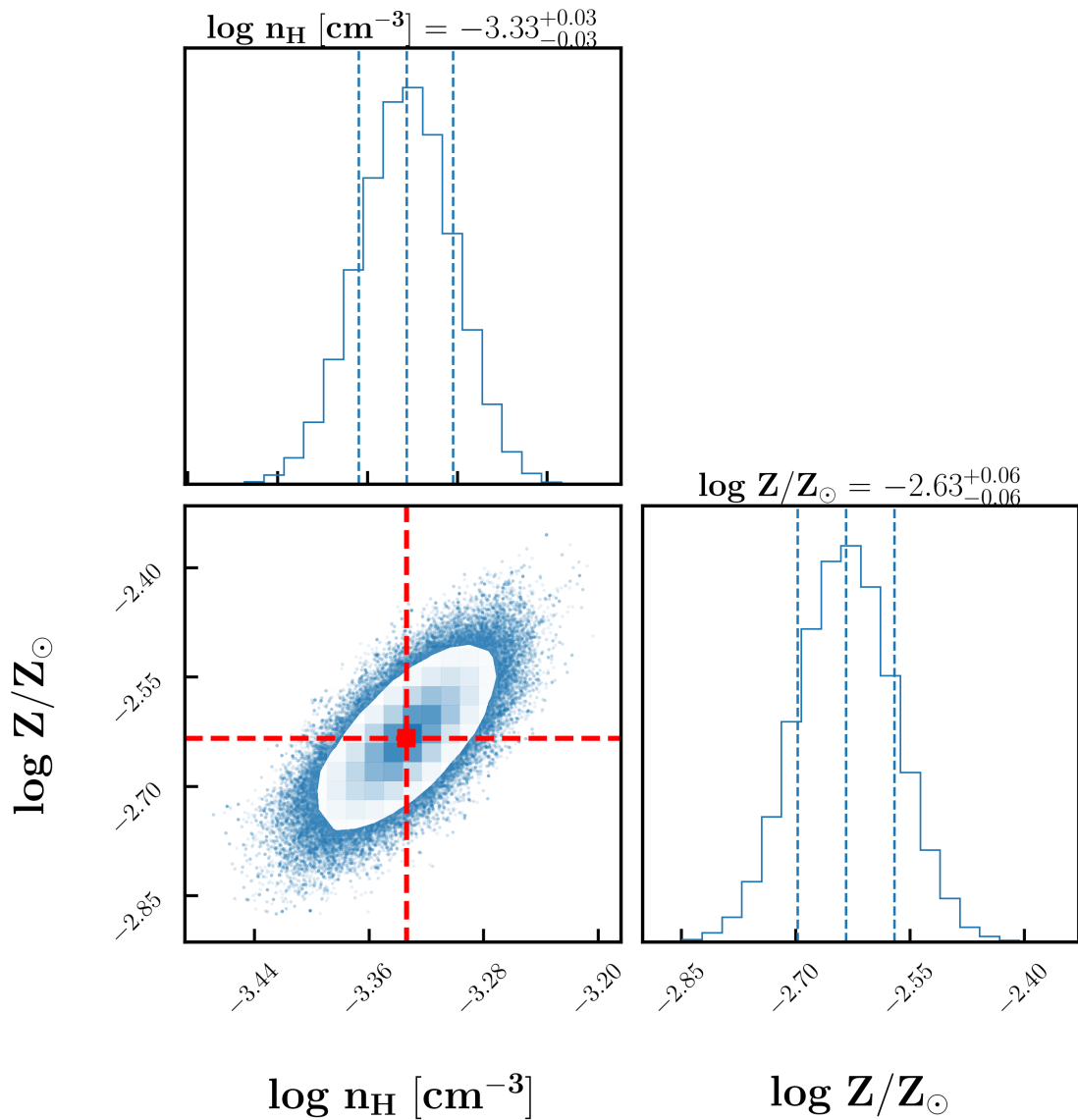


FIGURE 4.2: Posterior distribution of n_H and Z for the randomly selected model added with Gaussian noise

Chapter 5

Absorber towards PG 0003+158

In this chapter, we describe a multi-component absorber system with a BLA candidate at $z \sim 0.347$ towards the line of sight of quasar PG 0003+158 ($z_{em} = 0.4509$) which is a Sy1.2 AGN. We first fit the Voigt profiles to the absorption lines and then perform a detailed modelling of the ionization conditions in the absorber to know its ionisation state. We also analyse the galaxy neighbourhood of the absorber to understand the origins of the absorption system.

5.1 Component structure of the absorber system

We identified 3 components in the absorber system, i.e. three kinematically distinct absorption is seen. Table 5.1 lists the details of the components. We describe these components in subsequent sections.

5.1.1 Component I : $z \sim 0.346776$

This component is the simplest of the 3 components as it is detected only in Ly α and Ly β lines. Both the line are detected above 5σ significance levels. This component lies at $\sim -180 \text{ km s}^{-1}$ from the component II (from redshift of O VI line : $z = 0.347586$). The other ions covered in COS coverage like N V, C II, C III, Si II, Si III, Mg II, etc. are non-detections. Voigt profile fitting, as described in section 5.2, gives a H I column density, $\log N[\text{H I } (\text{cm}^{-2})] = 13.46 \pm 0.05$. The

Component	Ions	Δv (km s ⁻¹)
I	H I	-163
II	H I, O VI	0
III	H I, O VI, C II, C III, Si II, Si III	65

TABLE 5.1: Component structure of the absorber system. Reference velocity at $z = 0.347586$

b parameter measured from Voigt profile fitting gives an upper estimate of the temperature for the component to be $10^{4.94^{+0.14}_{-0.16}}$ K, assuming a complete thermal broadening of the line.

5.1.2 Component II : $z \sim 0.34758$

This component shows a number of Lyman lines from Ly α (23σ) to Ly δ (3.7σ) along with coincident absorption from O VI at above 10σ confidence level. The other ions in the COS coverage are non-detections. It hosts the Broad Lyman Absorber (BLA), having a b parameter of 62.5 ± 2.9 km s⁻¹ and a column density of $\log N[\text{H I} (\text{cm}^{-2})] = 14.13 \pm 0.02$. The broad line indicates a large temperature. The temperature can be directly estimated using the b values of H I and O VI, assuming that they both arise from same the gas phase. This gives a temperature of $10^{5.29^{+0.07}_{-0.08}}$ K (see section 5.4.1) , which lies in the temperature range of WHIM ($10^5 - 10^7$) K.

5.1.3 Component III : $z \sim 0.34790$

This lies at around 70 km s⁻¹ from the component II (from redshift of O VI line : $z = 0.347586$). It is kinematically more complex than the other two components. Lyman transitions are seen upto H I 914 Å with $\log N[\text{H I} (\text{cm}^{-2})] = 16.10 \pm 0.02$ together with 5 ionized metal absorption lines in form of O VI, C II, C III, Si II and

Si III. Metal line absorptions allows us to model the ionizing conditions prevailing in the absorbing clouds with more reliability as discussed in section 5.3 to estimate the physical conditions of the absorber.

5.2 Voigt profile fitting

Lyman lines are seen in varying numbers in different components of the absorber system. To better constraint the line parameters, we fit all the Lyman transitions upto H I 918 together. We exclude higher order Lyman lines than H I 918 because of their weak S/N. The Ly β has a contamination redward of the component III from Ly γ at $z=0.421883$. O VI 1032,1038 also shows two component structure. This doublet is fitted simultaneously with two components. Si II 1260 and Si III 1206 lines show single component structure and are fitted separately with single components. C II 1036 line shows a single component profile and hence fitted with one component. At first glance the C III 977 line looks like it has two component structure but it is contaminated from Ly α coming from $z=0.083078$, H I 926 from $z=0.421823$ and H I 926 from $z=0.386036, 0.386295$. So we fit this line with single C III component and these contaminations.

The system plot for the absorber system is shown in figure 5.1 over-plotted with fitted Voigt profiles. Horizontal axis is the rest-frame velocity of lines with respect to $z = 0.347586$ (redshift of O VI line of the component II) used as a proxy of wavelength and vertical axis represents the continuum normalized flux. The green step curve is the observed flux, the red solid curve is the Voigt profile fit, the blue dashed curves are the individual components that make the absorption profile with orange ones being the contamination (e.g in Ly β and C III 977), the light pink step curve is the continuum normalized error in observed flux and the vertical blue ticks shows the position of each component. Fitted parameters are tabulated in table 5.2.

VPFIT gives overestimated errors in the column densities and b values when the b value is significantly less than the COS spectral resolution ($\approx 17 \text{ km s}^{-1}$) as can be seen for C II, Si II and Si III lines. So, we used χ^2 of the fit to determine

Line	Component	v (km s⁻¹)	b (km s⁻¹)	log [N cm⁻²]
H I 918-1215	I	-163 ± 4	38 ± 6	13.46 ± 0.05
	II	1 ± 1	62 ± 3	14.13 ± 0.02
	III	68 ± 1	16 ± 1	16.10 ± 0.02
O VI 1032,1038	II	0 ± 1	30 ± 2	14.26 ± 0.09
	III	62 ± 1	13 ± 2	13.91 ± 0.04
C II 1036	III	64 ± 1	3 ± 28	14.21 ± 16.55
C III 977	III	70 ± 1	23 ± 2	13.81 ± 0.04
Si II 1260	III	65 ± 1	3 ± 23	13.19 ± 12.32
Si III 1206	III	68 ± 2	10 ± 12	12.87 ± 1.19

TABLE 5.2: Parameters from Voigt profile fitting of the absorption lines. Velocity is taken to be zero at the redshift of O VI line of component II, i.e. $z = 0.347586$

the uncertainties in the parameters. To do so, we fix all the parameters other than parameter whose uncertainty is to be determined. This free parameter is varied until χ^2 increases by 1 unit. The absolute difference between this value of parameter and best fit parameter gives $1-\sigma$ uncertainty in the parameter. We have one more source of uncertainty in the parameters, which manifests due to the continuum fitting, as the continuum fitting is subjective. To incorporate this uncertainty, we consider two more continuum, one at 3% above and 3% below the continuum used earlier. We again fit the lines, as described above to the spectrum normalised by these continuum. The absolute difference in the parameters from these fit and earlier fit is taken as the systematic error in the parameters. To be conservative,

we take maximum of the differences in the parameter values as systematic errors in the parameters and add them in the earlier errors. Table 5.3 gives the errors estimated in column densities using both the methods mentioned above.

Line	Component	χ^2	Continuum
H I 918-1215	I	0.04	0.07
	II	0.02	0.04
	III	0.02	0.03
O VI 1032,1038	II	0.02	0.03
	III	0.03	0.01
C II 1036	III	0.20	0.19
C III 977	III	0.03	0.01
Si II 1260	III	0.25	0.16
Si III 1206	III	0.06	0.02

TABLE 5.3: Error calculated using χ^2 and the systematic uncertainty in column densities due to continuum fitting given in units of $\log[N (\text{cm}^{-2})]$

PG0003 + 158 ($z_{\text{abs}} = 0.347586$)

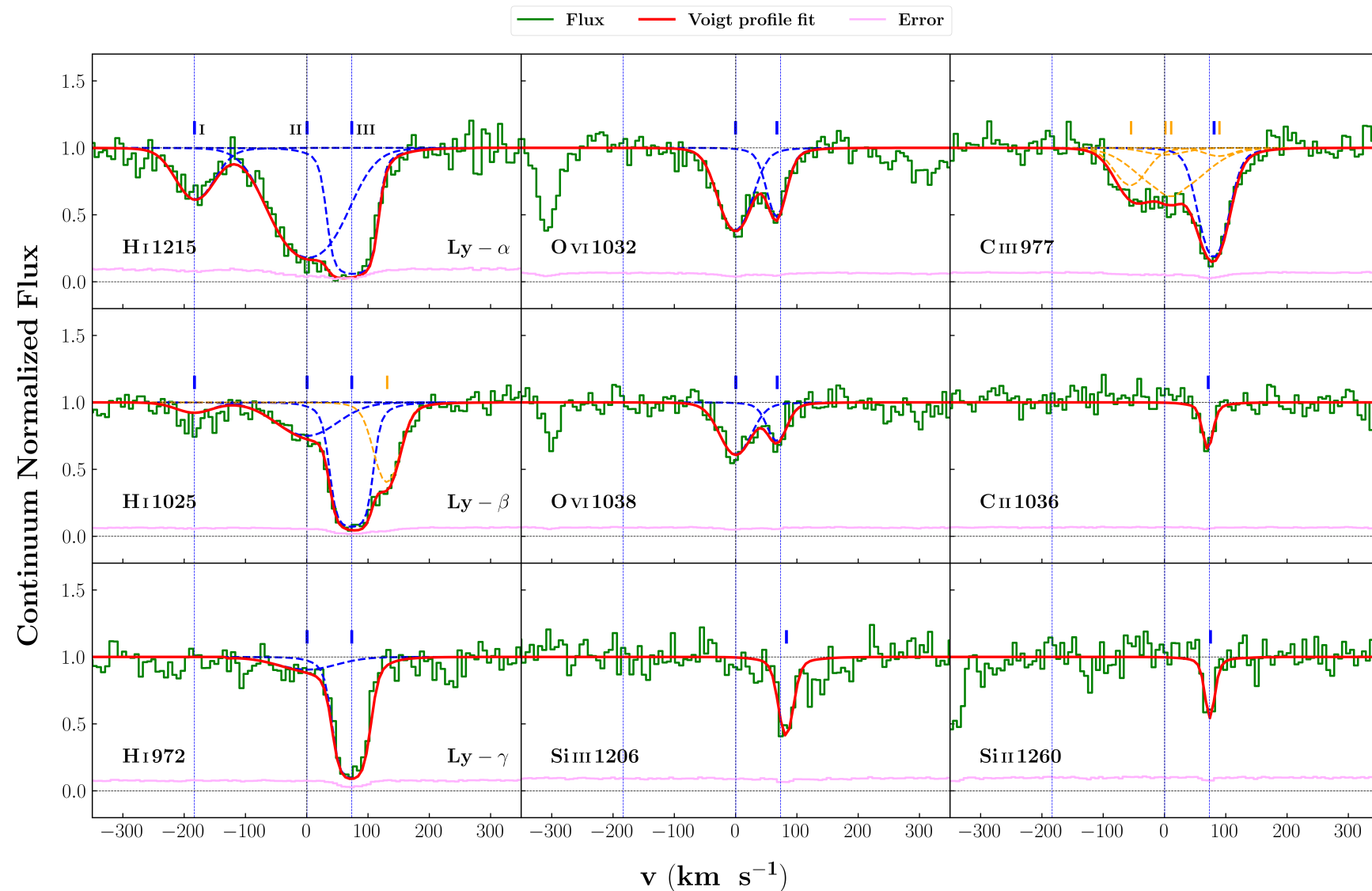


FIGURE 5.1: System plot of the absorption system. Reference velocity taken at $z = 0.347586$

5.3 Ionization Modelling of the Absorber

We have three components in our absorber system. But the first component has only H I absorption lines, we can't get anything than the upper limit on the temperature for this component, ionization modelling can't be performed for this component. So detailed modelling is done for components II and III only as discussed in subsequent sections.

5.3.1 Component II

For this component, we only have O VI absorption other than H I absorption. For modelling the ionizing conditions in this component we use very simplistic approach as we don't have much constraining parameters on the models. We consider both photoionisation and collisional ionisation scenarios for this component.

5.3.1.1 Photoionization modelling

Metallicity is an essential parameter for modelling the ionization conditions. But we cannot make an estimate of metallicity for this component directly. As this component and component III are separated by small velocity ($\approx 65 \text{ km s}^{-1}$), we assume that the metallicity change would not be significant between these components. So we take the metallicity of this component to be same as that of the component III, whose metallicity is estimated more rigorously as described in section 5.3.2. To estimate the density, we run a grid of photoionization (PIE) CLOUDY models with varying $\log n_H (\text{cm}^{-3})$ between -5 to 0 at steps of 0.02 and using the metallicity as what we get for the component III in section 5.3.2 and using $\log [\text{N(HI)} (\text{cm}^{-2})] = 14.13$ as stopping criteria. We then take the density of this component to be the density at which we recover the O VI observed column density for this component.

As discussed in section 5.3.2.1, we take the metallicity for this component to be what we get from excluding O VI case of the component III photoionization modelling (see section 5.3.2). Using this metallicity, we get the density , $\log n_H (\text{cm}^{-3}) = -4.51$. The modelled column densities of other ions detected in component

III (C II, C III, Si II and Si III) are in agreement with the upper limits based on non-detections obtained from apparent optical depth measurements. This solution predicts an equilibrium temperature of around 2.5×10^4 K, which contradicts with the temperature obtained from b value of H I and O VI by an order of magnitude as calculated in section 5.4.1. The total hydrogen column density predicted by this solution is $\log [N(H)\text{cm}^{-2}] = 18.45$, which results in line of sight thickness of around 30kpc, which is physically unrealistic given that CLOUDY models the clouds to be homogeneous. Such large structures don't produce simple systems like what we observed. So we discard this solution to be depicting the prevailing conditions in the absorbing cloud.

5.3.1.2 Collisional ionization modelling

We also perform a collisional ionization equilibrium (CIE) modelling for this component. We consider hybrid models where both photoionization (from ionizing extragalactic background) and collisional ionization are occurring simultaneously. We run a grid of CLOUDY models with varying the $\log n_H$ (cm^{-3}) from -5 to 0 with steps of 0.02 and $\log Z/Z_\odot$ from -3 to 2 with steps of 0.04 at a constant temperature of $10^{5.29}$ K, as calculated in section (temperature calculation). Though we have considered hybrid models, at these temperatures collisional ionisation would be a dominant process. We then find the metallicities where the observed O VI column density matches the modelled column density for different $\log n_H$ values.

We only have O VI column density as a constraining parameter in these models. We also use size as a constraint to arrive at the conditions prevailing in the component. As we have fairly simple absorber with just Lyman and O VI absorption, we profess that the size of the absorber must not be very large, since large absorber clouds would not produce such simple absorber systems. So we discard out the low density scenarios, as low density would result in large line of sight lengths to recover the observed column densities. This helps us to constrain the density as, $\log n_H$ (cm^{-3}) > -3 as viable conditions for the absorber cloud. As shown in figure 5.2, this corresponds to $\log Z/Z_\odot > 0.4$. Now we run a hybrid model with this density, metallicity at constant temperature of $\log T$ (K) = 5.29. This gives an upper limit

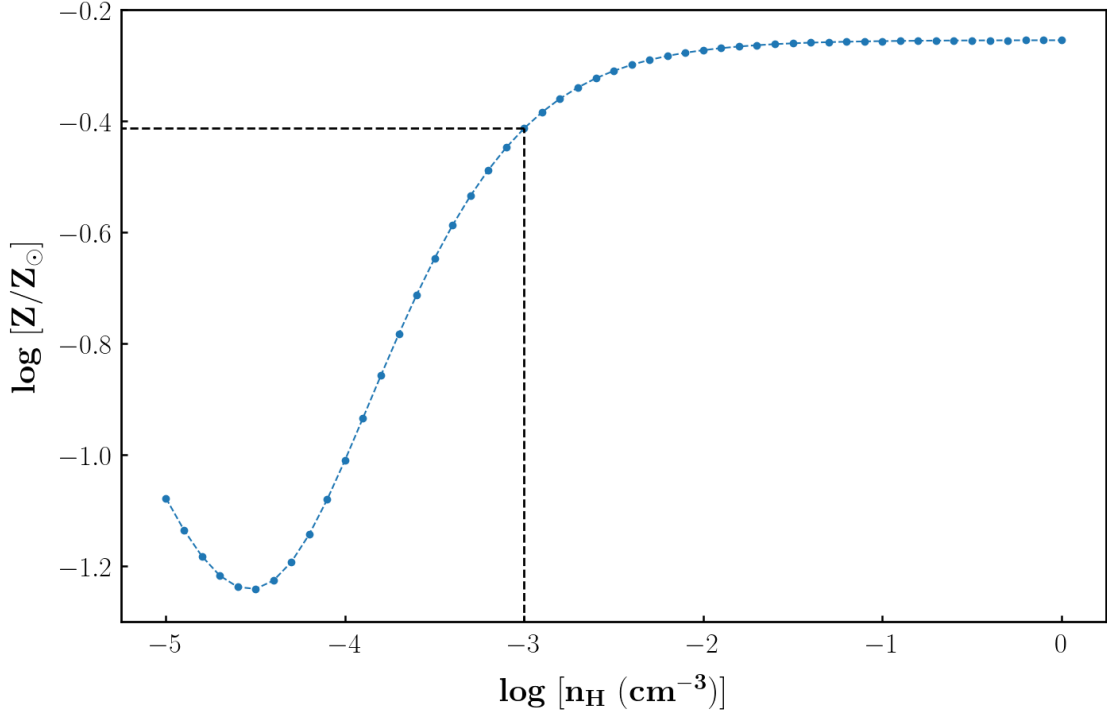


FIGURE 5.2: CIE solution for component II. The figure shows the metallicity found for various densities. At high densities no variation in metallicity is seen.

on total Hydrogen column density, $\log [N(\text{H}) \text{ cm}^{-2}] = 19.62$, which results in an upper estimate on the size to be ~ 13 kpc.

5.3.2 Component III

We consider only photoionization modelling for this component, as small b values indicate a low temperature for the component, as the contribution from collisional ionization will not be significant at low temperature.

5.3.2.1 Photoionization modelling

Along with H I, we have 5 metal ion detections viz. C II, C III, Si II, Si III and O VI in this component. We can estimate the density and metallicity for this component with the observed column densities of the detected metal ions by using CLOUDY

models. As discussed in section 4.3 we use the χ^2 minimisation technique described in Acharya & Khaire (2021) to estimate the density (n_H) and metallicity (Z) of the absorber. We consider a dense grid of photoionization equilibrium (PIE) CLOUDY models with varying $\log n_H$ and $\log Z$. We vary the $\log n_H$ (cm^{-3}) from -5 to 0 in steps of 0.02 and $\log Z/Z_\odot$ from -3 to 2 in steps of 0.04. The H I column density for this component is $\log N(H I)$ (cm^{-2}) = 16.10. So, we give the $\log [N(H I)]$ (cm^{-2}) = 16.10 as the stopping criteria for the CLOUDY calculations. The observed column densities and corresponding $1-\sigma$ errors for the ions used in the process are listed in table 5.4. The $1-\sigma$ errors are the sum of errors given in table 5.3, i.e we take in account the systematic uncertainty due to continuum fitting.

We first try to model this absorber by assuming all the ions are arising from same gas phase, i.e. considering all the observed ions for χ^2 minimization. We find that the solution can't match the modelled column densities with the observed column densities of the ions, except for O VI, whose column density matches the best out of all the ions, as shown in figure 5.3 (green filled circles). This predicts a temperature around 2.8×10^4 K and a low density of $\log n_H$ (cm^{-3}) = -3.88 and total Hydrogen column density, $\log [N(H)]$ (cm^{-2}) = 19.87, leading to a very large line of sight thickness of ≈ 180 kpc.

As the above solution couldn't fit the observations well, we consider another case where all ions other than O VI are arising from same gas phase. So, now we calculate the χ^2 from column densities of other ions than O VI and then minimise this χ^2 to fit the model. This solution gives a good fit for the observed column densities of all the ions but now the O VI is under-produced by orders of magnitude as seen in figure 5.3 (orange filled circles). This solution gives a temperature of about 1.0×10^4 K. This solution predicts a total Hydrogen column density, $\log [N(H)]$ (cm^{-2}) = 17.92, smaller by nearly 2 orders than the previous case and a higher density, $\log n_H$ (cm^{-3}) = -2.24. This gives a line of sight thickness for the cloud to be around 50 pc. As this case gives a better fit, we consider this to be the more correct description of the physical conditions in the absorber and draw our inferences based on this solution.

Ion	$\log[N \text{ (cm}^{-2}\text{)}]$	$\Delta \log[N \text{ (cm}^{-2}\text{)}]$
O VI	13.91	0.04
C II	14.21	0.39
C III	13.81	0.04
Si II	13.19	0.41
Si III	12.87	0.08

TABLE 5.4: Column densities and corresponding $1-\sigma$ errors of the ions used in PIE modelling of the component III

The $\log n_H$, $\log Z$ and χ^2 values for both the cases are given in table 5.5. And the physical properties of all the three components are listed in table 5.6 based on the ionization modelling used.

Case	$\log n_H \text{ (cm}^{-3}\text{)}$	$\log Z/Z_\odot$	χ^2
All ions	-3.88 ± 0.02	-1.51 ± 0.03	275.67
Excluding O VI	-2.24 ± 0.03	-0.31 ± 0.06	4.27

TABLE 5.5: Cloudy modelling solutions for absorber at $z \sim 0.34790$. In case of all ions χ^2 is calculated using the column densities of all the ions but for excluding O VI ion case, χ^2 is calculated by excluding O VI column density so as to show that this fits other ions very well.

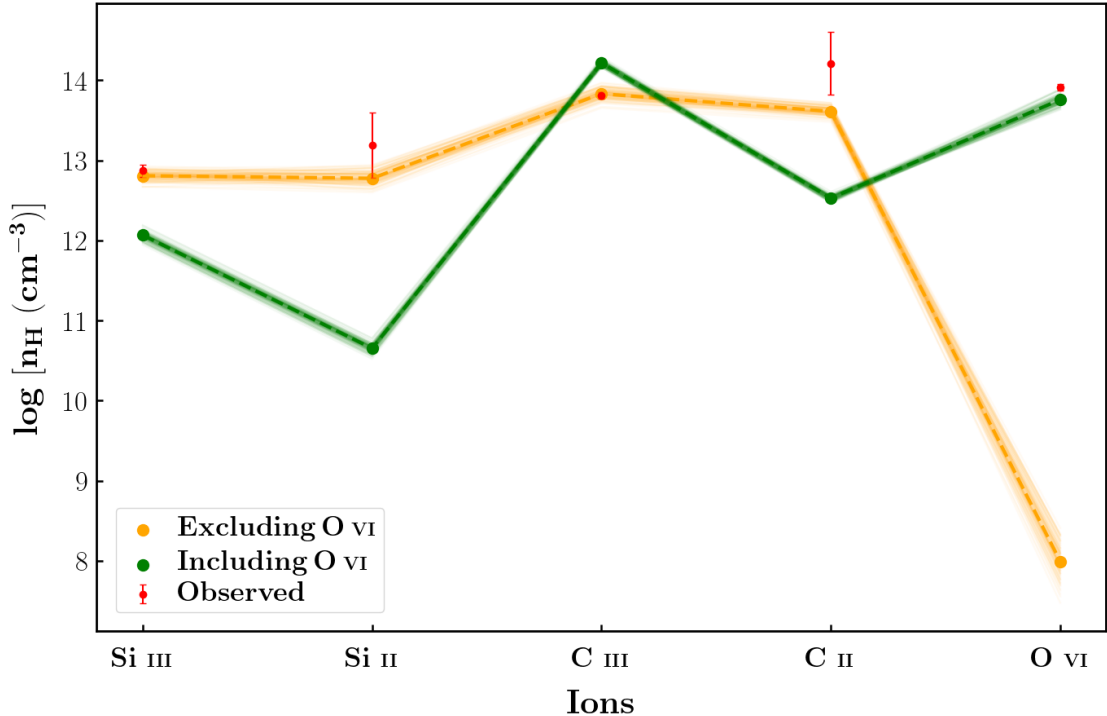


FIGURE 5.3: Modelled and observed column densities for the component III based on photoionization modelling. Red error bars shows the observed column densities and corresponding $1-\sigma$ errors in column densities. The green and orange filled circles are the modelled column densities for the including O VI and excluding O VI case of PIE modelling. And the light green and light orange lines are modelled column densities with densities and metallicity sampled from normal distributions of $\log n_H$ and $\log Z$ of including O VI and excluding O VI case respectively.

Absorber	Ions	$\log N(H\ I)$	Model	$\log N(H)$	$\log n_H$	$\log Z/Z_{\odot}$	Size	T	P/K
		(cm^{-2})		(cm^{-2})	(cm^{-3})		(kpc)	(K)	(cm^{-3} K)
$z \sim 0.34678$	H I	13.46	-	-	-	-	-	$\leq 8.7 \times 10^4$	-
$z \sim 0.34758$	H I, O VI	14.13	PIE Hybrid	18.45 $\lesssim 19.62$	-4.51 $\gtrsim -3$	-0.31 $\gtrsim -0.4$	29.47 $\lesssim 13.35$	2.5×10^4 1.9×10^5	0.77 $\gtrsim 194.98$
$z \sim 0.34790$	H I, O VI, C II, C III, Si II, Si III	16.10	PIE (All ions) PIE (Excluding O VI)	19.87 17.92	-3.88 -2.24	-1.51 -0.31	180.75 0.05	2.8×10^4 1.0×10^4	3.68 59.02

TABLE 5.6: Physical properties of the absorbers based on Voigt profile measurement and CLOUDY ionisation modelling. The PIE solution for absorber at $z \sim 0.34758$ is based on the excluding O VI case PIE solution of the absorber at $z \sim 0.34790$.

5.4 Origin of O VI in the Absorber

5.4.1 Component II

The large b value indicates a large value of the temperature. As we the O VI absorption is coincident with the BLA we can directly estimate this temperature using their b values. The b values which we get from Voigt profile have both thermal and non thermal contributions.

$$b(\text{H I}) = \sqrt{b_{\text{thermal}}^2(\text{H I}) + b_{\text{non-thermal}}^2} \quad (5.1)$$

$$b(\text{O VI}) = \sqrt{b_{\text{thermal}}^2(\text{O VI}) + b_{\text{non-thermal}}^2} \quad (5.2)$$

$$b_{\text{thermal}} = \sqrt{\frac{2kT}{m}} \quad (5.3)$$

Where, k , T and m are Boltzmann constant, temperature and atomic mass of the species respectively.

From equation 5.3 we have,

$$b_{\text{thermal}}(\text{H I}) = 4 b_{\text{thermal}}(\text{O VI}) \quad (5.4)$$

Solving above equations for T gives, $T = 10^{5.29^{+0.07}} \text{ K}$, which lies in the temperature range of WHIM. This temperature results in $b_{\text{thermal}}(\text{H I}) \sim 57 \text{ km s}^{-1}$ and $b_{\text{thermal}}(\text{O VI}) \sim 14 \text{ km s}^{-1}$. High temperature contributes to around 91 % of the broadening of the H I line whereas the O VI line broadening is dominated by non-thermal components. An inherent assumption in this calculation is that the both lines have same contributions from non-thermal components.

The ionization fraction of O VI in collisional ionization equilibrium peaks around $10^{5.7} \text{ K}$. We are getting a nearby temperature of $10^{5.29} \text{ K}$, so the O VI could be tracing a collisionally ionised gas phase.

5.4.2 Component III

As discussed in section 5.3.2.1, we consider two cases of photoionization models, one solution is able to explain O VI column density but can't model column densities of other ions. Another solution models the column densities of other ions but fails to explain the O VI column density. We discard the first case on grounds of poor fit and large line of sight length. And accept the second case to be more accurate description of the absorbing cloud conditions. We argue that as the other ions excluding O VI can be explained by photoionisation models, they must be arising from a cool photoionised gas phase. But the question still remains that from where the O VI absorption is coming from?

There have been similar instances in literature where the O VI can't be explained from photoionised phase and could possibly be tracing a warm phase (see e.g. Pradeep et al. 2020; Anshul et al. 2021). So, we assert that O VI absorption may be arising from a different hidden phase in the absorber and possibly tracing a collisionally ionised phase. However, to infer about this 'hidden' phase we need details on the associated Lyman α component. Since the Lyman α feature in absorber system is almost saturated with 3 components, we can't get any insights on the contributions from the hidden 4th component if there is any.

5.5 Galaxy environment of the absorber

Galaxies, galaxy groups or clusters can have large gaseous halos surrounding them, called the circumgalactic medium (CGM) extending upto kpc scales. Our absorber system could be tracing one such halo. So we lookout for the galaxies around the absorber to check if this is the case. We search galaxies with velocity separations within 1000 km s^{-1} from the absorber and within $15'$ on the plane of sky from the quasar line of sight, which spans around 4.4 Mpc at the absorber redshift⁵. No spectroscopically identified galaxies were found in the SDSS DR17 (Abdurro'uf et al. 2022) footprints with above constraints. SDSS' 90 per cent spectroscopic completeness limit of $r < 17.8$ (Strauss et al. 2002) gives luminosity

5. Assuming a flat Λ CDM cosmology with $H = 69.6 \text{ km s}^{-1} \text{ Mpc}^{-1}$

R.A.	Dec.	z	Δv (km s ⁻¹)	η (arcmin)	ρ (Mpc)	r	L (L*)
1.43341	15.97131	0.3351	-2564	12.1	3.6	20.387	0.24
1.52570	15.98456	0.3466	-200	10.9	3.2	21.719	0.07
1.48286	16.14235	0.3517	838	1.5	0.4	21.533	0.09
1.43069	16.16771	0.3582	2153	3.8	1.1	19.342	0.72
1.44071	16.16933	0.3593	2374	3.3	1.0	19.745	0.50

TABLE 5.7: Galaxies in the neighbourhood of the absorber system identified in VIMOS survey. Velocity is taken to be zero at z = 0.347586

limit of $L \gtrsim 2.77 L^*$ at $z \sim 0.347$ assuming luminosity functions calculated by Ilbert et al. (2005). This implies that the SDSS spectroscopic survey has only sampled the bright galaxies only. So there could be sub-L* galaxies present around the absorber system

Our line of sight was also observed under the VIMOS survey (Le Fèvre et al. 2013) (PI - Thomas Shanks, Program Id : 097.A-0535(D)). The VIMOS field of view in imaging mode comprises of 4 quadrants. The quasar PG0003+158 was centered in the 3rd quadrant out of this 4 quadrants. The field was observed in B (383-478 nm) and R (579-713) filters.

5 galaxies were identified within the field. We looked for these galaxies in the SDSS photometric survey and found all of the 5 galaxies providing us with the photometric data. The details of the galaxies are given in table 5.7. The table gives the position, redshift, velocity separation, separation on the plane of sky (η), projected distance on the plane of sky (ρ) and the SDSS r-band magnitude and luminosity of the galaxies. Two of the galaxies were within 1000 km s⁻¹ and 15' from the quasar line of sight. Figure 5.4 shows the galaxies around the absorber system color coded with the absolute velocity separation from the absorber system (z=0.347586). The cross mark in the center is the line of sight of PG 0003+158.

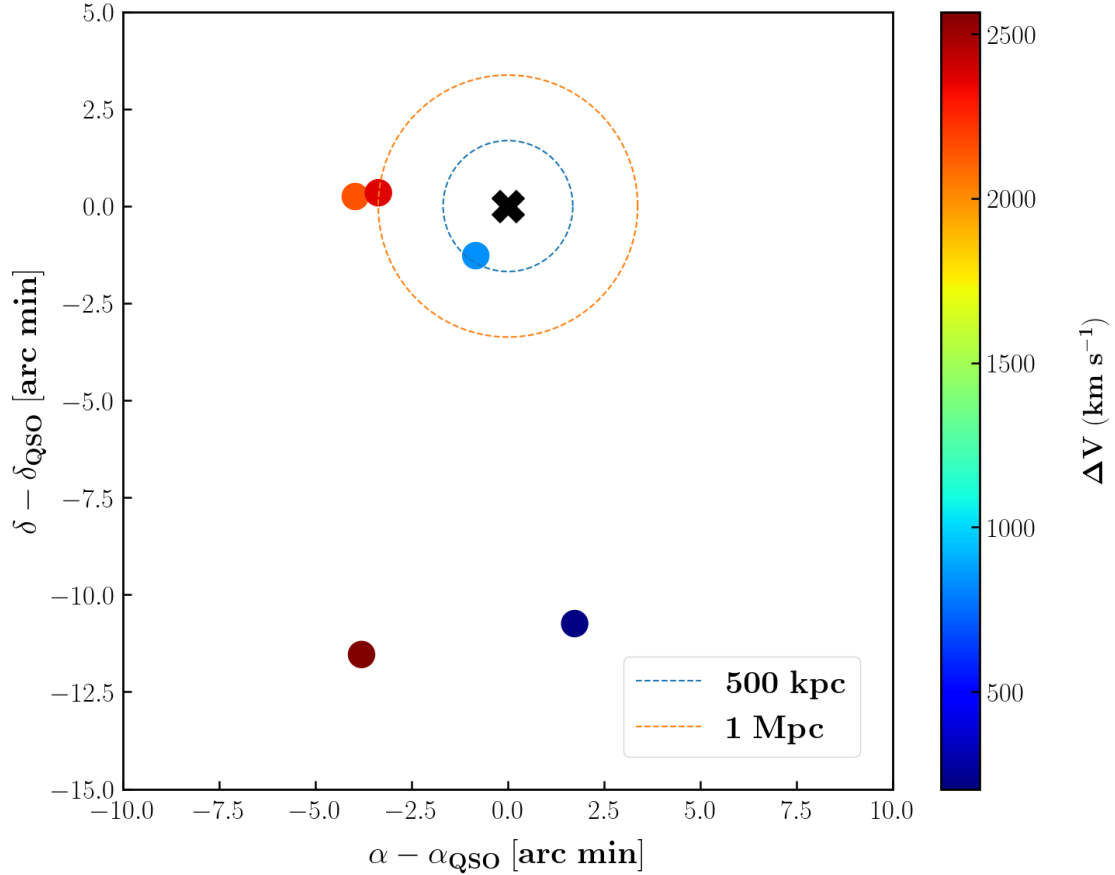


FIGURE 5.4: Galaxies around the absorber color-coded with their velocity separation from the absorber.

The blue and orange dashed curves show the projected distance at the absorber redshift ($z=0.347586$) of 500 kpc and 1 Mpc respectively. There is one galaxy within a projected separation of 500 kpc but it separated by around 838 km s^{-1} from the absorber. We find one galaxy at 200 km s^{-1} from the absorber but it is at a projected distance of around 3.2 Mpc from the line of sight.

[Prochaska et al. \(2011\)](#) gives the following scaling relation between luminosity and virial radius of a galaxy but warns that this is based on crude estimates and should serve as a mere guideline :

$$r_{vir} = r_{vir}^* \left(\frac{L}{L^*} \right)^\beta$$

with $r_{vir}^* = 250$ kpc and $\beta = 0.2$. For the galaxy at projected distance of 0.4 Mpc which is the closest in projected distance, r_{vir} comes out to be 155 kpc which is 2.6 times less than the projected distance. So the absorber is quite far from the CGM of this galaxy. The virial radii of other galaxies are also not large enough.

We see that the absorber lies in a galaxy under-dense region, so the absorber could be tracing a large scale filamentary structure in the cosmic web or CGM of a faint galaxy with a luminosity less than $0.07 L^*$ which is not sampled in the current observations.

Chapter 6

Hunt for BLAs : The Survey

The foremost goal of the current study is to do a survey of BLAs over a large data-set and then estimate their contribution in the closure density of Ω_b . In this chapter we describe our approach to carry out this exhaustive survey.

6.1 Shortlisting the BLA candidates

[Danforth et al. \(2016\)](#) have identified a total of 2611 absorber systems in their study of the low redshift intergalactic medium. We need to find suitable candidates for our survey of BLAs from these 2611 absorbers.

We use two criterias to select BLA candidates for our survey. First, we look for broad Ly α lines in all the 2611 absorbers. For a Ly α line to be adjudged as ‘broad’, we fix our threshold for b value to be greater than 45 km s^{-1} in the preliminary fitting done by [Danforth et al. \(2016\)](#). Assuming a complete thermal broadening, $b = 45 \text{ km s}^{-1}$ gives a temperature of $\approx 1.2 \times 10^5 \text{ K}$, which lies in the lower ranges of the temperature of WHIM. By giving this constrain, we get 568 such systems in the complete data-set.

As discussed in section 1.3, multiple lines or contaminations from other lines can blend together to give rise to broad absorption features. In such cases, we need to carefully model these broad lines and confirm that these are actually tracing hot collisionally ionised gas phase so that they are indeed probing WHIM and

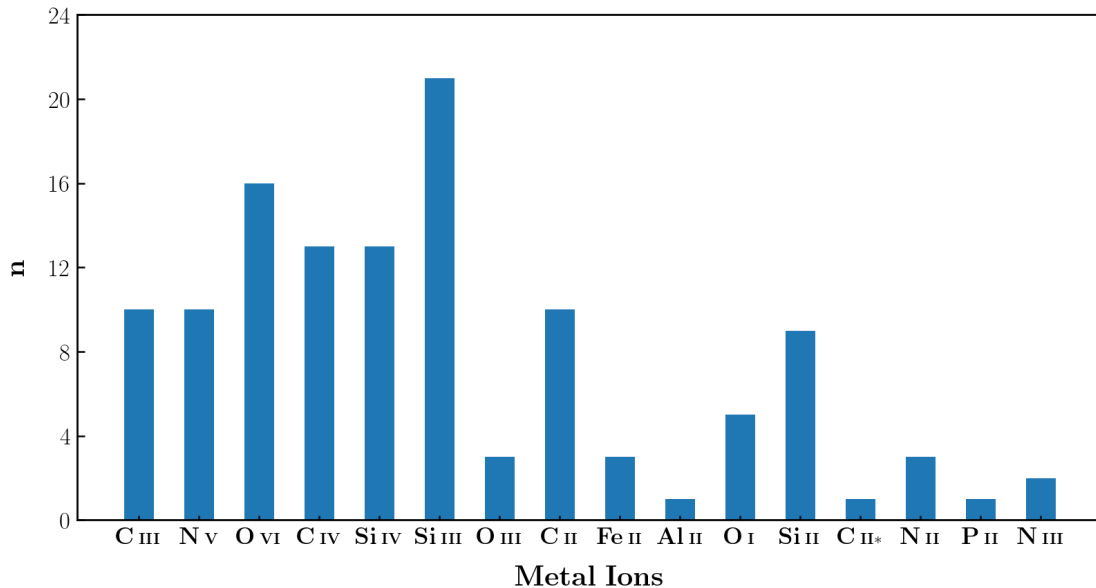


FIGURE 6.1: No. of different metal ions in all the 29 absorber systems.

not just cool photoionised phase. We need to perform ionisation modelling for it. To model the ionisation conditions of the absorber systems, we need metal ion column densities. So we search for systems showing metal line absorption in these 568 ‘broad’ systems. We need at least three distinct metal ions (not lines) to better constrain the ionisation state of an absorber system. This sets our second criteria that there should be minimum of three metal ion absorption in the absorber systems. Upon putting this constrain, we get 29 systems having at least 3 distinct metal ions out of 568 already identified systems. Out of these 29 systems, we have already studied one of the absorber in chapter 5. Table 6.1 lists the lines of sight, redshift of the absorber and the ions detected in the systems these 29 identified BLA candidate absorber systems. Figure 6.1 shows the distribution of different metal ions found in these 29 absorber systems. These 29 absorbers are found along 22 different sight lines. The details these lines of sight are given in appendix A. The details of the HST/COS observations of these 22 sight lines are given in appendix B

S. no.	Sight line	z_{abs}	Metal ions
1	1ES 1553+113	0.187731	C III, O VI, N V
2	3C 263	0.063275	C IV, Si III, Si IV
3	3C 263	0.140754	C IV, Si III, O VI
4	3C 57	0.077493	C IV, Si IV, N V
5	H 1821+643	0.170062	Si III, O VI, N V
6	H 1821+643	0.224832	Si III, O VI, C III
7	HE 0056-3622	0.043318	C IV, Si III, N V
8	PMN J1103-2329	0.003975	C IV, Si III, Si IV, N V
9	PG 0003+158	0.386094	C III, O VI, O III, N V
10	PG 0003+158	0.347586	C II, C III, Si II, Si III, O VI
11	PG 0003+158	0.421880	O VI, O III, C III
12	PG 0832+251	0.017520	C IV, Si IV, O I, Si III, C II, Si II, Fe II, Al II, N V
13	PG 1116+215	0.138527	C IV, Si IV, N II, P II, Si III, Si II, C II, O VI, N V
14	PG 1121+422	0.192434	Si IV, C III, Si III, Si II, C II, O VI
15	PG 1216+069	0.006390	O I, Si II, C II
16	PG 1216+069	0.282195	Si III, O VI, C III
17	PG 1222+216	0.054491	C IV, Si III, Si IV
18	PG 1222+216	0.378600	Si III, O VI, O III, C III
19	PG 1259+593	0.046107	C IV, Si III, Si IV
20	PG 1424+240	0.146789	C IV, Si III, O VI, Si IV
21	PHL 1811	0.080837	C IV, Si IV, N II, O I, Fe II, Si II, C II
22	PKS 0405-123	0.167125	Si IV, N II, C III, O I, Si III, Si II, C II, O VI, N III, N V
23	PKS 0637-752	0.161068	Si III, O VI, N V
24	PKS 0637-752	0.417573	Si III, O VI, C III
25	PKS 1302-102	0.094864	Si III, Si II, C II
26	RX J0439.6-5311	0.005602	C IV, Si III, Si IV
27	SDSS J135712.61+170444	0.097767	C IV, Si IV, Si III, C II, O VI
28	SBS 1108+560	0.463201	C III, O I, Si III, Si II, C II, O VI, N III
29	UKS 0242-724	0.063775	Fe II, Si II, C II

TABLE 6.1: Details of the 29 BLA candidate absorber system shortlisted for the survey.

6.2 Survey methodology

We have identified 28 additional BLA candidate systems for our survey. We need to do the Voigt profile fitting to the absorption lines identified in these systems. These will give us the column densities and Doppler parameters of the ions in the system and also their redshifts (velocities). We will further use these quantities to model the ionisation conditions in these absorber systems.

The distribution of these quantities can give valuable insights towards our understanding of the intergalactic medium and the baryon content within IGM. As discussed in chapter 1, that O VI is good tracer of WHIM. O VI absorption is seen in 16 out of these remaining 16 absorbers. For the remaining 12 candidates, O VI is not a non-detection. The O VI 1032, 1038 lines fall out the coverage of the HST/COS FUV channel at redshifts below ~ 0.093854 and all these remaining 12 systems are at redshift below 0.093854. So O VI is not covered in these systems. However, for one system which is along the LOS of PKS1302-102 at $z_{abs} = 0.094864$, the O VI 1038 line was just falling just on the edge of the spectrum where both S/N and sensitivity both low. So, O VI absorption was not considered for this system.

We first model the ionisation conditions in the 16 O VI absorbers and see if we can explain the origin of O VI through photoionisation models using the similar method used for the absorber in chapter 5. For, the remaining 12 non-O VI absorber, we model the ionisation conditions based on the ions detected in the systems to estimate the density and metallicity in these systems.

Then, we will use the results from this survey to estimate the baryon content in BLAs and their contribution to cosmic closure density, Ω_b , the details of which are described in the upcoming chapter.

The Voigt profile fitting and ionisation modelling results are given in appendix C after the references.

6.3 Survey statistics

In this section, we discuss the statistics and results of the survey from Voigt profile fitting and ionisation modelling of the 29 absorber systems.

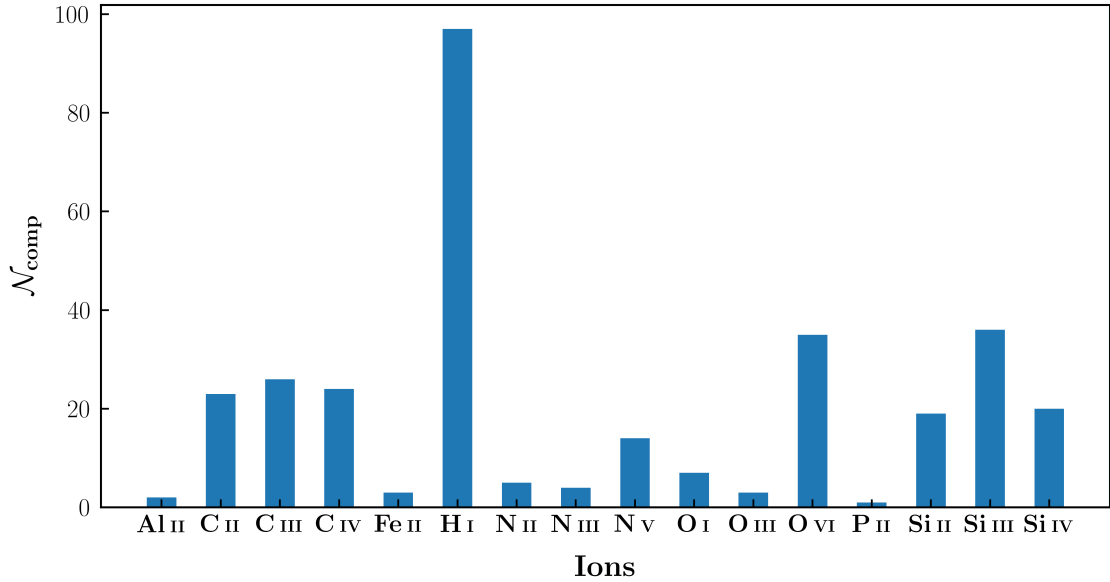


FIGURE 6.2: No. of components identified for H I and different metal ions.

6.3.1 Voigt profile fitting

This survey of 29 absorbers spanned 22 lines of sight. These 22 lines of sight have total H I (Lyman- α) redshift pathlength of $\Delta z = 5.561$. A total of 711 absorption lines were identified and fitted with Voigt profiles. These 711 lines shown absorption from 15 different metal ions apart from H I absorption. The figure 6.2 shows the total number of components identified for each species. For studies similar to current one, it is very insightful to describe the line density per unit redshift (dN/dz) and bivariate distribution of the absorbers with respect to column density and redshift ($\partial^2 N / \partial N \partial z$) (see e.g. [Danforth et al. \(2016\)](#); [Penton et al. \(2000\)](#); [Tilton et al. \(2012\)](#)). However, since our current sample is not statistically large, we don't describe these metrics while discussing the statistics of the survey.

6.3.1.1 H I absorbers

We have identified 97 H I components in our survey across 29 absorbers. The figure 6.3 shows the distribution of column densities and redshift of these 97 components. These components span seven orders of magnitude of column densities

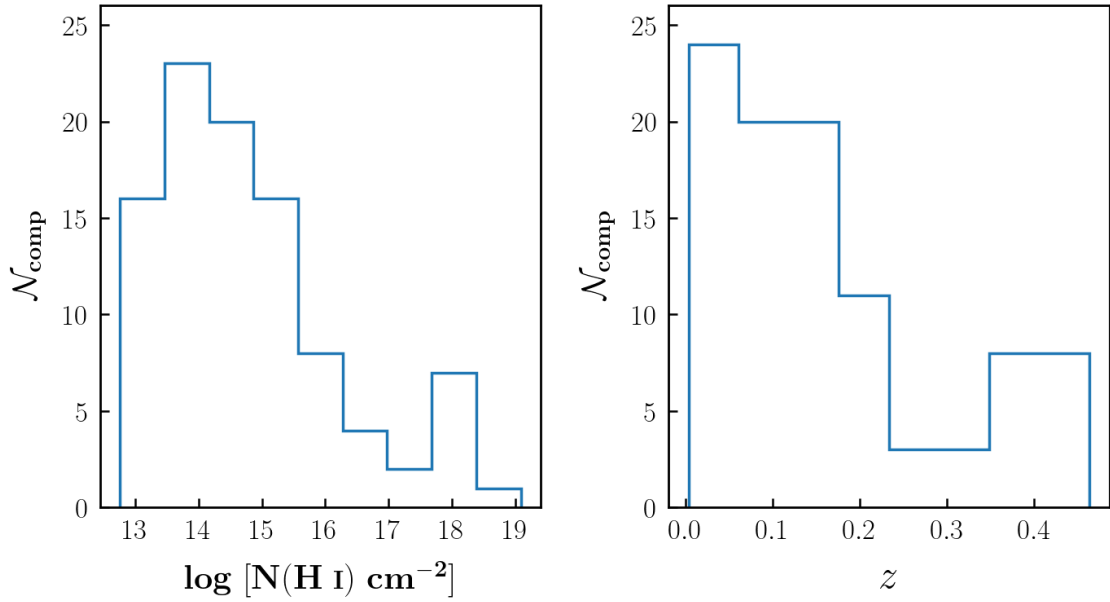
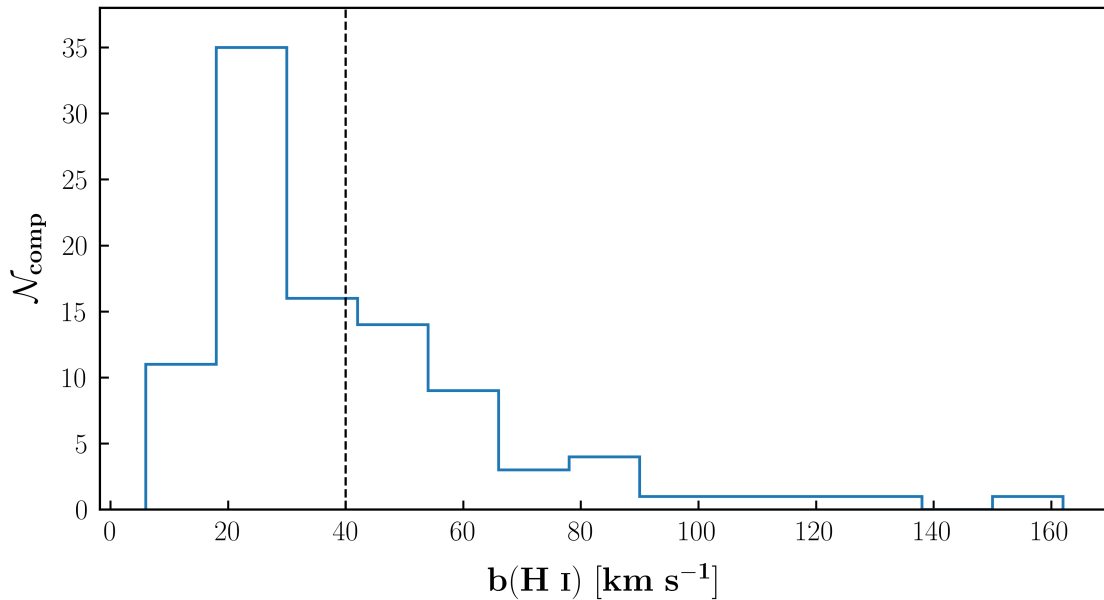


FIGURE 6.3: Distribution of column densities (left panel) and redshift (right panel) of 97 H I components.

starting from $\sim 10^{13}$ to 10^{19} cm^{-2} . We have many absorbers with the column densities in the range $10^{13} - 10^{15.5} \text{ cm}^{-2}$ but current sample is incomplete at rare large column density systems. In our current sample, we see H I absorption till $z \sim 0.45$. In redshift space also, we have more systems at lower redshifts ($z < 0.2$) and only few absorbers at higher redshifts.

Distribution of Doppler parameters

The figure 6.4 shows the distribution of Doppler b parameters of the 97 H I components. The vertical dashed line marks the cutoff for the line to be called as ‘BLA’ at $b=40 \text{ km s}^{-1}$. Assuming a complete thermal broadening, $b = 40 \text{ km s}^{-1}$ gives a temperature of 10^5 K . Out of 97 components, 37(34) components have Doppler parameters in excess of $40(45) \text{ km s}^{-1}$. Some components show large Doppler widths of above 100 km s^{-1} , for these components only saturated Ly α lines are seen, making the identification of velocity substructures of these lines difficult. This results in the large b values for these lines.

FIGURE 6.4: Distribution of b parameters of 97 H I components.

Temperature estimation using Doppler parameters

We make an estimate of the temperature of the absorbers directly from their Doppler parameters as done for the absorber in chapter 5. To do so we need the H I lines to be fairly aligned with some other metal ion. Because, if the species are aligned, then we can assume that they are co-spatial, so that there non-thermal broadening could be assumed to be same. However, we need to be cautious that aligned species need not be co-spatial always. HST/COS data may have wavelength calibration errors of 15-20 km s⁻¹, which could be as high as few resolution elements (Wakker et al. 2015). So, we consider species as aligned if they are separated by less than 20 km s⁻¹ in velocity within the fitting errors. We use O VI as the metal specie for estimating the temperature.

We plot the $b(\text{O VI})$ vs $b(\text{H I})$ in figure 6.5 for the 17 absorbers. The orange dashed line corresponds to points where $b(\text{H I}) = 4b(\text{O VI})$ which is the case for pure thermal broadening, i.e. non-thermal contributions are zero. The blue marks the region where the non-thermal broadening dominates the line broadening. This is $b(\text{H I}) = b(\text{O VI})$ line. And vertical green dashed line marks our cutoff for the

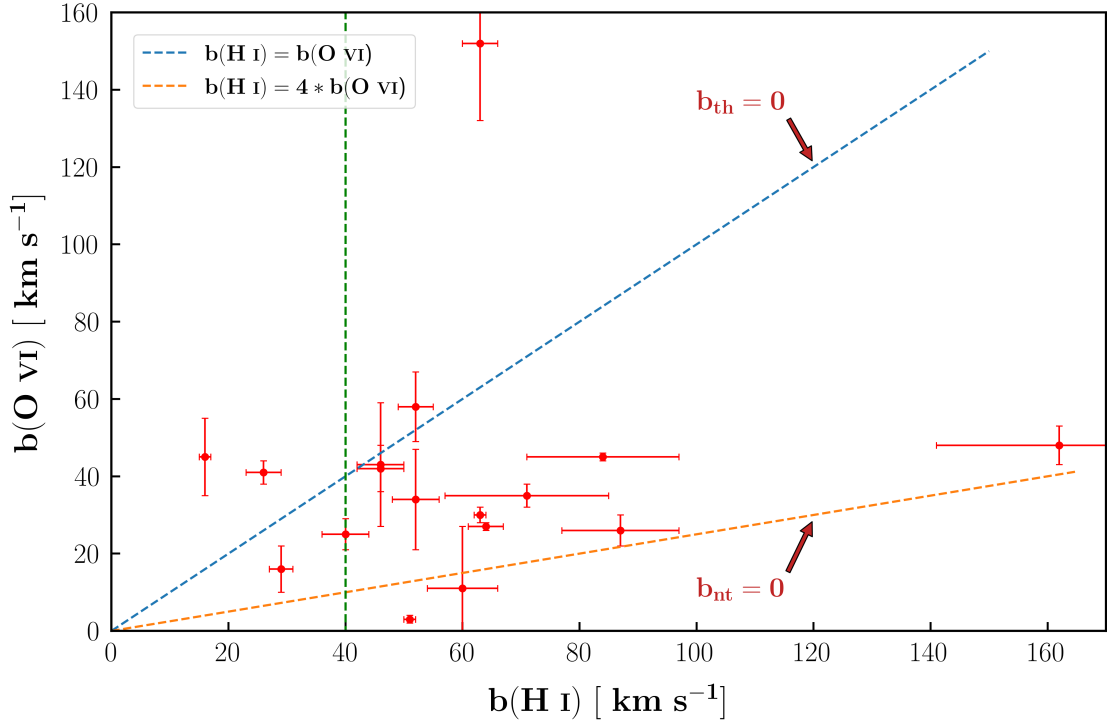


FIGURE 6.5: $b(\text{O VI})$ vs $b(\text{H I})$ plot. The orange dashed line is the $b(\text{H I}) = 4b(\text{O VI})$ line and blue dashed line shows the $b(\text{H I}) = b(\text{O VI})$ line.

line to be called as BLA. Now, we can estimate the temperature for a system if the b values of these two species lies within these orange and blue lines given that they are aligned.

We could estimate the temperature for 7 components where H I and O VI were aligned. We list the details of these systems in table 6.2. This estimation of temperature is important in our estimation of $\Omega_b(\text{BLA})$ (see section 7.2.1).

$N(\text{H I})$ - $b(\text{H I})$ distribution

We plot the H I column density with Doppler parameter in figure 6.6. We observe that lines with large Doppler widths are found within narrow range of column densities towards the lower end. It could possibly be because large b values indicates the presence of high temperature gas, where neutral fraction of Hydrogen will be small. We also see that the lines with large b values have large uncertainties

Sight line	z_{abs}	Δv^{a} (km s $^{-1}$)	$b(\text{H I})$ (km s $^{-1}$)	$b(\text{O VI})$ (km s $^{-1}$)	b_{th} (km s $^{-1}$)	$\log T$ (K)
PG 0003+158	0.347586	0 ± 1	62 ± 3	30 ± 2	56 ± 2	5.28 ± 0.05
PG 0003+158	0.386089	14 ± 9	40 ± 4	25 ± 4	32 ± 3	4.80 ± 0.11
1ES 1553+113	0.187764	$28 \pm 1^{\text{b}}$	51 ± 1	15 ± 3	50 ± 1	5.19 ± 0.04
PG 1222+216	0.378389	4 ± 15	52 ± 4	34 ± 13	41 ± 6	5.00 ± 0.17
PG 1222+216	0.378389	18 ± 4	43 ± 1	29 ± 13	33 ± 6	4.81 ± 0.19
PG 1116+215	0.138527	4 ± 9	71 ± 14	35 ± 3	64 ± 8	5.39 ± 0.21
H 1821+643	0.224981	19 ± 10	84 ± 13	45 ± 1	73 ± 8	5.51 ± 0.16

^a Velocity separation between H I and O VI components

^b Even though $\Delta v > 20$ km s $^{-1}$ we still assume it to be aligned.

TABLE 6.2: Details of temperature estimation from Doppler parameters.

also. It is because that most of these are coming from absorbers at lower redshifts where only Ly α is covered in COS/FUV, which is saturated. These large uncertainties affect our estimation of $\Omega_b(\text{BLA})$ value as discussed in next chapter (see section 7.2).

6.3.1.2 Metal absorbers

We have identified absorption from total of 15 distinct metal ions in our survey. In this section we discuss the statistics of some prominent ions in our sample.

O VI

We identified 35 O VI components in our survey across 17 absorber systems. O VI is the most common ion after Si III (36 components) in our sample, owing to the strong doublet lines at $\lambda_{\text{rest}} = 1031.927, 1037.616$ Å, with fairly large oscillator strengths of 0.1329 and 0.0661 respectively and large cosmic abundance of Oxygen. The figure 6.7 shows the distribution of column densities and redshifts

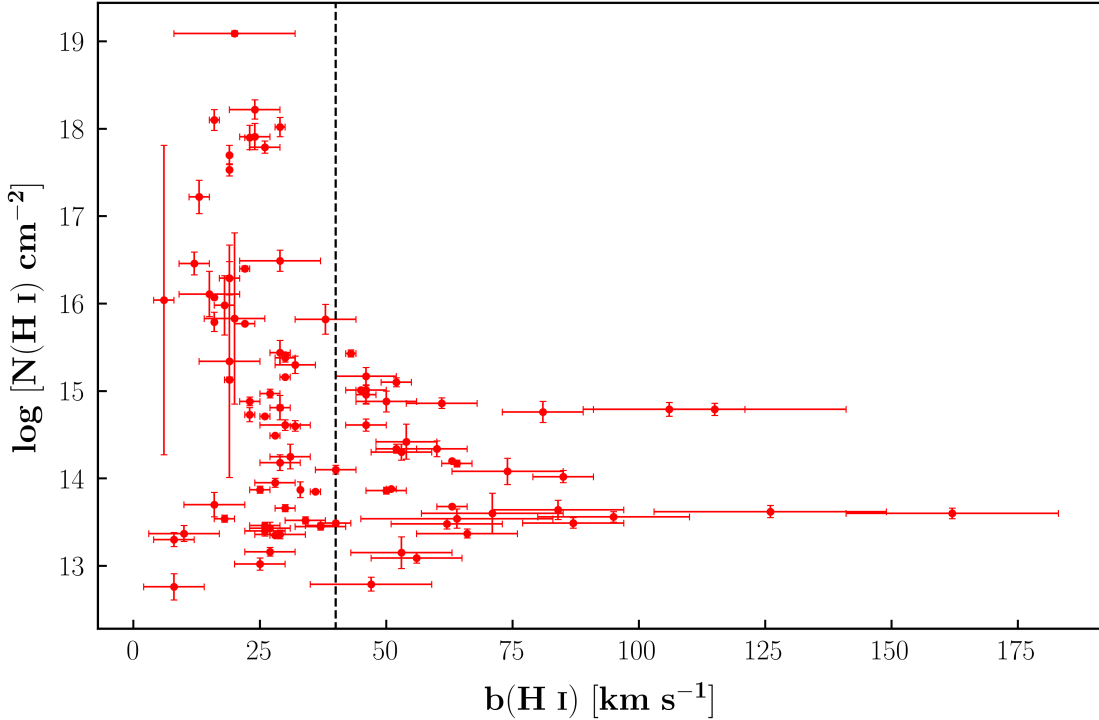


FIGURE 6.6: $N(\text{H I})$ vs $b(\text{H I})$ plot for the 97 H I components. The vertical black dashed line denotes our threshold for line to be considered as BLA.

of these 35 components. The O VI coverage starts from $z \sim 0.09$ in the HST/COS FUV G130M grating. Unlike H I, we find O VI column densities in narrow range of $\sim 10^{13} - 10^{14.5} \text{ cm}^{-2}$.

O VI is a good tracer of WHIM at temperatures in range of $10^5 - 10^6 \text{ K}$ as its ionisation fraction peaks at around $10^{5.7} \text{ K}$ in collisional ionisation (Gnat & Sternberg 2007). So, many studies of O VI absorbers have been done in detail in the past. Savage et al. (2014) have studied 14 QSO sight lines comprising a total of 56 O VI absorbers showing 85 O VI components. They estimate the baryonic content in warm gas traced by O VI as $\Omega_b(\text{O VI})_{\text{warm}} = (0.0019 \pm 0.0005)h_{70}^{-1}$.

Studies exploring the correlations between star formation and O VI have also been done. In their study, Tumlinson et al. (2011, 2013) found strong correlation between the specific star formation rate and the presence of O VI. They found that star-forming galaxies are surrounded by large halos ionised O VI of sizes $\sim 150 \text{ kpc}$,

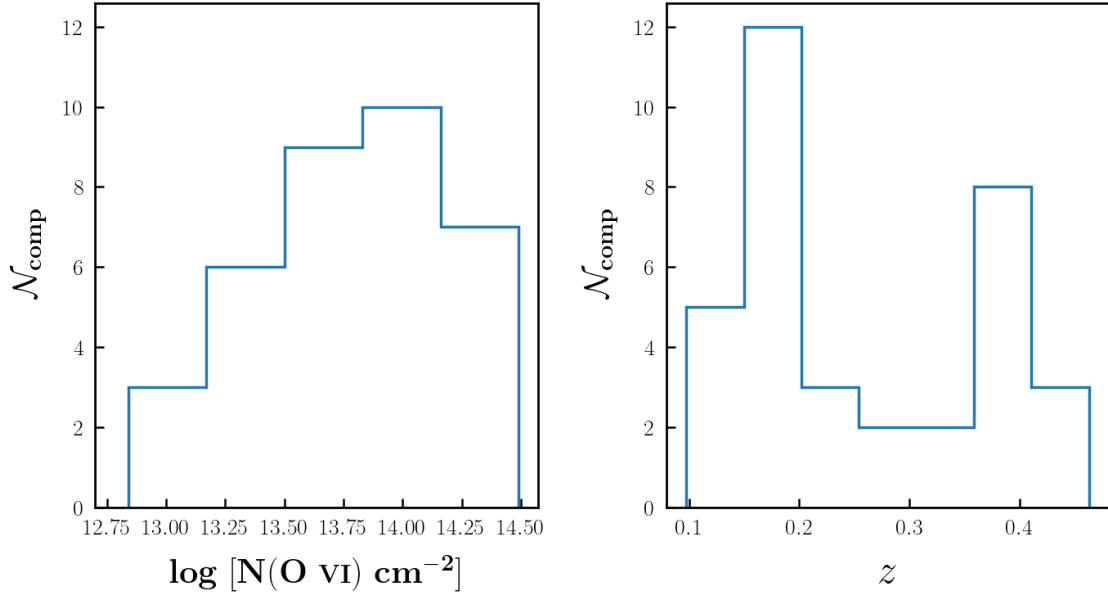


FIGURE 6.7: Distribution of column densities (left panel) and redshift (right panel) of 35 O VI components.

which were not much prominent around galaxies with little to no star-formation.

Si II, Si III and Si IV

We find good number of Si absorbers in the form of Si II, Si III and Si IV ions having 19, 36 and 20 components respectively. Si II shows a number of lines in the COS/FUV channel with $\lambda_{\text{rest}} = 1526.707, 1304.371, 1260.422 \text{ \AA}$ and doublet at 1190.416, 1193.289 \AA . Si III has the most components among the metal ions in our sample because of very high oscillator strength of 1.669 at $\lambda_{\text{rest}} = 1206.5 \text{ \AA}$. And Si IV shows doublet line at $\lambda_{\text{rest}} = 1393.760, 1402.772 \text{ \AA}$. Figures 6.8, 6.9 and 6.10 shows the distribution of column densities and redshifts of Si II, Si III and Si IV respectively.

C II, C III and C IV

C II, C III and C IV are some other common ions found in our survey which shows 23, 26 and 22 components respectively. Absorption from C II is from two transitions

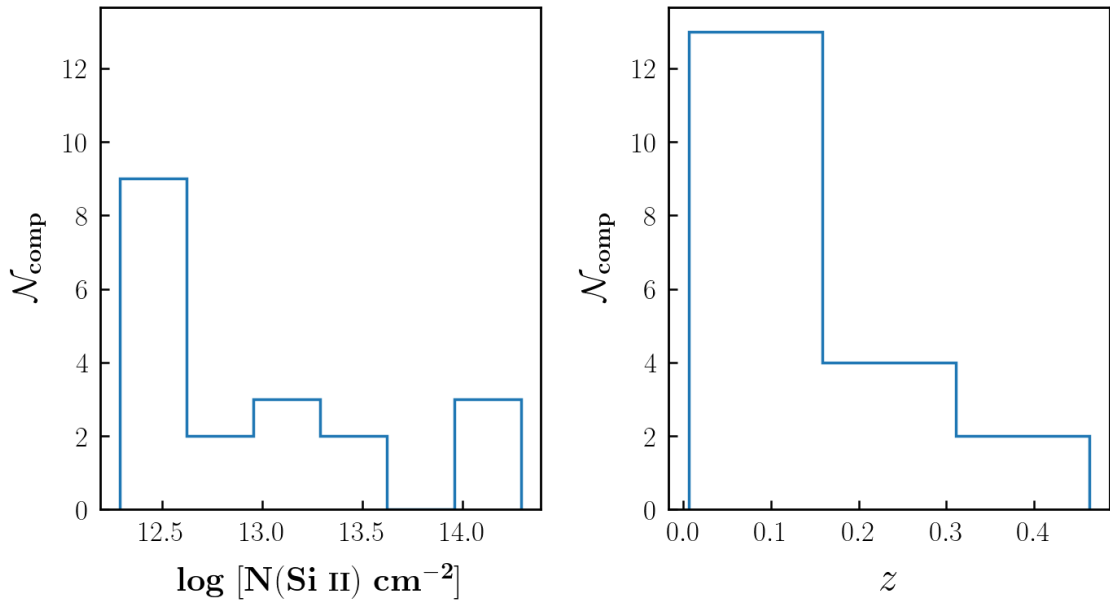


FIGURE 6.8: Distribution of column densities (left panel) and redshift (right panel) of 19 Si II components.

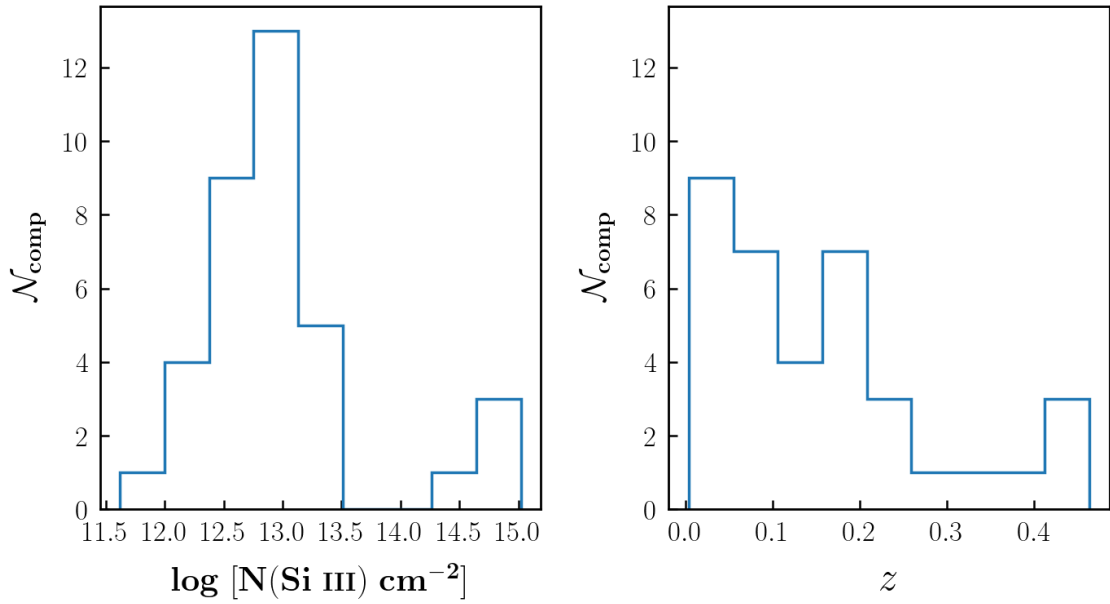


FIGURE 6.9: Distribution of column densities (left panel) and redshift (right panel) of 36 Si III components.

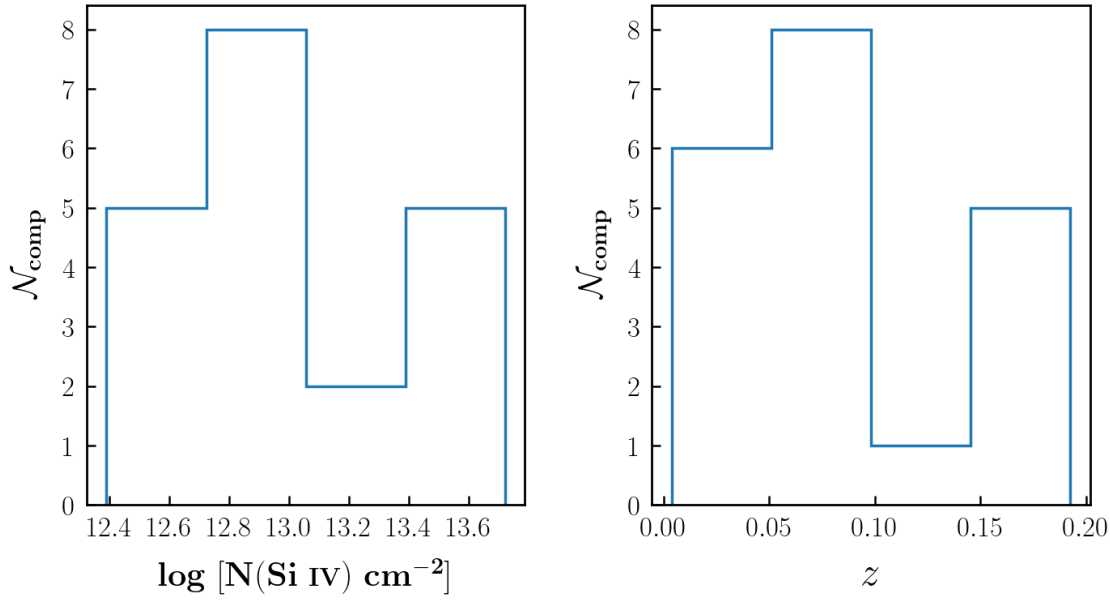


FIGURE 6.10: Distribution of column densities (left panel) and redshift (right panel) of 20 Si IV components.

with $\lambda_{\text{rest}} = 1036.3367, 1334.5323 \text{ \AA}$. The C III line with $\lambda_{\text{rest}} = 977.0201 \text{ \AA}$ has a high oscillator strength of 0.757 which results in prominent absorption from this line, hence it is very common ion found in IGM. C IV shows the absorption in the form doublet lines with $\lambda_{\text{rest}} = 1548.2041, 1550.7812 \text{ \AA}$. Figures 6.11, 6.12 and 6.13 shows the distribution of column densities and redshifts of C II, C III and C IV respectively. All the three ions have narrow ranges of column densities with a very few exceptional rare high column density components. We can see in the figure 6.12 that C III can be observed even at lower column densities of $\sim 10^{12.5} \text{ cm}^{-2}$ because of the large oscillator strength C III 977 transition. C IV doublet lines have a limited coverage in the HST/COS FUV channel as they fall out of the COS coverage at $z \gtrsim 0.15$ which could be seen in figure 6.13.

N V

We find only 14 N V components in our current survey, which could be attributed to the lower cosmic abundance of Nitrogen compared to rest of the pro-

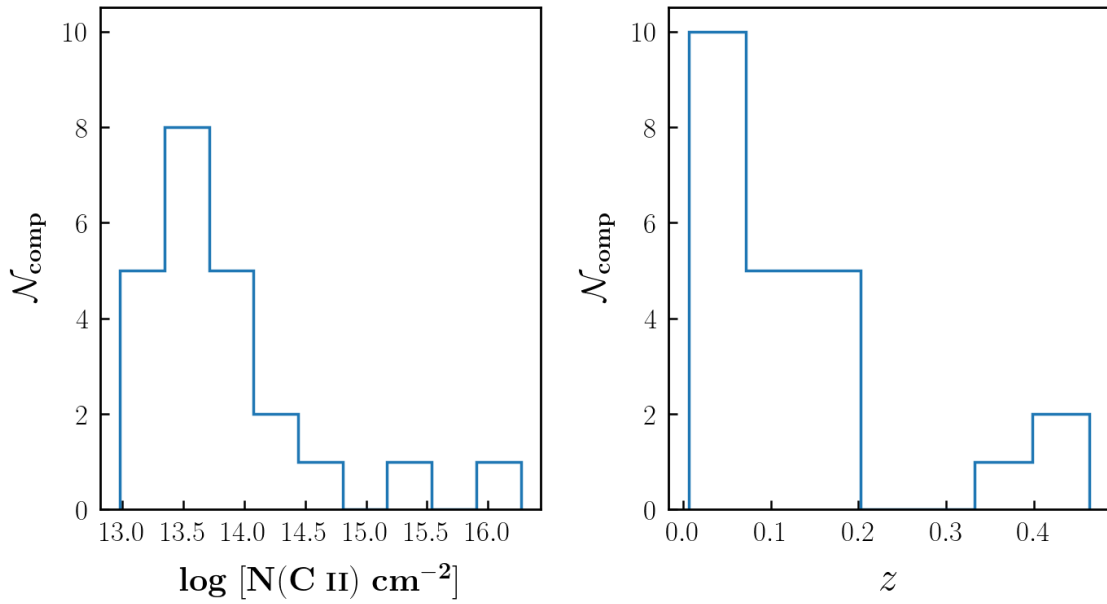


FIGURE 6.11: Distribution of column densities (left panel) and redshift (right panel) of 23 C II components.

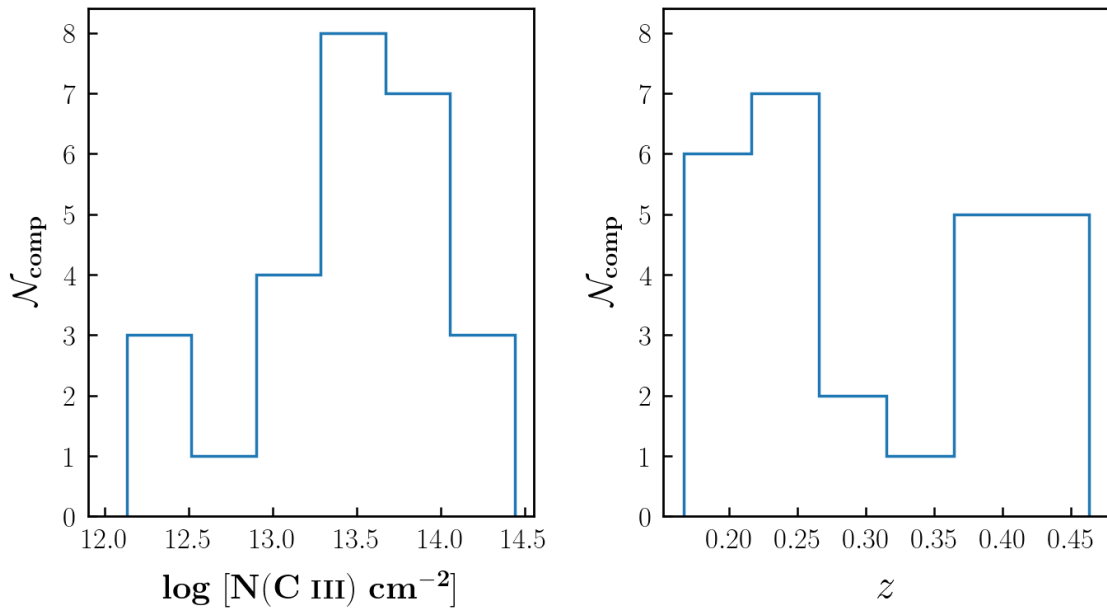


FIGURE 6.12: Distribution of column densities (left panel) and redshift (right panel) of 26 C III components.

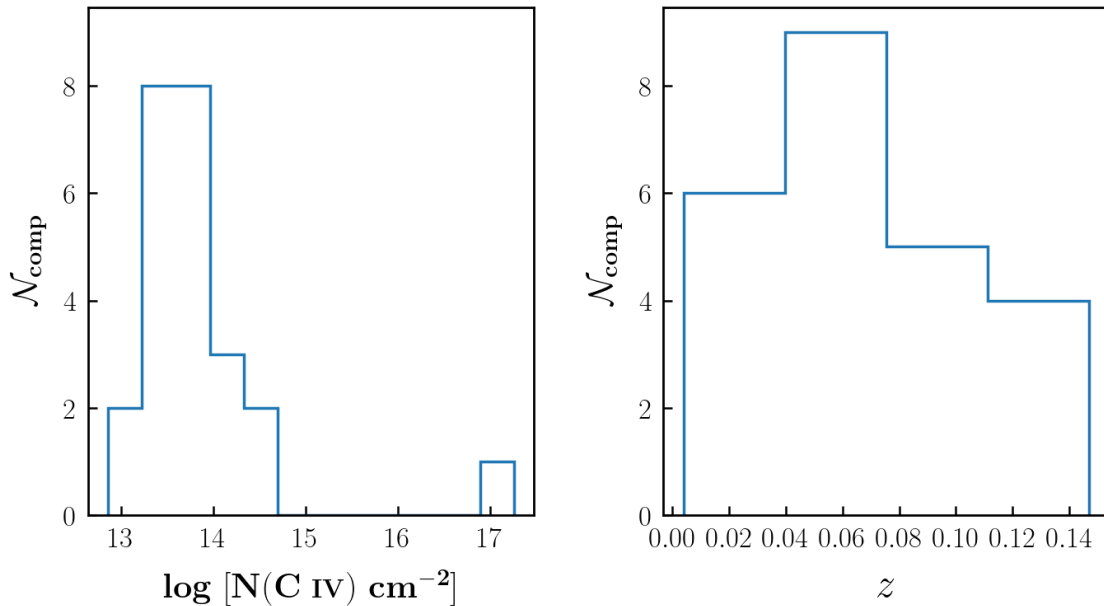


FIGURE 6.13: Distribution of column densities (left panel) and redshift (right panel) of 22 C IV components.

minent metals detected in our survey. It shows absorption from the doublet lines at $\lambda_{\text{rest}} = 1238.821, 1242.804 \text{ \AA}$. Figures 6.14 shows the distribution of column densities and redshifts of N V components. It could also trace gas with high temperature above 10^5 K and could also arise from photoionisation from highly energetic photons with energies in the range of $\sim 50 - 100 \text{ ev}$.

6.3.2 Ionisation modelling

We have done the ionisation modelling for a total of 39 components in 29 absorbers. Out of this, 25 components are from O VI absorbers and remaining are from non-O VI absorbers. We present the results from ionisation modelling of all these components in this section.

From ionisation modelling, we get the Hydrogen density⁶ (n_H) and metallicity (Z) of the absorbers, which dictates the prevalent ionising and physical conditions in the absorber clouds. The figure 6.15 shows these values for all the 39 components

6. We use this interchangeably with absorber density, i.e density at that component

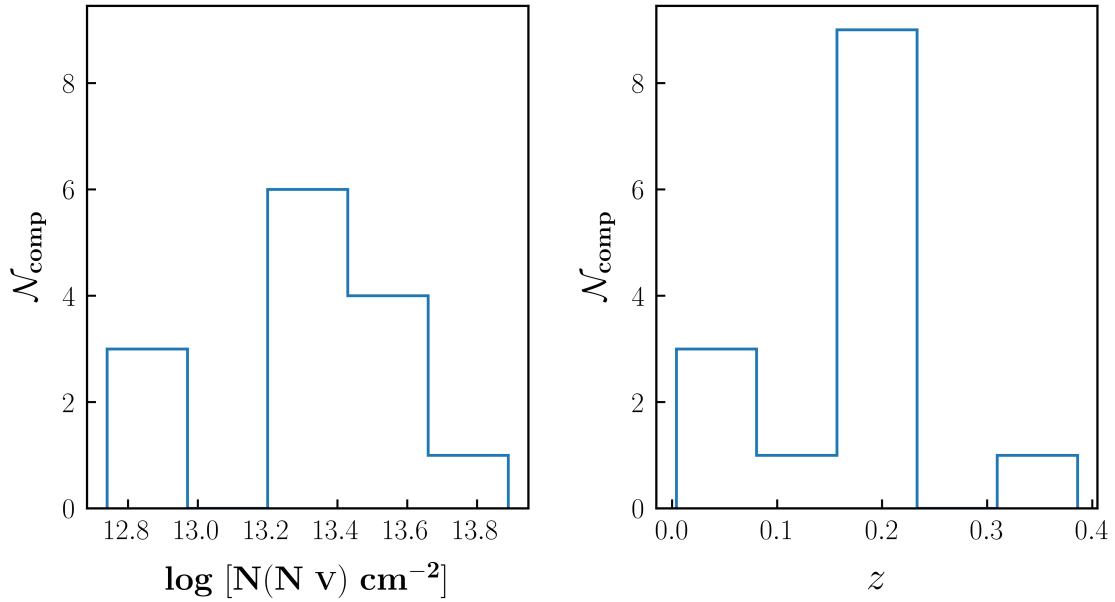


FIGURE 6.14: Distribution of column densities (left panel) and redshift (right panel) of 14 N v components.

plotted against each other. We don't see any correlations between the two quantities which is expected as these independently describe the physical conditions of the absorbers. The O VI absorbers are denoted with red and non-O VI absorbers are marked by green error bars.

However, when we see the variation of these two quantities with the underlying neutral Hydrogen column density ($\text{N}(\text{H I})$) in these components, we see some trends. Figure 6.16 shows the variation of density with $\text{N}(\text{H I})$. We see a feeble positive relation between n_H and $\text{N}(\text{H I})$ for the components from O VI absorbers. This is expected as higher column density would typically result in higher densities if the sizes of absorbers, ionisation corrections are of similar order. The lack of such correlation in the non-O VI case may be due to less number of components.

Unlike density, we find a negative correlation between the metallicity and $\text{N}(\text{H I})$ as shown in figure 6.17 which could be seen for both O VI and non-O VI absorbers. However, again due to less number of components for non-O VI absorbers, it less evident in them. This could be explained by the fact that as we get larger $\text{N}(\text{H I})$, the column densities of metals do not scale accordingly with $\text{N}(\text{H I})$, they remain

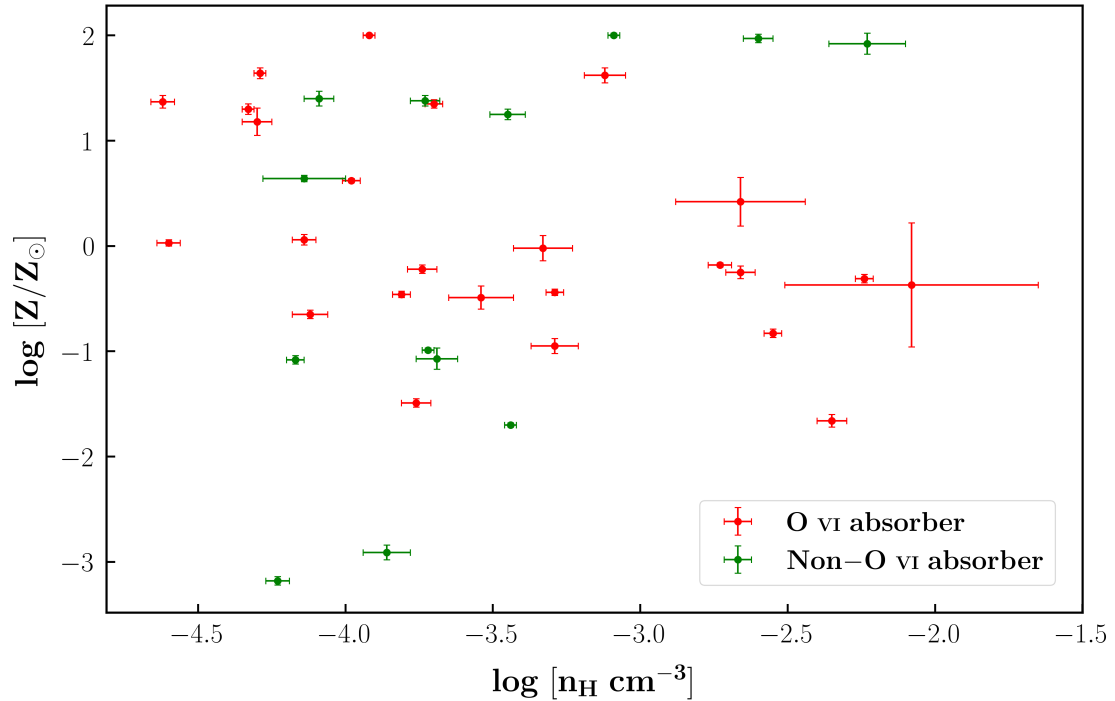


FIGURE 6.15: Metallicity vs density for all 39 components estimated from ionisation modelling. Red error bars are the O VI components and green error bars are non-O VI components

within the narrow ranges of their distribution. So to recover large N(H I), large line of sight thickness has to integrated with nearly same amount of metals, which results in the drop in metallicity.

6.3.2.1 Origin of O VI in the absorbers

The 17 O VI absorbers have immense importance in our current study so are there ionisation conditions. Based on the results of these 17 absorbers, we estimate the $\Omega_b(\text{BLA})$ value as discussed in next chapter. For these 17 systems, having 25 components, we want to find the origin of O VI in these absorbers so that we could see if they are tracing warm-hot gas or cool photoionised gas phase. So, if they arise from a warm-hot plasma, we could infer that the BLA candidate found with O VI could also be thermally broadend. Figure 6.18 shows the bar plot of the inferred

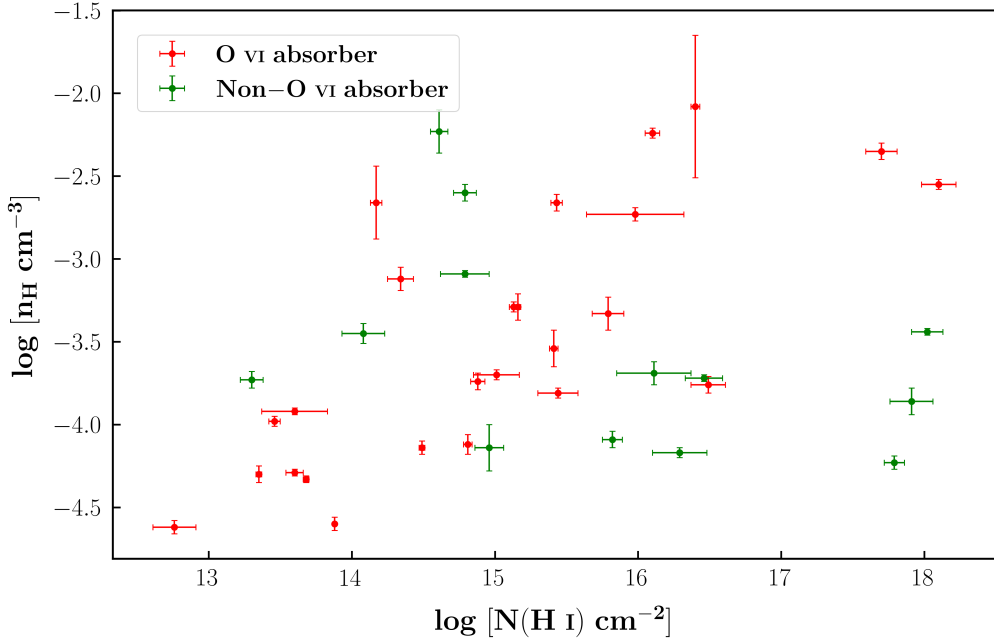


FIGURE 6.16: Variation of density with N(HI) for all 39 components. Red error bars are from O VI absorbers and green error are from non-O VI absorbers

origin of these 25 components. 20 of the components could not be explained with photoionisation (PI) models, so possibly tracing a collisional ionised (CI) phase. One of the components, shown agreement with PI models and in 4 components the origin of O VI remained uncertain due to models failing to predict the column densities of other ions detected. The absorber which has this PI component also shows CI origin in another component. Out of the 4 uncertain components, two of them do not show good solution, however, in other two components O VI could be tentatively collisionally ionised, the bad solution is due to large number of ions present in the absorbers where our models fail considerably. However, to be conservative we do not count them in CI case. Table 6.3 gives the details of all these 25 components.

Figure 6.19 shows an example of CI origin of O VI, where other ions could be explained with PI models but not O VI (orange color). Figure 6.20 shows the only example of PI origin of O VI, where we get similar solution for excluding and including O VI cases, indicating that all ions could be explained with PI models.

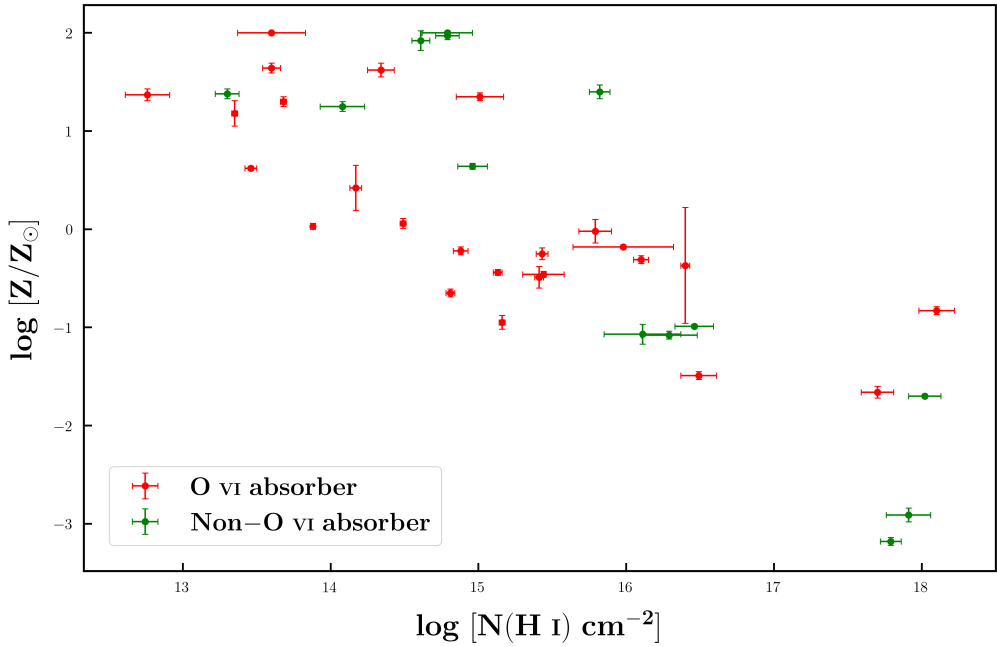


FIGURE 6.17: Variation of metallicity with $N(\text{H I})$ for all 39 components. Red error bars are the O VI components and green error bars are non-O VI components

Figure 6.21 shows uncertain case, where our model fails to predict the column densities of other ions as well.

Ionisation modelling of these absorbers shows that the gas in these absorbers, which are possibly tracing WHIM, is multiphase in nature, having ions arising from photoionisation as well as collisional ionisation. In the next chapter, we use these results from ionisation modelling as well as Voigt profile fitting to estimate the baryon content in BLAs.

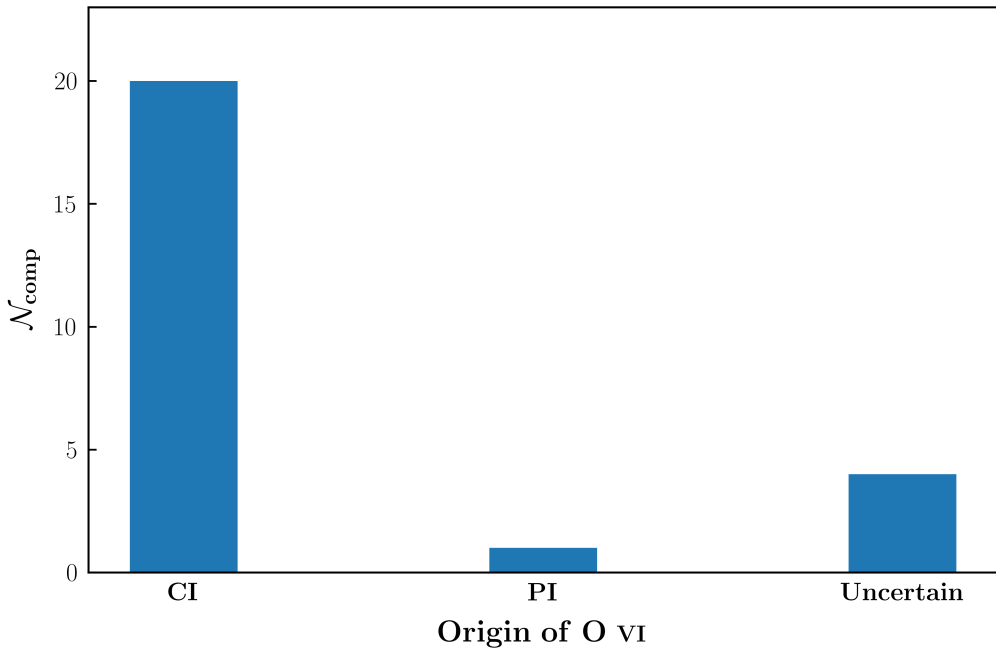
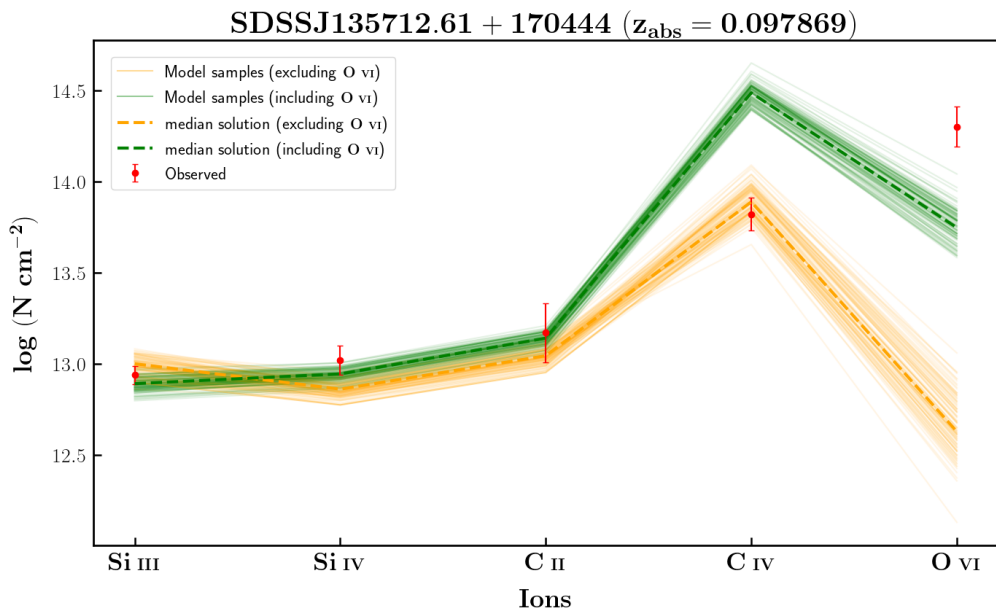


FIGURE 6.18: Origin of O VI in 25 components from 17 O VI absorbers.

FIGURE 6.19: An example of CI case for an absorber towards the line of sight of SDSS J135712.61+170444 at $z_{\text{abs}} = 0.097869$ with $\log N(\text{H I}) [\text{cm}^{-2}] = 16.49$

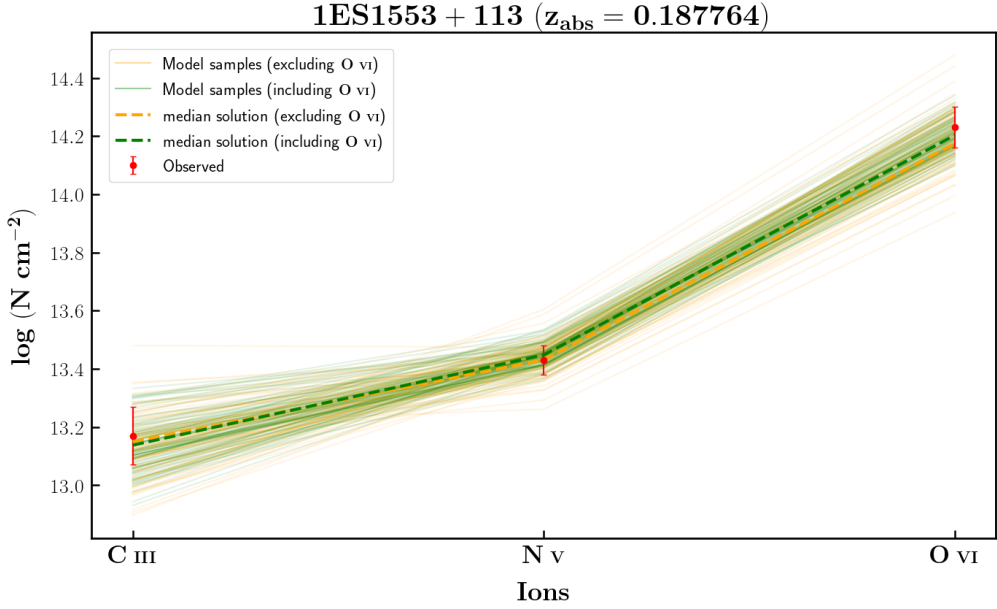


FIGURE 6.20: Only example of PI case for an absorber towards the line of sight of 1ES 1553+113 at $z_{abs} = 0.187764$ with $\log N(\text{H I}) [\text{cm}^{-2}] = 12.76$

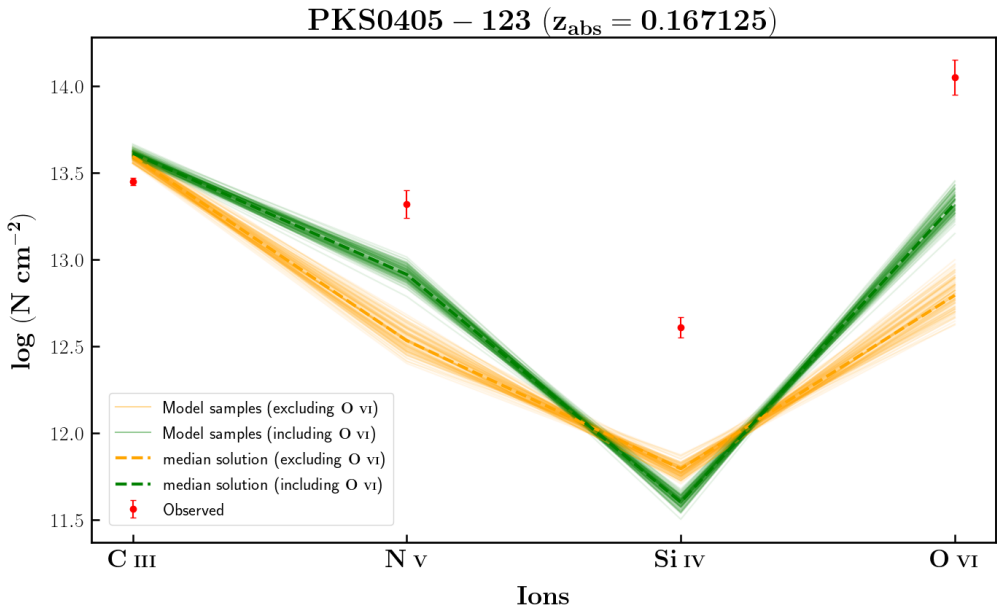


FIGURE 6.21: An example of uncertain case for an absorber towards the line of sight of PKS 0405-123 at $z_{abs} = 0.167125$ with $\log N(\text{H I}) [\text{cm}^{-2}] = 13.46$

Sight line	z_{abs}	$\log N(\text{H I})$	Origin of O VI (cm^{-2})
3C 263	0.140756	14.49	CI
PKS 0637-752	0.161064	13.60	CI
PKS 0637-752	0.417539	15.41	CI
PG 1424+240	0.147104	14.88	CI
PG 1424+240	0.147104	15.44	CI
PG 0003+158	0.347586	16.10	CI
PG 0003+158	0.386089	14.81	uncertain ^a
PG 0003+158	0.421923	14.17	CI
PG 1216+069	0.282286	16.40	CI
SDSS J135712.61+170444	0.097869	15.01	CI
SDSS J135712.61+170444	0.097869	16.49	CI
1ES 1553+113	0.187764	12.76	PI
1ES 1553+113	0.187764	13.88	CI
SBS 1108+560	0.463207	15.79	CI
SBS 1108+560	0.463207	18.10	uncertain ^b
PG 1222+216	0.378389	15.43	CI
PG 1116+215	0.138527	13.60	uncertain ^b
H 1821+643	0.170006	13.35	CI
H 1821+643	0.170006	13.68	CI
H 1821+643	0.224981	15.13	CI
H 1821+643	0.224981	15.16	CI
PG 1121+422	0.192393	14.34	CI
PG 1121+422	0.192393	17.70	CI
PKS 0405-123	0.167125	13.46	uncertain ^a
PKS 0405-123	0.167125	15.98	CI

^a Other ions also could not be explained

^b Bad solution due to many ions

TABLE 6.3: 25 O VI components and origin of O VI in them

Chapter 7

Estimating $\Omega_b(\text{BLA})$

In this chapter we discuss the estimation of the baryon energy density trapped in BLAs, i.e. $\Omega_b(\text{BLA})$, using our BLA survey which is the cornerstone of the current work. We will statistically estimate the $\Omega_b(\text{BLA})$ from our survey results. And then we will determine how much BLAs contribute to the baryon budget (Ω_b) of the current universe.

7.1 Methodology to determine $\Omega_b(\text{BLA})$

The baryon content of any ion in terms of the current critical density (ρ_{cr}) of the universe can be estimated by integrating over the bivariate frequency distribution of the absorbers as function of column density and redshift of that ion as given in [Becker et al. \(2011\)](#) by following equation :

$$\Omega_{\text{ion}} = \frac{H_0 m_{\text{ion}}}{c \rho_{\text{cr}}} \int \frac{\partial^2 \mathcal{N}}{\partial N \partial X} N dN \quad (7.1)$$

Where, H_0 is the current value of Hubble's constant,

m_{ion} is the mass of ion,

c is the speed of light in vacuum,

\mathcal{N} is the number of absorbers at column density N and path length X

The path length X is function of redshift (z) and denotes the total absorption path length available for absorption. A non-evolving population of absorbers will show an invariant number density per unit absorption pathlength (Becker et al. 2011). It is defined as :

$$X(z) = \int_0^z (1+z')^2 \frac{H_0}{H(z')} dz' \quad (7.2)$$

(Bahcall & Peebles 1969). Now, assuming a flat Λ CDM cosmology, we can write the Hubble's constant at any z as :

$$H(z) = H_0 [\Omega_m(1+z)^3 + \Omega_\Lambda]^{1/2} \quad (7.3)$$

with $\Omega_m = 0.31$ and $\Omega_\Lambda = 0.69$ (Planck Collaboration et al. 2020). This gives,

$$X(z) = \int_0^z \frac{(1+z')^2}{[\Omega_m(1+z')^3 + \Omega_\Lambda]^{1/2}} dz' \quad (7.4)$$

However, whole pathlength of X may not be available for absorption due to the presence of Ly α forest lines, absorption from strong ISM lines and intervening IGM lines also in the spectrum. And regions near to the quasar also needs to be excluded, as the intrinsic radiation from quasar could photoionise the species and give rise to some unwanted features in the spectrum. This is called the proximity effect (Tripp et al. 2008b). So , we exclude regions blueward of 5000 km s^{-1} from the quasar. So, we need to make these correction to get the unblocked absorption pathlength. To calculate this correction, we have developed an interactive program, where we manually select the wavelength regions showing strong absorption features from the above mentioned lines along each sight line. So we exclude these wavelength regions and regions in the proximity of quasar to calculate the unblocked absorption pathlength available for Ly α absorption.

Now, to get the baryon content of BLAs using equation 7.1, we can use total Hydrogen column density, $N(H)$, and $m_{ion} = \mu \cdot m_H$, where μ is the mean atomic mass in a.m.u. and m_H is the mass of Hydrogen atom. We take $\mu = 1.32$ for $Y_{He} = 0.2446$ (Peimbert et al. 2016) taking in account the Helium abundance in the universe. But $N(H)$ is not a directly observable quantity, instead we can

get neutral Hydrogen column density, $N(H\ I)$, from observations. So we need the correct for the ionisation of Hydrogen to get $N(H)$ from observable $N(H\ I)$. This ionisation correction is not trivial and require number of assumptions.

If the gas is collisionally ionised, then we can estimate the hydrogen ionization fraction, which is the ratio of amount of total hydrogen and neutral hydrogen, in equilibrium using the models given by [Sutherland & Dopita \(1993\)](#) which related the ionisation fraction to the temperature of the gas. It gives following relation :

$$\log f_H \approx 5.4 \log T - 0.33(\log T)^2 - 13.9 \quad (7.5)$$

This relation is valid in the temperature regimes of $10^5 - 10^7$ K. Figure 7.1 shows the variation of f_H with T based on above relation . We can use this to convert $N(H\ I)$ to $N(H)$. However, we need to note that at densities lower than $n_H < 10^{-5}$ cm $^{-3}$, photoionisation from UV background could result in higher hydrogen ionization fraction. But since we don't have the hydrogen densities in the absorbers, so we could possibly underestimate the f_H in such cases (see [Richter \(2020\)](#); [Fang & Bryan \(2001\)](#) for more details). So this would give us an lower limit on the baryon content in this absorbers. Still, we need the temperature to get the ionisation correction. We could only estimate the temperature where the BLA is aligned with some other ion like O VI. We have only few such cases. In rest of the cases, where we don't have an estimate of temperature, we use the Doppler width, b , of the BLA to estimate the temperature assuming pure thermal broadening. This gives us an upper limit on the temperature of the absorber. Now, $b^2 = 2kT/m_H$, so $T = (m_H/2k)b^2$.

Now, as the neutral fraction of hydrogen is very low at the temperatures in WHIM, we can write :

$$\log f_H = \log \left(\frac{H\ I + H\ II}{H\ I} \right) \approx \log \left(\frac{H\ II}{H\ I} \right) \Rightarrow H\ II = f_H H\ I$$

$$\Rightarrow N(H) = N(H\ I) + N(H\ II) = (1 + f_H)N(H\ I) \approx f_H N(H\ I)$$

Since don ;t have the bivariate frequency distribution function, we approximate

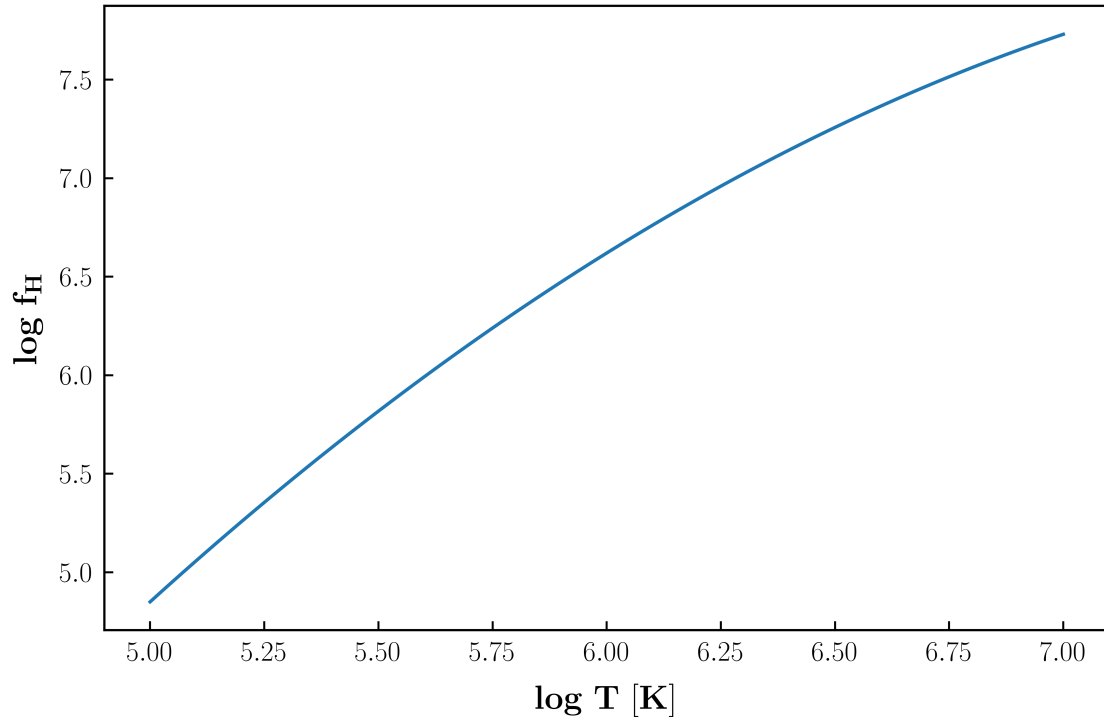


FIGURE 7.1: Hydrogen ionisation fraction as a function of temperature.

the integral in equation 7.1, which is commonly done, as :

$$\int \frac{\partial^2 \mathcal{N}}{\partial N \partial X} N dN \simeq \frac{\sum N_{obs}}{\Delta X} \quad (7.6)$$

Where N_{obs} is the observed column density of the ion and ΔX is the total unblocked pathlength available. Now using equation 7.1, the approximation in equation 7.6 and including ionisation correction we can estimate $\Omega_b(BLA)$ as :

$$\Omega_b(BLA) = \frac{H_0 \mu m_H}{c \rho_{cr}} \sum_{i,j} f_{H_{i,j}} N(H\ I)_{i,j} \left/ \sum_j \Delta X_j \right. \quad (7.7)$$

Where j represents a line of sight and i refers to the absorber along sight line j . So numerator is the sum over all the absorbers and the denominator is summed over all the lines of sight. We use error propagation to find the uncertainty in the value of $\Omega_b(BLA)$. We consider error in f_H , which depend on temperature, which in turn depend on the measured b values and error in H I column densities.

In the next section we describe the sample of absorbers we will be using to estimate the $\Omega_b(\text{BLA})$.

7.2 Selecting the absorber samples

We have a total of 29 absorber systems in our survey. These systems have 97 H I components in total. Out of these 97 components, 37(34) components have Doppler parameters above 40(45) km s⁻¹. But as discussed multiple times throughout this work that just having large b value does not ensure we have a ‘true’ BLA. So we have to carefully select the candidates which are actually BLAs from these 37(34) components to estimate the baryon content of BLAs.

7.2.1 Based on Temperature and Ionisation Modelling

Since, we need the temperature to estimate the ionisation fraction, we consider candidates whose temperatures could be estimated from the Doppler parameters of H I and O VI. We estimated temperatures for 7 systems as discussed in section 6.3.1.1. However, two of the systems had temperatures below 10^5 K, we exclude these candidates as the ionisation correction relation is valid for temperatures above 10^5 K. We put another constrain from ionisation modelling that O VI should be collisionally ionised in these systems, which further ensures that we are tracing warm-hot plasma.

So we get 5 such systems with one-one components each. We call this as sample A and are labelled so in table 7.1. This sample will give us a conservative lower limit on the baryon content in BLAs. Using this sample of absorbers we get $\Omega_b(\text{BLA}) = (1.8 \pm 0.5) \times 10^{-3} h_{70}^{-1}$. Table 7.2 gives the details of the individual sight lines in this sample.

7.2.2 Based on Ionisation Modelling

As discussed in chapter 6 we have modelled the ionising conditions in 25 components of 17 O VI absorbers. And found that 20 of the components could not be

explained with photoionisation models, so these could possibly be arising from collisionally ionised gas phase. So these absorbers could potentially be tracing warm hot plasma in WHIM. So we take absorbers where the O VI could not be explained with photoionisation models and has a broad Ly α line ($b > 40 \text{ km s}^{-1}$). This will give us a little ambitious lower limit on the $\Omega_b(\text{BLA})$ value. We have 14 such systems, which have a total of 21 BLA components. However, we exclude one component towards the sight line of PKS 0637-752 at $z_{comp} = 0.161013$ because it has unexpectedly high Doppler parameter of 162 km s^{-1} which affects the estimate of $\Omega_b(\text{BLA})$ drastically. We get a value of $(7.2 \pm 1.3) \times 10^{-3} h_{70}^{-1}$ for $\Omega_b(\text{BLA})$ using these 20 BLA components. However, if we include the excluded component we get a value of $(9.3 \pm 2.0) \times 10^{-3} h_{70}^{-1}$ which is about 27% higher than the other value. Table 7.2 gives the details of the individual sight lines in this sample. We could see that individual sight lines have large uncertainties in the $\Omega_b(\text{BLA})$ value, but the value calculated for whole sample has low uncertainty because of more number of points, hence reducing the statistical errors.

7.2.3 Full sample

We also consider the whole sample of BLA components to calculate $\Omega_b(\text{BLA})$ value. This is a very optimistic view that all the absorbers we identified as BLA components are true BLAs. We call this as sample C. It is clear that sample A is subset of sample B, which in turn is subset of the whole sample, ie. sample C. So, we have put sample label as ‘A’ and ‘B’ in table 7.1 if the BLA component is in sample A or B respectively, rest all components are labelled as C for the sake of clarity. For this full sample, we get a very high value of $\Omega_b(\text{BLA}) = (27.1 \pm 13.8) \times 10^{-3} h_{70}^{-1}$. We see that the uncertainty in this estimate is much larger compared to previous two estimates. In table 7.4, we can see that some sight lines have very large values of $\Omega_b(\text{BLA})$ and also have uncertainties which are greater than the measured values. This results in large uncertainty in total value also. These large uncertainties are from the very broad components, which have higher uncertainties in both their column density and b parameters. If we exclude this high value and high uncertainty sight lines, then we get value for $\Omega_b(\text{BLA})$ as

$(10.0 \pm 2.2) \times 10^{-3} h_{70}^{-1}$. Both the estimates using this sample should be trusted with caution as it can include components which might not be true BLAs and overestimate the value.

z_{BLA}	b	log N(H I)	log T	log f_H	log N(H)	Sample
	(km s ⁻¹)	(cm ⁻²)	(K)		(cm ⁻²)	
3C 263						
0.140702	87 ± 10	13.49 ± 0.06	5.66	6.09	19.58	B
0.063272	50 ± 6	14.88 ± 0.12	5.18	5.22	20.10	C
0.063397	54 ± 6	14.42 ± 0.20	5.25	5.35	19.77	C
PKS 0637-752						
0.161013	162 ± 21	13.60 ± 0.06	6.20	6.90	20.50	B ^b
0.161060	45 ± 1	15.01 ± 0.02	5.09	5.03	20.04	B
0.417645	46 ± 4	14.61 ± 0.07	5.11	5.07	19.68	B
PG 1424+240						
0.147946	40 ± 3	13.49 ± 0.02	4.99	4.82	18.31	B
PG 0003+158						
0.347586	63 ± 0	14.20 ± 0.02	5.28 ^a	5.41	19.61	A
0.386294	40 ± 4	14.10 ± 0.05	4.99	4.82	18.92	C
0.420469	66 ± 10	13.37 ± 0.05	5.42	5.68	19.05	B
0.421837	64 ± 3	14.17 ± 0.04	5.39	5.63	19.80	B
PG 1216+069						
0.282145	52 ± 3	15.10 ± 0.05	5.21	5.29	20.39	B
0.283054	53 ± 10	13.15 ± 0.18	5.23	5.32	18.47	B
0.005547	95 ± 15	13.56 ± 0.06	5.74	6.22	19.78	C
0.006100	81 ± 8	14.76 ± 0.12	5.60	5.99	20.75	C

Continued on next page

z_{BLA}	b (km s ⁻¹)	$\log N(\text{H I})$ (cm ⁻²)	$\log T$ (K)	$\log f_{\text{H}}$	$\log N(\text{H})$ (cm ⁻²)	Sample
0.006328	106 ± 15	14.79 ± 0.08	5.83	6.37	21.16	C
SDSS J135712.61+170444						
0.097869	46 ± 4	15.01 ± 0.16	5.11	5.07	20.08	B
1ES 1553+113						
0.187650	51 ± 1	13.88 ± 0.01	5.19 ^a	5.24	19.12	A
PG 1222+216						
0.376596	64 ± 19	13.54 ± 0.11	5.39	5.63	19.17	B
0.377236	52 ± 4	14.34 ± 0.05	5.00 ^a	4.85	19.19	A
0.378547	43 ± 1	15.43 ± 0.04	5.05	4.95	20.38	B
0.054437	74 ± 11	14.08 ± 0.15	5.52	5.85	19.93	C
PG 1116+215						
0.138508	71 ± 14	13.60 ± 0.23	5.39 ^a	5.62	19.22	A
H 1821+643						
0.170006	63 ± 3	13.68 ± 0.02	5.38	5.60	19.28	B
0.224900	84 ± 13	13.64 ± 0.11	5.51 ^a	5.84	19.48	A
0.226156	62 ± 11	13.48 ± 0.06	5.37	5.58	19.06	B
PG 1121+422						
0.192397	60 ± 6	14.34 ± 0.09	5.34	5.52	19.86	B

Continued on next page

z_{BLA}	b (km s ⁻¹)	$\log N(\text{H I})$ (cm ⁻²)	$\log T$ (K)	$\log f_{\text{H}}$	$\log N(\text{H})$ (cm ⁻²)	Sample
PKS 0405-123						
0.166496	56 ± 9	13.09 ± 0.06	5.28	5.41	18.50	B
HE 0056-3622						
0.043265	85 ± 6	14.02 ± 0.07	5.64	6.06	20.08	C
RX J0439.6-5311						
0.005568	53 ± 6	14.30 ± 0.09	5.23	5.32	19.62	C
UKS 0242-724						
0.063850	46 ± 6	15.17 ± 0.10	5.11	5.07	20.24	C
PG 1259+593						
0.044224	47 ± 12	12.79 ± 0.08	5.13	5.11	17.90	C
0.046284	61 ± 7	14.86 ± 0.06	5.35	5.55	20.41	C
PKS 1302-102						
0.094839	46 ± 2	14.96 ± 0.10	5.11	5.07	20.03	C
3C 57						
0.077430	50 ± 4	13.86 ± 0.04	5.18	5.22	19.08	C
PHL 1811						
0.080928	126 ± 23	13.62 ± 0.07	5.98	6.60	20.22	C

Continued on next page

z_{BLA}	b (km s ⁻¹)	$\log N(\text{H I})$ (cm ⁻²)	$\log T$ (K)	$\log f_{\text{H}}$	$\log N(\text{H})$ (cm ⁻²)	Sample
PG 0832+251						
0.017505	115 ± 26	14.79 ± 0.07	5.90	6.48	21.27	C

TABLE 7.1: CIE properties of 37 BLA components. ^a Temperature estimated from Doppler parameters. ^b The excluded BLA component discussed in section 7.2.2

Sight line	z_{em}	$\log N(\text{H})$ (cm ⁻²)	ΔX	$\Omega_b(\text{BLA})$ ($\times 10^{-2} h_{70}^{-1}$)
PG 0003+158	0.451	19.61	0.454	0.24 ± 0.05
1ES 1553+113	0.414	19.12	0.449	0.08 ± 0.01
PG 1222+216	0.432	19.19	0.424	0.10 ± 0.08
PG 1116+215	0.176	19.22	0.134	0.33 ± 0.31
H 1821+643	0.297	19.48	0.239	0.34 ± 0.23
Total		20.06	1.700	0.18 ± 0.05

TABLE 7.2: $\Omega_b(\text{BLA})$ estimation using sample A

7.3 Comparison with literature

Many past studies have been done to estimate the baryon content in BLAs. [Danforth et al. \(2010\)](#) put the $\Omega_b(\text{BLA})$ value at $(6.3^{+1.1}_{-0.8}) \times 10^{-3} h_{70}^{-1}$ from their study which includes seven AGN sight lines using HST/STIS observations. This value is within our estimate for $\Omega_b(\text{BLA})$ calculated from sample B. A similar study done by [Lehner et al. \(2007\)](#) using FUSE and STIS observations gives two $\Omega_b(\text{BLA})$ values of $3.6 \times 10^{-3} h_{70}^{-1}$ and $(9.1) \times 10^{-3} h_{70}^{-1}$ depending the ionisation correction used to convert $N(\text{H I})$ to $N(\text{H})$. [Richter et al. \(2006\)](#) also used STIS observations and calculated the $\Omega_b(\text{BLA})$ value using two samples. Their restricted samples gives the minimum limit of $2.7 \times 10^{-3} h_{70}^{-1}$ and their full sample yields a

Sight line	z_{em}	$\log N(\text{H})$ (cm $^{-2}$)	ΔX	$\Omega_b(\text{BLA})$ ($\times 10^{-2} h_{70}^{-1}$)
3C 263	0.646	19.58	0.535	0.19 ± 0.17
PKS 0637-752	0.650	20.20	0.435	0.98 ± 0.29
PG 1424+240	0.604	18.31	0.579	0.01 ± 0.01
PG 0003+158	0.451	20.14	0.454	0.81 ± 0.17
PG 1216+069	0.331	20.39	0.322	2.05 ± 1.08
SDSS J135712.61+170444	0.150	20.08	0.123	2.64 ± 2.36
1ES 1553+113	0.414	19.13	0.449	0.08 ± 0.01
PG1116+215	0.176	19.22	0.134	0.33 ± 0.31
PG 1222+216	0.432	20.47	0.424	1.89 ± 0.47
H 1821+643	0.297	19.90	0.239	0.89 ± 0.70
PG 1121+422	0.225	19.86	0.203	0.97 ± 0.86
PKS 0405-123	0.574	18.50	0.535	0.02 ± 0.02
Total		21.08	4.432	0.72 ± 0.13

TABLE 7.3: $\Omega_b(\text{BLA})$ estimation using sample B

very high value of $38.1 \times 10^{-3} h_{70}^{-1}$ because it includes tentative BLA candidates with large Doppler widths also just like our sample C. We see that our estimation for $\Omega_b(\text{BLA})$ using sample B is in agreement with various existing studies and that using sample A is a very conservative lower limit as discussed already.

7.4 Contribution to Ω_b

We conclude this work by putting the last nail in the coffin by calculating the contribution of BLAs to the total cosmic baryon energy density. The latest CMB measurements puts the value of Ω_b at $(45.7 \pm 0.2) \times 10^{-3} h_{70}^{-2}$ (Planck Collaboration et al. 2020). This implies that BLAs contribute a minimum of around $(4 \pm 1)h_{70} \%$ based on the lower limit from the estimate using sample A. $\Omega_b(\text{BLA})$ value from sample B puts the contribution of BLAs at $(16 \pm 3)h_{70} \%$. While our optimistic

Sight line	z_{em}	$\log N(\text{H})$ (cm $^{-2}$)	ΔX	$\Omega_b(\text{BLA})$ ($\times 10^{-2} h_{70}^{-1}$)
3C 263	0.646	20.35	0.535	1.12 ± 0.80
PKS 0637-752	0.650	20.67	0.435	2.92 ± 1.56
PG 1424+240	0.604	18.31	0.579	0.01 ± 0.01
PG 0003+158	0.451	20.16	0.454	0.86 ± 0.18
PG 1216+069	0.331	21.36	0.322	$19.30 \pm 13.03^{\text{a}}$
SDSS J135712.61+170444	0.150	20.08	0.123	2.64 ± 2.36
1ES 1553+113	0.414	19.13	0.449	0.08 ± 0.01
PG 1222+216	0.432	20.58	0.424	2.43 ± 0.83
PG1116+215	0.176	19.22	0.134	0.33 ± 0.31
H 1821+643	0.297	19.90	0.239	0.89 ± 0.70
PG 1121+422	0.225	19.86	0.203	0.97 ± 0.86
PKS 0405-123	0.574	18.50	0.535	0.02 ± 0.02
HE 0056-3622	0.164	20.08	0.096	3.37 ± 1.91
RX J0439.6-5311	0.243	19.62	0.221	$0.50 \pm 0.52^{\text{a}}$
UKS 0242-724	0.102	20.24	0.029	$16.19 \pm 20.08^{\text{a}}$
PG 1259+593	0.478	20.41	0.522	1.33 ± 1.32
PKS 1302-102	0.278	20.03	0.259	1.12 ± 0.52
3C 57	0.671	19.08	0.507	0.06 ± 0.05
PHL 1811	0.192	20.22	0.141	$3.13 \pm 3.85^{\text{a}}$
PG 0832+251	0.330	21.27	0.329	$15.14 \pm 23.82^{\text{a}}$
Total		21.82	6.536	2.71 ± 1.38

^a excluding these systems we get $\Omega_b(\text{BLA}) = (1.00 \pm 0.22) \times 10^{-2} h_{70}^{-1}$

TABLE 7.4: $\Omega_b(\text{BLA})$ estimation using sample C

sample C yields an exceedingly high fraction of baryons in BLA, at $(60 \pm 30)h_{70}\%$, which exceeds the prediction of baryon content in WHIM of around 50% from cosmological simulations (Cen & Ostriker 1999, 2006). When we calculate the fraction by excluding the large value and large uncertainty sight lines in sample C,

Sample	$\Omega_b(\text{BLA})$ ($\times 10^{-3} h_{70}^{-1}$)	$\Omega_b(\text{BLA})/\Omega_b$ ($\times h_{70} \%$)
A	1.8 ± 0.5	4 ± 1
B	7.2 ± 1.3	16 ± 3
C	27.1 ± 13.8	60 ± 30
C ^a	10.0 ± 2.2	22 ± 5

^a Excluding high uncertainty sight lines from sample C

TABLE 7.5: Baryon fraction in BLAs.

we get a value of $(22 \pm 5)h_{70} \%$. Table 7.5 summarise these values.

We see that BLAs can contribute around 15-20 % to the baryon energy density in the current universe. So, BLAs could potentially be the reservoirs of the ‘missing’ baryons. We need to face the reality that we cannot estimate the whole contribution of BLAs to Ω_b as the absorbers which contribute the most would not be detectable because those will be very shallow features.

Chapter 8

Conclusions and Future Work

8.1 Conclusions

The motivation for the current work comes from ‘the missing baryon problem’ in the current universe. According, to which around 30% of the baryons are missing from our observations in the current universe. Cosmological simulations show that these baryons could be residing in Warm Hot Intergalactic Medium at high temperatures ($10^5 - 10^7$) K and very low densities ($10^{-4} - 10^{-6}$ cm $^{-3}$). This makes it difficult to detect WHIM, which has lead to uncertainties in the baryon census in this phase. In the current work we aim to address these uncertainties by surveying the broad Lyman- α absorbers (BLAs), which are thermally broadend to large Doppler widths above 40-45 km s $^{-1}$. But detecting broad features does not mean that we are always probing WHIM or high temperature gas phase. Broad features could also arise due to contaminations from other lines, line blending effects, poor S/N in the spectra. To ensure that the detected broad feature is indeed tracing WHIM and not other case mentioned above, we need to model the ionisation conditions in these absorber systems. If we find that the species in the absorbers are coming from collisionally ionised phase, then we could be sure that BLA candidate is tracing a warm-hot plasma as collisional ionisation is prominently seen at high temperatures. One such specie is O VI, which is an excellent tracer of WHIM, as it’s ionisation fraction in collisional ionisation peaks around temperatures of $T \sim 10^{5.7}$

K.

We use high S/N HST/COS FUV observations for the current work. In the low redshift IGM survey done by [Danforth et al. \(2016\)](#), they have studied 82 quasar sight lines, which have the highest quality available data. They have done the preliminary Voigt profile measurements on the absorption lines along these 82 sight lines. But we need more accurate Voigt profile measurements for our survey. So, we look for suitable candidates for our survey in their dataset. We shortlist systems which have H_I Doppler parameters above 45 km s⁻¹ in their preliminary measurements. Since we also need to model the ionisation conditions in these absorbers, which require metal ions. So we further put constrain that the absorbers should have absorption from atleast 3 distinct metal ions to model the ionisation conditions robustly. We find 29 absorber systems which satisfies these two constrains. These 29 systems are distributed along 22 different sight lines. The survey has a total unblocked H_I (Lyman- α) redshift pathlength of $\Delta z = 5.561$. We find a total of 37 BLA components in these systems. Out of the 29 absorbers, 17 systems show absorption from O VI. We have identified a total 711 absorption lines in these 29 systems and have modelled the ionisation conditions in 39 components of these systems. In case of O VI systems, we find that 20 out of 25 O VI components could be tracing collisionally ionised gas phase and possibly probing warm-hot plasma.

We make use of the results from this survey to estimate the baryon content in BLAs. We consider three sample of absorbers for this. First, we use absorbers where reliable estimate of temperature is available and ionisation modelling suggests collisional ionisation of O VI, this gives us a very conservative lower limit on $\Omega_b(\text{BLA})$ to be $(1.8 \pm 0.5) \times 10^{-3} h_{70}^{-1}$. Our second sample considers absorbers where O VI is found to be collisionally ionised. For this, we estimate the temperature from Doppler parameters assuming complete thermal broadening. This gives us $\Omega_b(\text{BLA}) = (7.2 \pm 1.3) \times 10^{-3} h_{70}^{-1}$. The last sample includes all the BLA components found in our survey. This yields a very large value of $\Omega_b(\text{BLA}) = (27.1 \pm 13.8) \times 10^{-3} h_{70}^{-1}$, which exceeds the prediction of baryon content in WHIM from cosmological simulations of around 50%. We discuss the

sources on uncertainties in these estimates. We finally compare these values with the total baryon energy density and find that BLAs can contribute around 15-20 % to the total cosmic baryon budget in the current universe.

8.2 Future work

The future work includes incorporating more sight lines in the survey to improve the statistics. We can extend the results from this survey to larger data set of general population of BLA systems to get the more robust estimate of the baryon content in these BLAs. Future studies could also be aimed to explore the correlations between these BLAs and galaxies by doing systematic survey of galaxies around these absorber system. This can allow us to understand the origin of these absorbers. This would allow us to get insights on the metal enrichment of the IGM from the galaxies. This could also shed light on the various feedback processes happening in the circumgalactic medium of the galaxies, which play crucial rule in the formation and evolution of the galaxies.

References

- Abdurro'uf et al., 2022, [The Astrophysical Journal Supplement Series](#), 259, 35
- Acharya A., Khaire V., 2021, [Monthly Notices of the Royal Astronomical Society](#), 509, 5559
- Anshul P., Narayanan A., Muzahid S., Beckett A., Morris S. L., 2021, [Monthly Notices of the Royal Astronomical Society](#), 503, 3243
- Bahcall J. N., Peebles P. J. E., 1969, [The Astrophysical Journal Letters](#), 156, L7
- Becker G. D., Sargent W. L. W., Rauch M., Calverley A. P., 2011, [The Astrophysical Journal](#), 735, 93
- Carswell R. F., Webb J. K., 2014, [Astrophysics Source Code Library](#), p. ascl :1408.015
- Cen R., Ostriker J. P., 1999, [The Astrophysical Journal](#), 514, 1
- Cen R., Ostriker J. P., 2006, [The Astrophysical Journal](#), 650, 560
- Danforth C. W., Shull J. M., 2008, [The Astrophysical Journal](#), 679, 194
- Danforth C. W., Stocke J. T., Shull J. M., 2010, [The Astrophysical Journal](#), 710, 613
- Danforth C. W., et al., 2016, [The Astrophysical Journal](#), 817, 111
- Fang T., Bryan G. L., 2001, [The Astrophysical Journal Letters](#), 561, L31

- Ferland G. J., Korista K. T., Verner D. A., Ferguson J. W., Kingdon J. B., Verner E. M., 1998, [PASP](#), **110**, 761
- Ferland G. J., et al., 2017, [doi:10.48550/ARXIV.1705.10877](#)
- Fukugita M., Hogan C. J., Peebles P. J. E., 1998, [The Astrophysical Journal](#), **503**, 518
- Gnat O., Sternberg A., 2007, [The Astrophysical Journal Supplement Series](#), **168**, 213
- Grevesse N., Asplund M., Sauval A. J., Scott P., 2010, [Astrophysics and Space Science](#), **328**, 179
- Hussain T., Khaire V., Srianand R., Muzahid S., Pathak A., 2017, [Monthly Notices of the Royal Astronomical Society](#), **466**, 3133
- Ilbert O., et al., 2005, [Astronomy and Astrophysics](#), **439**, 863
- Khaire V., Srianand R., 2019, [Monthly Notices of the Royal Astronomical Society](#), **484**, 4174
- Le Fèvre O., et al., 2013, [Astronomy & Astrophysics](#), **559**, A14
- Lehner N., Savage B. D., Wakker B. P., Sembach K. R., Tripp T. M., 2006, [The Astrophysical Journal Supplement Series](#), **164**, 1
- Lehner N., Savage B. D., Richter P., Sembach K. R., Tripp T. M., Wakker B. P., 2007, [The Astrophysical Journal](#), **658**, 680
- Morton D. C., Smith W. H., 1973, [The Astrophysical Journal Supplement Series](#), **26**, 333
- Peimbert A., Peimbert M., Luridiana V., 2016, [Rev. Mex. Astron. Astrofis.](#), **52**, 419
- Penton S. V., Stocke J. T., Shull J. M., 2000, [The Astrophysical Journal Supplement Series](#), **130**, 121

- Planck Collaboration et al., 2020, *Astronomy & Astrophysics*, 641, A6
- Pradeep J., Sankar S., Umasree T. M., Narayanan A., Khaire V., Gebhardt M., Sammeer Charlton J. C., 2020, *Monthly Notices of the Royal Astronomical Society*, 493, 250
- Prochaska J. X., Weiner B., Chen H. W., Mulchaey J., Cooksey K., 2011, *The Astrophysical Journal*, 740, 91
- Richter P., 2020, *The Astrophysical Journal*, 892, 33
- Richter P., Savage B. D., Tripp T. M., Sembach K. R., 2004, *The Astrophysical Journal Supplement Series*, 153, 165
- Richter P., Savage B. D., Sembach K. R., Tripp T. M., 2006, *Astronomy and Astrophysics*, 445, 827
- Savage B. D., Kim T. S., Wakker B. P., Keeney B., Shull J. M., Stocke J. T., Green J. C., 2014, *The Astrophysical Journal Supplement Series*, 212, 8
- Shull J. M., Smith B. D., Danforth C. W., 2012, *The Astrophysical Journal*, 759, 23
- Strauss M. A., et al., 2002, *The Astronomical Journal*, 124, 1810
- Sutherland R. S., Dopita M. A., 1993, *The Astrophysical Journal Supplement Series*, 88, 253
- Tepper-García T., Richter P., Schaye J., 2013, *Monthly Notices of the Royal Astronomical Society*, 436, 2063
- Tilton E. M., Danforth C. W., Shull J. M., Ross T. L., 2012, *The Astrophysical Journal*, 759, 112
- Tripp T. M., Sembach K. R., Bowen D. V., Savage B. D., Jenkins E. B., Lehner N., Richter P., 2008b, *The Astrophysical Journal Supplement Series*, 177, 39

- Tripp T. M., Sembach K. R., Bowen D. V., Savage B. D., Jenkins E. B., Lehner N., Richter P., 2008a, [The Astrophysical Journal Supplement Series](#), 177, 39
- Tumlinson J., et al., 2011, [Science](#), 334, 948
- Tumlinson J., et al., 2013, [The Astrophysical Journal](#), 777, 59
- Wakker B. P., Hernandez A. K., French D. M., Kim T.-S., Oppenheimer B. D., Savage B. D., 2015, [The Astrophysical Journal](#), 814, 40
- Yao Y., Shull J. M., Wang Q. D., Cash W., 2012, [The Astrophysical Journal](#), 746, 166

A

Sight lines shortlisted for survey

This appendix gives the details of the 22 sight lines along which our 29 absorber systems lies.

S. no.	Sight line	R.A. (J2000)	Dec. (J2000)	z_{AGN}	Flux ^a	AGN type
1	1ES 1553+113	15 :55 :43.04	+11 :11 :24.4	>0.4140	15.9	BLLac/FSRQ
2	3C 263	11 :39 :56.99	+65 :47 :49.2	0.6460	10.4	FR2/Sy1.2
3	3C 57	02 :01 :57.16	-11 :32 :33.1	0.6705	6.6	Sy1.2
4	H 1821+643	18 :21 :57.30	+64 :20 :36.0	0.2968	53.0	Sy1.2
5	HE 0056-3622	00 :58 :37.39	-36 :06 :05.0	0.1641	17.3	Sy1
6	PMN J1103-2329	11 :03 :37.60	-23 :29 :30.0	0.1860	2.1	BLLac/FSRQ
7	PG 0003+158	00 :05 :59.24	+16 :09 :49.0	0.4509	7.7	Sy1.2
8	PG 0832+251	08 :35 :35.80	+24 :59 :41.0	0.3298	3.5	QSO
9	PG 1116+215	11 :19 :08.60	+21 :19 :18.0	0.1763	45.7	Sy1.0
10	PG 1121+422	11 :24 :39.18	+42 :01 :45.0	0.2250	7.4	Sy1.0
11	PG 1216+069	12 :19 :20.93	+06 :38 :38.5	0.3313	12.3	NLSy1
12	PG 1222+216	12 :24 :54.45	+21 :22 :46.3	0.4320	17.0	Blazar
13	PG 1259+593	13 :01 :12.90	+59 :02 :07.0	0.4778	15.3	Sy1.0
14	PG 1424+240	14 :27 :00.39	+23 :48 :00.0	>0.6035	15.2	BLLac
15	PHL 1811	21 :55 :01.50	-09 :22 :25.0	0.1920	56.2	NLSy1
16	PKS 0405-123	04 :07 :48.43	-12 :11 :36.7	0.5740	32.1	Sy1.2
17	PKS 0637-752	06 :35 :46.50	-75 :16 :16.8	0.6500	8.0	FSRQ
18	PKS 1302-102	13 :05 :33.00	-10 :33 :19.0	0.2784	14.9	FSRQ/Sy1.2
19	RX J0439.6-5311	04 :39 :38.64	-53 :11 :31.6	0.2430	3.5	Sy1
20	SDSS J135712.61+170444	13 :57 :12.60	+17 :04 :44.0	0.1500	4.7	QSO
21	SBS1108+560	11 :11 :32.20	+55 :47 :26.0	0.7666	4.9	QSO
22	UKS0242-724	02 :43 :09.60	-72 :16 :48.4	0.1018	10.3	Sy1.2

^a Median observed continuum flux in the COS/FUV band in units of 10^{-15} erg cm $^{-2}$ s $^{-1}$ Å $^{-1}$.

TABLE A.1: 22 sight lines selected for the survey. Table 1 of [Danforth et al. \(2016\)](#).

B

HST/COS observations

This appendix gives the details of the HST/COS observations in FUV channel in G130M and G160M gratings of 22 sight lines selected for the survey.

S. no.	Sight line	Exp. (ks)	S/N	Exp. (ks)	S/N
		(G130M)	(G130M) ^a	(G160M)	(G160M) ^a
1	1ES 1553+113	10.8	38	11.9	30
2	3C 263	15.4	40	18.0	28
3	3C 57	11.0	29	8.7	17
4	H 1821+643	12.0	59	0.5	14
5	HE 0056-3622	5.0	32	5.7	20
6	PMN J1103-2329	13.3	19	13.3	11
7	PG 0003+158	10.4	27	10.9	22
8	PG 0832+251	6.1	15	6.8	13
9	PG1 116+215	4.7	43	5.5	32
10	PG 1121+422	5.0	23	5.8	14
11	PG 1216+069	5.1	27	5.6	21
12	PG 1222+216	3.4	21	7.7	26
13	PG 1259+593	9.2	39	11.2	29
14	PG 1424+240	3.8	24	7.9	25
15	PHL 1811	3.5	42	3.1	27
16	PKS 0405-123	24.2	76	11.1	35
17	PKS 0637-752	9.6	26	8.7	18
18	PKS 1302-102	6.0	31	6.9	23
19	RX J0439.6-5311	8.2	21	8.9	12
20	SDSS J135712.61+170444	4.2	18	6.8	12
21	SBS 1108+560	8.4	5	8.9	15
22	UKS 0242-724	2.1	20	3.2	14

^a Median S/N per resolution element in the G130M and G160M channels.

TABLE B.1: HST/COS FUV observation details of the 22 sight lines selected for the survey. Table 2 of [Danforth et al. \(2016\)](#).

C

Survey results

This appendix gives Voigt profile fitting results in the form of system plots and fitted parameters table and ionisation modelling results for all 29 absorber systems.

The line of sight and the redshift of the absorber (z_{abs}) are given in the title of the system plots. In each of the plots horizontal axis is the rest-frame velocity of lines with respect to $z = z_{abs}$ and vertical axis represents the continuum normalized flux. The green step curve is the observed flux, the red solid curve is the Voigt profile fit, the blue dashed curves are the individual components that make the absorption profile with orange ones being the contamination from other lines and the light pink step curve is the error in observed flux.

For O VI absorbers, we give n_H and Z values for both excluding and including O VI cases. The orange lines and the green lines are the model predicted column densities of ions for excluding and including O VI case respectively. Red errorbars are the observed column densities of ions from Voigt profile fitting. For non-O VI absorbers we give solutions from the available ions.

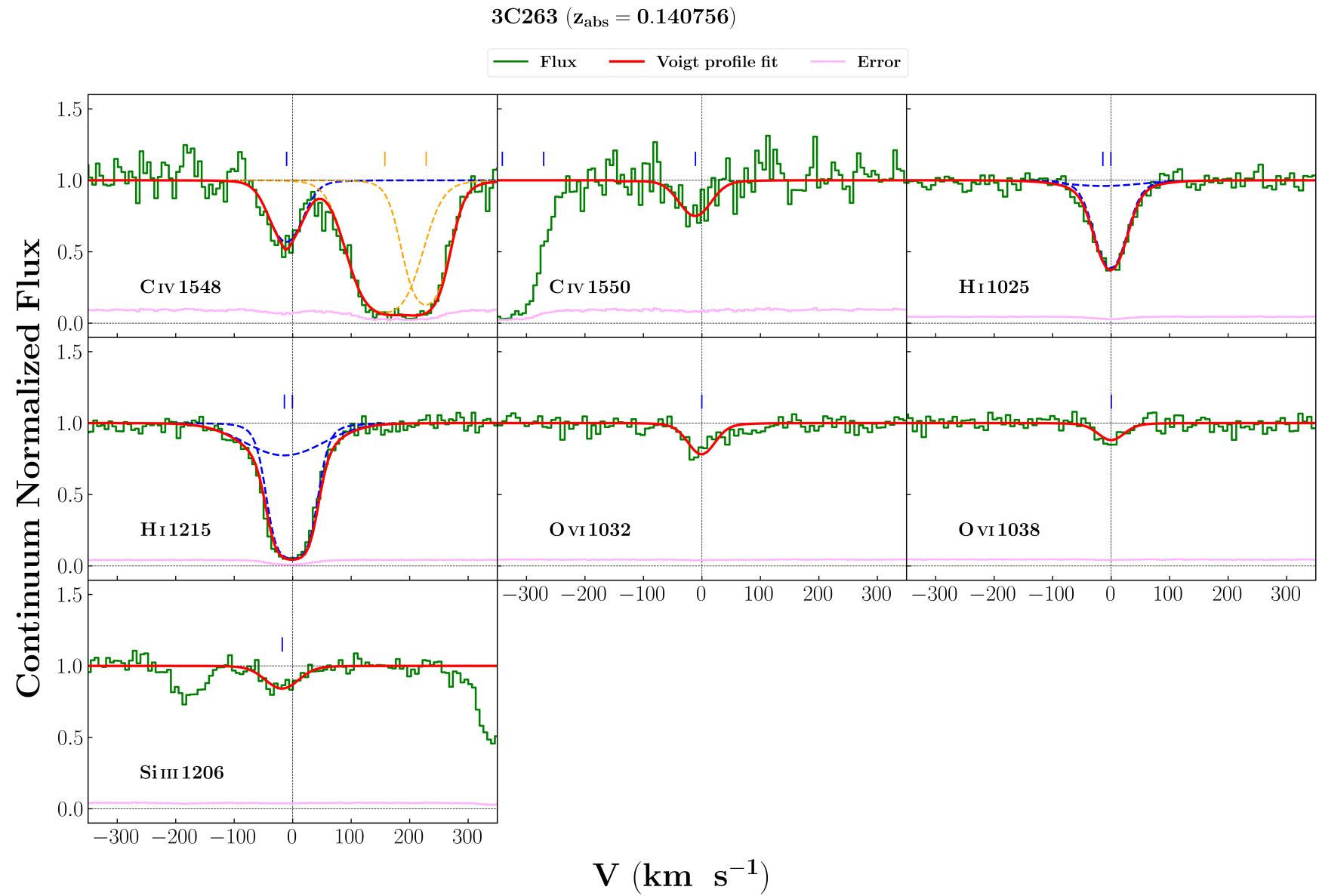


FIGURE C.1: System plot for the absorber along the LOS of 3C 263 at $z_{\text{abs}} = 0.140756$.

Ion	v (km s ⁻¹)	b (km s ⁻¹)	log [N cm ⁻²]
Si III	-18 ± 8	35 ± 11	12.39 ± 0.09
C IV	-10 ± 3	33 ± 0	13.71 ± 0.04
O VI	0 ± 2	26 ± 4	13.63 ± 0.04
H I	-14 ± 1	87 ± 10	13.49 ± 0.06
H I	0 ± 1	28 ± 1	14.49 ± 0.02

$$\log N(H I) [\text{cm}^{-2}] = 14.49$$

Excluding O VI : $\log n_H (\text{cm}^{-3}) = -4.14 \pm 0.04$	$\log Z/Z_{\odot} = 1.69 \pm 0.08$
Including O VI : $\log n_H (\text{cm}^{-3}) = -4.45 \pm 0.01$	$\log Z/Z_{\odot} = 1.30 \pm 0.05$

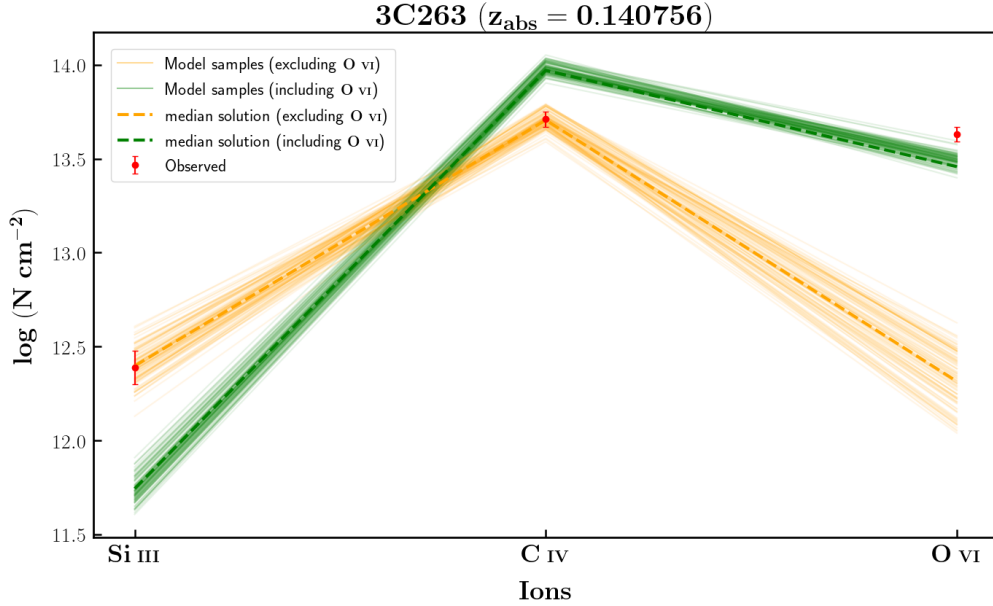


FIGURE C.2: $\log N(H I) [\text{cm}^{-2}] = 13.49$

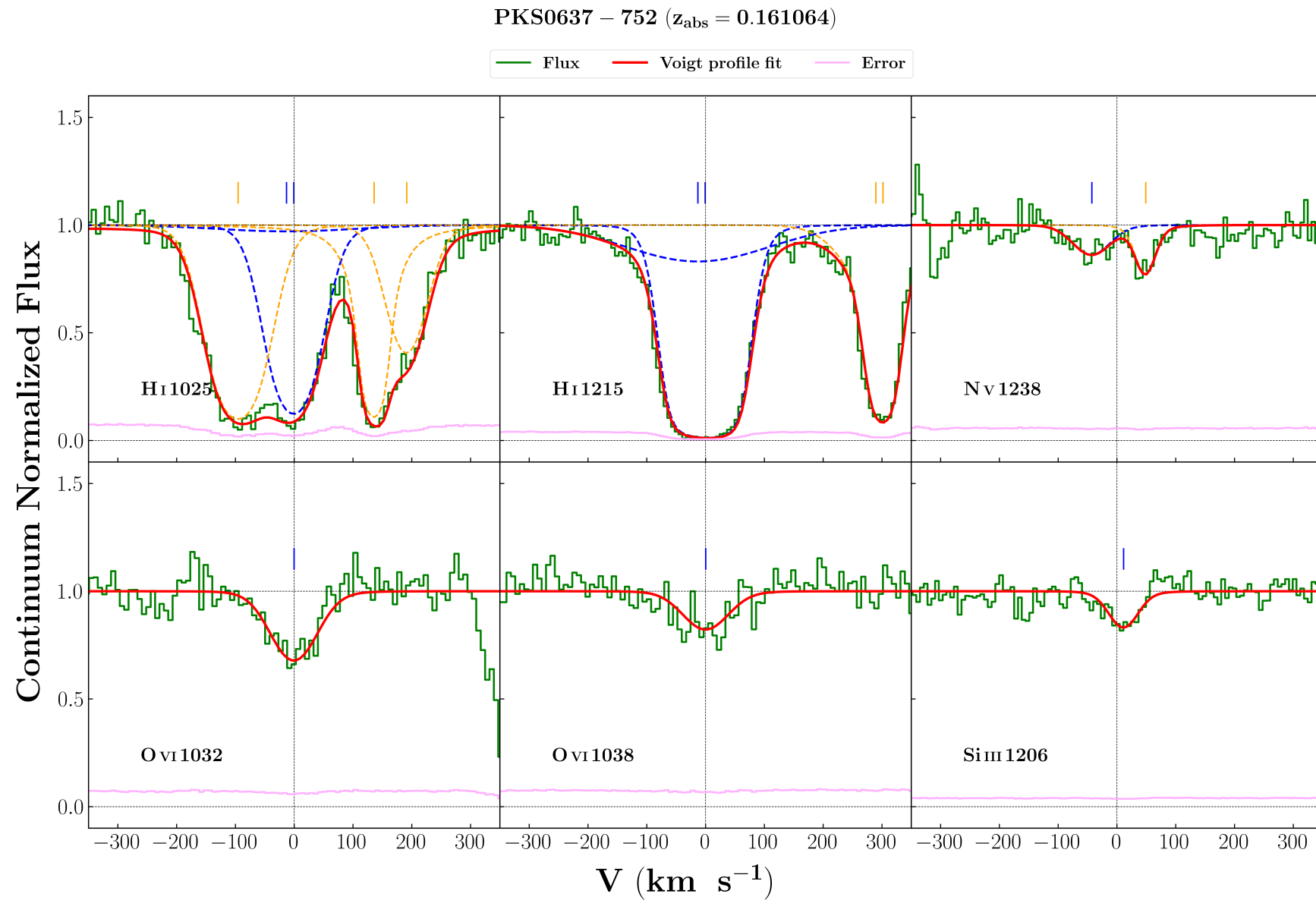


FIGURE C.3: System plot for the absorber along the LOS of PKS 0637-752 at $z_{\text{abs}} = 0.161064$.

Ion	v (km s ⁻¹)	b (km s ⁻¹)	log [N cm ⁻²]
N V	-42 ± 6	40 ± 9	13.37 ± 0.07
Si III	11 ± 4	30 ± 7	12.37 ± 0.06
O VI	0 ± 3	48 ± 5	14.02 ± 0.03
H I	-13 ± 2	162 ± 21	13.6 ± 0.06
H I	-1 ± 1	45 ± 1	15.01 ± 0.02

$$\log N(\text{H I}) [\text{cm}^{-2}] = 13.60$$

Excluding O VI : $\log n_H (\text{cm}^{-3}) = -4.29 \pm 0.02$	$\log Z/Z_\odot = 1.64 \pm 0.05$
Including O VI : $\log n_H (\text{cm}^{-3}) = -4.42 \pm 0.01$	$\log Z/Z_\odot = 1.69 \pm 0.04$

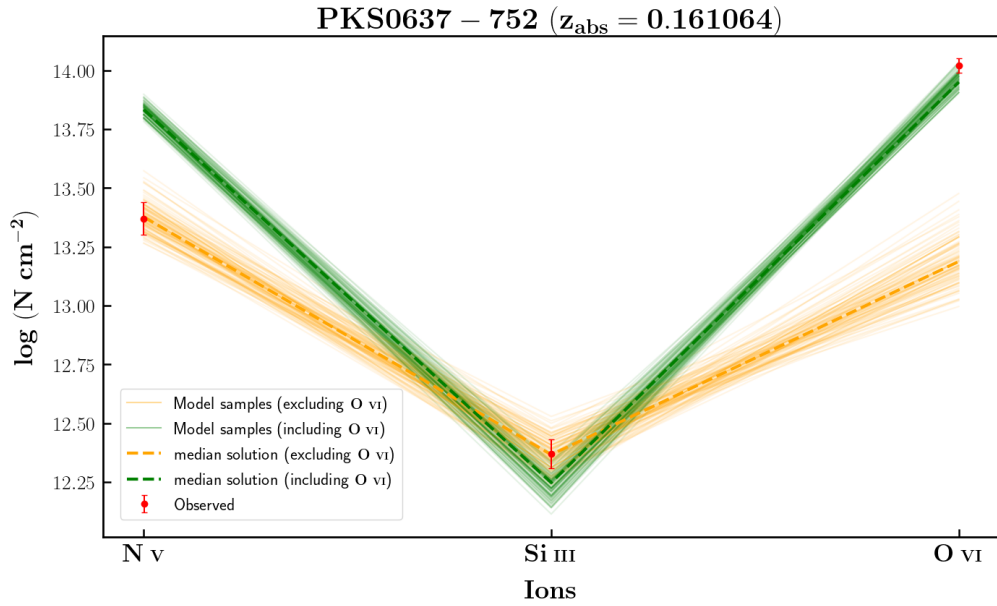


FIGURE C.4: $\log N(\text{H I}) [\text{cm}^{-2}] = 13.60$

PKS0637 – 752 ($z_{\text{abs}} = 0.417539$)

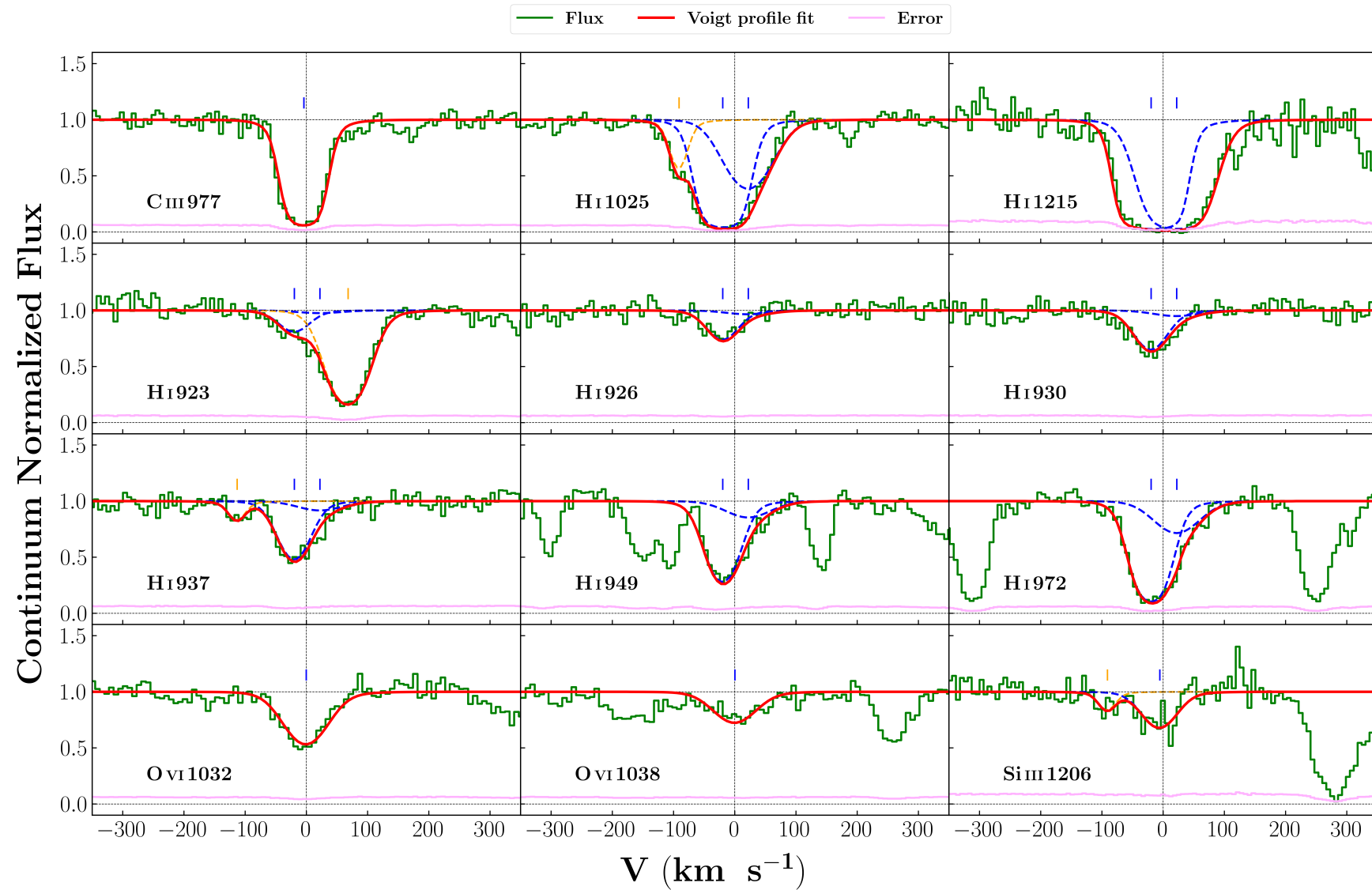


FIGURE C.5: System plot for the absorber along the LOS of PKS 0637-752 at $z_{\text{abs}} = 0.417539$.

Ion	v (km s ⁻¹)	b (km s ⁻¹)	log [N cm ⁻²]
Si III	-5 ± 4	35 ± 7	12.74 ± 0.06
C III	-4 ± 1	24 ± 2	14.44 ± 0.15
O VI	0 ± 1	42 ± 6	14.19 ± 0.05
H I	-17 ± 1	30 ± 1	15.41 ± 0.03
H I	20 ± 1	46 ± 4	14.61 ± 0.07

$$\log N(\text{H I}) [\text{cm}^{-2}] = 15.41$$

Excluding O VI : $\log n_H (\text{cm}^{-3}) = -3.54 \pm 0.11$	$\log Z/Z_{\odot} = -0.49 \pm 0.11$
Including O VI : $\log n_H (\text{cm}^{-3}) = -3.74 \pm 0.02$	$\log Z/Z_{\odot} = -0.23 \pm 0.04$

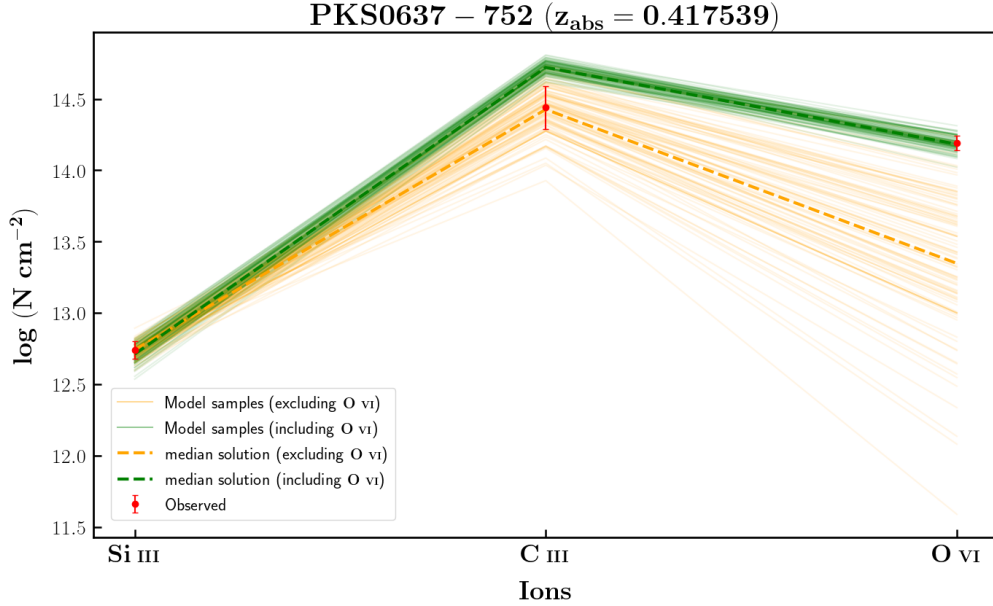


FIGURE C.6: $\log N(\text{H I}) [\text{cm}^{-2}] = 15.41$

PG1424 + 240 ($z_{\text{abs}} = 0.147104$)

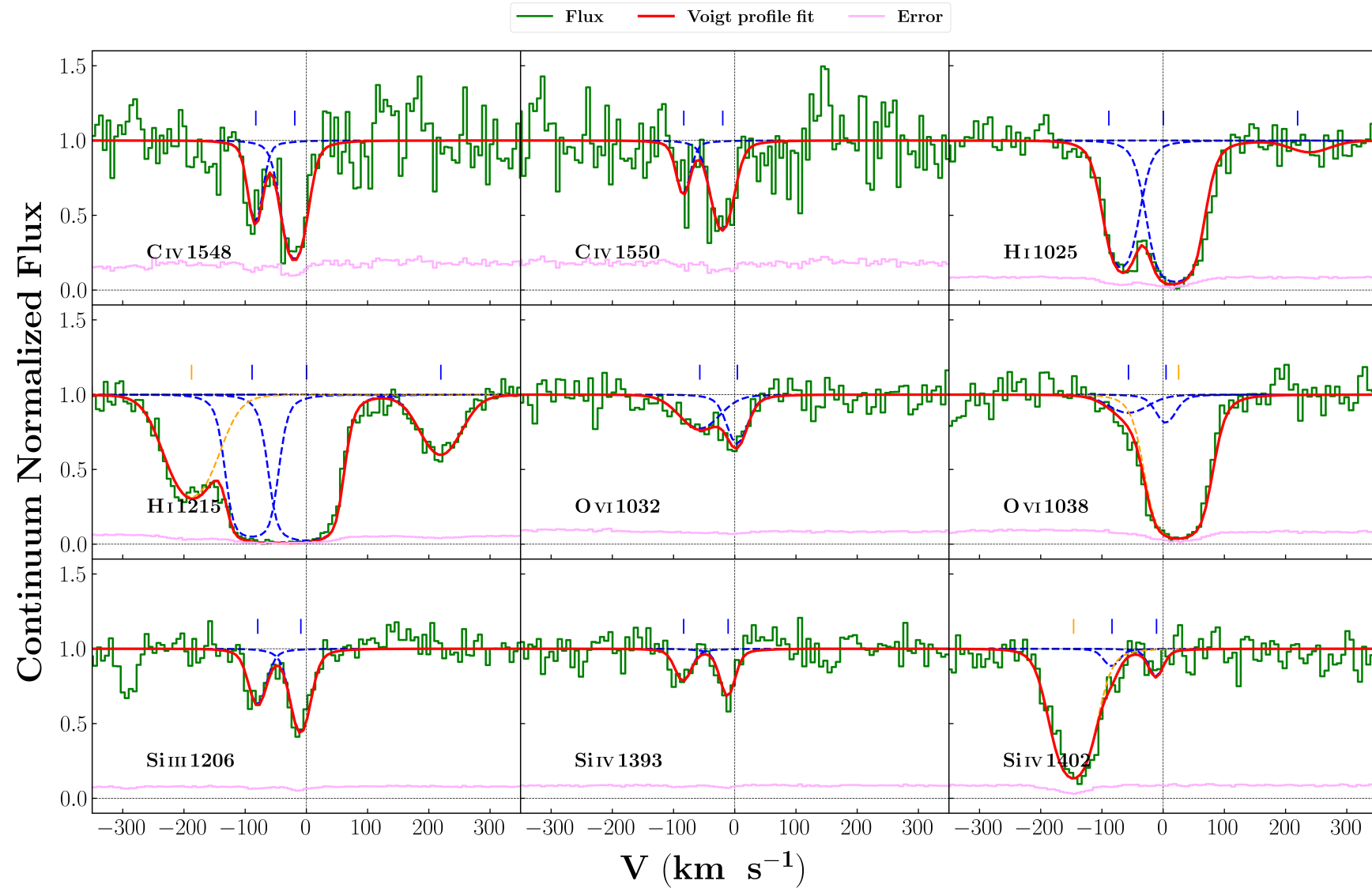


FIGURE C.7: System plot for the absorber along the LOS of PG 1424+240 at $z_{\text{abs}} = 0.147104$.

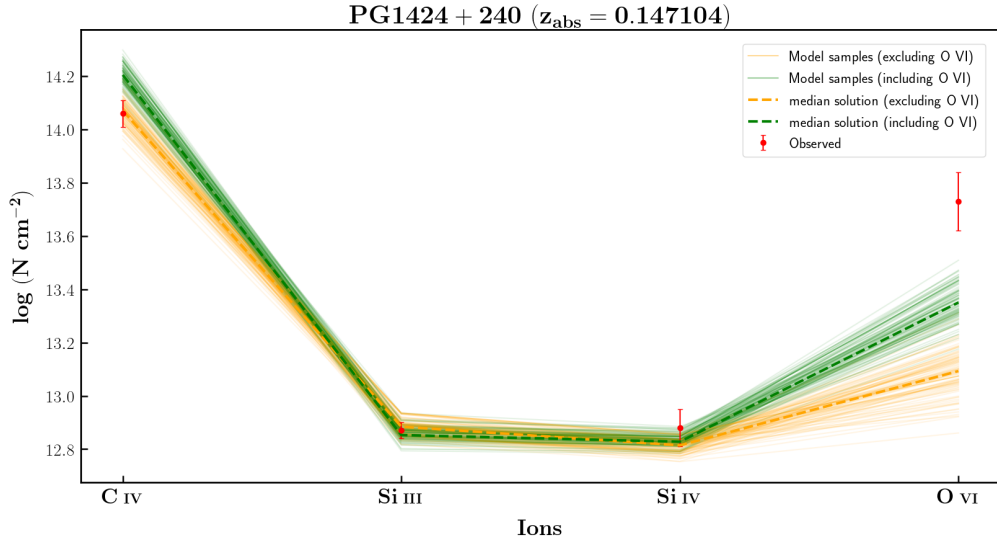
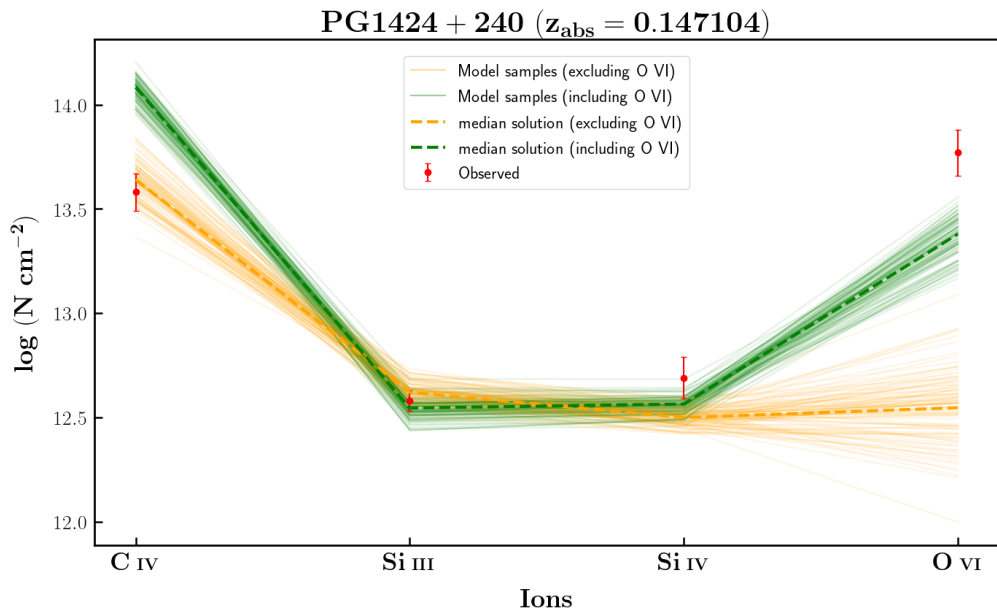
Ion	v (km s⁻¹)	b (km s⁻¹)	log [N cm⁻²]
C IV	-81 ± 2	11 ± 4	13.58 ± 0.09
C IV	-18 ± 2	20 ± 3	14.06 ± 0.05
Si III	-78 ± 2	15 ± 3	12.58 ± 0.05
Si III	-9 ± 1	16 ± 2	12.87 ± 0.03
Si IV	-82 ± 4	13 ± 7	12.69 ± 0.1
Si IV	-11 ± 2	11 ± 5	12.88 ± 0.07
O VI	-56 ± 9	39 ± 13	13.77 ± 0.11
O VI	4 ± 4	16 ± 6	13.73 ± 0.11
H I	-454 ± 3	27 ± 5	13.16 ± 0.05
H I	-87 ± 3	23 ± 2	14.88 ± 0.05
H I	0 ± 3	29 ± 2	15.44 ± 0.14
H I	216 ± 2	40 ± 3	13.49 ± 0.02

$$\log N(H I) [\text{cm}^{-2}] = 15.44$$

Excluding O VI : $\log n_H (\text{cm}^{-3}) = -3.81 \pm 0.03$	log $Z/Z_{\odot} = -0.46 \pm 0.03$
Including O VI : $\log n_H (\text{cm}^{-3}) = -3.88 \pm 0.02$	log $Z/Z_{\odot} = -0.42 \pm 0.02$

$$\log N(H I) [\text{cm}^{-2}] = 14.88$$

Excluding O VI : $\log n_H (\text{cm}^{-3}) = -3.74 \pm 0.05$	log $Z/Z_{\odot} = -0.22 \pm 0.04$
Including O VI : $\log n_H (\text{cm}^{-3}) = -3.96 \pm 0.03$	log $Z/Z_{\odot} = -0.07 \pm 0.04$

FIGURE C.8: $\log N(\text{H I}) [\text{cm}^{-2}] = 15.44$ FIGURE C.9: $\log N(\text{H I}) [\text{cm}^{-2}] = 14.88$

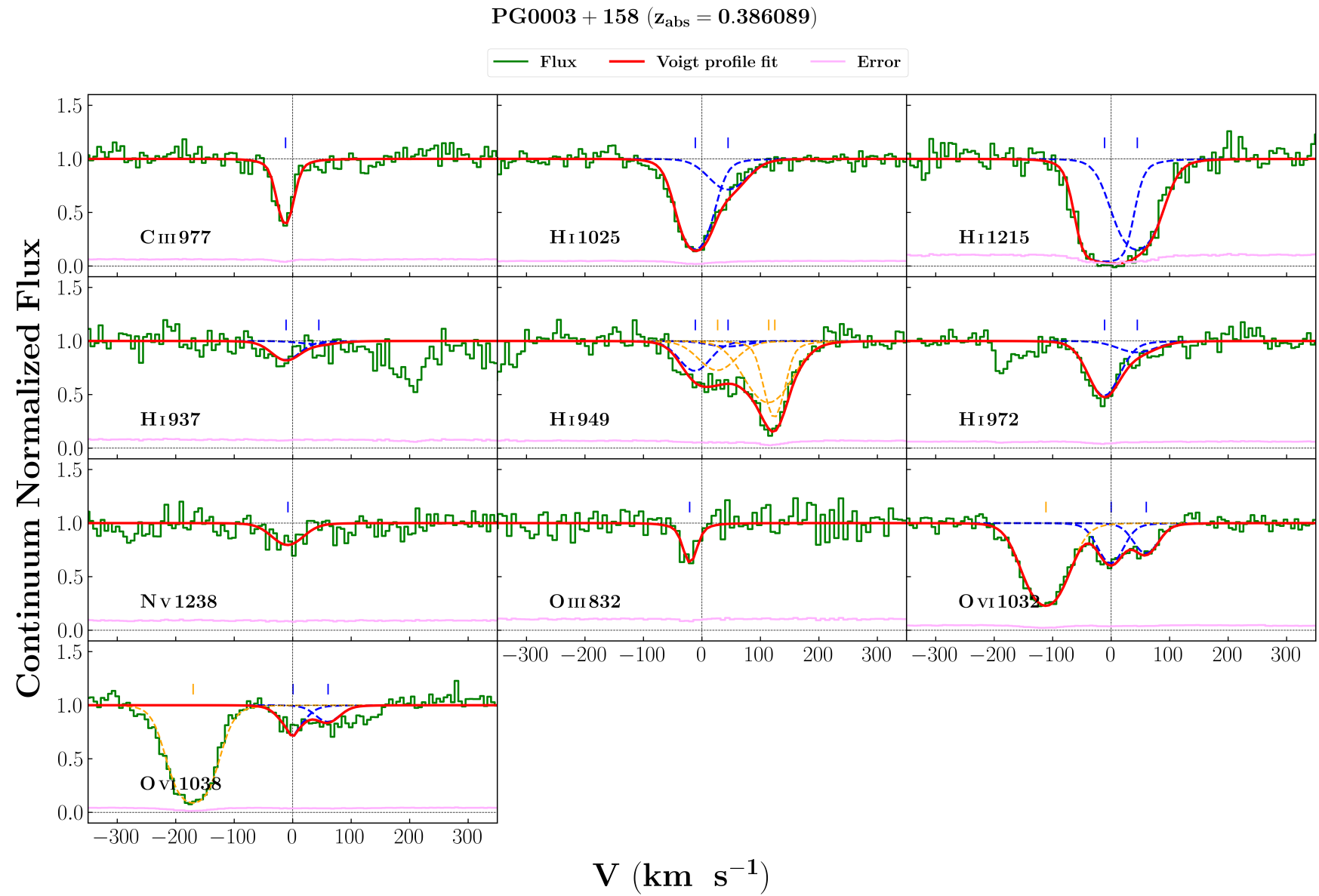


FIGURE C.10: System plot for the absorber along the LOS of PG 0003+158 at $z_{\text{abs}} = 0.386089$.

Ion	v (km s ⁻¹)	b (km s ⁻¹)	log [N cm ⁻²]
O III	-18 ± 2	9 ± 5	13.93 ± 0.08
C III	-11 ± 1	13 ± 2	13.35 ± 0.05
N V	-7 ± 1	33 ± 11	13.49 ± 0.11
O VI	0 ± 2	25 ± 3	13.87 ± 0.04
O VI	54 ± 3	25 ± 4	13.71 ± 0.06
H I	-10 ± 1	29 ± 0	14.81 ± 0.03
H I	40 ± 9	40 ± 4	14.1 ± 0.05

$$\log N(\text{H I}) [\text{cm}^{-2}] = 14.81$$

Excluding O VI : $\log n_H (\text{cm}^{-3}) = -4.12 \pm 0.06$	$\log Z/Z_{\odot} = -0.65 \pm 0.04$
Including O VI : $\log n_H (\text{cm}^{-3}) = -4.07 \pm 0.02$	$\log Z/Z_{\odot} = -0.68 \pm 0.03$

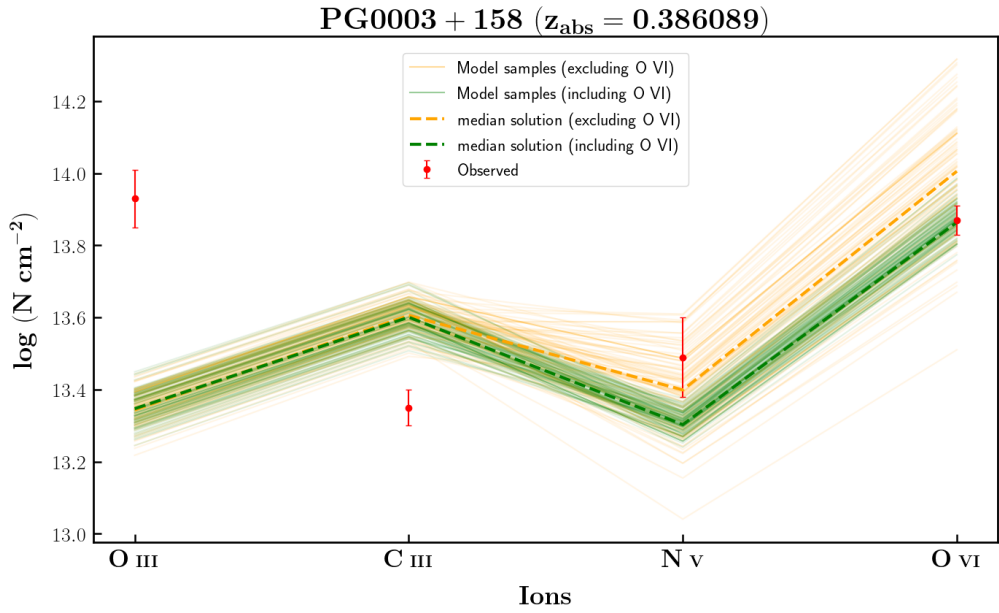


FIGURE C.11: $\log N(\text{H I}) [\text{cm}^{-2}] = 14.81$

PG0003 + 158 ($z_{\text{abs}} = 0.421923$)

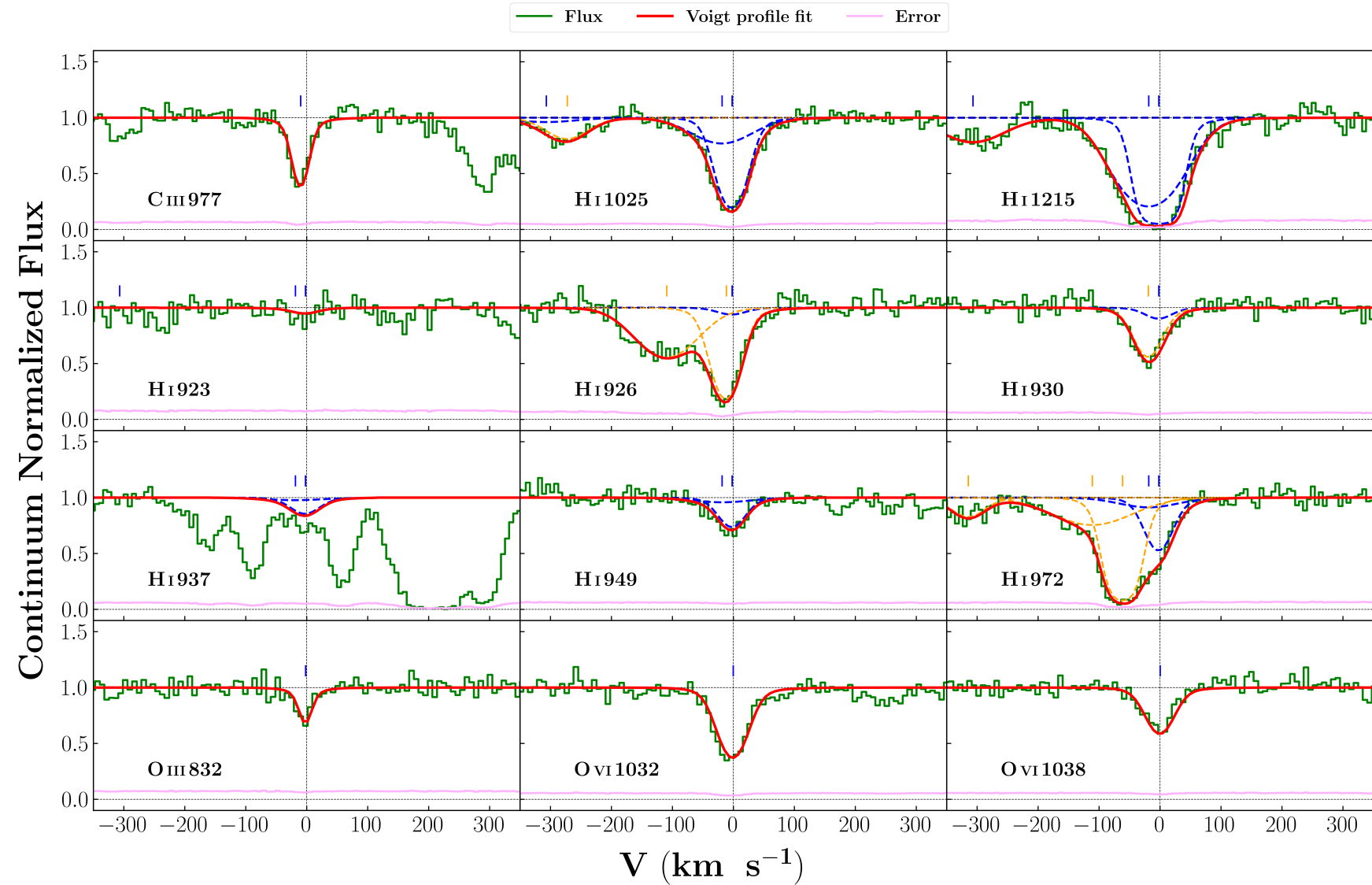


FIGURE C.12: System plot for the absorber along the LOS of PG 0003+158 at $z_{\text{abs}} = 0.421923$.

Ion	v (km s ⁻¹)	b (km s ⁻¹)	log [N cm ⁻²]
C III	-9 ± 1	13 ± 1	13.35 ± 0.04
O III	-1 ± 2	7 ± 5	13.83 ± 0.13
O VI	0 ± 1	27 ± 1	14.27 ± 0.02
H I	-272 ± 6	66 ± 10	13.37 ± 0.05
H I	-16 ± 1	64 ± 3	14.17 ± 0.04
H I	-2 ± 1	26 ± 1	14.71 ± 0.02

$$\log N(\text{H I}) [\text{cm}^{-2}] = 14.17$$

Excluding O VI : $\log n_H (\text{cm}^{-3}) = -2.66 \pm 0.22$ $\log Z/Z_\odot = 0.42 \pm 0.23$
 Including O VI : $\log n_H (\text{cm}^{-3}) = -4.24 \pm 0.02$ $\log Z/Z_\odot = -0.09 \pm 0.03$

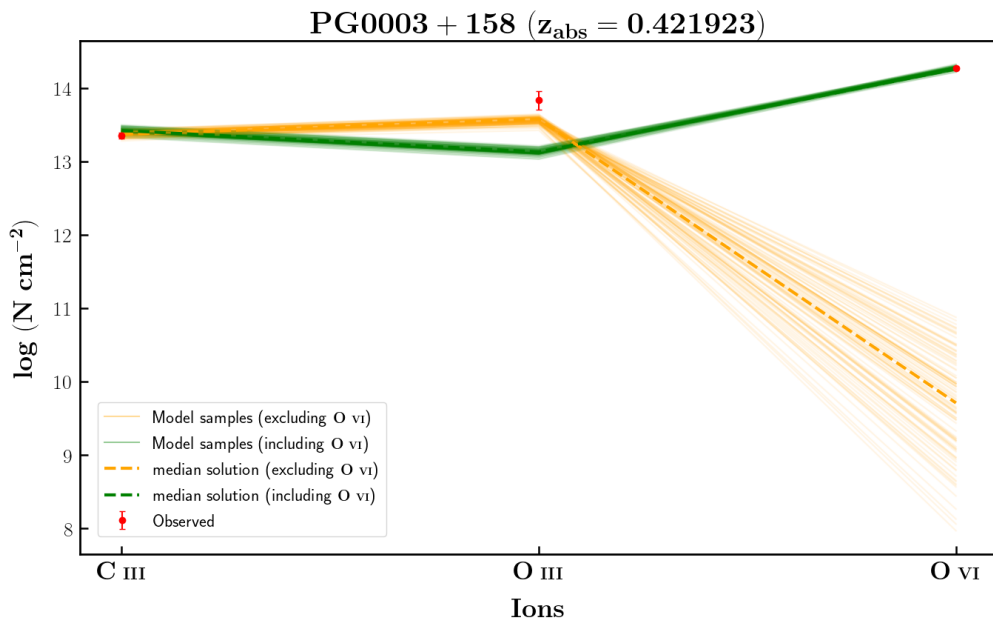


FIGURE C.13: $\log N(\text{H I}) [\text{cm}^{-2}] = 14.17$

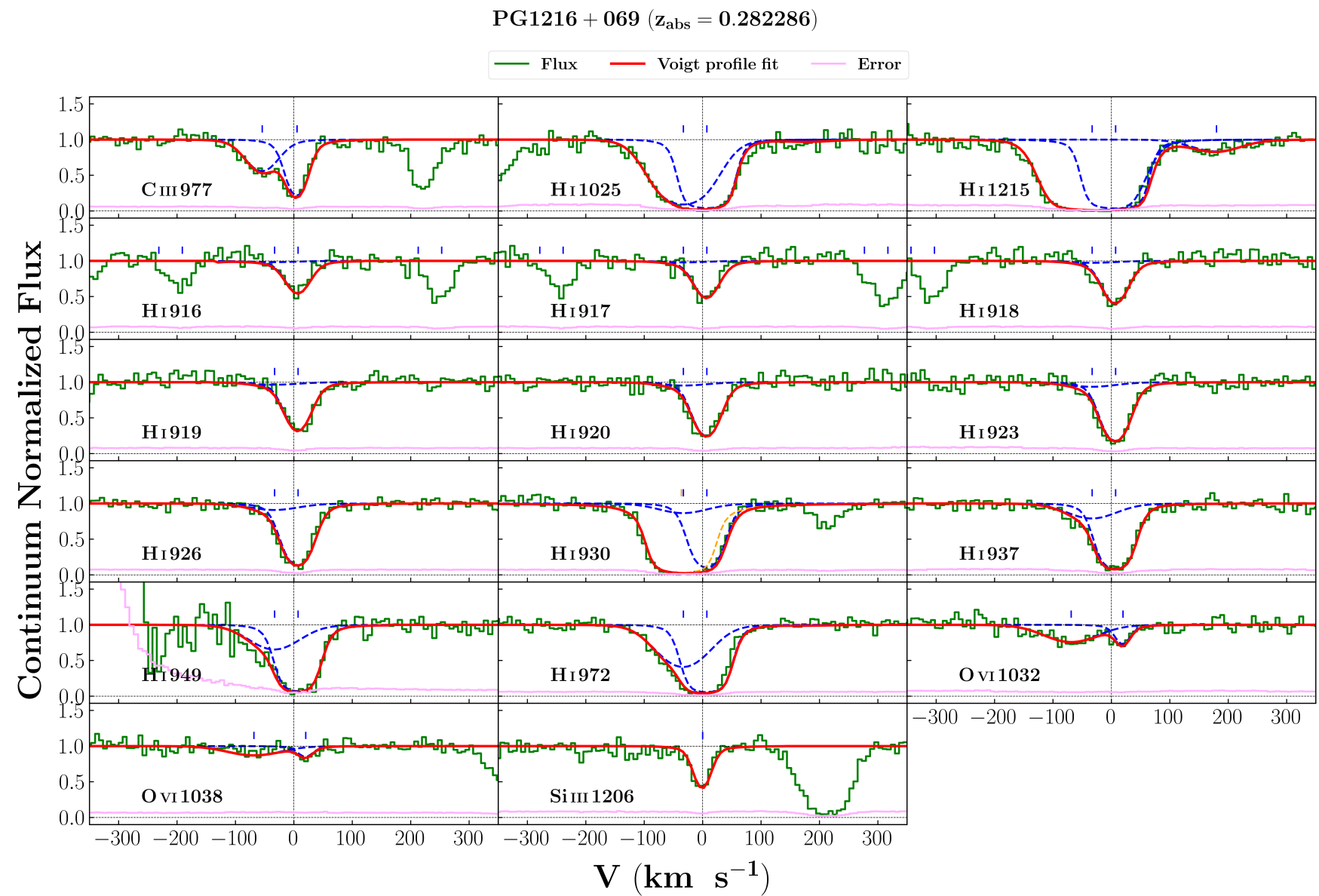


FIGURE C.14: System plot for the absorber along the LOS of PG 1216+069 at $z_{\text{abs}} = 0.282286$.

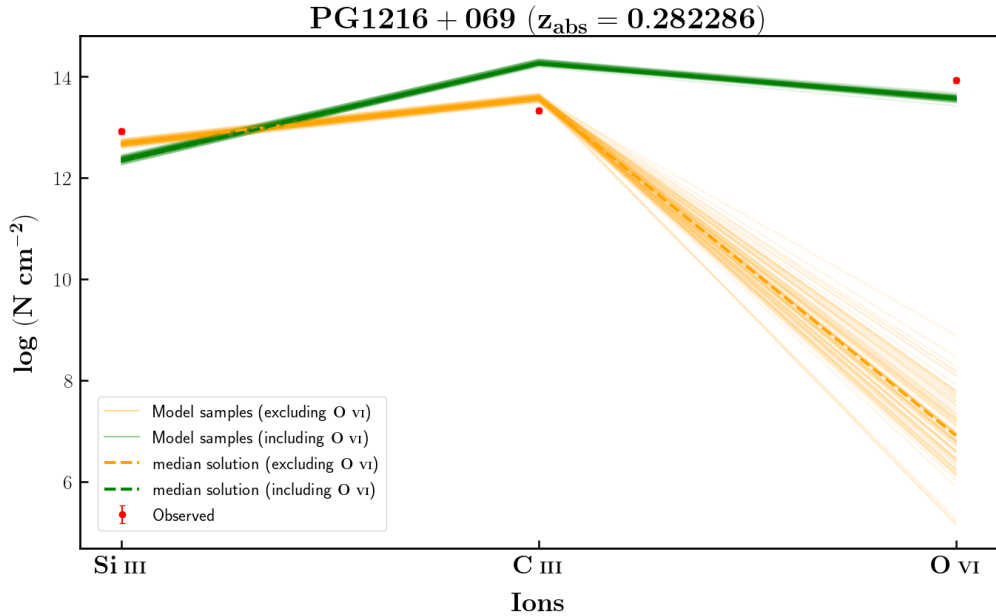
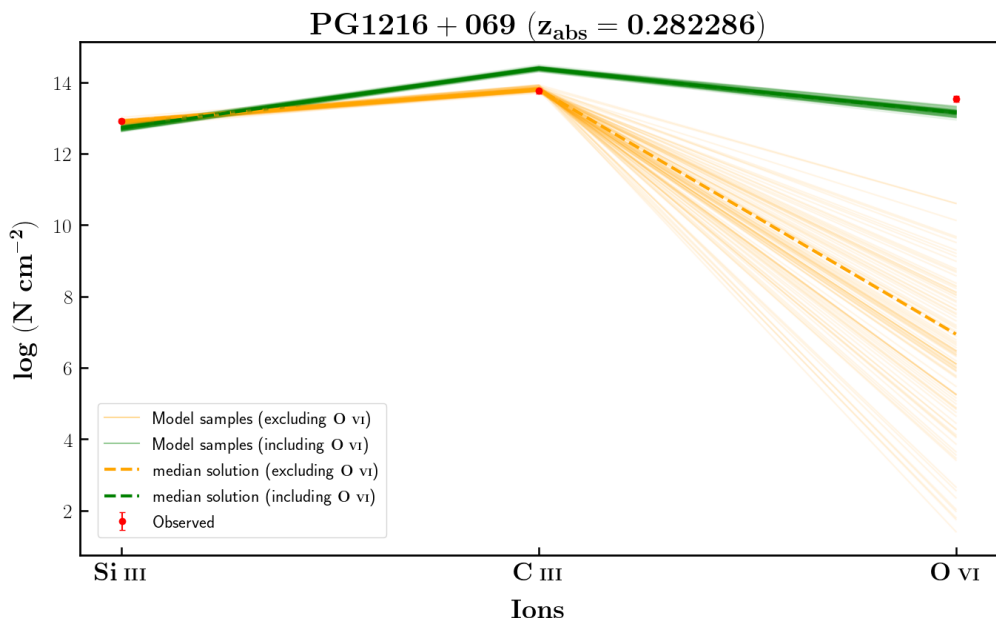
Ion	v (km s⁻¹)	b (km s⁻¹)	log [N cm⁻²]
Si III	0 ± 1	14 ± 3	12.92 ± 0.05
C III	-51 ± 3	32 ± 5	13.33 ± 0.05
C III	5 ± 1	16 ± 2	13.76 ± 0.07
O VI	-64 ± 6	58 ± 9	13.93 ± 0.05
O VI	19 ± 2	12 ± 5	13.54 ± 0.09
H I	-31 ± 1	52 ± 3	15.1 ± 0.05
H I	7 ± 1	22 ± 1	16.4 ± 0.03
H I	169 ± 22	53 ± 10	13.15 ± 0.18

$$\log N(H I) [\text{cm}^{-2}] = 15.10$$

Excluding O VI : $\log n_H (\text{cm}^{-3}) = -2.13 \pm 0.15$	$\log Z/Z_\odot = 0.65 \pm 0.22$
Including O VI : $\log n_H (\text{cm}^{-3}) = -3.86 \pm 0.02$	$\log Z/Z_\odot = -0.37 \pm 0.03$

$$\log N(H I) [\text{cm}^{-2}] = 16.40$$

Excluding O VI : $\log n_H (\text{cm}^{-3}) = -2.08 \pm 0.43$	$\log Z/Z_\odot = -0.37 \pm 0.59$
Including O VI : $\log n_H (\text{cm}^{-3}) = -3.68 \pm 0.02$	$\log Z/Z_\odot = -1.55 \pm 0.04$

FIGURE C.15: $\log \text{N(HI)} [\text{cm}^{-2}] = 15.10$ FIGURE C.16: $\log \text{N(HI)} [\text{cm}^{-2}] = 16.40$

SDSSJ135712.61 + 170444 ($z_{\text{abs}} = 0.097869$)

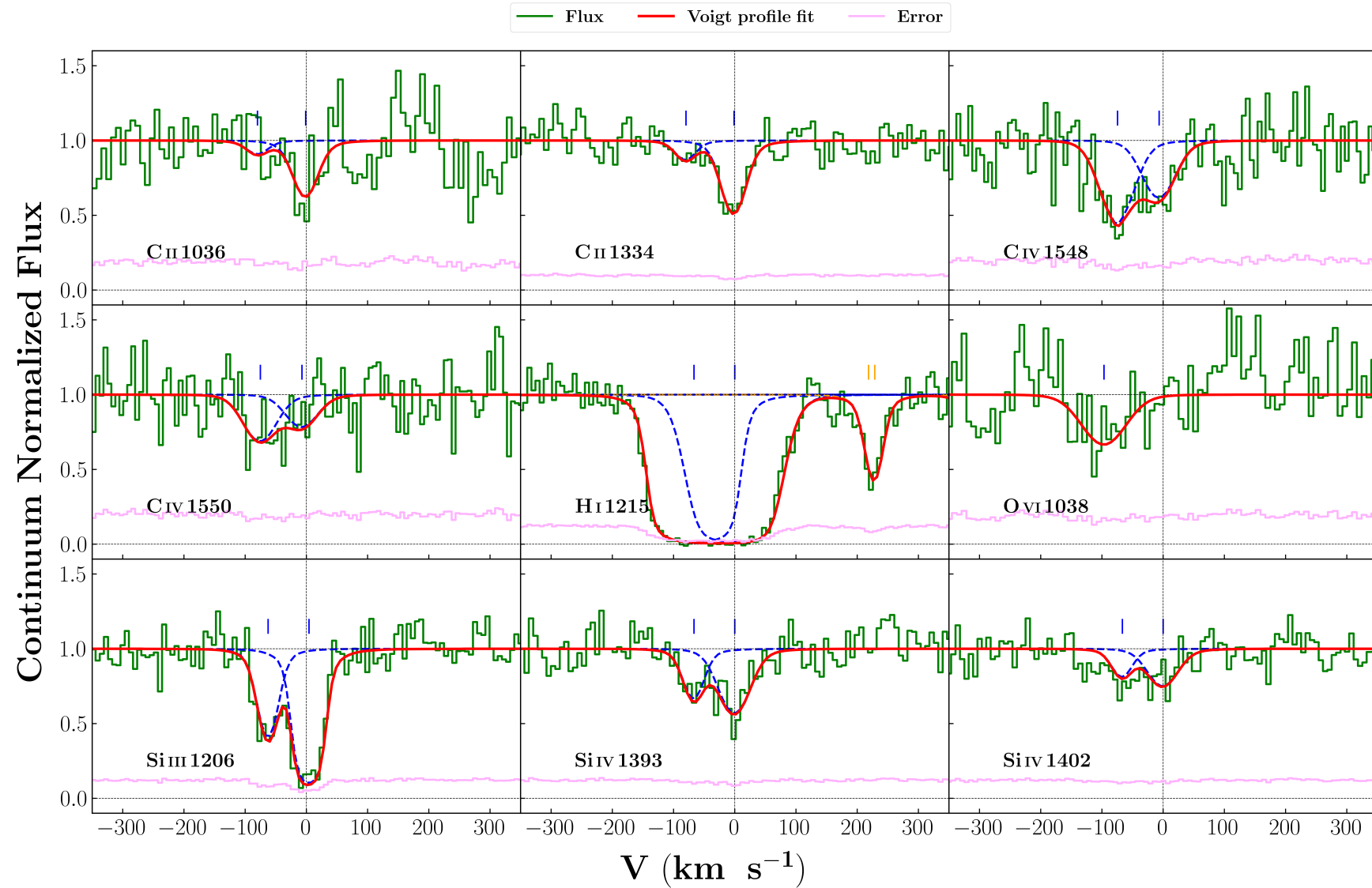


FIGURE C.17: System plot for the absorber along the LOS of SDSS J135712.61+170444 at $z_{\text{abs}} = 0.097869$.

Ion	v (km s ⁻¹)	b (km s ⁻¹)	log [N cm ⁻²]
Si III	-62 ± 2	17 ± 3	12.94 ± 0.05
Si III	4 ± 1	13 ± 10	14.67 ± 2.87
C IV	-74 ± 6	33 ± 1	13.82 ± 0.09
C IV	-7 ± 8	32 ± 12	13.63 ± 0.12
Si IV	-66 ± 4	18 ± 6	13.02 ± 0.08
Si IV	0 ± 4	29 ± 5	13.3 ± 0.05
C II	-79 ± 8	19 ± 14	13.17 ± 0.16
C II	-1 ± 2	22 ± 3	13.92 ± 0.04
O VI	-96 ± 10	43 ± 16	14.3 ± 0.11
H I	-536 ± 3	29 ± 5	13.36 ± 0.05
H I	-66 ± 0	29 ± 8	16.49 ± 0.12
H I	0 ± 0	46 ± 4	15.01 ± 0.16
H I	424 ± 3	34 ± 4	13.52 ± 0.04

$$\log N(\text{H I}) [\text{cm}^{-2}] = 16.49$$

Excluding O VI : $\log n_H (\text{cm}^{-3}) = -3.76 \pm 0.05$

Including O VI : $\log n_H (\text{cm}^{-3}) = -4.06 \pm 0.02$

$$\log Z/Z_{\odot} = -1.49 \pm 0.04$$

$$\log Z/Z_{\odot} = -1.32 \pm 0.04$$

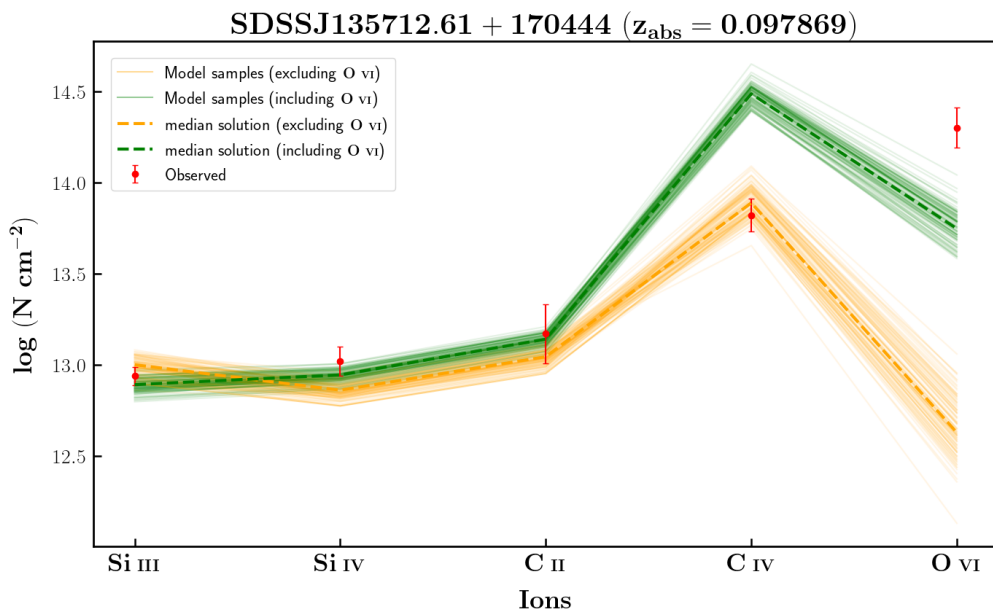


FIGURE C.18: $\log N(\text{H I}) [\text{cm}^{-2}] = 16.49$

1ES1553 + 113 ($z_{\text{abs}} = 0.187764$)

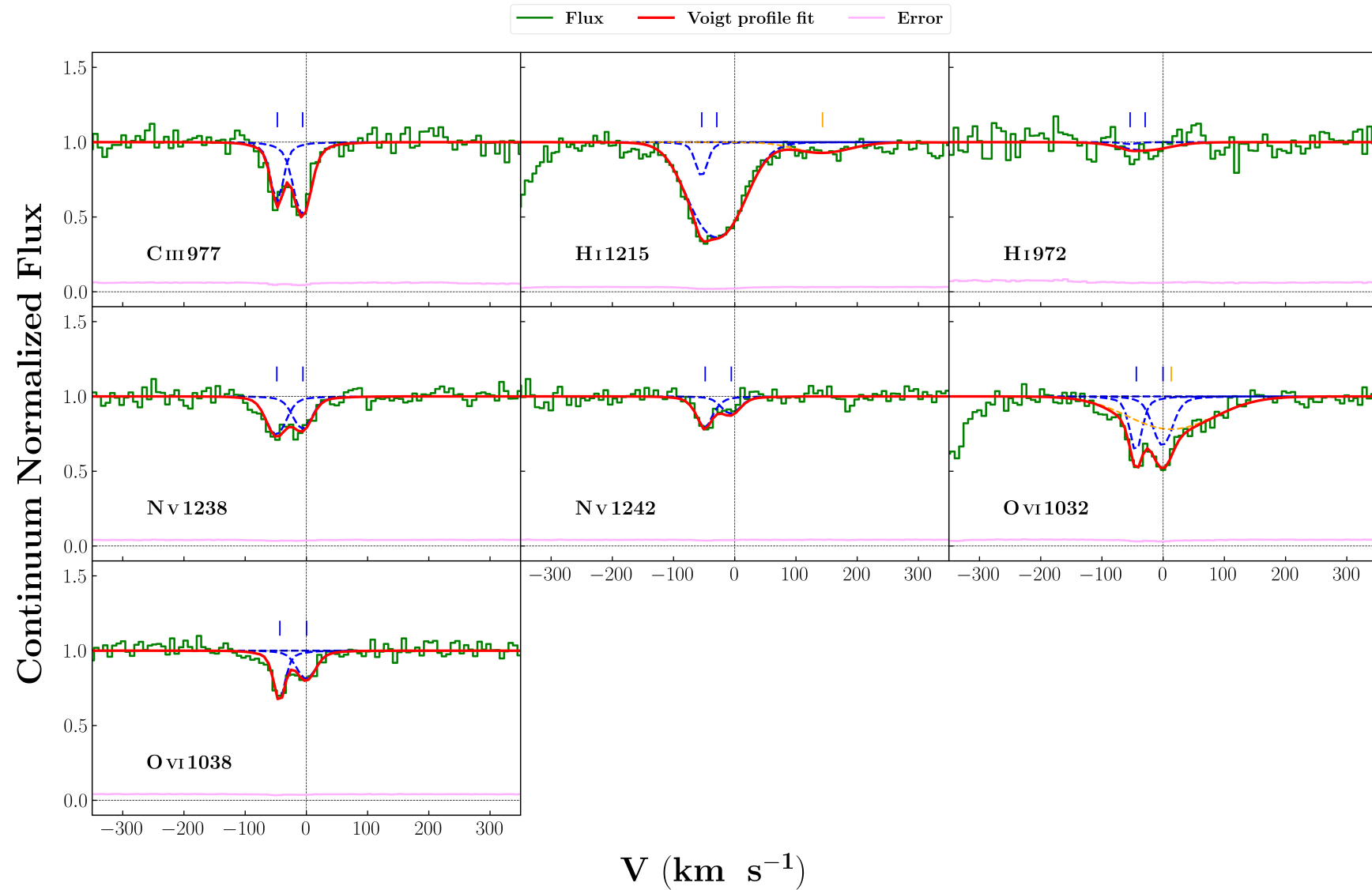


FIGURE C.19: System plot for the absorber along the LOS of 1ES 1553+113 at $z_{\text{abs}} = 0.187764$.

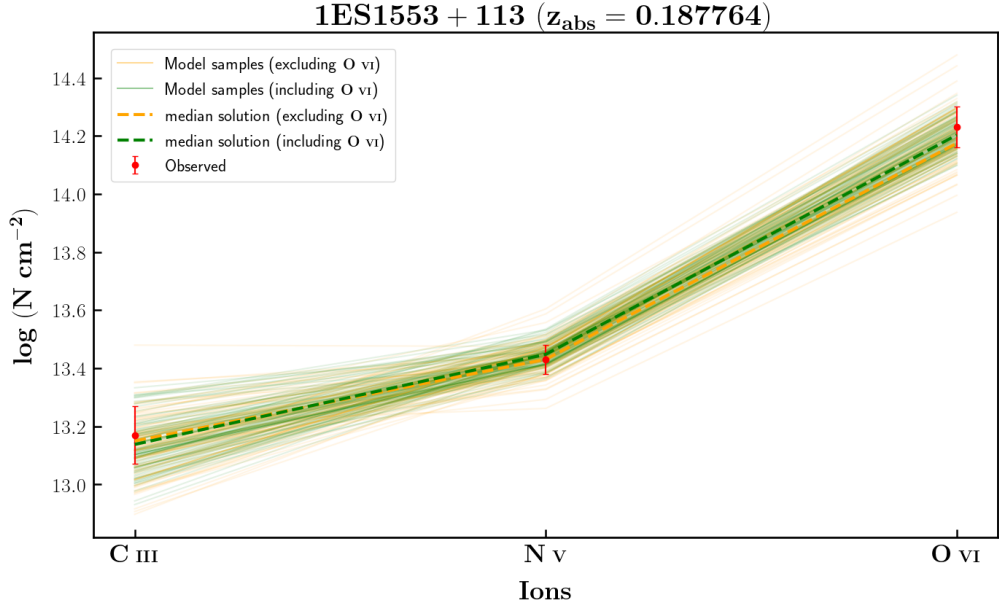
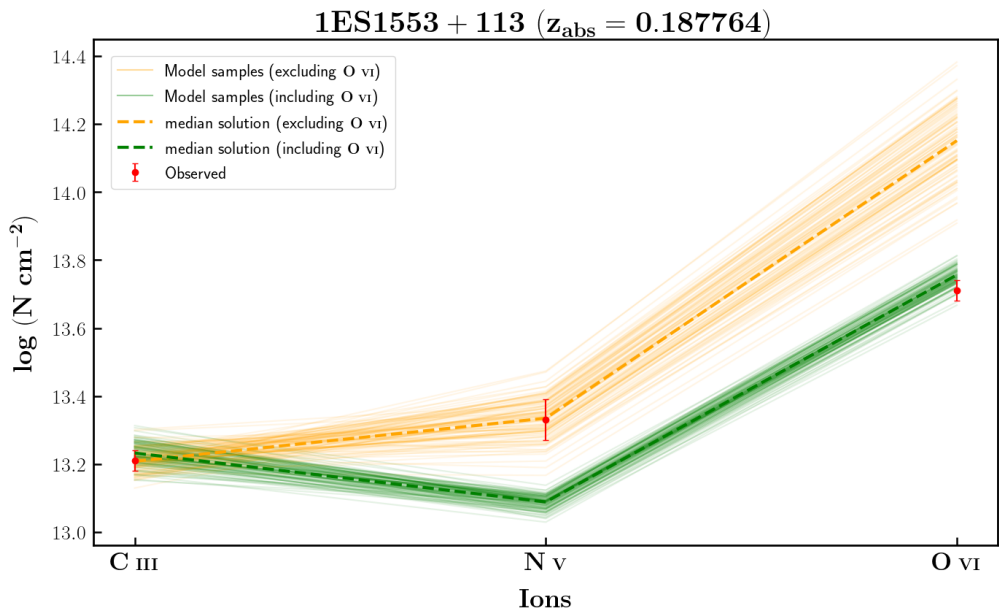
Ion	v (km s⁻¹)	b (km s⁻¹)	log [N cm⁻²]
C III	-46 ± 1	5 ± 4	13.17 ± 0.46
C III	-6 ± 1	13 ± 2	13.21 ± 0.03
N V	-47 ± 2	17 ± 0	13.43 ± 0.05
N V	-5 ± 2	16 ± 4	13.33 ± 0.06
O VI	-42 ± 1	3 ± 1	14.23 ± 0.33
O VI	0 ± 1	15 ± 3	13.71 ± 0.03
O VI	511 ± 3	28 ± 5	13.49 ± 0.05
H I	-52 ± 3	8 ± 6	12.76 ± 0.15
H I	-28 ± 1	51 ± 1	13.88 ± 0.01
H I	425 ± 3	25 ± 5	13.02 ± 0.07
H I	496 ± 2	37 ± 3	13.46 ± 0.03

$$\log N(H I) [\text{cm}^{-2}] = 12.76$$

Excluding O VI : $\log n_H (\text{cm}^{-3}) = -4.62 \pm 0.04$	$\log Z/Z_{\odot} = 1.37 \pm 0.06$
Including O VI : $\log n_H (\text{cm}^{-3}) = -4.63 \pm 0.03$	$\log Z/Z_{\odot} = 1.37 \pm 0.06$

$$\log N(H I) [\text{cm}^{-2}] = 13.88$$

Excluding O VI : $\log n_H (\text{cm}^{-3}) = -4.6 \pm 0.04$	$\log Z/Z_{\odot} = 0.03 \pm 0.03$
Including O VI : $\log n_H (\text{cm}^{-3}) = -4.44 \pm 0.02$	$\log Z/Z_{\odot} = -0.06 \pm 0.02$

FIGURE C.20: $\log \text{N(HI)} [\text{cm}^{-2}] = 12.76$ FIGURE C.21: $\log \text{N(HI)} [\text{cm}^{-2}] = 13.88$

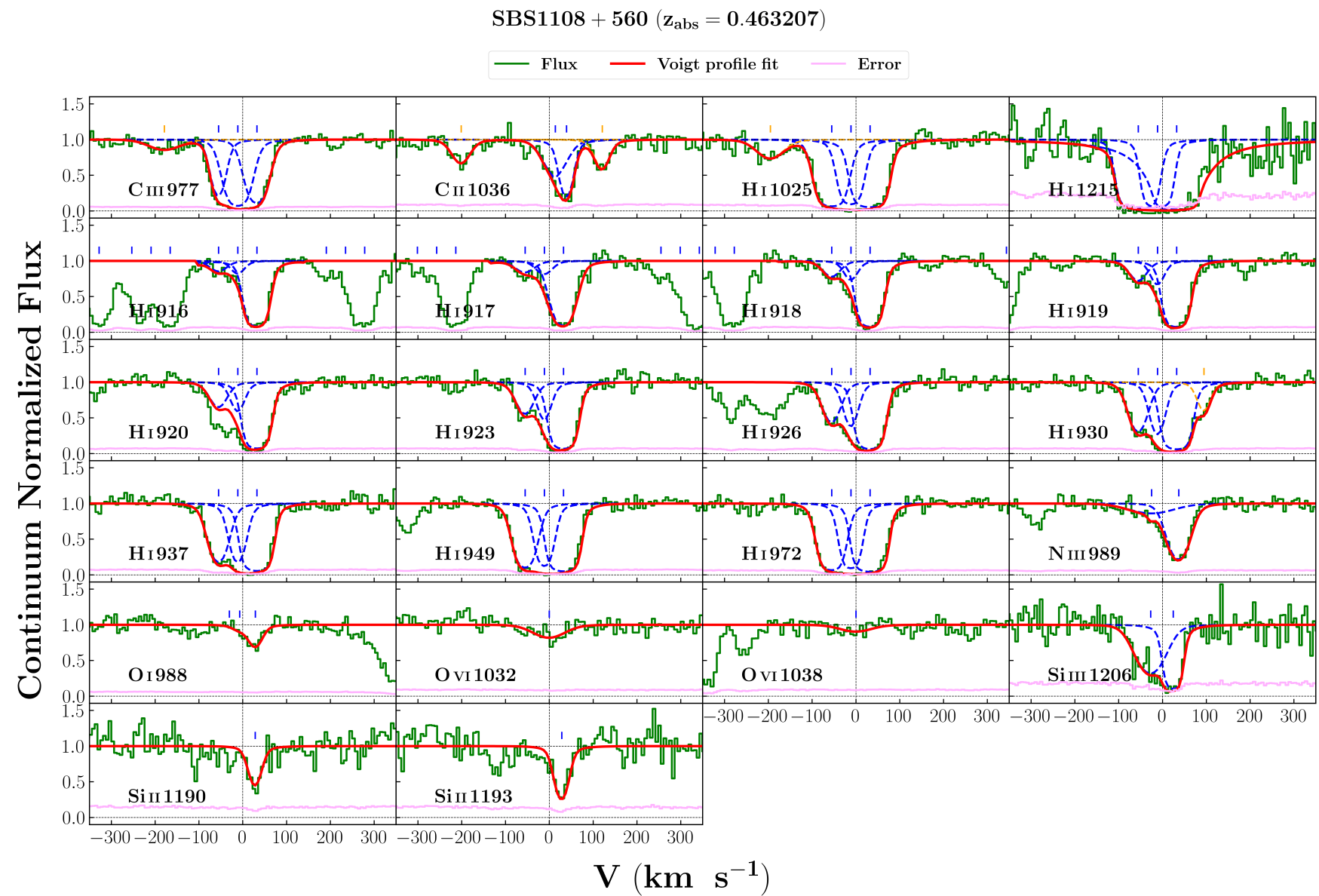


FIGURE C.22: System plot for the absorber along the LOS of SBS 1108+560 at $z_{\text{abs}} = 0.463207$.

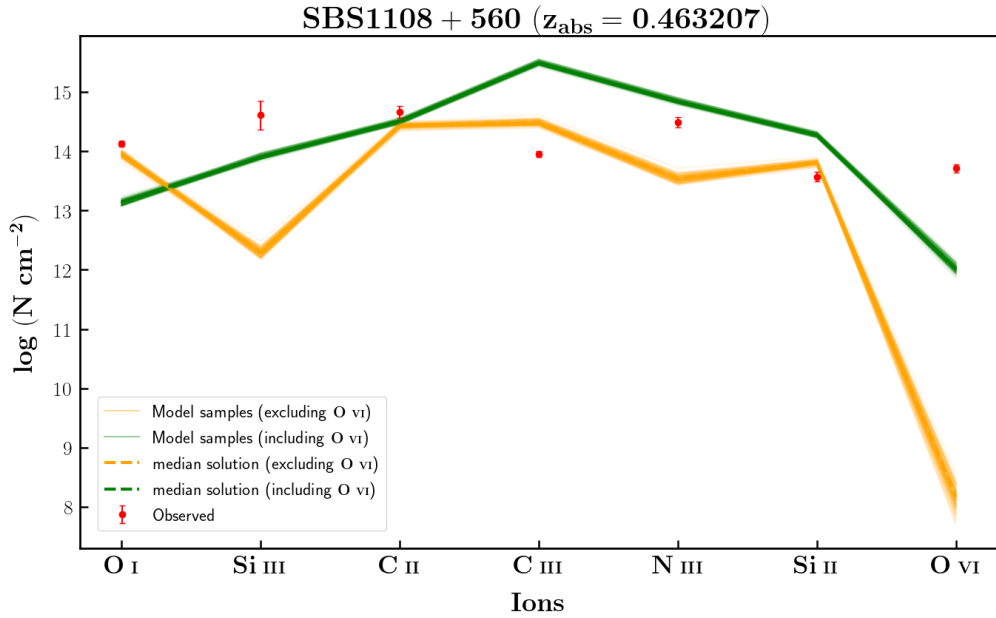
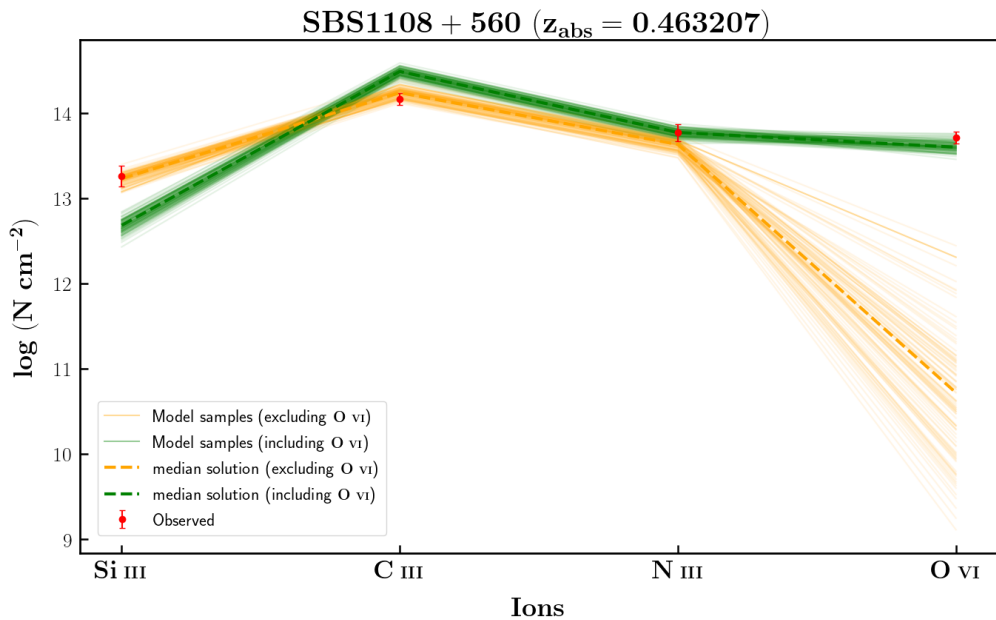
Ion	v (km s⁻¹)	b (km s⁻¹)	log [N cm⁻²]
O I	25 ± 2	18 ± 4	14.13 ± 0.05
Si III	-23 ± 9	39 ± 12	13.26 ± 0.12
Si III	21 ± 2	13 ± 15	14.61 ± 0.24
C II	12 ± 9	31 ± 4	14.15 ± 0.05
C II	34 ± 2	12 ± 5	14.67 ± 0.1
C III	-48 ± 3	15 ± 1	13.66 ± 0.08
C III	-10 ± 3	26 ± 7	14.16 ± 0.07
C III	28 ± 3	24 ± 1	13.95 ± 0.05
N III	-22 ± 59	67 ± 61	13.77 ± 0.1
N III	32 ± 2	26 ± 4	14.49 ± 0.09
Si II	25 ± 1	15 ± 1	13.57 ± 0.08
O VI	0 ± 6	45 ± 10	13.71 ± 0.07
H I	-48 ± 0	22 ± 2	15.77 ± 0.02
H I	-10 ± 2	16 ± 0	15.79 ± 0.11
H I	28 ± 1	16 ± 1	18.1 ± 0.12

$$\log N(H I) [\text{cm}^{-2}] = 18.10$$

Excluding O VI : $\log n_H (\text{cm}^{-3}) = -2.55 \pm 0.03$	log $Z/Z_{\odot} = -0.83 \pm 0.04$
Including O VI : $\log n_H (\text{cm}^{-3}) = -3.49 \pm 0.01$	log $Z/Z_{\odot} = -0.92 \pm 0.03$

$$\log N(H I) [\text{cm}^{-2}] = 15.79$$

Excluding O VI : $\log n_H (\text{cm}^{-3}) = -2.65 \pm 0.22$	log $Z/Z_{\odot} = 1.60 \pm 0.22$
Including O VI : $\log n_H (\text{cm}^{-3}) = -3.56 \pm 0.03$	log $Z/Z_{\odot} = 1.16 \pm 0.05$

FIGURE C.23: $\log N(\text{H I})$ [cm $^{-2}$] = 18.10FIGURE C.24: $\log N(\text{H I})$ [cm $^{-2}$] = 15.79

PG1222 + 216 ($z_{\text{abs}} = 0.378389$)

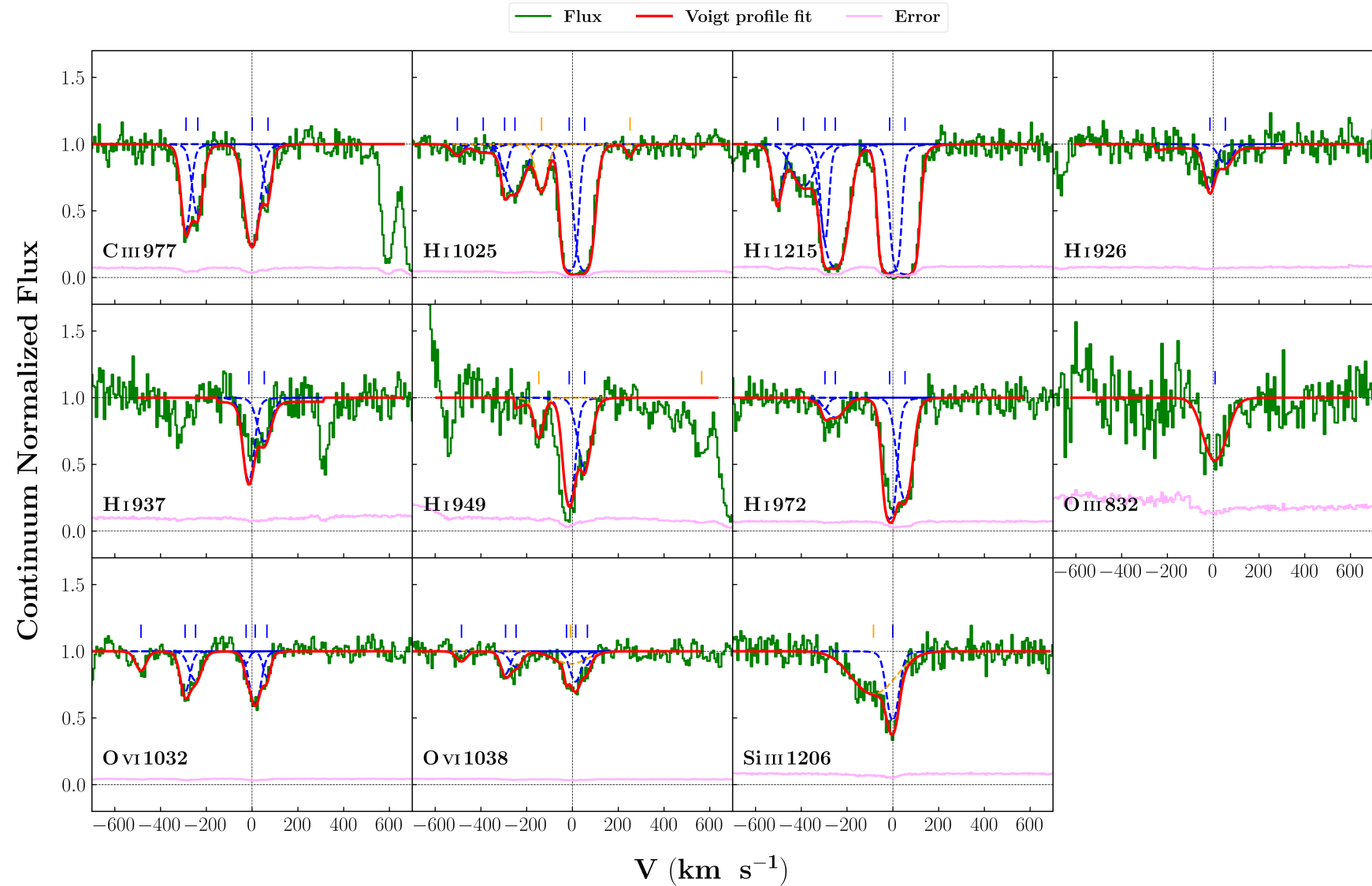


FIGURE C.25: System plot for the absorber along the LOS of PG 1222+216 at $z_{\text{abs}} = 0.378389$.

Ion	v (km s⁻¹)	b (km s⁻¹)	log [N cm⁻²]
O III	7 ± 5	61 ± 8	14.51 ± 0.04
Si III	0 ± 2	30 ± 3	12.98 ± 0.03
C III	-261 ± 3	17 ± 5	13.54 ± 0.06
C III	-215 ± 5	22 ± 6	13.40 ± 0.08
C III	0 ± 2	32 ± 3	13.79 ± 0.02
C III	63 ± 3	13 ± 6	13.12 ± 0.07
O VI	-439 ± 3	28 ± 5	13.42 ± 0.06
O VI	-264 ± 6	24 ± 6	13.75 ± 0.2
O VI	-223 ± 14	34 ± 13	13.68 ± 0.24
O VI	-24 ± 12	14 ± 18	13.00 ± 0.11
O VI	13 ± 4	29 ± 13	13.95 ± 0.16
O VI	59 ± 6	18 ± 7	13.42 ± 0.23
H I	-455 ± 3	26 ± 4	13.40 ± 0.06
H I	-353 ± 9	64 ± 19	13.54 ± 0.11
H I	-268 ± 1	16 ± 6	13.70 ± 0.14
H I	-227 ± 5	52 ± 4	14.34 ± 0.05
H I	-27 ± 2	23 ± 1	14.73 ± 0.08
H I	31 ± 2	43 ± 1	15.43 ± 0.04

$$\log N(H I) [\text{cm}^{-2}] = 15.43$$

Excluding O VI : $\log n_H (\text{cm}^{-3}) = -2.66 \pm 0.05$	$\log Z/Z_{\odot} = -0.25 \pm 0.06$
Including O VI : $\log n_H (\text{cm}^{-3}) = -3.16 \pm 0.03$	$\log Z/Z_{\odot} = -0.66 \pm 0.02$

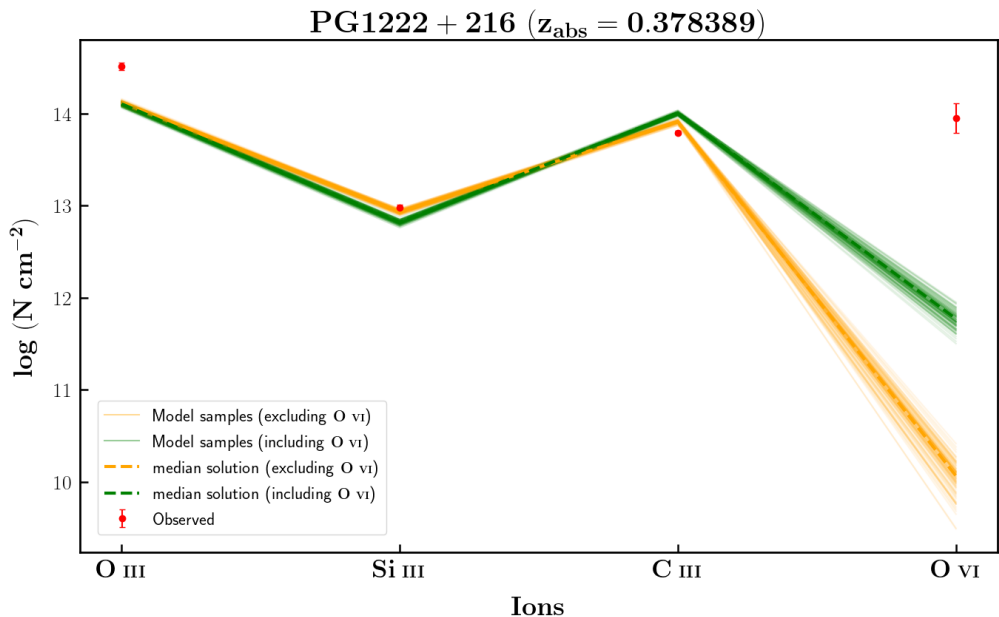


FIGURE C.26: $\log N(\text{H I}) [\text{cm}^{-2}] = 15.43$

PG1116 + 215 ($z_{\text{abs}} = 0.138527$)

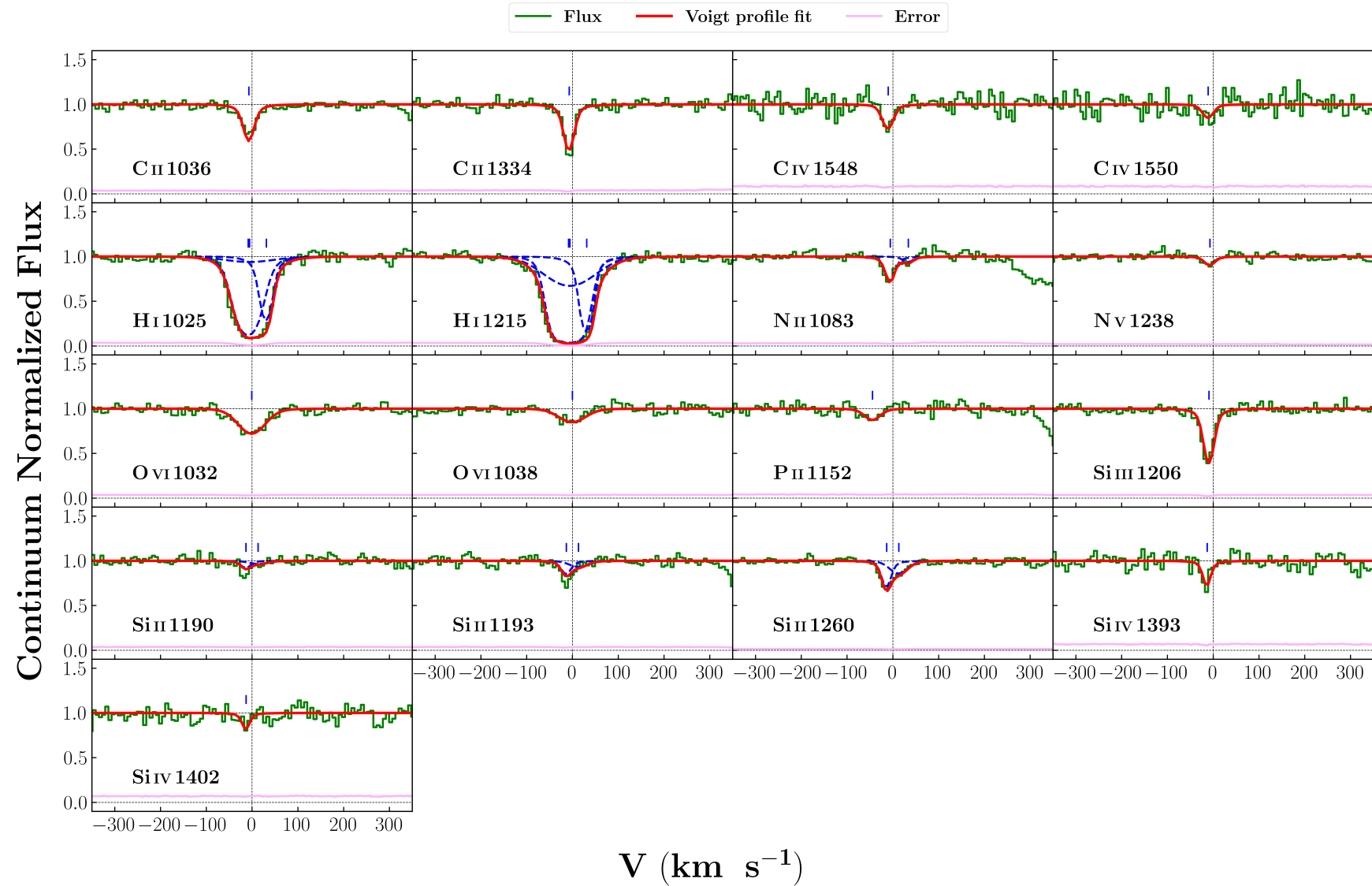


FIGURE C.27: System plot for the absorber along the LOS of PG 1116+215 at $z_{\text{abs}} = 0.138527$.

Ion	v (km s ⁻¹)	b (km s ⁻¹)	log [N cm ⁻²]
N V	-7 ± 3	12 ± 6	12.84 ± 0.09
N II	-5 ± 1	6 ± 3	13.62 ± 0.11
N II	33 ± 6	8 ± 13	12.85 ± 0.15
P II	-44 ± 5	19 ± 8	12.94 ± 0.09
Si II	-13 ± 1	9 ± 1	12.46 ± 0.06
Si II	13 ± 1	23 ± 3	12.31 ± 0.04
Si III	-9 ± 1	10 ± 1	12.92 ± 0.04
Si IV	-13 ± 2	4 ± 3	12.84 ± 0.09
O VI	-1 ± 1	35 ± 3	13.84 ± 0.02
C IV	-10 ± 3	13 ± 4	13.17 ± 0.07
C II	-7 ± 1	9 ± 1	13.85 ± 0.04
H I	-8 ± 3	27 ± 2	14.97 ± 0.05
H I	-5 ± 9	71 ± 14	13.6 ± 0.23
H I	31 ± 2	6 ± 2	16.04 ± 1.77

$$\log N(\text{H I}) [\text{cm}^{-2}] = 13.60$$

Excluding O VI : $\log n_H (\text{cm}^{-3}) = -3.24 \pm 0.03$	$\log Z/Z_{\odot} = 1.92 \pm 0.03$
Including O VI : $\log n_H (\text{cm}^{-3}) = -3.88 \pm 0.01$	$\log Z/Z_{\odot} = 1.87 \pm 0.02$

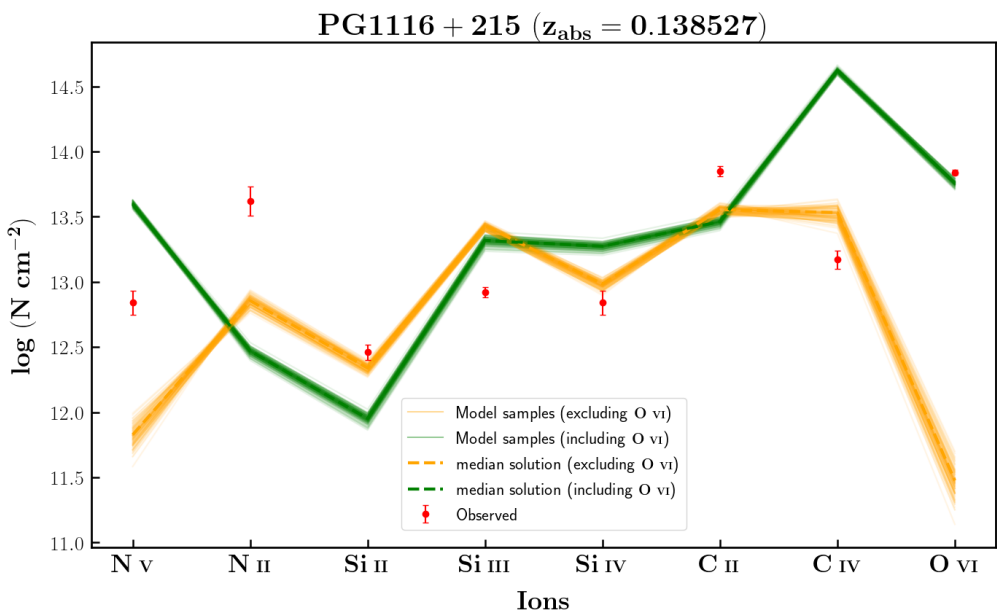


FIGURE C.28: $\log N(\text{H I}) [\text{cm}^{-2}] = 13.60$

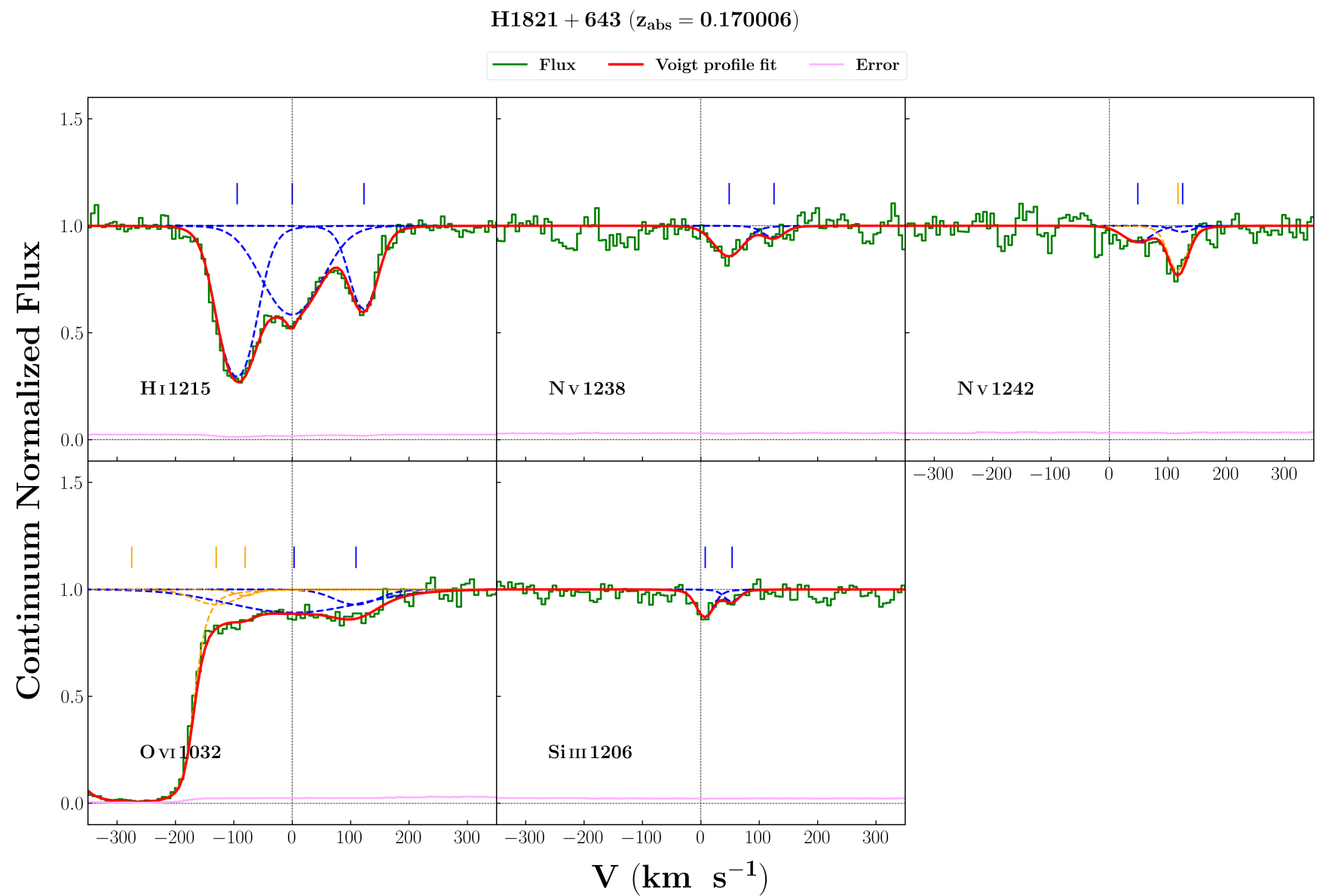


FIGURE C.29: System plot for the absorber along the LOS of H 1821+643 at $z_{abs} = 0.170006$.

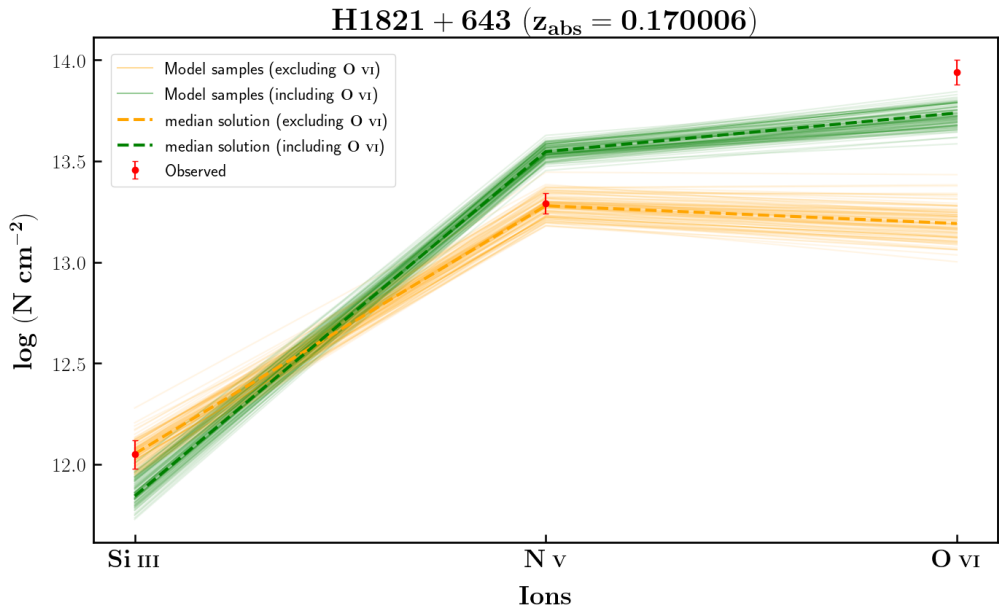
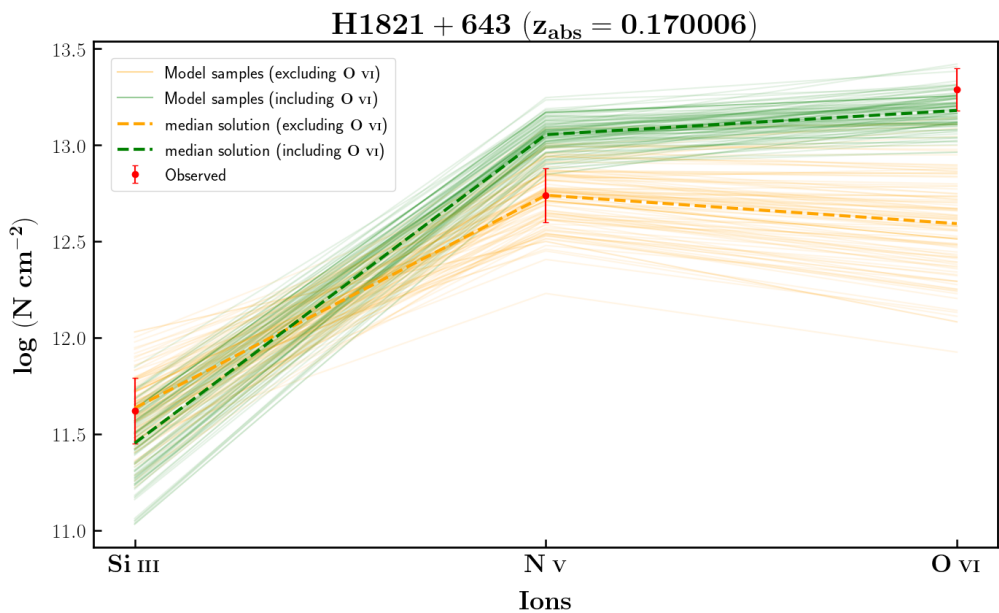
Ion	v (km s⁻¹)	b (km s⁻¹)	log [N cm⁻²]
Si III	7 ± 3	17 ± 5	12.05 ± 0.07
Si III	52 ± 6	14 ± 10	11.62 ± 0.17
N V	47 ± 3	31 ± 5	13.29 ± 0.05
N V	122 ± 7	21 ± 11	12.74 ± 0.14
O VI	3 ± 28	152 ± 20	13.94 ± 0.06
O VI	107 ± 9	48 ± 12	13.29 ± 0.11
H I	-92 ± 1	36 ± 1	13.85 ± 0.02
H I	0 ± 2	63 ± 3	13.68 ± 0.02
H I	120 ± 1	28 ± 1	13.35 ± 0.02

$$\log N(H I) [\text{cm}^{-2}] = 13.68$$

Excluding O VI : $\log n_H (\text{cm}^{-3}) = -4.33 \pm 0.02$	$\log Z/Z_\odot = 1.30 \pm 0.05$
Including O VI : $\log n_H (\text{cm}^{-3}) = -4.43 \pm 0.01$	$\log Z/Z_\odot = 1.25 \pm 0.05$

$$\log N(H I) [\text{cm}^{-2}] = 13.35$$

Excluding O VI : $\log n_H (\text{cm}^{-3}) = -4.30 \pm 0.05$	$\log Z/Z_\odot = 1.18 \pm 0.13$
Including O VI : $\log n_H (\text{cm}^{-3}) = -4.41 \pm 0.02$	$\log Z/Z_\odot = 1.15 \pm 0.12$

FIGURE C.30: $\log \text{N(HI)} [\text{cm}^{-2}] = 13.68$ FIGURE C.31: $\log \text{N(HI)} [\text{cm}^{-2}] = 13.35$

H1821 + 643 ($z_{abs} = 0.224981$)

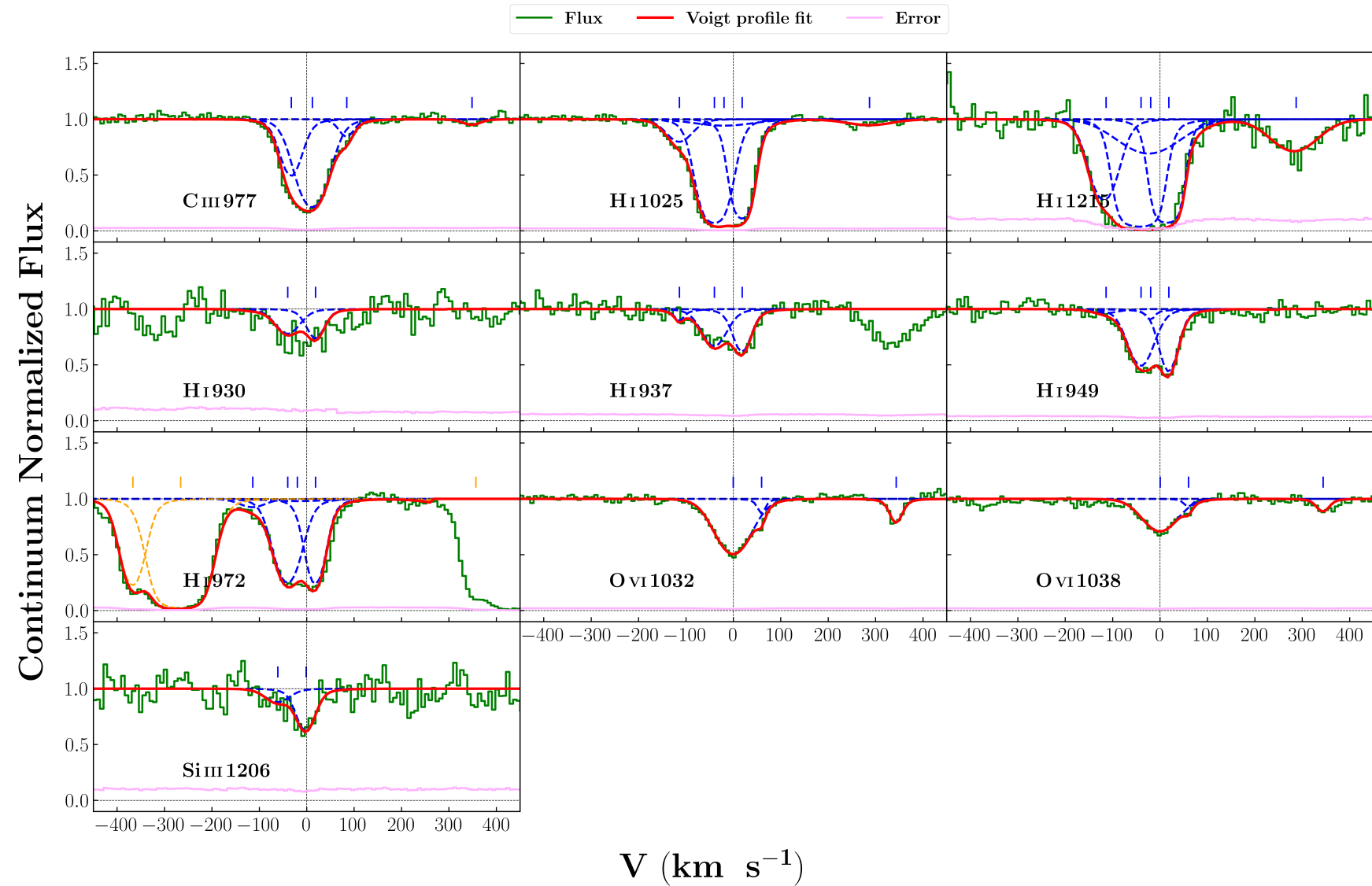


FIGURE C.32: System plot for the absorber along the LOS of H 1821+643 at $z_{abs} = 0.224981$.

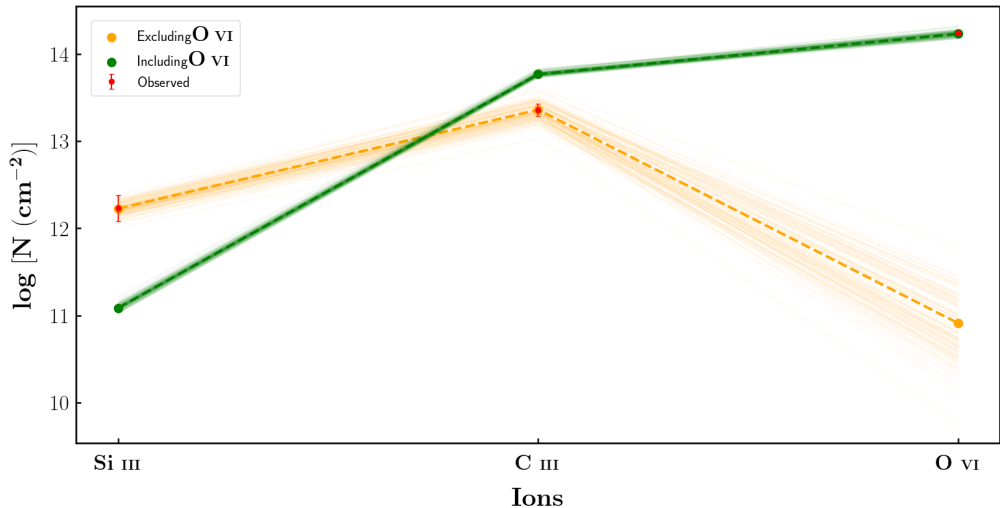
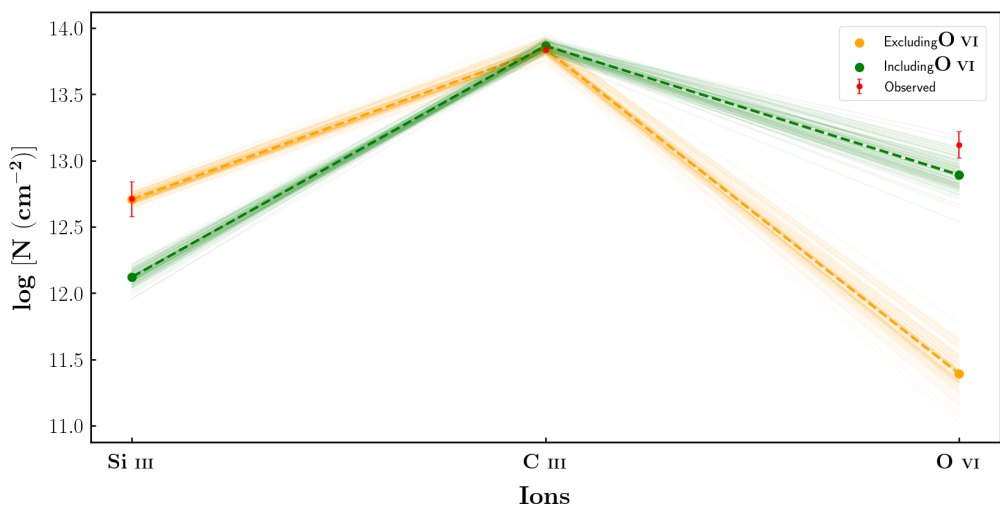
Ion	v (km s⁻¹)	b (km s⁻¹)	log [N cm⁻²]
Si III	-59 ± 13	31 ± 18	12.23 ± 0.15
Si III	-1 ± 6	22 ± 9	12.71 ± 0.13
C III	-31 ± 1	24 ± 2	13.36 ± 0.07
C III	12 ± 1	36 ± 2	13.84 ± 0.02
C III	81 ± 3	15 ± 5	12.6 ± 0.09
C III	335 ± 7	20 ± 10	12.13 ± 0.11
O VI	0 ± 1	45 ± 1	14.24 ± 0.01
O VI	57 ± 2	3 ± 3	13.12 ± 0.1
O VI	330 ± 1	13 ± 2	13.42 ± 0.03
H I	-109 ± 3	33 ± 0	13.87 ± 0.09
H I	-38 ± 1	30 ± 1	15.16 ± 0.02
H I	-19 ± 10	84 ± 13	13.64 ± 0.11
H I	18 ± 1	19 ± 1	15.13 ± 0.03
H I	276 ± 7	62 ± 11	13.48 ± 0.06

$$\log N(H I) [\text{cm}^{-2}] = 15.16$$

Excluding O VI : $\log n_H (\text{cm}^{-3}) = -3.29 \pm 0.08$	$\log Z/Z_{\odot} = -0.95 \pm 0.07$
Including O VI : $\log n_H (\text{cm}^{-3}) = -4.36 \pm 0.02$	$\log Z/Z_{\odot} = -0.81 \pm 0.04$

$$\log N(H I) [\text{cm}^{-2}] = 15.13$$

Excluding O VI : $\log n_H (\text{cm}^{-3}) = -3.29 \pm 0.03$	$\log Z/Z_{\odot} = -0.44 \pm 0.03$
Including O VI : $\log n_H (\text{cm}^{-3}) = -3.83 \pm 0.04$	$\log Z/Z_{\odot} = -0.77 \pm 0.03$

FIGURE C.33: $\log N(\text{H I}) [\text{cm}^{-2}] = 15.16$ FIGURE C.34: $\log N(\text{H I}) [\text{cm}^{-2}] = 15.13$

PG1121 + 422 ($z_{\text{abs}} = 0.192393$)

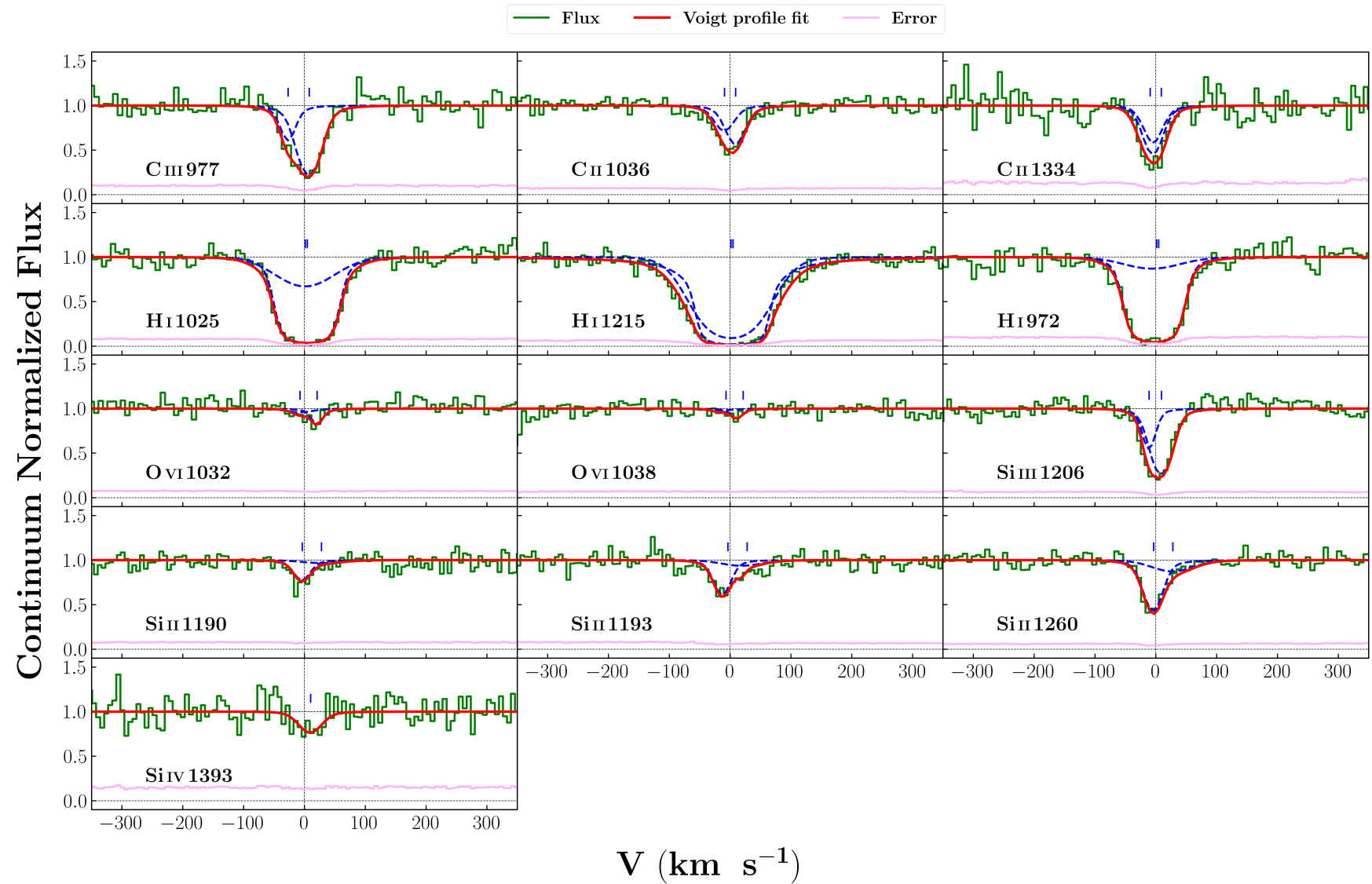


FIGURE C.35: System plot for the absorber along the LOS of PG 1121+422 at $z_{\text{abs}} = 0.192393$.

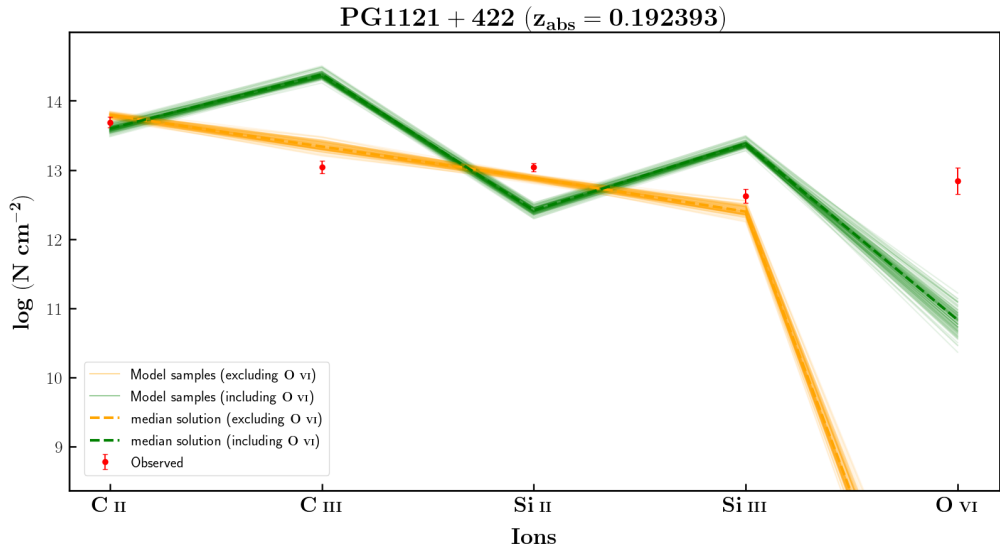
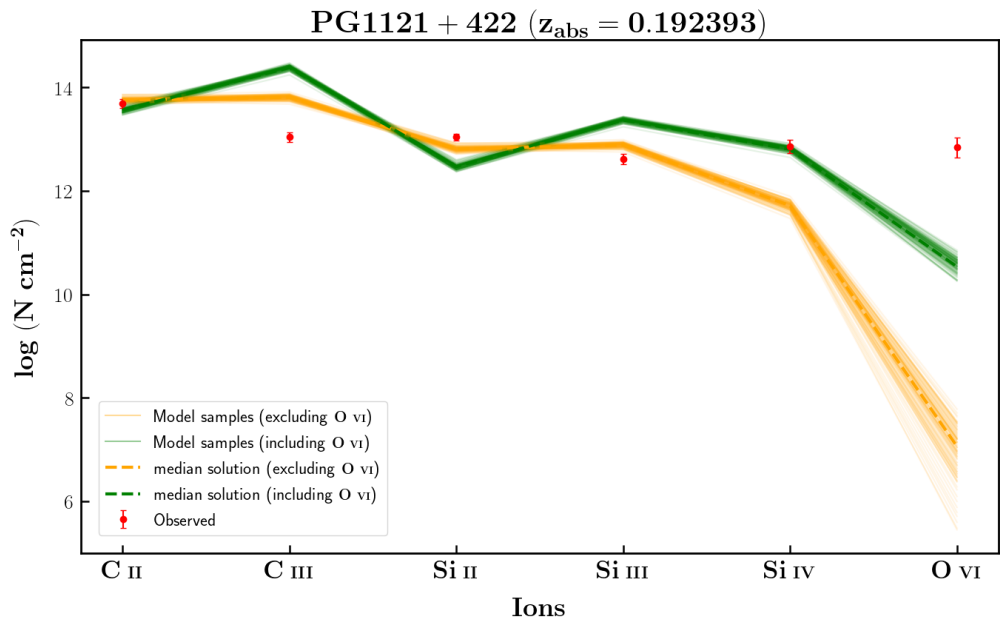
Ion	v (km s⁻¹)	b (km s⁻¹)	log [N cm⁻²]
Si III	-11 ± 13	10 ± 3	12.62 ± 0.10
Si III	9 ± 13	18 ± 4	13.14 ± 0.04
C III	-26 ± 10	10 ± 7	13.04 ± 0.09
C III	8 ± 5	18 ± 6	13.74 ± 0.11
C II	-9 ± 3	17 ± 5	13.69 ± 0.08
C II	9 ± 2	16 ± 3	13.93 ± 0.05
Si IV	10 ± 7	22 ± 11	12.86 ± 0.13
Si II	-3 ± 1	15 ± 2	13.04 ± 0.06
Si II	27 ± 19	42 ± 1	12.48 ± 0.23
O VI	-7 ± 13	11 ± 16	12.84 ± 0.19
O VI	20 ± 3	3 ± 4	13.37 ± 0.12
H I	1 ± 2	60 ± 6	14.34 ± 0.09
H I	5 ± 1	19 ± 1	17.7 ± 0.11

$$\log N(H I) [\text{cm}^{-2}] = 14.34$$

Excluding O VI : $\log n_H (\text{cm}^{-3}) = -1.78 \pm 0.05$	$\log Z/Z_{\odot} = 1.97 \pm 0.04$
Including O VI : $\log n_H (\text{cm}^{-3}) = -3.00 \pm 0.04$	$\log Z/Z_{\odot} = 1.25 \pm 0.04$

$$\log N(H I) [\text{cm}^{-2}] = 17.70$$

Excluding O VI : $\log n_H (\text{cm}^{-3}) = -2.35 \pm 0.05$	$\log Z/Z_{\odot} = -1.66 \pm 0.06$
Including O VI : $\log n_H (\text{cm}^{-3}) = -3.08 \pm 0.04$	$\log Z/Z_{\odot} = -2.08 \pm 0.05$

FIGURE C.36: $\log N(\text{H I}) [\text{cm}^{-2}] = 14.34$ FIGURE C.37: $\log N(\text{H I}) [\text{cm}^{-2}] = 17.70$

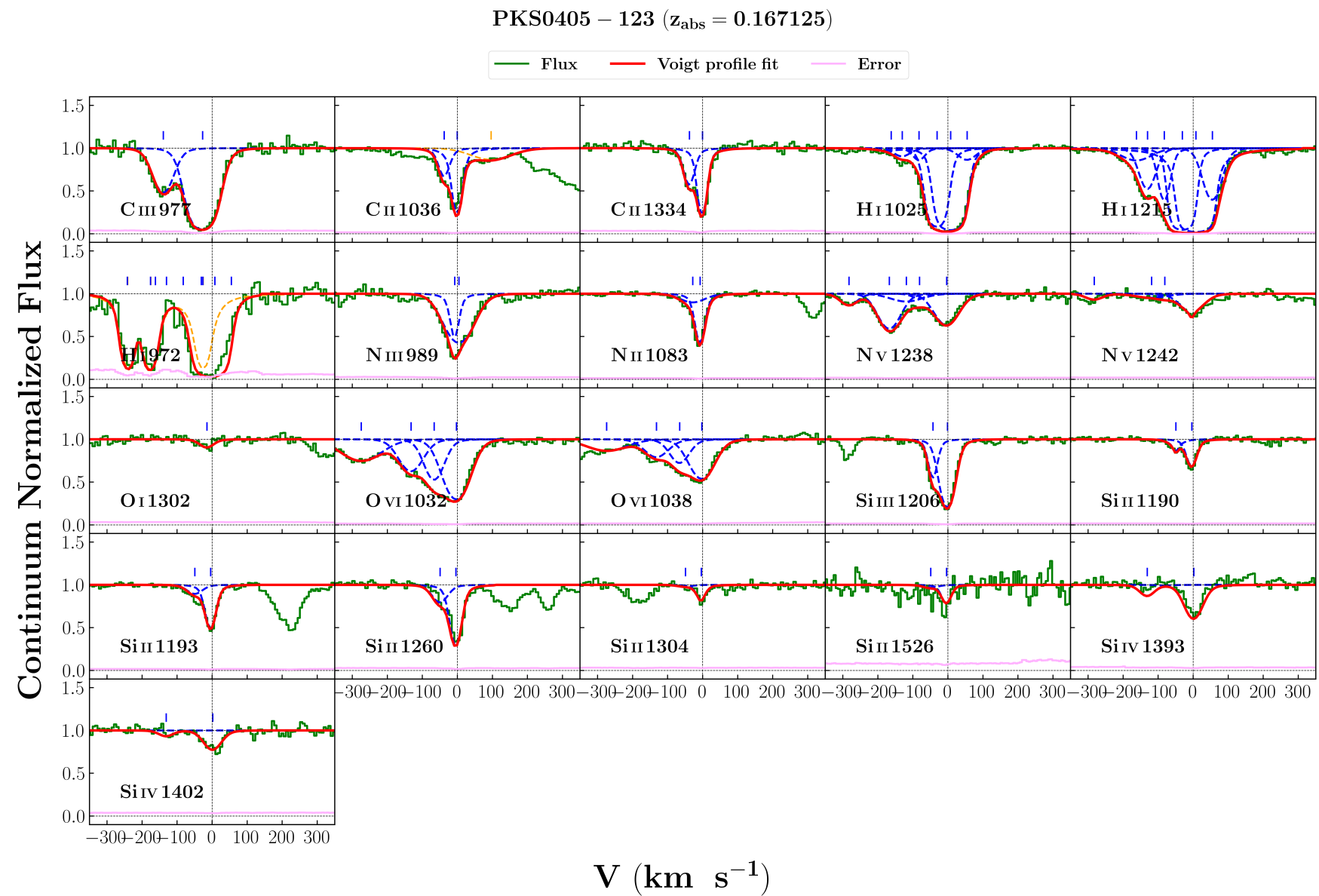


FIGURE C.38: System plot for the absorber along the LOS of PKS 0405-123 at $z_{\text{abs}} = 0.167125$.

Ion	v (km s⁻¹)	b (km s⁻¹)	log [N cm⁻²]
O I	-14 ± 5	23 ± 7	13.52 ± 0.08
C II	-37 ± 2	16 ± 2	13.76 ± 0.02
C II	-1 ± 1	6 ± 1	16.27 ± 0.12
C III	-136 ± 2	32 ± 2	13.45 ± 0.02
C III	-26 ± 0	37 ± 2	14.33 ± 0.04
N II	-27 ± 6	44 ± 5	13.47 ± 0.09
N II	-7 ± 1	12 ± 1	14.11 ± 0.02
N III	-7 ± 0	9 ± 4	14.06 ± 0.08
N III	5 ± 0	50 ± 2	14.43 ± 0.02
N V	-276 ± 3	30 ± 0	13.25 ± 0.05
N V	-116 ± 0	59 ± 9	13.32 ± 0.08
N V	-79 ± 13	24 ± 12	12.77 ± 0.19
N V	-3 ± 2	43 ± 3	13.89 ± 0.03
Si III	-41 ± 3	13 ± 4	12.66 ± 0.10
Si III	-1 ± 2	22 ± 2	13.28 ± 0.03
Si IV	-128 ± 0	25 ± 5	12.61 ± 0.06
Si IV	2 ± 1	31 ± 2	13.25 ± 0.02
Si II	-48 ± 5	26 ± 8	12.54 ± 0.09
Si II	-4 ± 1	15 ± 0	13.24 ± 0.02
O VI	-268 ± 0	74 ± 5	14.05 ± 0.02
O VI	-129 ± 8	41 ± 3	14.05 ± 0.10
O VI	-64 ± 5	32 ± 2	14.11 ± 0.17
O VI	-2 ± 4	43 ± 3	14.49 ± 0.05
H I	-158 ± 0	56 ± 9	13.09 ± 0.06
H I	-127 ± 4	26 ± 3	13.46 ± 0.04
H I	-80 ± 1	18 ± 2	13.54 ± 0.04
H I	-30 ± 0	18 ± 2	15.98 ± 0.34
H I	8 ± 49	19 ± 0	17.53 ± 0.07
H I	54 ± 90	30 ± 2	13.66 ± 0.04

$$\log N(\text{H I}) [\text{cm}^{-2}] = 13.46$$

Excluding O VI : $\log n_H (\text{cm}^{-3}) = -3.98 \pm 0.03$

$$\log Z/Z_{\odot} = 0.62 \pm 0.02$$

Including O VI : $\log n_H (\text{cm}^{-3}) = -4.17 \pm 0.02$

$$\log Z/Z_{\odot} = 0.63 \pm 0.02$$

$$\log N(\text{H I}) [\text{cm}^{-2}] = 15.98$$

Excluding O VI : $\log n_H (\text{cm}^{-3}) = -2.73 \pm 0.04$

$$\log Z/Z_{\odot} = -0.18 \pm 0.02$$

Including O VI : $\log n_H (\text{cm}^{-3}) = -3.27 \pm 0.03$

$$\log Z/Z_{\odot} = -0.33 \pm 0.02$$

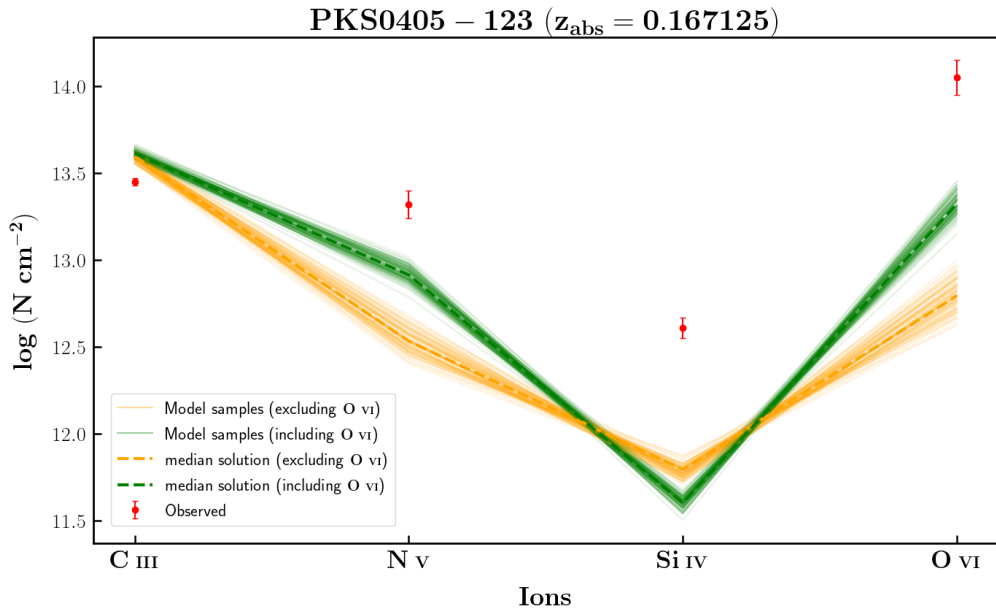


FIGURE C.39: $\log N(\text{H I}) [\text{cm}^{-2}] = 13.46$

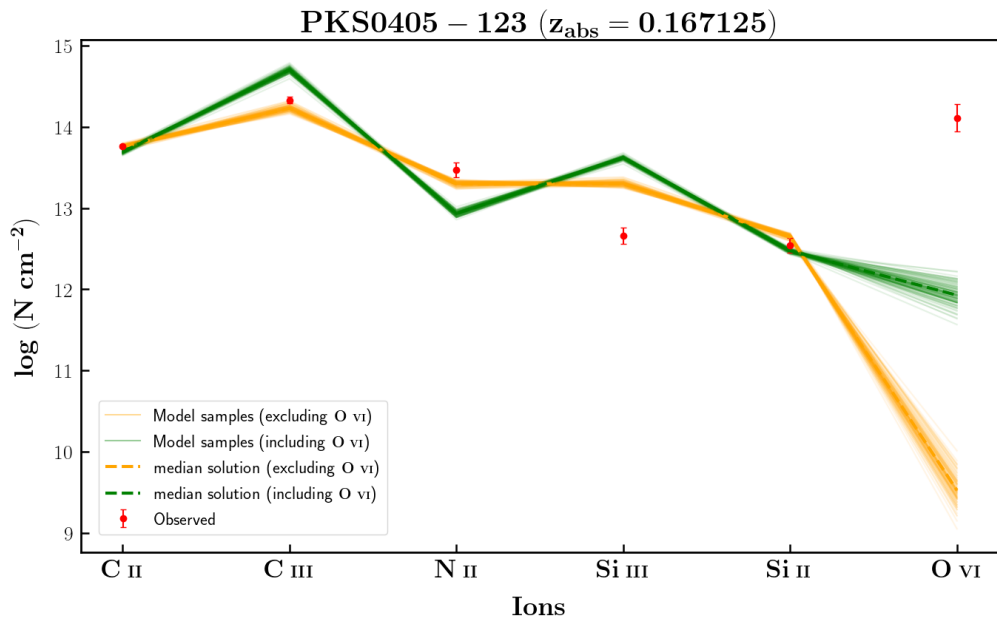


FIGURE C.40: $\log N(\text{H I}) [\text{cm}^{-2}] = 15.98$

HE0056 – 3622 ($z_{abs} = 0.043265$)

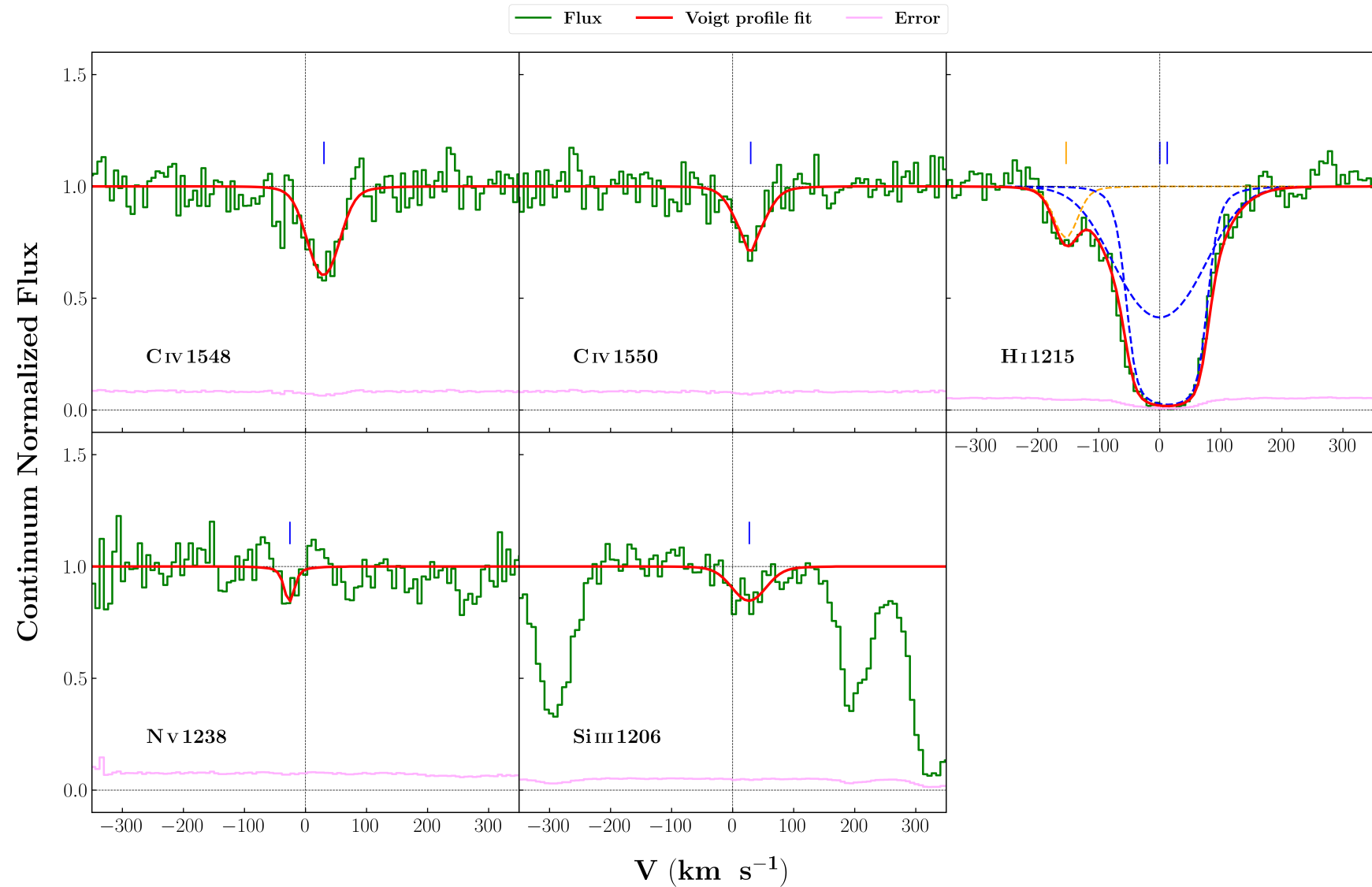


FIGURE C.41: System plot for the absorber along the LOS of HE 0056-3622 at $z_{abs} = 0.043265$.

Ion	v (km s ⁻¹)	b (km s ⁻¹)	log [N cm ⁻²]
Si III	27 ± 6	34 ± 9	12.37 ± 0.07
N V	-26 ± 4	1 ± 8	13.42 ± 0.46
C IV	30 ± 2	31 ± 0	13.64 ± 0.03
H I	0 ± 3	85 ± 6	14.02 ± 0.07
H I	12 ± 1	32 ± 4	15.3 ± 0.1

$$\log N(\text{H I}) [\text{cm}^{-2}] = 15.30$$

$$\text{Solution : } \log n_H (\text{cm}^{-3}) = -4.03 \pm 0.03 \quad \log Z/Z_{\odot} = -0.78 \pm 0.04$$

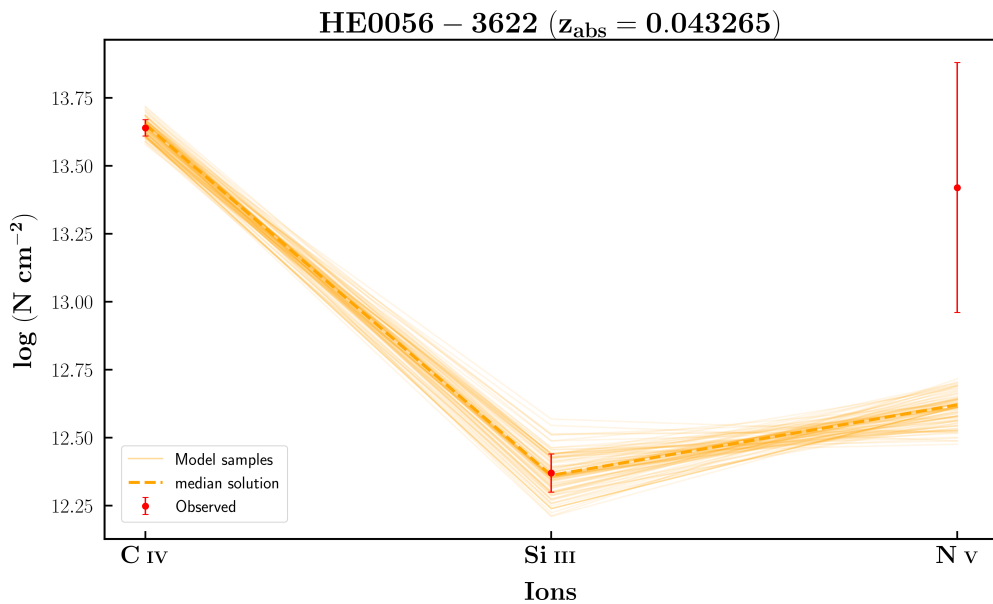


FIGURE C.42: $\log N(\text{H I}) [\text{cm}^{-2}] = 15.30$

PG1216 + 069 ($z_{\text{abs}} = 0.006328$)

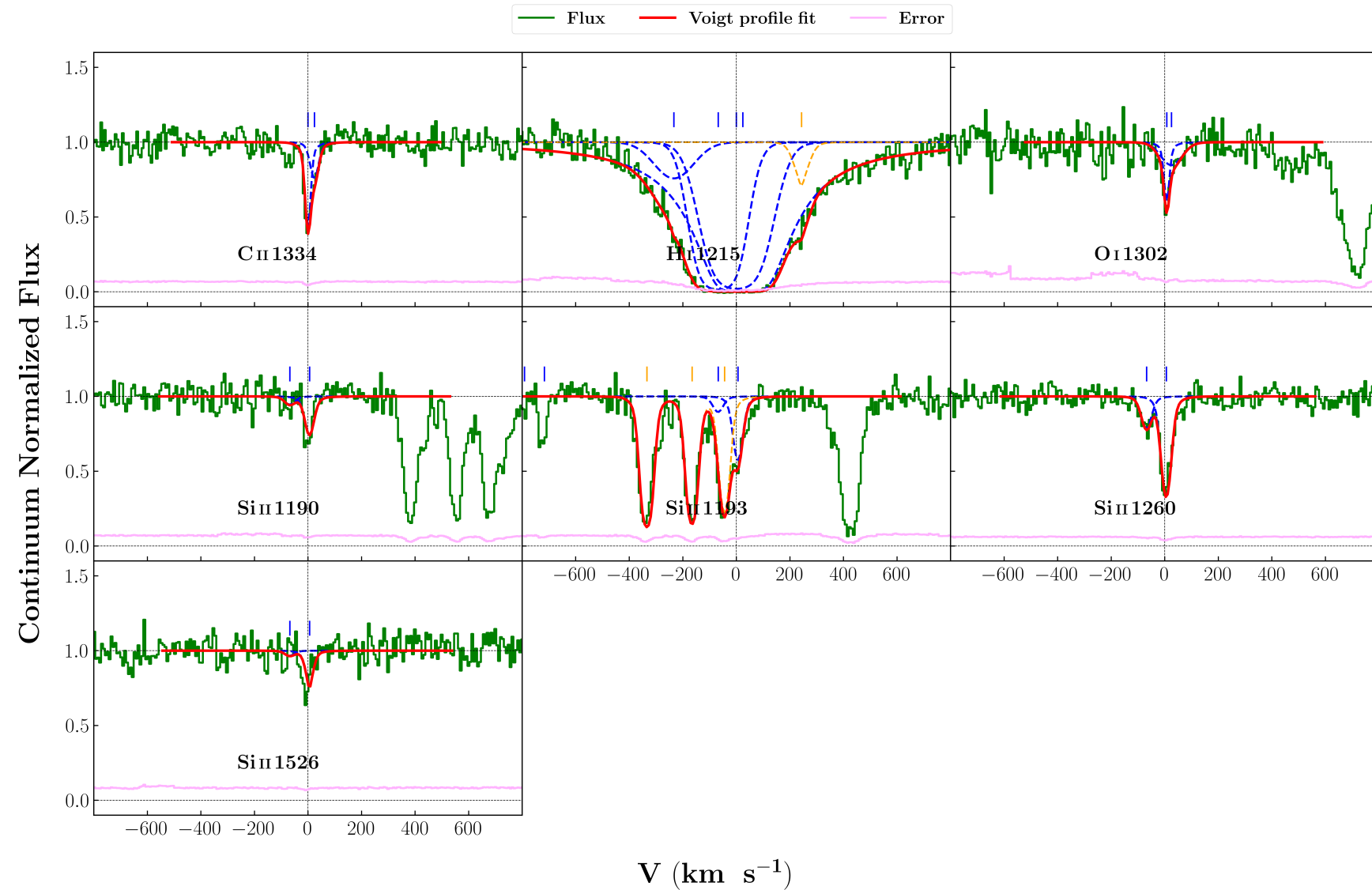


FIGURE C.43: System plot for the absorber along the LOS of PG 1216+069 at $z_{\text{abs}} = 0.006328$.

Ion	v (km s ⁻¹)	b (km s ⁻¹)	log [N cm ⁻²]
O I	8 ± 2	7 ± 5	14.07 ± 0.16
O I	25 ± 12	50 ± 13	14.0 ± 0.11
C II	0 ± 3	7 ± 5	13.98 ± 0.08
C II	24 ± 19	17 ± 6	13.43 ± 0.09
Si II	-68 ± 4	21 ± 6	12.51 ± 0.06
Si II	6 ± 1	18 ± 0	13.2 ± 0.02
H I	-233 ± 110	95 ± 15	13.56 ± 0.06
H I	-68 ± 0	81 ± 8	14.76 ± 0.12
H I	0 ± 0	106 ± 15	14.79 ± 0.08
H I	24 ± 0	20 ± 12	19.09 ± 0.03

$$\log N(H I) [\text{cm}^{-2}] = 14.79$$

$$\text{Solution : } \log n_H (\text{cm}^{-3}) = -2.69 \pm 0.05 \quad \log Z/Z_{\odot} = 1.97 \pm 0.04$$

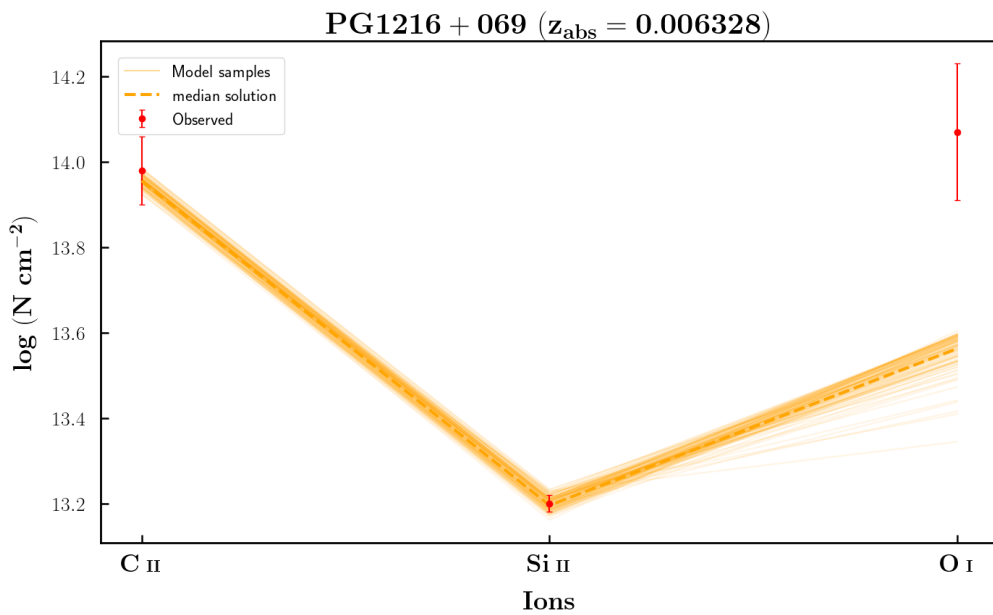


FIGURE C.44: $\log N(H I) [\text{cm}^{-2}] = 14.79$

3C263 ($z_{abs} = 0.063397$)

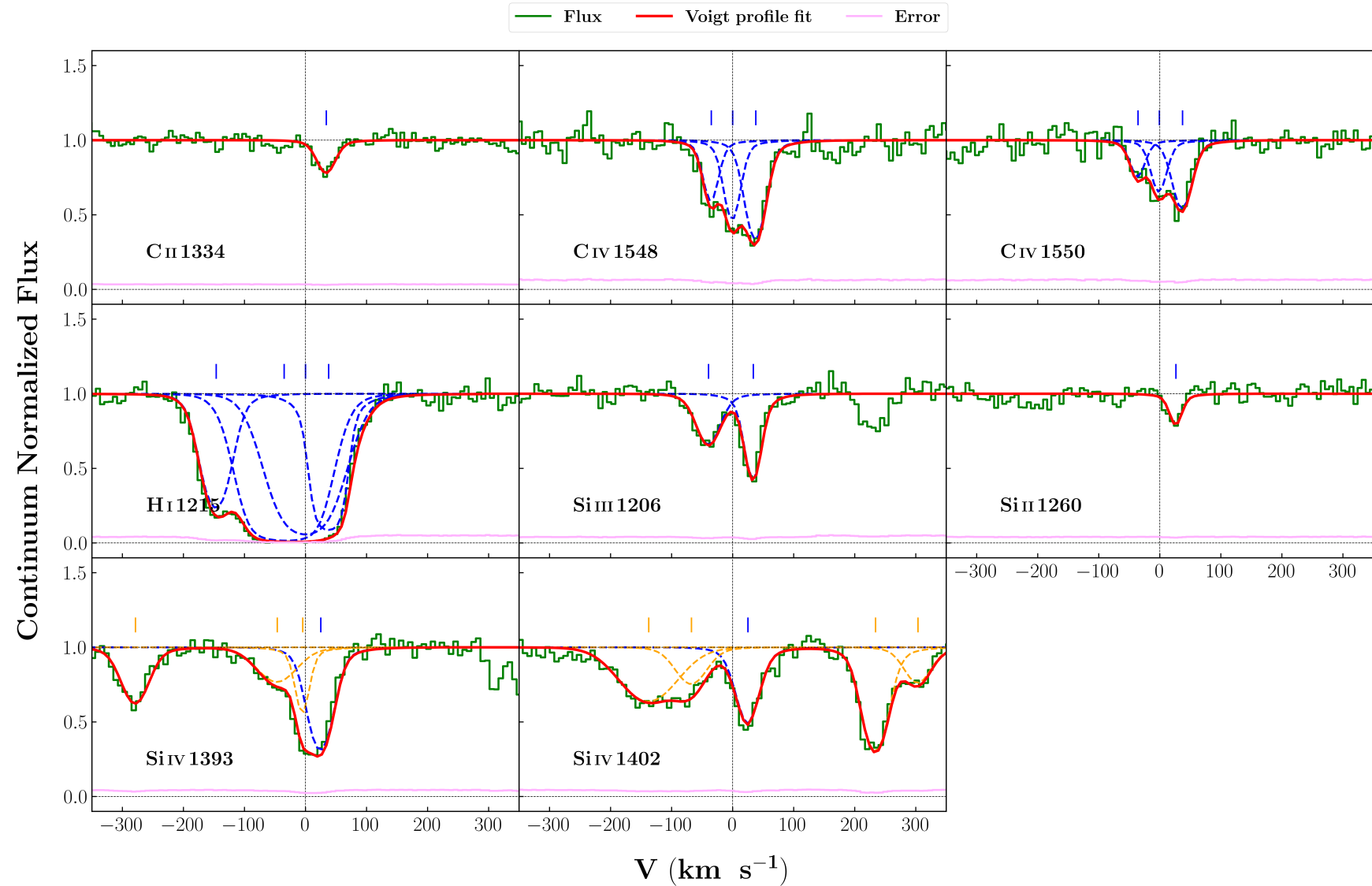


FIGURE C.45: System plot for the absorber along the LOS of 3C 263 at $z_{abs} = 0.063397$.

Ion	v (km s ⁻¹)	b (km s ⁻¹)	log [N cm ⁻²]
Si II	26 ± 2	8 ± 4	12.29 ± 0.06
Si III	-39 ± 1	21 ± 2	12.64 ± 0.03
Si III	34 ± 1	12 ± 1	12.91 ± 0.04
Si IV	25 ± 1	22 ± 0	13.57 ± 0.02
C IV	-35 ± 1	12 ± 3	13.42 ± 0.06
C IV	0 ± 2	13 ± 3	13.63 ± 0.06
C IV	38 ± 2	17 ± 2	13.86 ± 0.04
C II	34 ± 2	17 ± 3	13.37 ± 0.04
H I	-146 ± 2	25 ± 2	13.87 ± 0.04
H I	-35 ± 0	50 ± 6	14.88 ± 0.12
H I	0 ± 0	54 ± 6	14.42 ± 0.2
H I	38 ± 0	12 ± 3	16.46 ± 0.13

$$\log N(HI) [\text{cm}^{-2}] = 16.46$$

Solution : $\log n_H (\text{cm}^{-3}) = -3.72 \pm 0.02$ $\log Z/Z_{\odot} = -0.99 \pm 0.02$

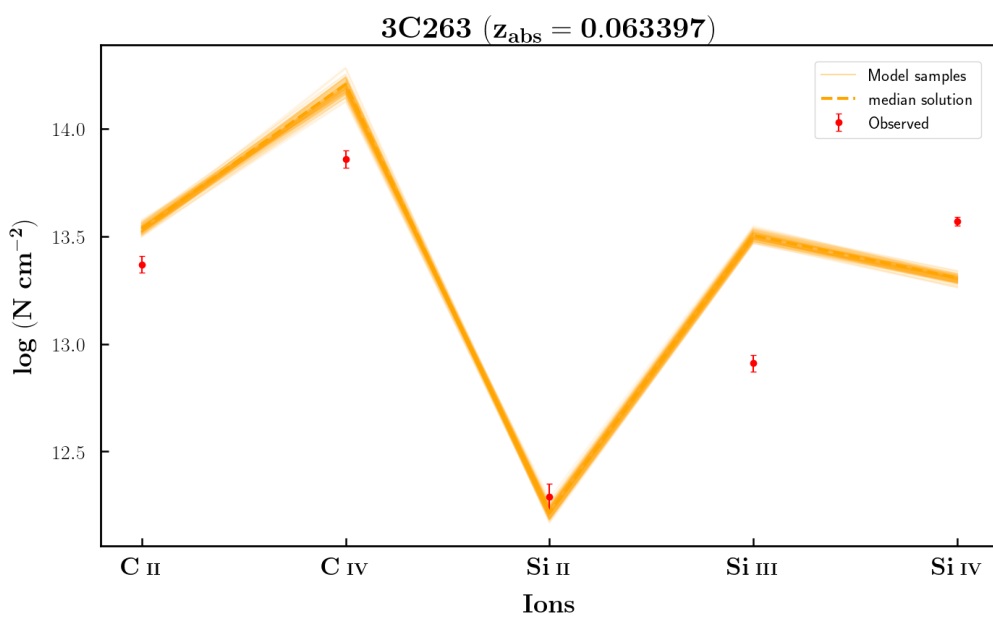


FIGURE C.46: $\log N(HI) [\text{cm}^{-2}] = 16.46$

PG1222 + 216 ($z_{\text{abs}} = 0.054479$)

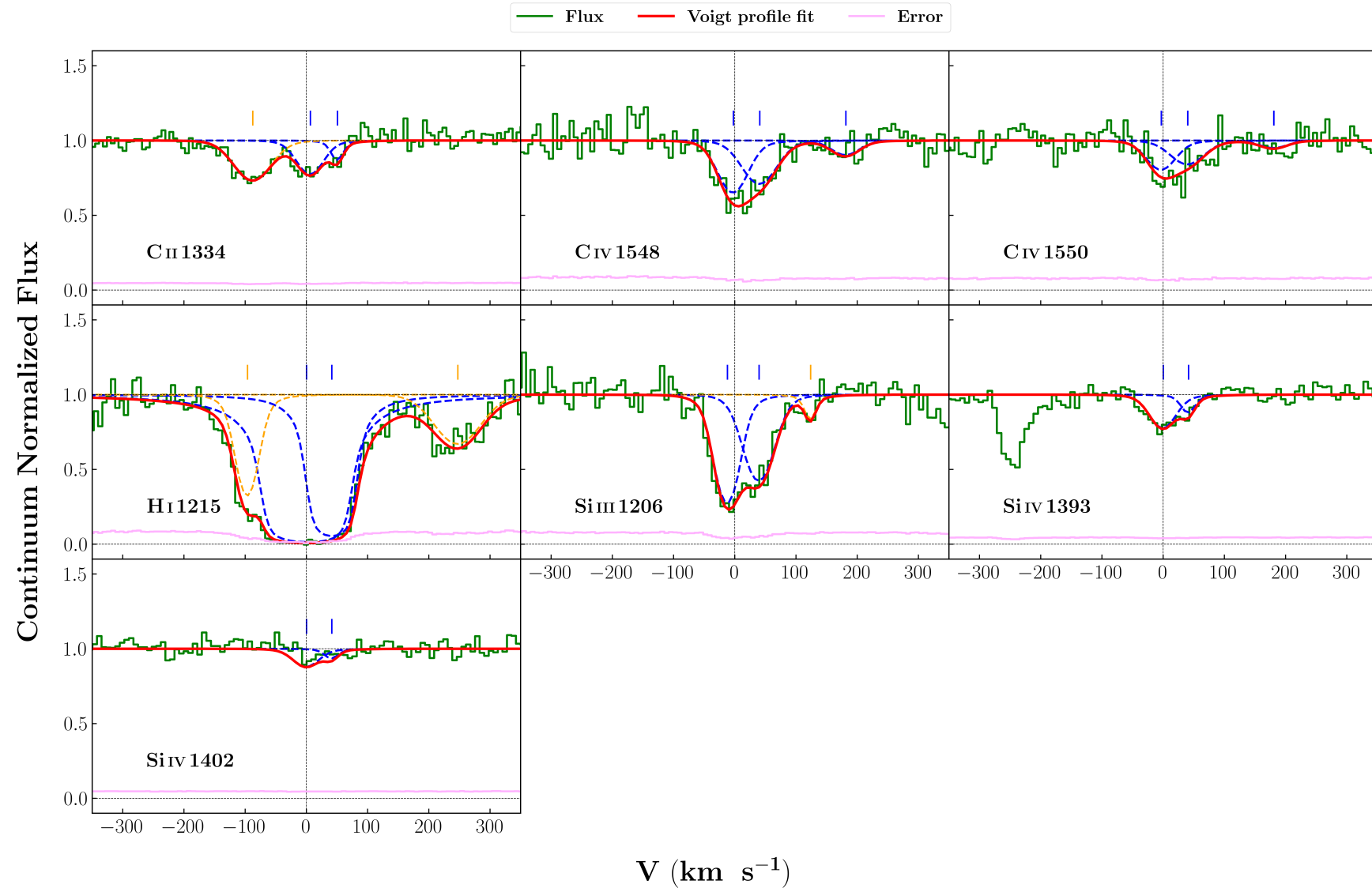


FIGURE C.47: System plot for the absorber along the LOS of PG 1222+216 at $z_{\text{abs}} = 0.054479$.

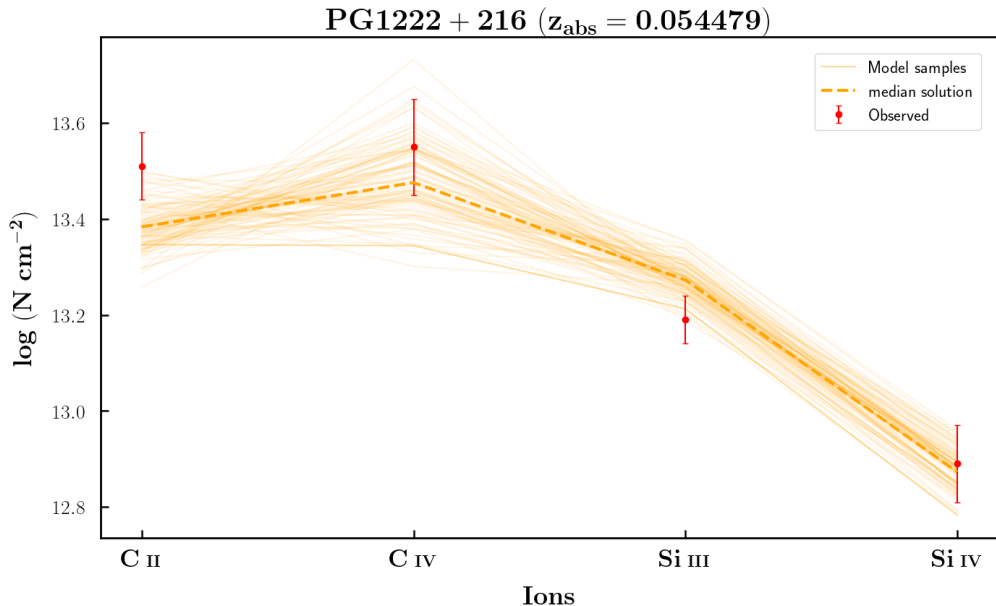
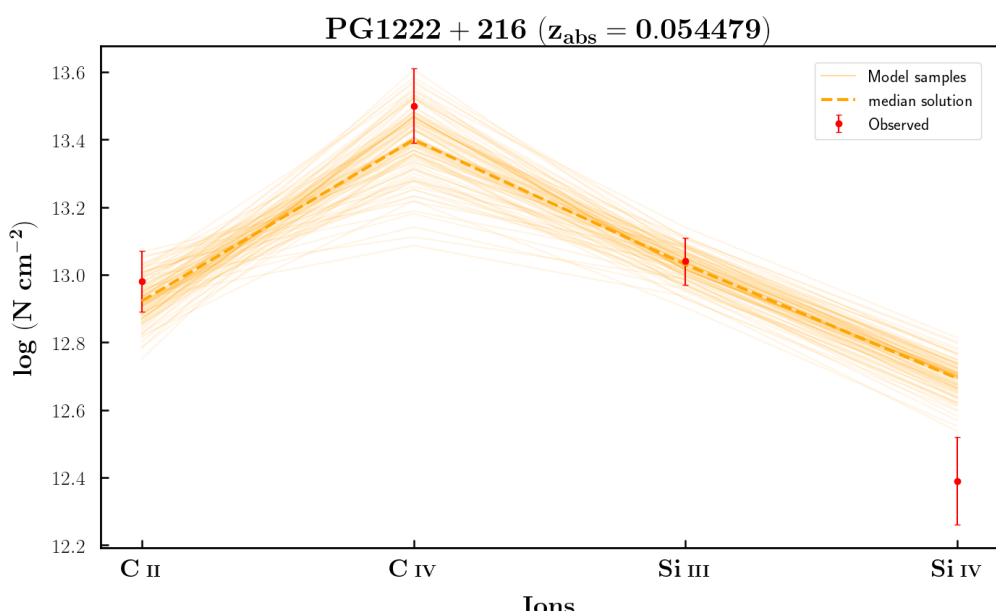
Ion	v (km s⁻¹)	b (km s⁻¹)	log [N cm⁻²]
Si III	-12 ± 3	20 ± 3	13.19 ± 0.05
Si III	40 ± 5	27 ± 5	13.04 ± 0.07
Si IV	0 ± 1	25 ± 8	12.89 ± 0.08
Si IV	41 ± 4	10 ± 7	12.39 ± 0.13
C IV	-2 ± 1	29 ± 6	13.55 ± 0.1
C IV	41 ± 8	34 ± 6	13.5 ± 0.11
C IV	182 ± 10	26 ± 15	12.86 ± 0.15
C II	7 ± 4	26 ± 6	13.51 ± 0.07
C II	51 ± 4	10 ± 6	12.98 ± 0.09
H I	-12 ± 23	74 ± 11	14.08 ± 0.15
H I	5 ± 4	24 ± 3	17.91 ± 0.15

$$\log N(H I) [\text{cm}^{-2}] = 14.08$$

$$\text{Solution : } \log n_H (\text{cm}^{-3}) = -3.45 \pm 0.06 \quad \log Z/Z_{\odot} = 1.25 \pm 0.05$$

$$\log N(H I) [\text{cm}^{-2}] = 17.91$$

$$\text{Solution : } \log n_H (\text{cm}^{-3}) = -3.86 \pm 0.08 \quad \log Z/Z_{\odot} = -2.91 \pm 0.07$$

FIGURE C.48: $\log N(\text{H I}) [\text{cm}^{-2}] = 14.08$ FIGURE C.49: $\log N(\text{H I}) [\text{cm}^{-2}] = 17.91$

RXJ0439.6 – 5311 ($z_{\text{abs}} = 0.005568$)

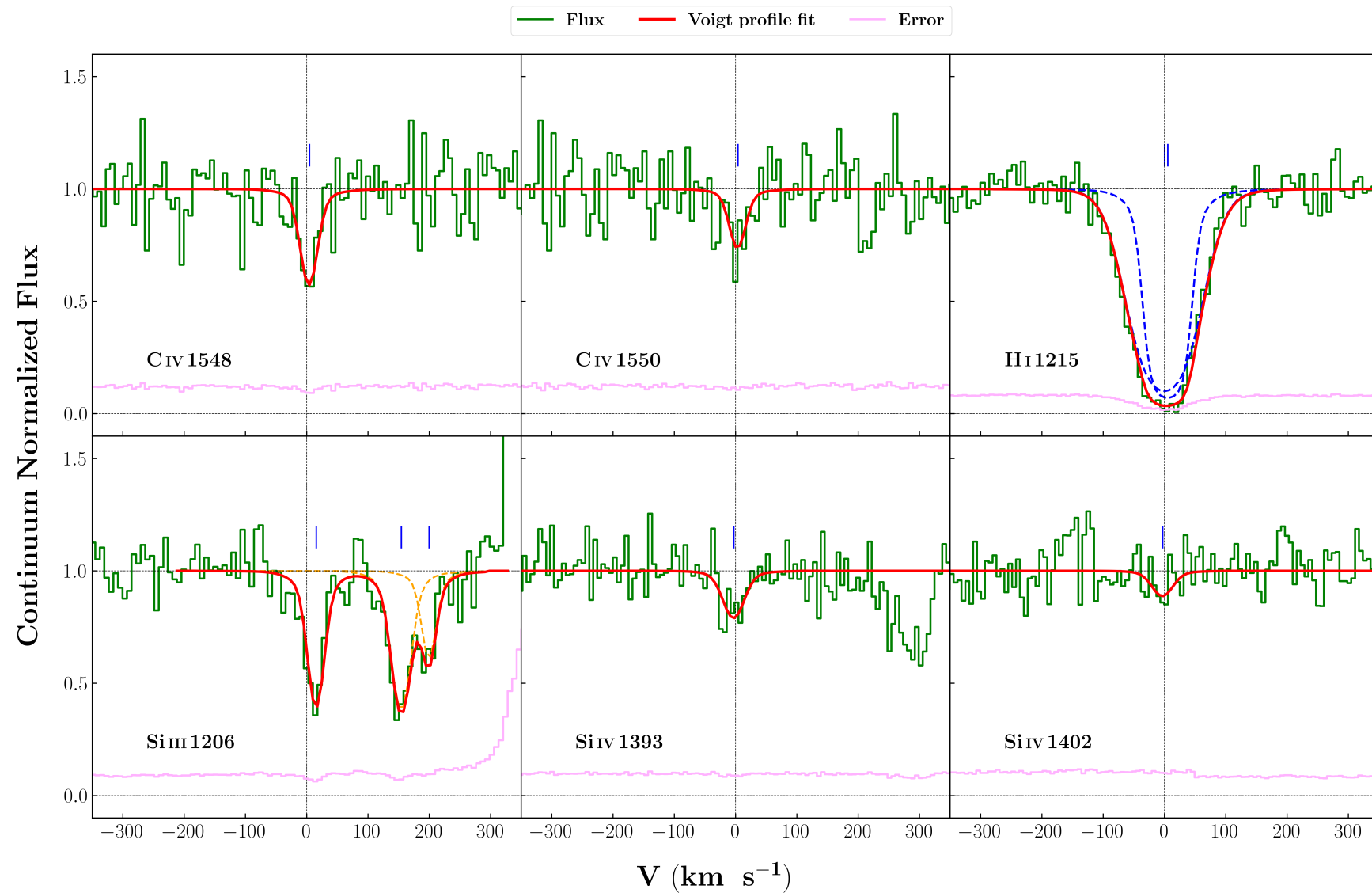


FIGURE C.50: System plot for the absorber along the LOS of RX J0439.6-5311 at $z_{\text{abs}} = 0.005568$.

Ion	v (km s ⁻¹)	b (km s ⁻¹)	log [N cm ⁻²]
Si III	16 ± 1	11 ± 3	13.01 ± 0.12
Si IV	-3 ± 4	20 ± 6	12.77 ± 0.08
C IV	4 ± 3	13 ± 5	13.5 ± 0.07
H I	0 ± 2	53 ± 6	14.3 ± 0.09
H I	5 ± 3	15 ± 6	16.11 ± 0.26

$$\log N(\text{H I}) [\text{cm}^{-2}] = 16.11$$

$$\text{Solution : } \log n_H (\text{cm}^{-3}) = -3.69 \pm 0.07 \quad \log Z/Z_{\odot} = -1.07 \pm 0.1$$

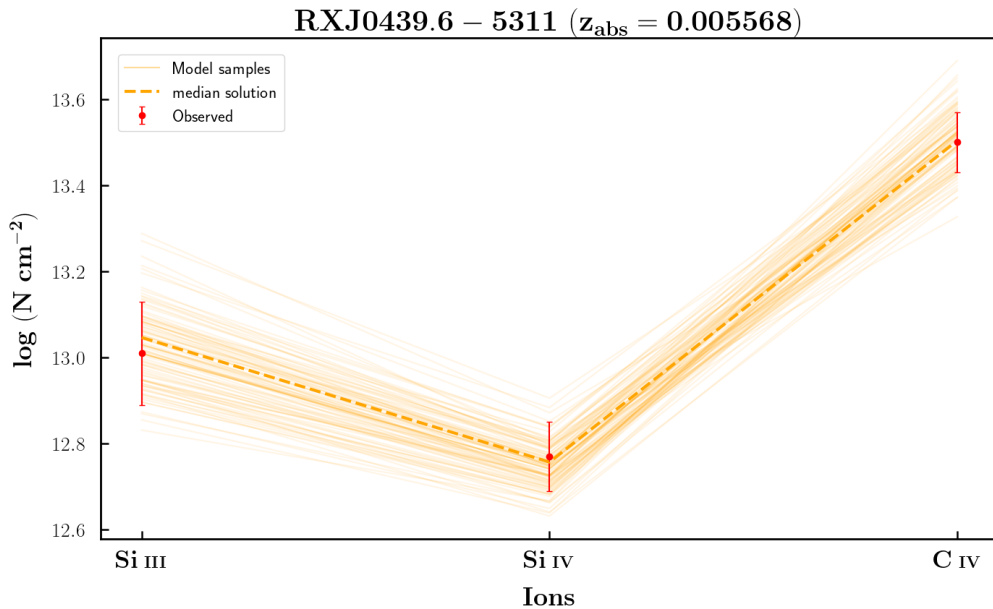


FIGURE C.51: $\log N(\text{H I}) [\text{cm}^{-2}] = 16.11$

UKS0242 – 724 ($z_{\text{abs}} = 0.063850$)

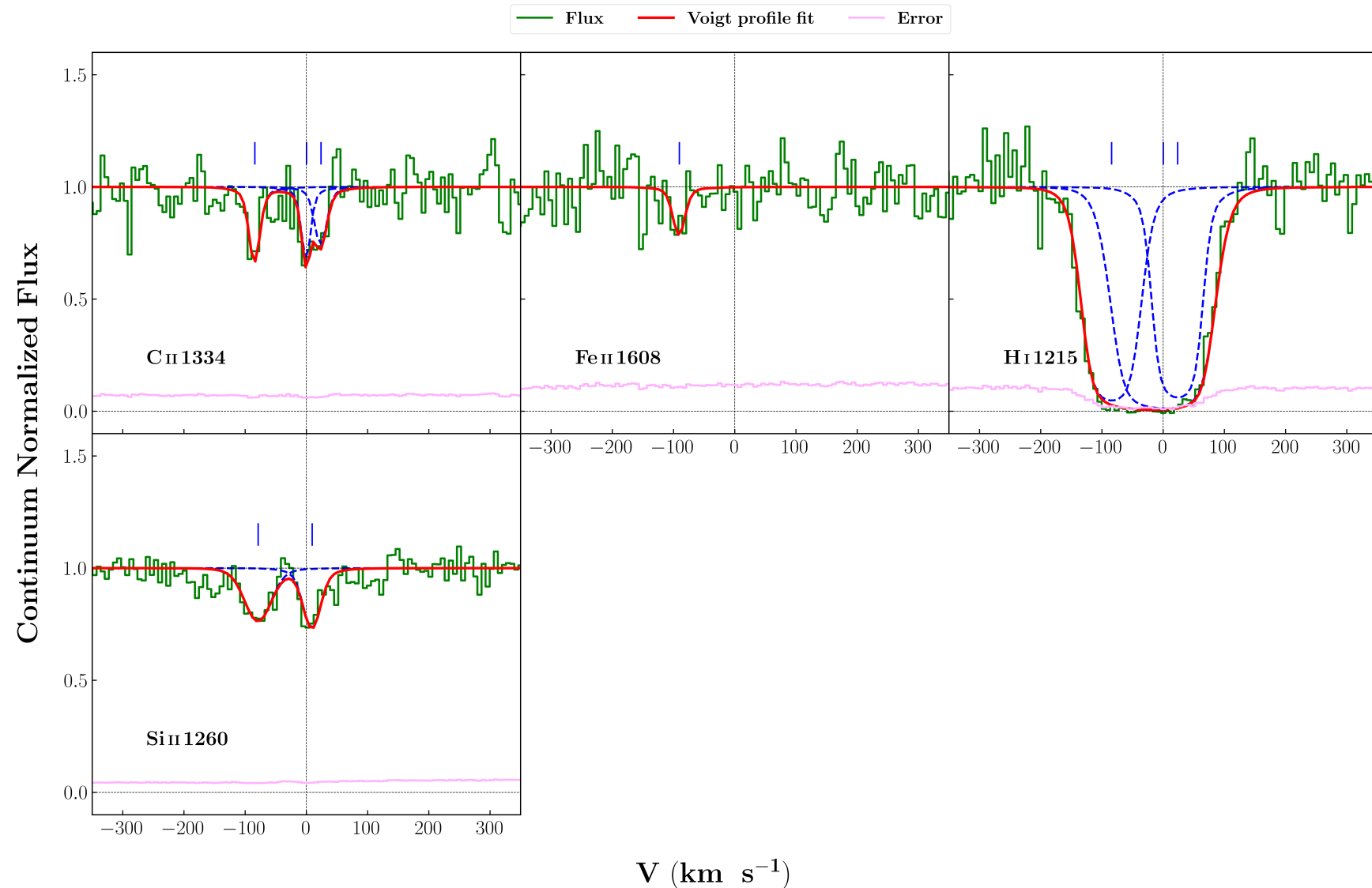


FIGURE C.52: System plot for the absorber along the LOS of UKS 0242-724 at $z_{\text{abs}} = 0.063850$.

Ion	v (km s ⁻¹)	b (km s ⁻¹)	log [N cm ⁻²]
Fe II	-90 ± 4	9 ± 9	13.49 ± 0.14
C II	-84 ± 2	7 ± 5	13.46 ± 0.11
C II	0 ± 3	3 ± 7	13.55 ± 0.16
C II	24 ± 5	9 ± 6	13.32 ± 0.1
Si II	-78 ± 3	25 ± 5	12.6 ± 0.05
Si II	10 ± 2	15 ± 4	12.52 ± 0.06
H I	-84 ± 0	30 ± 5	14.61 ± 0.06
H I	0 ± 0	46 ± 6	15.17 ± 0.1
H I	24 ± 0	19 ± 6	15.34 ± 1.33

$$\log N(H I) [\text{cm}^{-2}] = 14.61$$

$$\text{Solution : } \log n_H (\text{cm}^{-3}) = -2.23 \pm 0.13 \quad \log Z/Z_{\odot} = 1.92 \pm 0.10$$

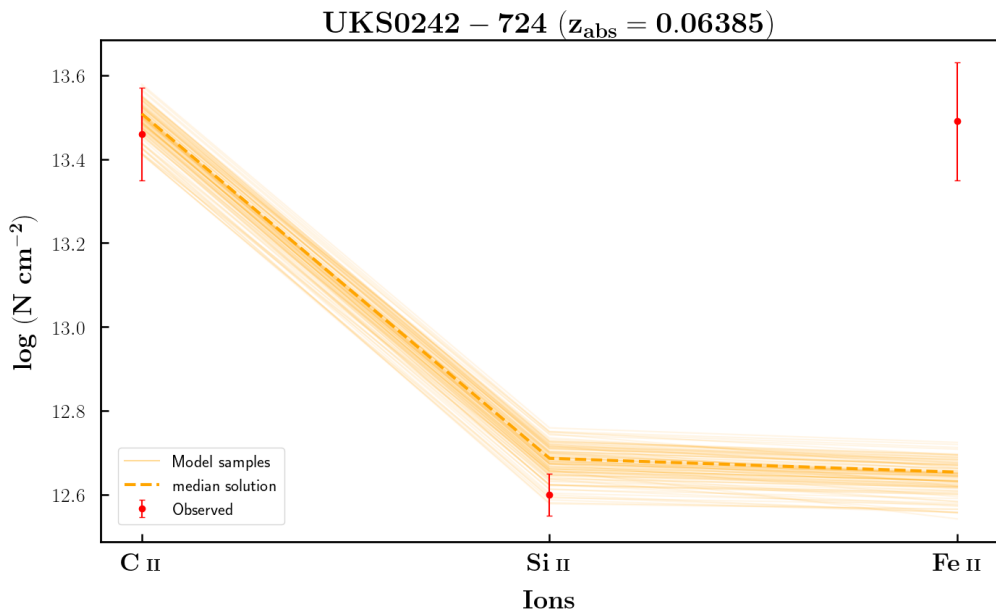


FIGURE C.53: $\log N(H I) [\text{cm}^{-2}] = 14.61$

PG1259 + 593 ($z_{\text{abs}} = 0.046284$)

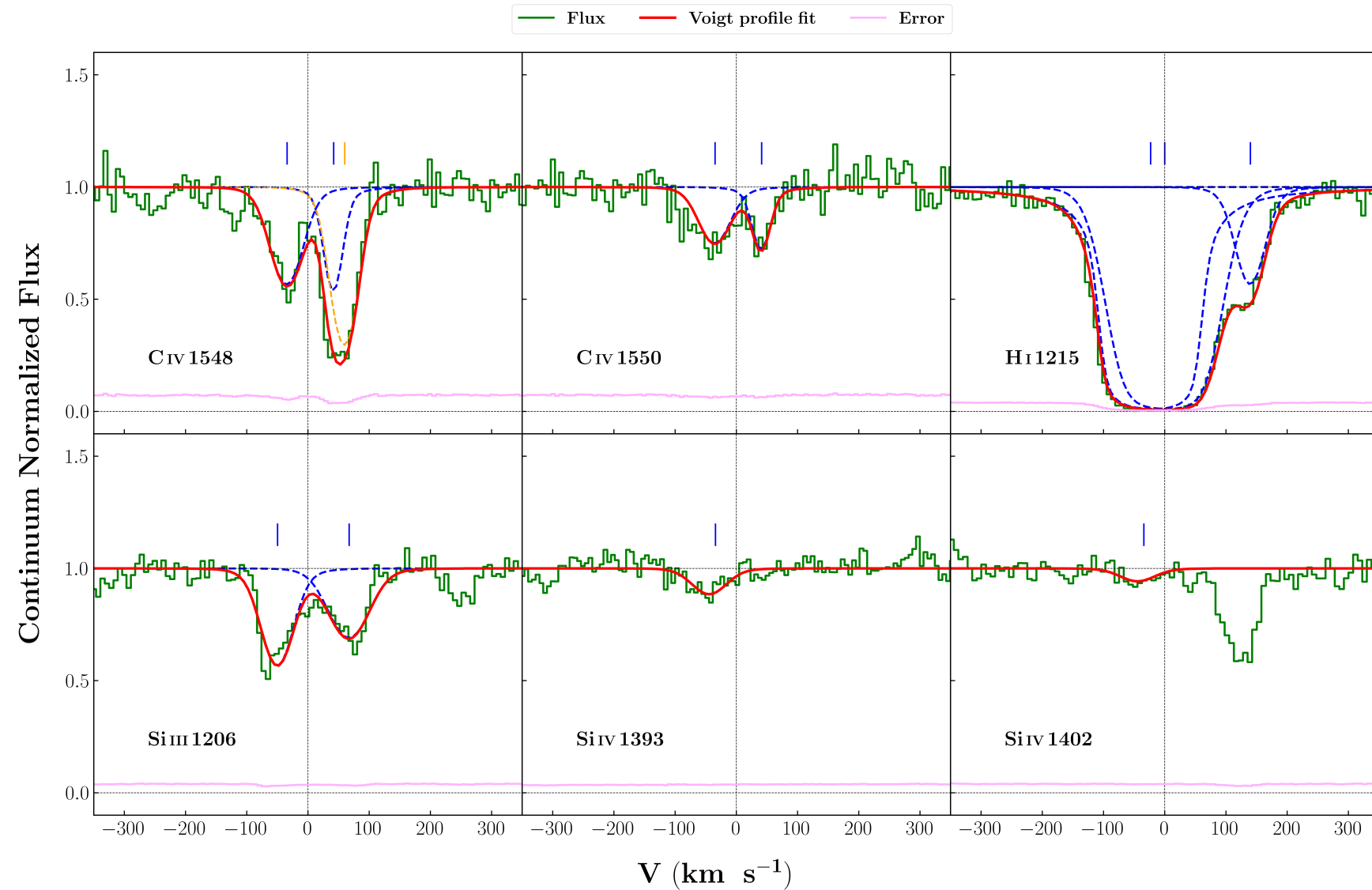


FIGURE C.54: System plot for the absorber along the LOS of PG 1259+593 at $z_{\text{abs}} = 0.046284$.

Ion	v (km s ⁻¹)	b (km s ⁻¹)	log [N cm ⁻²]
C IV	-34 ± 2	31 ± 3	13.7 ± 0.03
C IV	42 ± 2	16 ± 3	13.56 ± 0.05
Si IV	-43 ± 4	35 ± 6	12.67 ± 0.05
Si III	-50 ± 2	29 ± 3	12.87 ± 0.03
Si III	67 ± 3	40 ± 5	12.78 ± 0.04
H I	-590 ± 8	47 ± 12	12.79 ± 0.08
H I	-23 ± 7	26 ± 3	17.79 ± 0.07
H I	0 ± 5	61 ± 7	14.86 ± 0.06
H I	140 ± 3	27 ± 4	13.43 ± 0.07

$$\log N(H I) [\text{cm}^{-2}] = 17.79$$

Solution : $\log n_H (\text{cm}^{-3}) = -4.23 \pm 0.04$ $\log Z/Z_{\odot} = -3.18 \pm 0.04$

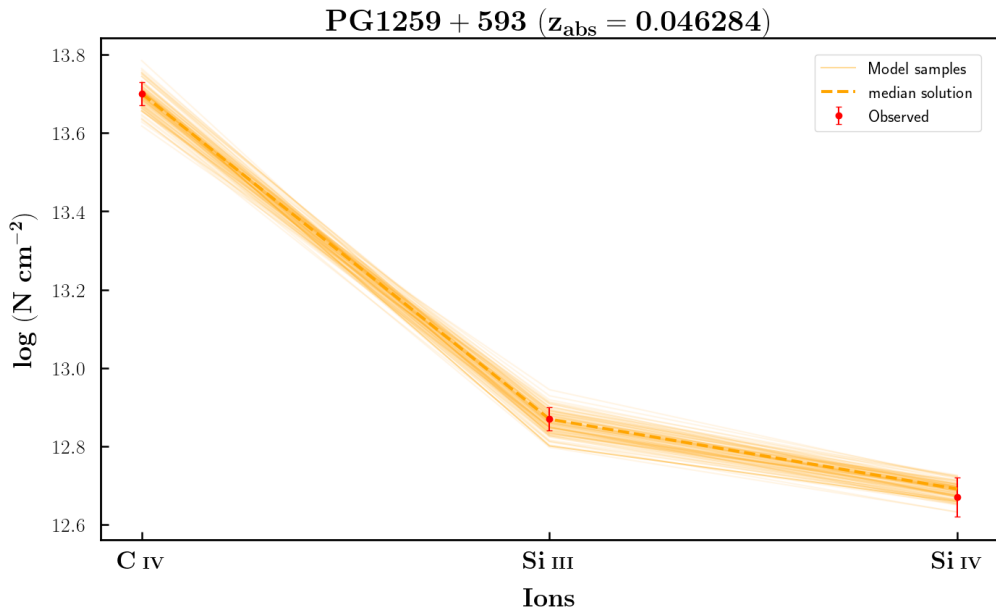


FIGURE C.55: $\log N(H I) [\text{cm}^{-2}] = 17.79$

PKS1302 – 102 ($z_{abs} = 0.094839$)

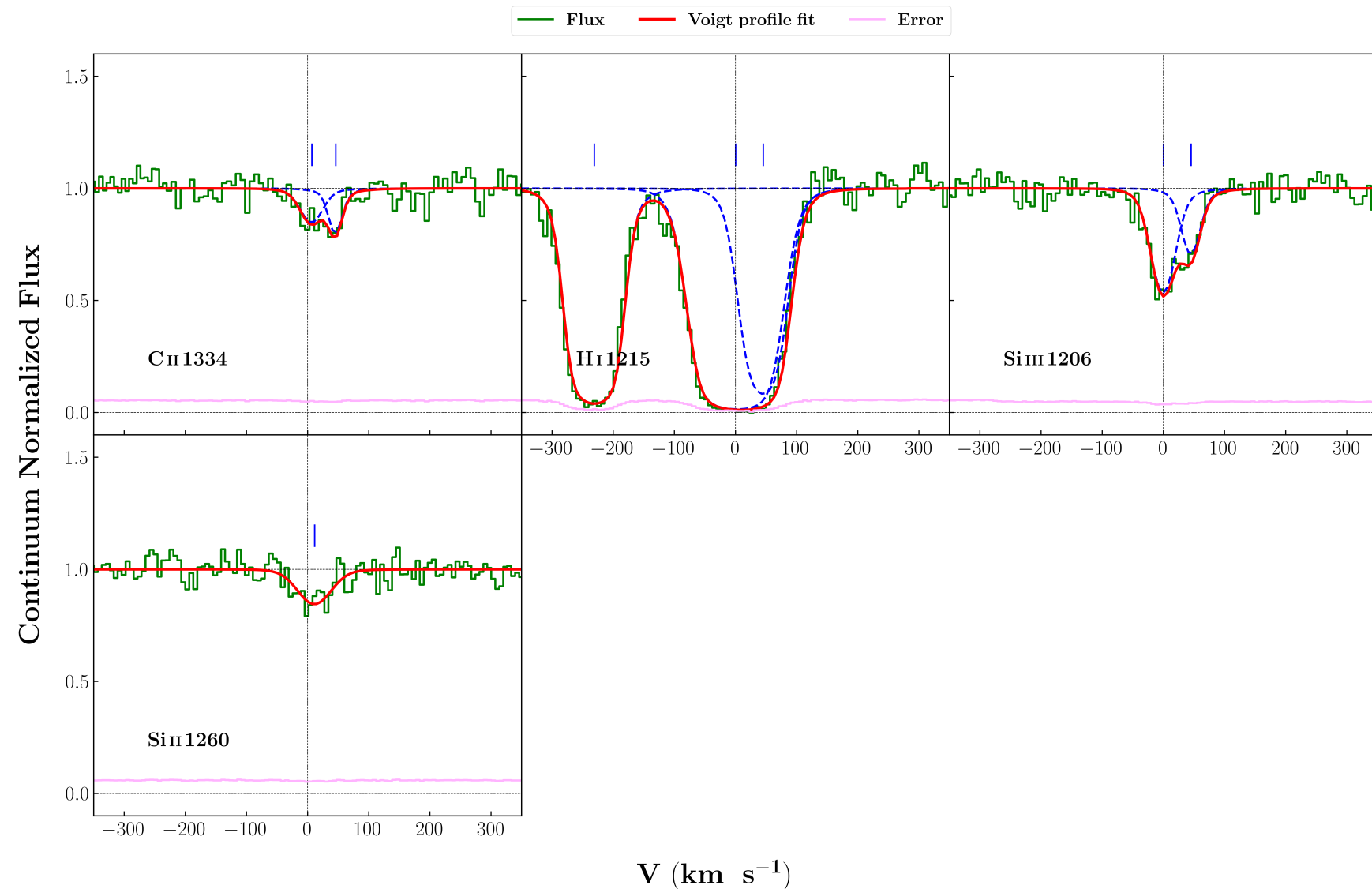


FIGURE C.56: System plot for the absorber along the LOS of PKS 1302-102 at $z_{abs} = 0.094839$.

Ion	v (km s ⁻¹)	b (km s ⁻¹)	log [N cm ⁻²]
Si III	0 ± 2	22 ± 3	12.82 ± 0.04
Si III	45 ± 3	16 ± 4	12.48 ± 0.08
Si II	11 ± 5	34 ± 7	12.48 ± 0.06
C II	7 ± 8	21 ± 8	13.27 ± 0.09
C II	46 ± 4	10 ± 5	13.25 ± 0.09
H I	-229 ± 1	29 ± 2	14.81 ± 0.14
H I	0 ± 0	46 ± 2	14.96 ± 0.1
H I	45 ± 0	31 ± 4	14.25 ± 0.14

$$\log N(H I) [\text{cm}^{-2}] = 14.96$$

$$\text{Solution : } \log n_H (\text{cm}^{-3}) = -4.14 \pm 0.04 \quad \log Z/Z_{\odot} = 0.64 \pm 0.03$$

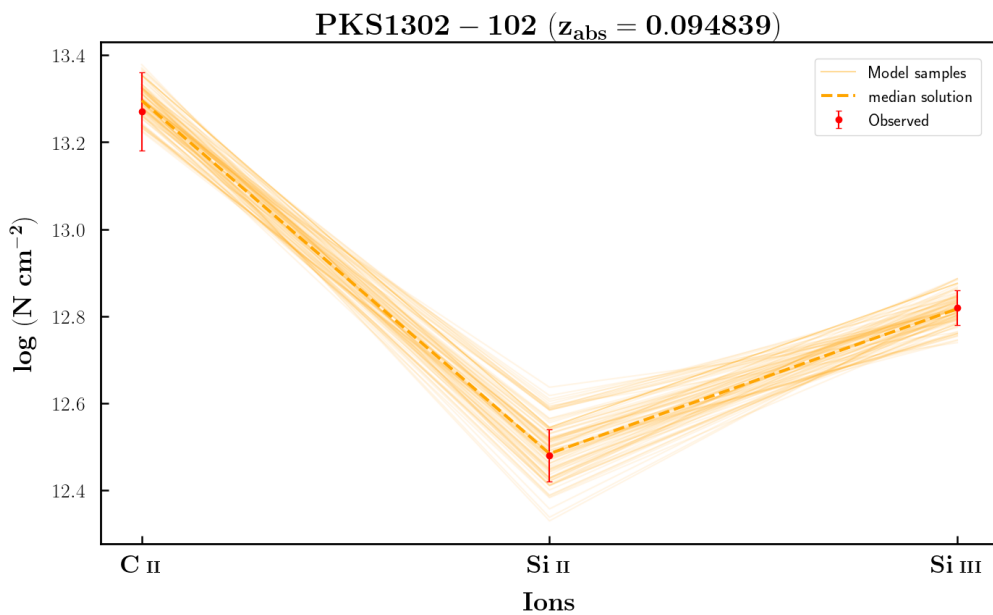


FIGURE C.57: $\log N(H I) [\text{cm}^{-2}] = 14.96$

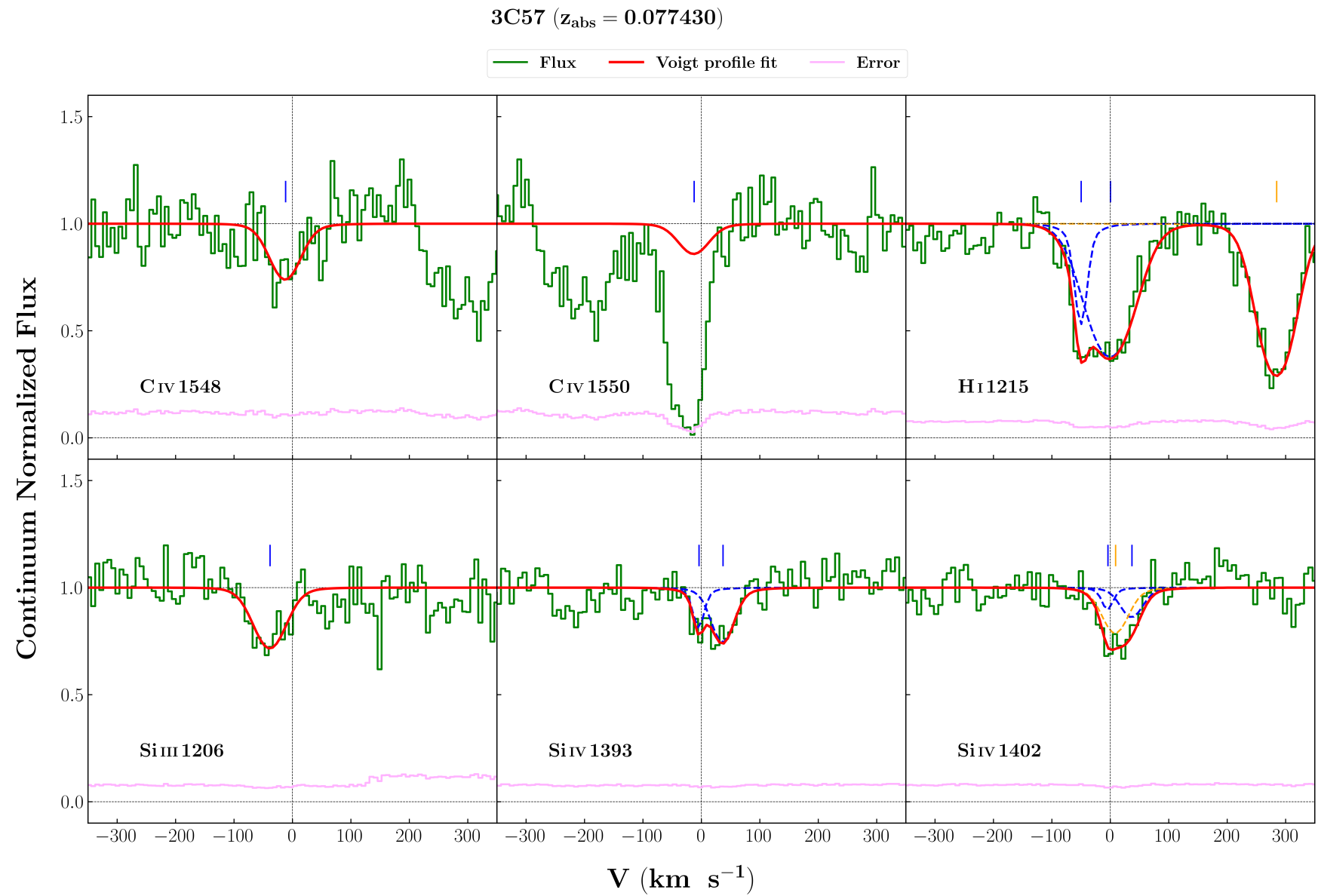


FIGURE C.58: System plot for the absorber along the LOS of 3C 57 at $z_{\text{abs}} = 0.077430$.

Ion	v (km s ⁻¹)	b (km s ⁻¹)	log [N cm ⁻²]
C IV	-12 ± 6	32 ± 9	13.43 ± 0.08
Si IV	-4 ± 4	7 ± 6	12.54 ± 0.09
Si IV	37 ± 4	22 ± 6	12.92 ± 0.07
Si III	-38 ± 5	34 ± 7	12.67 ± 0.06
H I	-50 ± 2	8 ± 4	13.3 ± 0.08
H I	0 ± 4	50 ± 4	13.86 ± 0.04

$$\log N(\text{H I}) [\text{cm}^{-2}] = 13.30$$

$$\text{Solution : } \log n_H (\text{cm}^{-3}) = -3.73 \pm 0.05 \quad \log Z/Z_{\odot} = 1.38 \pm 0.05$$

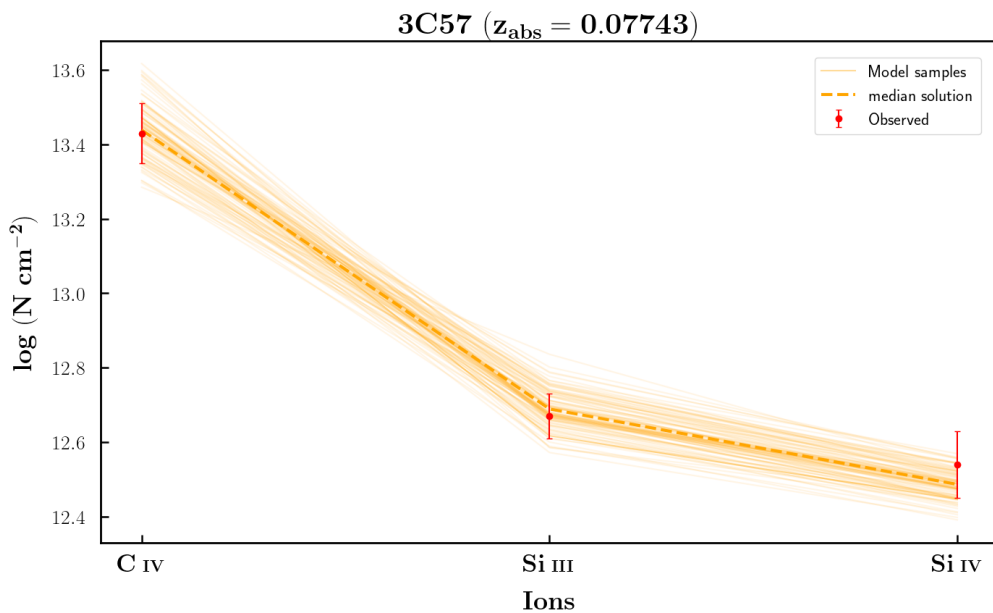


FIGURE C.59: $\log N(\text{H I}) [\text{cm}^{-2}] = 13.30$

PMNJ1103 – 2329 ($z_{\text{abs}} = 0.003934$)

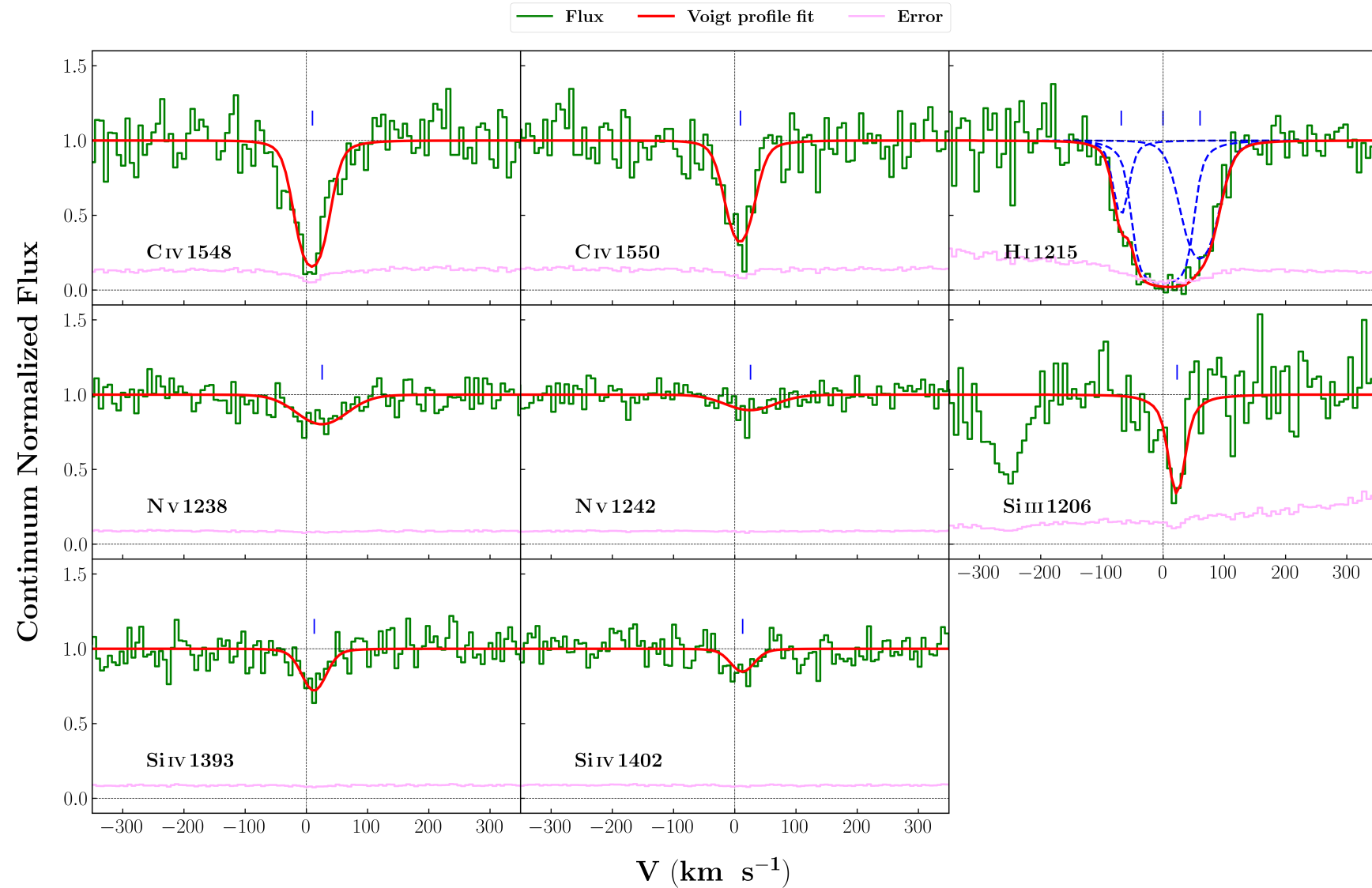


FIGURE C.60: System plot for the absorber along the LOS of PMN J1103-2329 at $z_{\text{abs}} = 0.003934$.

Ion	v (km s ⁻¹)	b (km s ⁻¹)	log [N cm ⁻²]
Si III	23 ± 3	4 ± 3	15.02 ± 0.22
Si IV	13 ± 3	23 ± 5	12.96 ± 0.06
N V	22 ± 5	52 ± 8	13.65 ± 0.05
C IV	10 ± 1	24 ± 2	14.26 ± 0.04
H I	-68 ± 6	10 ± 7	13.37 ± 0.09
H I	0 ± 12	19 ± 2	16.29 ± 0.19
H I	60 ± 27	28 ± 4	13.95 ± 0.05

$$\log N(\text{H I}) [\text{cm}^{-2}] = 16.29$$

Solution : $\log n_H (\text{cm}^{-3}) = -4.17 \pm 0.03$ $\log Z/Z_{\odot} = -1.08 \pm 0.04$

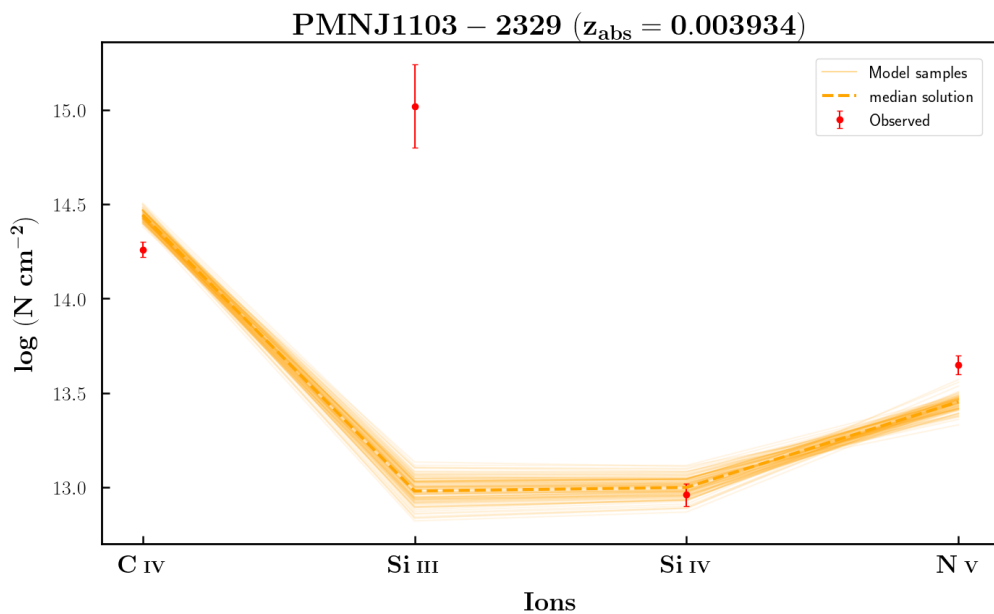


FIGURE C.61: $\log N(\text{H I}) [\text{cm}^{-2}] = 16.29$

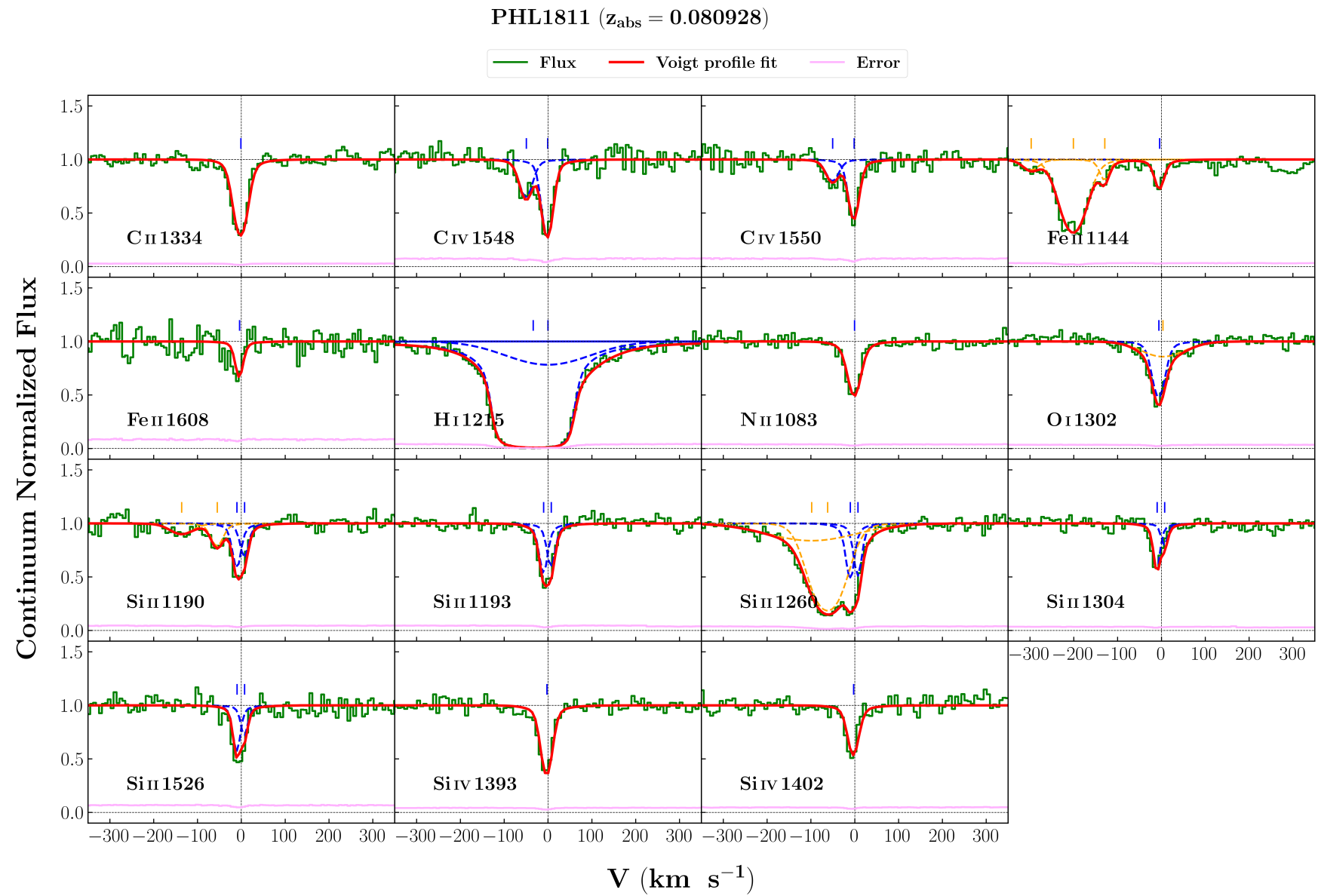


FIGURE C.62: System plot for the absorber along the LOS of PHL 1811 at $z_{\text{abs}} = 0.080928$.

Ion	v (km s⁻¹)	b (km s⁻¹)	log [N cm⁻²]
O I	-6 ± 1	15 ± 2	14.29 ± 0.05
C II	-1 ± 1	16 ± 1	14.15 ± 0.02
N II	-1 ± 1	13 ± 1	14.06 ± 0.03
C IV	-49 ± 2	16 ± 3	13.38 ± 0.04
C IV	-1 ± 1	11 ± 1	13.93 ± 0.04
Si IV	-2 ± 1	11 ± 1	13.46 ± 0.03
Fe II	-4 ± 1	7 ± 3	13.7 ± 0.07
Si II	-10 ± 1	3 ± 1	14.24 ± 0.07
Si II	7 ± 1	4 ± 1	13.33 ± 0.08
H I	-875 ± 1	32 ± 1	14.6 ± 0.06
H I	-528 ± 0	30 ± 2	15.38 ± 0.05
H I	-34 ± 1	29 ± 1	18.02 ± 0.11
H I	0 ± 19	126 ± 23	13.62 ± 0.07

$$\log N(H I) [\text{cm}^{-2}] = 18.02$$

Using all ions :

$$\text{Solution : } \log n_H (\text{cm}^{-3}) = -3.11 \pm 0.01 \quad \log Z/Z_{\odot} = -1.28 \pm 0.01$$

Using C II, C IV, Si II and Si IV :

$$\text{Solution : } \log n_H (\text{cm}^{-3}) = -3.44 \pm 0.02 \quad \log Z/Z_{\odot} = -1.7 \pm 0.02$$

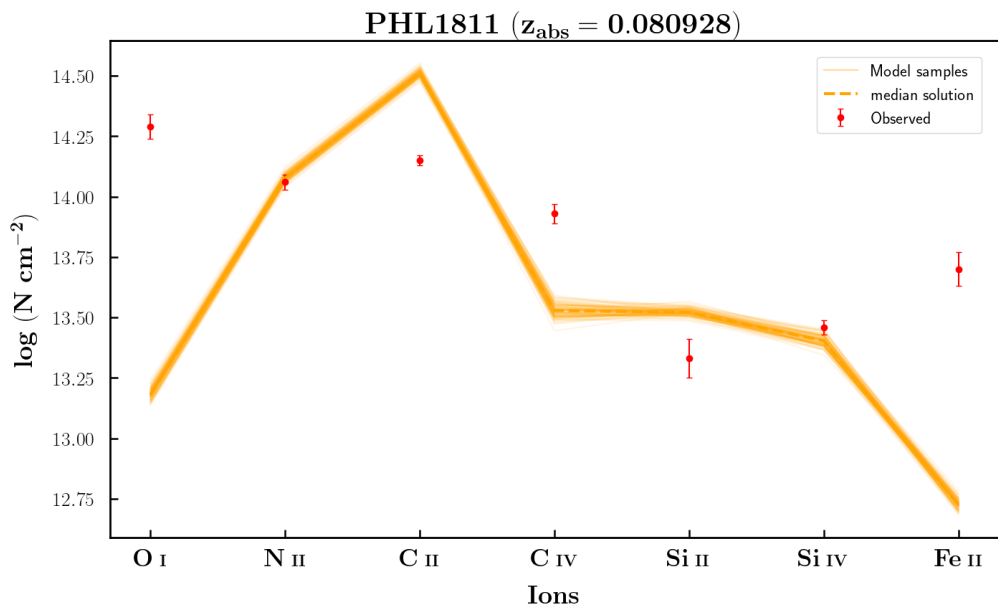


FIGURE C.63: $\log N(\text{H I}) [\text{cm}^{-2}] = 18.02$, all ions

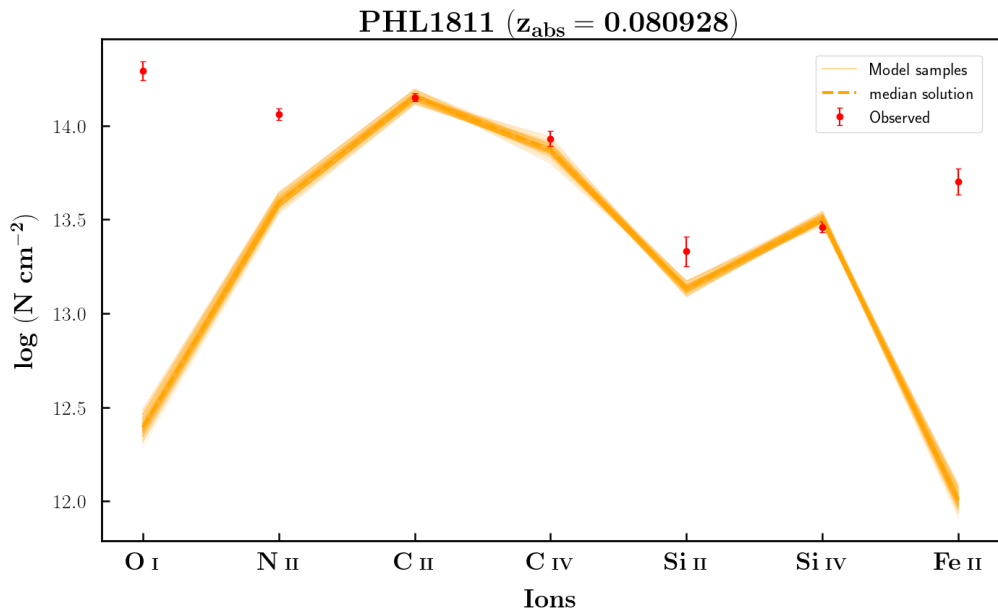


FIGURE C.64: $\log N(\text{H I}) [\text{cm}^{-2}] = 18.02$, C II, C IV, Si II and Si IV

PG0832 + 251 ($z_{\text{abs}} = 0.017505$)

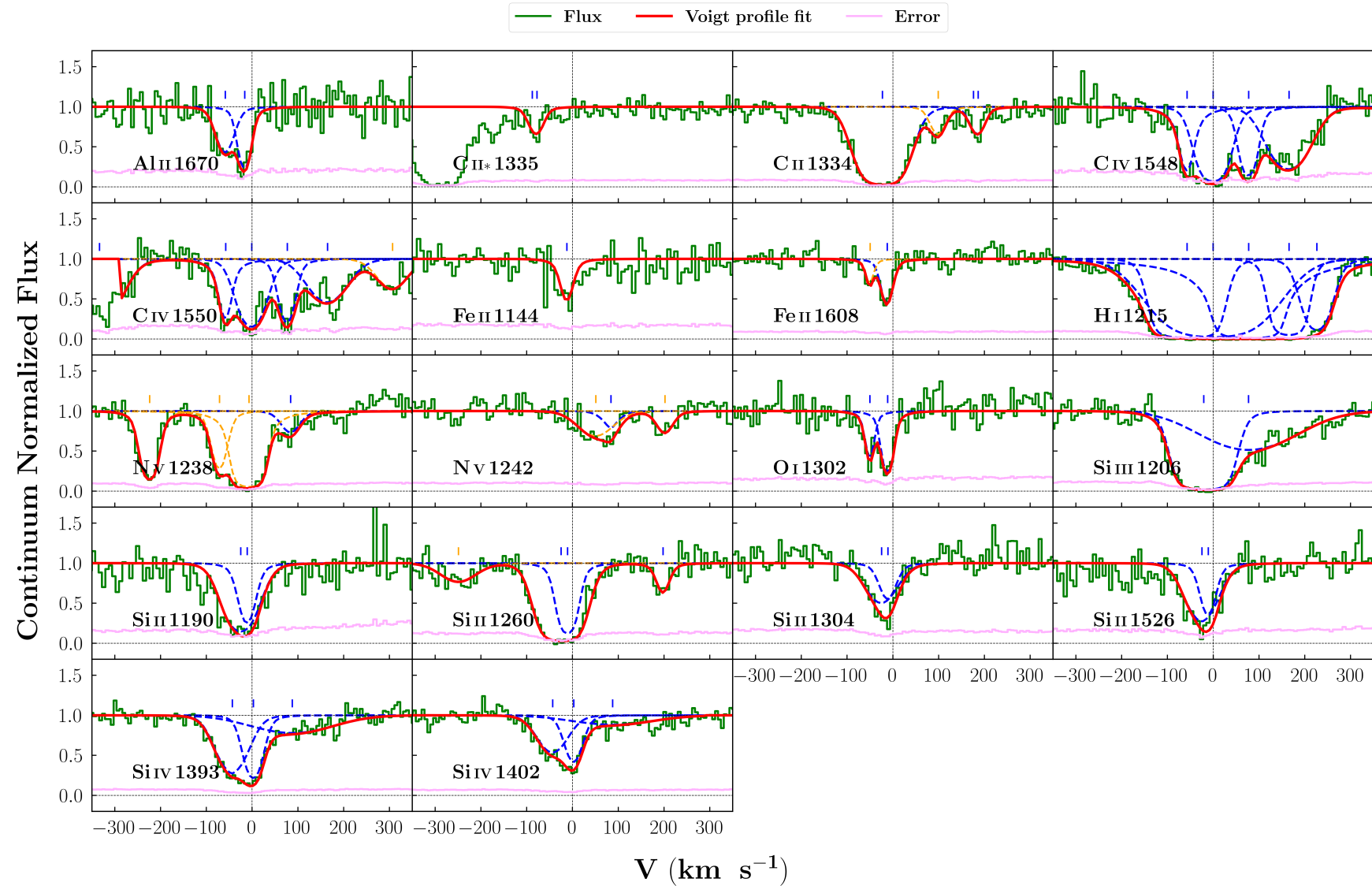


FIGURE C.65: System plot for the absorber along the LOS of PG 0832+251 at $z_{\text{abs}} = 0.017505$.

Ion	v (km s⁻¹)	b (km s⁻¹)	log [N cm⁻²]
Al II	-58 ± 7	21 ± 6	12.76 ± 0.08
Al II	-16 ± 4	12 ± 4	13.04 ± 0.11
O I	-50 ± 2	4 ± 2	15.28 ± 0.41
O I	-11 ± 1	7 ± 3	15.76 ± 0.28
Fe II	-12 ± 1	12 ± 3	14.16 ± 0.07
Si IV	-43 ± 8	39 ± 6	13.72 ± 0.1
Si IV	3 ± 3	21 ± 3	13.68 ± 0.11
Si IV	88 ± 1	120 ± 15	13.46 ± 0.05
C IV	-57 ± 2	4 ± 1	17.26 ± 0.12
C IV	0 ± 3	31 ± 3	14.59 ± 0.08
C IV	78 ± 1	15 ± 3	14.45 ± 0.07
C IV	166 ± 3	51 ± 4	14.31 ± 0.03
Si II	-25 ± 1	38 ± 2	14.29 ± 0.06
Si II	-11 ± 4	15 ± 2	14.02 ± 0.13
Si II	198 ± 4	13 ± 7	12.7 ± 0.09
Si III	-21 ± 2	38 ± 7	14.67 ± 0.06
Si III	77 ± 17	130 ± 14	13.48 ± 0.07
N V	84 ± 6	23 ± 7	13.53 ± 0.08
C II	-23 ± 1	43 ± 3	15.2 ± 0.1
C II	-78 ± 3	10 ± 0	13.7 ± 0.08
H I	-57 ± 0	38 ± 6	15.82 ± 0.17
H I	0 ± 0	115 ± 26	14.79 ± 0.07
H I	78 ± 0	24 ± 5	18.22 ± 0.11
H I	166 ± 0	20 ± 6	15.83 ± 0.98
H I	227 ± 0	29 ± 4	14.18 ± 0.09

$$\log N(\text{H I}) [\text{cm}^{-2}] = 15.82$$

Solution : $\log n_H (\text{cm}^{-3}) = -4.09 \pm 0.05$

$$\log Z/Z_{\odot} = 1.4 \pm 0.07$$

$$\log N(\text{H I}) [\text{cm}^{-2}] = 14.79$$

Solution : $\log n_H (\text{cm}^{-3}) = -3.74 \pm 0.02$

$$\log Z/Z_{\odot} = 2.0 \pm 0.0$$

Excluding O I, Fe II and Al II

Solution : $\log n_H (\text{cm}^{-3}) = -4.11 \pm 0.02$

$$\log Z/Z_{\odot} = 2.0 \pm 0.01$$

$$\log N(\text{H I}) [\text{cm}^{-2}] = 18.22$$

Solution : $\log n_H (\text{cm}^{-3}) = -4.68 \pm 0.07$

$$\log Z/Z_{\odot} = -2.97 \pm 0.08$$

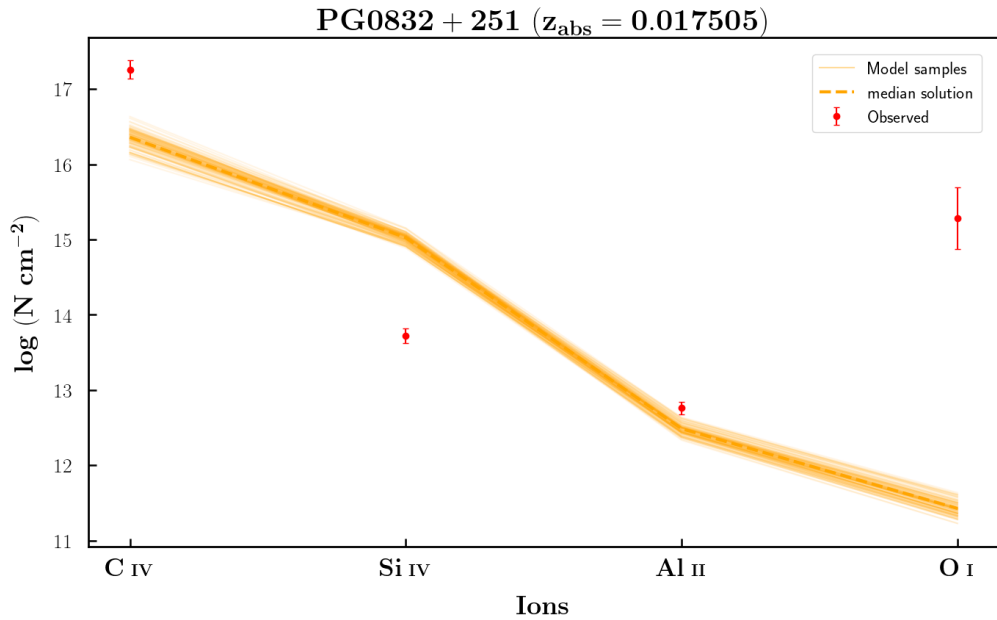


FIGURE C.66: $\log N(\text{H I}) [\text{cm}^{-2}] = 15.82$

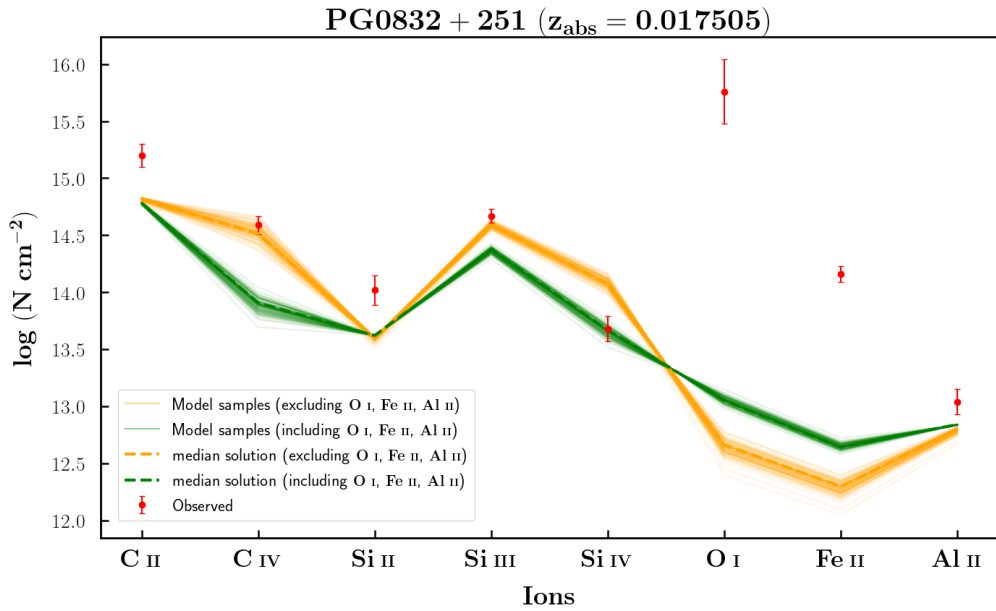


FIGURE C.67: $\log N(\text{H I}) [\text{cm}^{-2}] = 14.79$, excluding O I, Fe II and Al II

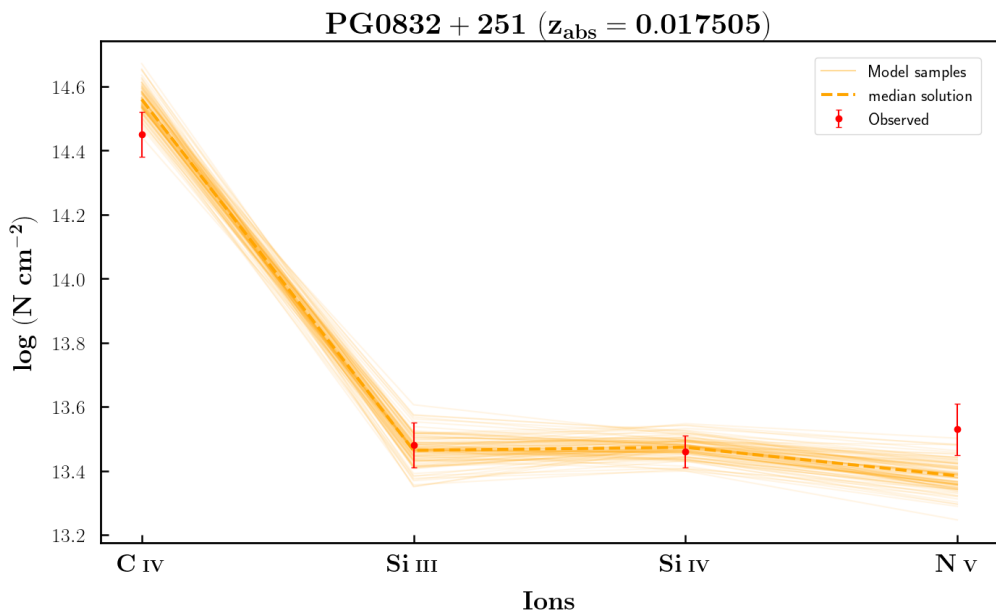


FIGURE C.68: $\log N(\text{H I}) [\text{cm}^{-2}] = 18.22$